CUTTING-EDGE ANALOGUE MODELING TECHNIQUES APPLIED TO STUDY EARTH SYSTEMS

EDITED BY: Mélody Philippon, Christoph Von Hagke, Jacqueline E. Reber
and Alain Zanella
PUBLISHED IN: Frontiers in Earth Science

frontiers Research Topics

ISSN 1664-8714
ISBN 978-2-88963-286-2
DOI 10.3389/978-2-88963-286-2

About Frontiers

Frontiers is more than just an open-access publisher of scholarly articles: it is a pioneering approach to the world of academia, radically improving the way scholarly research is managed. The grand vision of Frontiers is a world where all people have an equal opportunity to seek, share and generate knowledge. Frontiers provides immediate and permanent online open access to all its publications, but this alone is not enough to realize our grand goals.

Frontiers Journal Series

The Frontiers Journal Series is a multi-tier and interdisciplinary set of open-access, online journals, promising a paradigm shift from the current review, selection and dissemination processes in academic publishing. All Frontiers journals are driven by researchers for researchers; therefore, they constitute a service to the scholarly community. At the same time, the Frontiers Journal Series operates on a revolutionary invention, the tiered publishing system, initially addressing specific communities of scholars, and gradually climbing up to broader public understanding, thus serving the interests of the lay society, too.

Dedication to Quality

Each Frontiers article is a landmark of the highest quality, thanks to genuinely collaborative interactions between authors and review editors, who include some of the world's best academicians. Research must be certified by peers before entering a stream of knowledge that may eventually reach the public - and shape society; therefore, Frontiers only applies the most rigorous and unbiased reviews.
Frontiers revolutionizes research publishing by freely delivering the most outstanding research, evaluated with no bias from both the academic and social point of view. By applying the most advanced information technologies, Frontiers is catapulting scholarly publishing into a new generation.

What are Frontiers Research Topics?

Frontiers Research Topics are very popular trademarks of the Frontiers Journals Series: they are collections of at least ten articles, all centered on a particular subject. With their unique mix of varied contributions from Original Research to Review Articles, Frontiers Research Topics unify the most influential researchers, the latest key findings and historical advances in a hot research area! Find out more on how to host your own Frontiers Research Topic or contribute to one as an author by contacting the Frontiers Editorial Office: researchtopics@frontiersin.org

CUTTING-EDGE ANALOGUE MODELING TECHNIQUES APPLIED TO STUDY EARTH SYSTEMS

Topic Editors:
Mélody Philippon, UMR5243 Géosciences Montpellier, France
Christoph Von Hagke, RWTH Aachen University, Germany
Jacqueline E. Reber, Iowa State University, United States
Alain Zanella, Le Mans Université, France

Citation: Philippon, M., Von Hagke, C., Reber, J. E., Zanella, A., eds. (2019). Cutting-Edge Analogue Modeling Techniques Applied to Study Earth Systems. Lausanne: Frontiers Media SA. doi: 10.3389/978-2-88963-286-2

Table of Contents

frontiers
in Earth Science

EDITORIAL
published: 16 October 2019
doi: 10.3389/feart.2019.00265

Editorial: Cutting-Edge Analogue Modeling Techniques Applied to Study Earth Systems

Christoph von Hagke[1]*, *Jacqueline Reber*[2] *and Mélody Philippon*[3]

[1] Institute of Geology and Paleontology, RWTH Aachen University, Aachen, Germany, [2] Department of Geological and Atmospheric Sciences, Iowa State University, Ames, IA, United States, [3] Université des Antilles, UMR 5243 Géosciences Montpellier, Pointe-a-Pitre, France

Keywords: analog modeling, tectonics, structural geology, editorial, scaling and modeling

Editorial on the Research Topic

Cutting-Edge Analogue Modeling Techniques Applied to Study Earth Systems

Our understanding of Earth systems is built on field observations, geological and geophysical investigations and modeling. For over two hundred years, geologists are building analog models to test theories and understand the physics leading to field observations. Analog models do not aim to reproduce nature but rather to simplify the system so that parameters like geometry, kinematics, or dynamics can be isolated and investigated. Analog models allow to investigate complex three-dimensional problems at high-resolution. In addition to deciphering outcrop observations, analog models offer the opportunity to predict structures not accessible for direct observation. Analog models provide a full 4-D view of geological processes, allowing for investigating the time evolution of structures.

To develop new and successful analog experiments several challenges need to be overcome. Firstly, the governing physical processes in nature need to be identified and isolated and adequate modeling techniques need to be identified. This will govern the applied boundary conditions, model material, and it will determine the limitations of the experiment. Experiments then have to be benchmarked against field or geophysical observations to ensure their relevance. Secondly, new model materials with adequate physical properties need to be developed and tested to quantify their dependence on (i) strain and strain rate; (ii) temperature; (iii); and interaction with the boundaries or other materials. For example, the lithosphere was historically modeled as a two to four-layer brittle/ductile sandwich to crudely approximate the seismically observed rheology. However, the recent development of semi-brittle and temperature dependent model materials will change the way lithosphere and crustal-scale models are constructed. Thirdly, deformation apparatuses need to be developed emulating physical parameters such as erosion through rain, overpressure, or temperature gradients. Designing and tuning relevant Earth science experiments often involves genuine engineering and technical developments. And finally, the outcomes of the model need to be quantified with accurate tools such as particle image velocimetry (PIV), stress and strain sensors, strain maps, elevation maps (erosion rates, uplift rates).

This Research Topic compiles eight contributions either introducing and using new analog modeling techniques or using analog models to investigate geological observations in a new light.

DEVELOPMENT OF NEW ANALOG MODELING TECHNIQUES

Rudolf et al. present a technique to capture earthquake events in a sandbox without oversampling the interseismic period. Modeling earthquakes in a sandbox is challenging, as the speeds of plate motion and seismic slip vary by several orders of magnitude. Moreover, the recurrence

Edited and reviewed by:
Valerio Acocella,
Roma Tre University, Italy

***Correspondence:**
Christoph von Hagke
christoph.vonhagke@emr.rwth-aachen.de

Specialty section:
This article was submitted to Structural Geology and Tectonics, a section of the journal Frontiers in Earth Science

Received: *05 July 2019*
Accepted: *25 September 2019*
Published: *16 October 2019*

Citation:
von Hagke C, Reber J and Philippon M (2019) Editorial: Cutting-Edge Analogue Modeling Techniques Applied to Study Earth Systems. Front. Earth Sci. 7:265. doi: 10.3389/feart.2019.00265

intervals of earthquakes are impossible to forecast, even under controlled conditions of an experiment. The study introduces a new technique on how to monitor rate dependent processes in analog experiments.

Poppe et al. study intrusion of magma into host rock. Understanding intrusion geometries and monitoring their surface response helps forecasting volcanic eruptions. Results show that the strength of the host rock systematically affects the 3-D geometry and time- evolution of magma intrusions. Different endmember geometries can be distinguished. Intrusions into complex host rheology can result in filled mode-1-fractures and formation of mixed-mode fractures.

Svanes Bertelsen et al. investigate the mechanics of magma emplacement in Earth's crust. Experiments show strong correlation between intrusion shapes and host matrix deformation modes. These are the first experiments to produce the natural diversity of intrusion shapes and host deformation mechanisms. They also show that the use of a polariscope in gel experiments is essential to unravel the mechanics of emplacement within a rheologically complex host material.

To accurately monitor advection and uplift of material in analog models, horizontal and vertical displacements need to be measured. Toeneboehn et al.; Toeneboehn et al. present a cost-effective solution requiring only two DSLR cameras and Matlab® toolboxes. The authors demonstrate how the combination of PIV, PTV, and stereovision analysis reveals the evolution of a fault system and three-dimensional advection of material in an experiment simulating the Mount McKinley restraining bend.

NEW LOOK AT GEOLOGICAL PROBLEMS

Beniest et al. conduct a series of lithosphere-scale analog models to investigate how strength variations of the margin influence margin geometries. Results show that rheologies control strain localization and geometries. Consistently, the weaker section of the experiment is stretched, and deformation does not localize at the rheological contrast between the two different crusts. The results show comparability to the passive margin geometries observed on both sides of the Atlantic.

Large transform faults have been suggested as one setting where subduction initiation could take place. Analog models by Boutelier and Beckett show that at constant convergence rate subduction initiation requires formation of new thrusts near the transform fault. Only at specific orientations of these weak zones will the older, less buoyant plate become the subducted plate. The model results can be applied to a variety of natural examples, including the New Hebrides or the Caribbean subduction zone.

von Hagke et al. investigate the influence of obliquity of slip on the evolution and geometry of dilatant faults to quantitatively determine which surface structures are characteristic features to determine slip kinematics. They show that dilatancy changes progressively with increasing obliquity. Open fractures may occur at depth of > 1 km. These findings have implications for our understanding of the connectivity of faults at depth, and geothermal systems.

Experiments by Brun and Fort show that continental shelves are sensitive to changes in the tectonic history, and therefore are important for understanding the time-evolution of passive margins. They show that transfer zones develop connecting two shelf breaks, and these transfer zones are markers for kinematic analyses. This study shows that complex systems such as passive margins are accessible using analog models.

The presented collection of papers provides insights into the state of the art in analog modeling. They demonstrate how new techniques are driving the field in an increasingly quantitative direction and illustrate the breadth of questions that can be addressed with analog modeling. Analog models will continue to play an essential role alongside field observations and theoretical considerations in driving our understanding of tectonic processes in new directions.

The figure accompanying this editorial can be found at: "https://figshare.com/articles/CvH_et_al_Analog_Modeling_FES_jpg/8983862."

AUTHOR CONTRIBUTIONS

All authors listed have made a substantial, direct and intellectual contribution to the work, and approved it for publication.

ACKNOWLEDGMENTS

We would like to thank all reviewers for their contributions to the manuscripts. We also would like to thank editors in Chief Valerio Acocella and Agust Gudmundsson and the Frontiers Team for their support.

Conflict of Interest: The authors declare that the research was conducted in the absence of any commercial or financial relationships that could be construed as a potential conflict of interest.

frontiers
in Earth Science

METHODS
published: 10 October 2018
doi: 10.3389/feart.2018.00152

Stereovision Combined With Particle Tracking Velocimetry Reveals Advection and Uplift Within a Restraining Bend Simulating the Denali Fault

Kevin Toeneboehn*[1]**, *Michele L. Cooke*[1]*, *Sean P. Bemis*[2]*, *Anne M. Fendick*[3]* and *Jeff Benowitz*[4]

[1] Geomechanics Laboratory, Department of Geosciences, University of Massachusetts Amherst, Amherst, MA, United States, [2] Global Forum on Urban and Regional Resilience, Virginia Polytechnic Institute and State University, Blacksburg, VA, United States, [3] Department of Earth and Environmental Sciences, University of Kentucky, Lexington, KY, United States, [4] Department of Tectonics and Sedimentation, Geophysical Institute, University of Alaska Fairbanks, Fairbanks, AK, United States

Edited by:
Jacqueline E. Reber,
Iowa State University, United States

Reviewed by:
Tim Dooley,
The University of Texas at Austin, United States
Caroline M. Burberry,
University of Nebraska–Lincoln, United States
Michael Rudolf,
Helmholtz-Gemeinschaft Deutscher Forschungszentren (HZ), Germany

***Correspondence:**
Kevin Toeneboehn
toeneboehn.kevin@gmail.com

Specialty section:
This article was submitted to Structural Geology and Tectonics, a section of the journal Frontiers in Earth Science

Received: *30 June 2018*
Accepted: *20 September 2018*
Published: *10 October 2018*

Citation:
Toeneboehn K, Cooke ML, Bemis SP, Fendick AM and Benowitz J (2018) Stereovision Combined With Particle Tracking Velocimetry Reveals Advection and Uplift Within a Restraining Bend Simulating the Denali Fault. Front. Earth Sci. 6:152. doi: 10.3389/feart.2018.00152

Scaled physical experiments allow us to directly observe deformational processes that take place on time and length scales that are impossible to observe in the Earth's crust. Successful evaluation of advection and uplift of material within a restraining bend along a strike-slip fault zone depends on capturing the evolution of strain in three dimensions. Consequently, we require deformation within the horizontal plane as well as vertical motions. While 3D digital image correlation systems can provide this information, their high costs have prompted us to develop techniques that require only two DSLR cameras and a few Matlab® toolboxes, which are available to researchers at many institutions. Matlab® plug-ins can perform particle image velocimetry (PIV), a technique used in many analog modeling studies to map the incremental displacements fields. For tracking material advection throughout experiments more suitable Matlab® plug-ins perform particle tracking velocimetry (PTV), which tracks the complete two-dimensional displacement path of individual particles. To capture uplift the Matlab® *Computer Vision Toolbox*™, uses pairs of photos to capture the evolving topography of the experiment. The stereovision approach eliminates the need to stop the experiment to perform 3D laser scans, which can be problematic when working with materials that have time dependent rheology. We demonstrate how the combination of PIV, PTV, and stereovision analysis of experiments that simulate the Mount McKinley restraining bend reveal the evolution of the fault system and three-dimensional advection of material through the bend.

Keywords: stereovision, particle tracking velocimetry, digital image correlation, analog model, restraining bend, Denali fault, computer vision

INTRODUCTION

At restraining bends along strike slip faults, horizontal slip rates decrease (e.g., McGill et al., 2013; Elliott et al., 2018) and local contraction within the bend is accommodated by deformation off of the primary fault (e.g., Cunningham and Mann, 2007). For example, this off-fault deformation is manifested by the three-dimensional migration of material along, and through, a restraining bend, such as where Denali (6,190 m; formerly Mount McKinley) and adjacent high peaks have formed along the strike-slip Denali fault, Alaska at Mount McKinley (**Figure 1**). The local contraction within restraining bends produces uplift so that the migration of material adjacent to the fault includes both a horizontal and a vertical component. Consequently, the rocks exposed at Denali record an exhumation history that reflects their uplift while also being transported laterally along the Denali fault (Fitzgerald et al., 1995; Burkett et al., 2016; Lease et al., 2016). Interpreting the exhumation history of such rocks can be facilitated by laboratory experiments that reproduce the loading and boundary conditions using carefully scaled analog materials. Such experiments allow us to directly observe millions of years of deformation within minutes and document material advection that can validate our interpretations of crustal deformation within restraining bends, such as the Mount McKinley restraining bend (**Figure 1**).

Deformation along the modern Alaska Range associated with the Denali fault began in the early Miocene, 16–23 million years ago (e.g., Ridgway et al., 2007; Benowitz et al., 2011). Exhumation and uplift associated with growth of the Alaska Range was spatially variable (Benowitz et al., 2011, 2013; Bemis et al., 2012), with the most prominent feature of the Alaska Range, Denali, initiating rapid exhumation at ∼6 Ma (e.g., Fitzgerald et al., 1995). This exhumation is associated with a major left-step in the Denali fault, forming highly asymmetric and localized topography, within a restraining bend termed the Mount McKinley restraining bend (Fitzgerald et al., 2014; Burkett et al., 2016). Through new quaternary geologic mapping across the eastern portion of the restraining bend, Burkett et al. (2016) identified a number of previously unknown active faults and argued that the locations and sense of slip on these faults place clear limitations on the evolution of the restraining bend system and associated advection of material. However, the limitations of field data and uncertainties of dating deformation make it difficult to directly relate the structural evolution to exhumation recorded in exposed units. Scaled physical experiments can strengthen our field interpretations by demonstrating the relationships between fault system evolution and exhumation path and timings.

Carefully scaled physical experiments reproduce crustal deformational processes that take place on time and length scales, which are otherwise impossible to directly witness (e.g., Cooke et al., 2016; Reber et al., 2017). Scaled experiments of restraining bends have provided critical insights into the development of these structures (Richard et al., 1995; McClay and Bonora, 2001; Dooley and Schreurs, 2012; Cooke et al., 2013; Hatem et al., 2015). These experiments use a variety of techniques to capture the deformation within restraining bends, such as tracking the horizontal displacement of surface marks between photos (McClay and Bonora, 2001; Dooley and Schreurs, 2012; Cooke et al., 2013) and laser scans for uplift (Dooley and Schreurs, 2012; Cooke et al., 2013). Hatem et al. (2015) used successive images taken from a single consumer level DSLR camera and processed using the digital image correlation (DIC) tool, particle image velocimetry (PIV) software, to provide high-resolution displacement perpendicular to the camera view angle. PIV identifies unique patterns of pixels in successive digital images and calculates the displacement vector between them using a Eulerian reference frame. Previous analog modeling studies have successfully demonstrated how PIV can document two-dimensional deformation in a variety of analog materials (e.g., Adam et al., 2005; Cruz et al., 2008; Hatem et al., 2017; Rosenau et al., 2017; Ritter et al., 2018). Similar to PIV, particle tracking velocimetry (PTV) uses image correlation to compare successive images and calculate displacements. Unlike PIV though, PTV identifies individual surface markers between images and calculates a Lagrangian flow path for each marker.

Determining the three-dimensional migration of material in the Mount McKinley restraining bend requires linking horizontal advection with vertical displacement of material in the experiment. Two-dimensional DIC methods (PIV and PTV) use a single camera perspective and fail to provide information about movements in the z plane. For this paper, we will consider that the camera is set up above the experiment to observe horizontal displacement with PIV and PTV but misses uplift deformation. As of 2018, currently available three-dimensional PIV systems (e.g., LaVision DaVis StrainMaster®) require proprietary software and highly specialized cameras costing upward of $50,000. Here, we present a cost-effective methodology to determine the full three-dimensional advection path of materials using two standard DSLR cameras and a combination of PIV, PTV, and stereovision techniques. The stereovision methodology uses computer vision methods to document vertical deformation within the laboratory. The combination of stereovision with traditional two-dimensional DIC to quantify the vertical and horizontal displacements can be accomplished for less than a tenth of the cost of alternative three-dimensional PIV systems and requires only consumer level cameras, a current Matlab® license, and several Matlab® Toolboxes. By adding a second camera to the system, we are able to use stereovision to measure displacement in the *z* plane (toward and away from the camera) to record the complete three-dimensional deformation. Here, we show how to combine PIV, PTV, and stereovision tools to produce three-dimensional migration paths and show how these methods contribute to our understanding of material movement through the Mount McKinley restraining bend, both horizontal advection along and uplift within the restraining bend.

MATERIALS AND METHODS

In this section, we first describe how we set up an experiment to simulate deformation within the Mount McKinley restraining bend and then outline the stereovision and PTV methods and approach used to document movement of material through the experimental restraining bend.

Simulating the Mount McKinley Restraining Bend in the Laboratory

To simulate deformation of the restraining bend along the Denali fault, we use bi-viscous wet kaolin. With ∼70% by weight water, the low cohesive strength of wet kaolin provides a material that can scale crustal deformation within a table-top experiment (e.g., Cooke et al., 2016). This material has been used for investigations

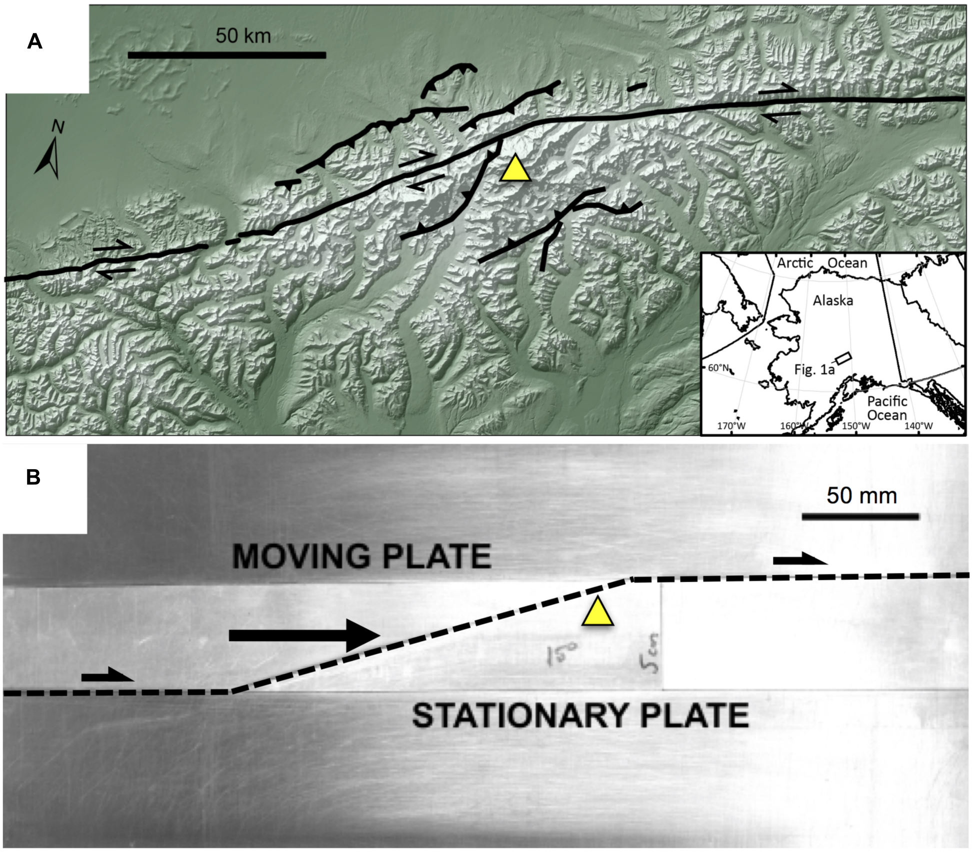

FIGURE 1 | (A) Digital elevation model of the Mt. McKinley restraining bend with Denali peak (triangle) and fault trace indicated. Fault traces simplified from Haeussler (2008), Koehler et al. (2012), and Burkett et al. (2016). Shaded-relief base derived from the 2 arcsecond National Elevation Dataset DEM (https://nationalmap.gov/). **(B)** Basal plate restraining bend configuration (15°, 5 cm stepover) for experimental setup.

into the evolution of normal faulting (e.g., Adam et al., 2005; Leever et al., 2011; Hatem et al., 2015), thrust faulting (Cooke and van der Elst, 2012), and strike-slip faulting (e.g., Henza et al., 2010). By adjusting the water content, the clay is prepared to a shear strength of ~100 Pa, to ensure proper length scaling, and set onto restraining bend configured base plates following Hatem et al. (2015). Using an electrified probe to minimize drag, we precut a 15° restraining bend across a 4 cm thick layer of wet kaolin to approximate the Denali fault's geometry (**Figure 2**). Computer controlled stepper motors drive displacement of one of the basal plates to produce a discontinuity at the base of the fault.

To scale the table top experiment to the crustal features of the Mount McKinley restraining bend, two factors need to be considered: the scale of the restraining bend and the slip rate on the fault. Past experiments with wet kaolin have scaled the length of the experiments to the crust (e.g., Henza et al., 2010; Hatem et al., 2015, 2017; Bonanno et al., 2017), but have not considered how the rate of viscous stress relaxation in the kaolin scales to stress relaxation in the crust. Viscous flow within the bi-viscous wet kaolin can simulate the stress dissipation by various pervasive deformation mechanisms in the crust (e.g., cleavage development, microcracking, etc.) if the strain rates are appropriately scaled. The limited range of motor speed necessitated some compromise in scaling of both fault slip rate and length. To scale the fault slip rate, we consider the time-dependent rheology of both the crust and the wet kaolin. The crust has a viscous stress relaxation time of ~2 Mya (e.g., Bonanno et al., 2017), whereas the relaxation time for kaolin is ~15 min (e.g., Cooke et al., 2013; Hatem et al., 2015, 2017). Within 15 min of experiment time, we want the fault to accommodate the equivalent of slip that accumulates along Denali fault over 2 Ma. The average slip rate outside of the Mount McKinley restraining bend is approximately 6.5 mm/year (e.g., Turcotte and Schubert, 2014) producing ~14 km of slip over a period of 2 Mya. Using the fastest motor speed of 2.5 mm/min, the experiment can produce 37.5 mm of slip within 15 min. Setting the 15 min of lab deformation equivalent to 14 km of slip over 2 Ma of crustal deformation gives a length scaling of 1 cm of clay to 3.8 km of crust. This length scaling is consistent with the calculated range of scaling for similar strength wet kaolin (Henza et al., 2010). The restraining segment along the Denali fault measures between 65–70 km in length and forms an ~18° bend along its trace (Cooke and van der Elst, 2012). Using the length scaling (1 cm: 3.8 km), we simulate this restraining bend in our device using a 15° bend with 19 cm

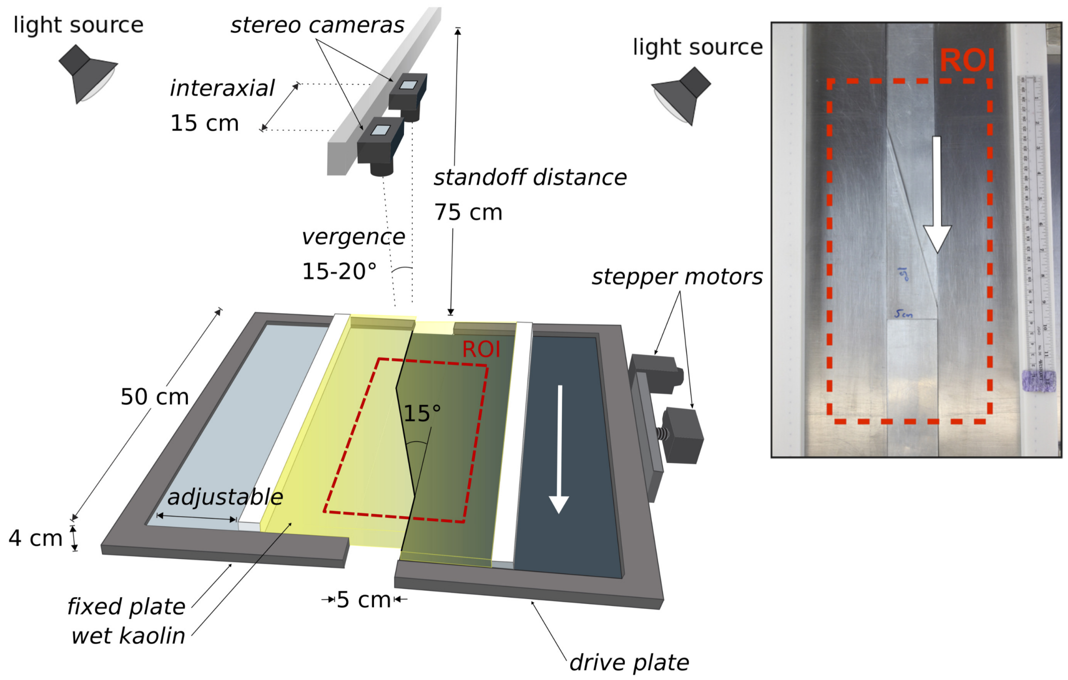

FIGURE 2 | Setup for the experiment that simulates the Mount McKinley restraining bend. (Inset) Basal steel plates fitted with triangular aluminum inserts (15°, 5 cm wide) drive the overlying wet kaolin clay with right-lateral displacement. The triangular restraining segment is attached to the fixed plate and overlaps the driving plate. The red dashed box indicates the fixed region of interest (ROI) for image analysis.

restraining segment (**Figure 1**). The 4 cm thickness of the clay layer means that we simulate only the upper 15 km of the crust.

We use computer software to take photographs at regular intervals throughout the experiment. The most effective time interval for DIC (PIV and PTV) and stereovision depends on resolution of horizontal and vertical motions and differs for the different techniques as discussed below. Generally, PIV has the finest displacement resolution and all photos are taken at the optimal interval for this analysis. For PTV and stereovision, we use subsets of the recorded photos that represent the optimal time intervals for these analyses. For DIC, photos should be undistorted prior to analysis. Both camera and lens type contribute to distortion. We perform the undistortion in batch form using Adobe Photoshop. This software can also be used to convert color images to black and white, which reduces file size and expedites image analysis. **Table 1** lists the material, hardware and software used for the experimental analysis of this study.

Stereovision

Stereovision combines two images taken from two different angles to generate depth information for a shared field of view. Before creating a three-dimensional view, the cameras and images must be calibrated. By calibrating the cameras with a grid of known spacing and distance from the imaging sensors, the elevation of common points in the images are correlated to the change in pixel location (pixel disparity). Using the Matlab® Image Processing Toolbox and the *Stereo Camera Calibrator App* in the *Computer Vision System Toolbox*,™ the user can extract depth information from the two-dimensional image pairs of the experiment.

Acquiring accurate depth information from a photo pair requires several considerations, including:

(1) the desired working distance (standoff distance),
(2) the angle and spacing of the cameras (vergence and interaxial distance),
(3) the focal length of the lenses,
(4) the amount of available light,
(5) the desired spatial and temporal resolution.

Since the total uplift in the restraining bend claybox experiments ranges from a few millimeters to 2 cm, we require very fine vertical resolution in order to capture the incremental elevation change at stages throughout the experiment. Increasing resolution requires either increasing focal length, reducing the working distance, or using a higher resolution sensor. In order to maintain a cost-effective system, we use the standard 18.0 Megapixel complementary metal oxide semiconductor (CMOS) sensors from a pair of consumer grade DSLR cameras at 75 cm standoff distance (**Figure 2**). Therefore, to improve resolution we are limited to increasing the focal length and/or decreasing the standoff distance—actions that also reduce the field of view. The field of view must remain large enough, however, to capture the faulted region of interest within the experiment. This balance between field of view and resolution must be adjusted on a case-by-case basis.

TABLE 1 | List of materials used to conduct physical experiments and the necessary software for processing the data.

HARDWARE	SOFTWARE
Stainless steel plates (25 cm × 50 cm × 0.15 cm) (2)	Adobe Photoshop®
Aluminum insert (18 cm × 5 cm, cut to 15°) (1)	MathWorks Matlab® (v.2014b)
Aluminum insert (18 cm × 5 cm, spacer) (2)	Matlab® *Image Processing Toolbox*™
Heavy gage wire (probe) (∼0.2 cm thick, 10 cm) attached to non-conductive handle	Matlab® *Computer Vision System Toolbox*™
Insulated flexible copper wiring (∼40–50 cm length) connected to voltage regulator, probe	*Stereo Camera Calibrator App*™ *(v.2014b)*
Wooden probe template cut to match 15°, 5 cm aluminum insert	*Mach3* CNC controller *(unlicensed version)*
PE plastic sidewalls (5 cm × 4 cm × 50 cm)	
Wet kaolin clay (50 lb moist pottery clay)	
3 A *Nema23* stepper motors (2)	
T-slot style extruded aluminum framing for overhead camera mount (1)	
Canon Rebel T3i® cameras (2)	
Canon Rebel T3i® 18–55 mm lens kit (1) lamps; soft-box light diffuser (2)	
1,600 W LED bulbs (8)	
Medium grainsize sand (red, black)	
Black craft glitter (∼0.1 cm^2)	
Duct tape (one roll)	

A pair of *Canon Rebel T3i*® cameras with standard 18–55 mm kit lenses provide sub-millimeter vertical resolution. The cameras have an interaxial spacing of 15 cm (**Figure 2**) combined with a standoff distance of 75 cm and lens focal length of 35 mm, shutter speed (1/60), ISO 100. For this application, we found using a converging field of view (vergence) between 15°–20° as the best compromise between the size of the field of view and the accuracy of depth measurements (**Figure 2**). Brightly lit surfaces with minimal glare serve best for stereo analysis. We use two identical lamps (four 1600 Lumen LED bulbs) with soft-box light diffusers to provide illumination and turn off the laboratory's overhead fluorescent to reduce glare on the horizontal surface of the clay (**Figure 2**).

Calibration and Validation

Extracting depth information from stereo pair images requires careful calibration. Each camera and camera lens have unique intrinsic and extrinsic parameters that vary with focal length and camera position. Before undistorting the images and extracting accurate depth information, we must first measure each of these parameters. Furthermore, we must perform a new calibration any time that the position or focus of a camera is changed. Consequently, once calibrations are completed, we take great care not to disturb the cameras throughout the duration of the experiment.

To determine the calibration parameters, we capture a minimum of 20 stereo pair images of a calibration grid (black and white checkerboard, 23.1 mm squares) that is set at varying orientations and load the photos into the *Stereo Camera Calibrator App* in the *Computer Vision Toolbox*™ of Matlab®. The software identifies the corners of the grid in each image and determines its three-dimensional orientation. Accurate corner detection requires sharp printing and a consistently flat grid surface. Depending on laboratory humidity, paper may distort between calibration sessions reducing calibration accuracy. We recommend printing on either an overhead transparency sheet or Mylar paper to maintain a dimensionally consistent grid. To calculate depth, the images are rectified or row aligned, reducing the problem to two dimensions (position along x-axis and pixel disparity). The pixel disparity is a measure of change in pixel location between common points from each camera view. The *Computer Vision Toolbox*™ combines the known calibration grid spacing to convert the pixel disparity maps to real-world distance maps. We repeat the calibration, removing, and replacing stereo pairs, until the overall mean reproduction error reported by the *Stereo Camera Calibrator App* is less than 1 pixel. The reproduction error is a measure of the average pixel distance between a detected point projected in the image and the same point reprojected after processing (MathWorks®, 2018). The *Stereo Camera Calibrator* application produces a unique stereo parameters object that contains both intrinsic and extrinsic parameters and can be exported and combined with new pairs of photos to generate suites of digital elevation models of the clay surface for each experiment using functions within the *Computer Vision Toolbox*™ of Matlab®.

We import the parameters calculated from the calibration procedure into the built-in Matlab® *Computer Vision Toolbox*™ function *rectifyStereoImage*. Using the functions *stereoAnaglyph*, and *disparity* provided in the *Computer Vision Toolbox*™, we, respectively, create and then convert the pixel disparity map generated from the pairs of photos taken throughout the experiment, into real-world distances from the camera. By subtracting the known distance of the camera from the working surface (working distance), we can then convert these data into a digital elevation model. We validate the calibrated system by comparing the stereovision created digital elevation model of a simple wedge with direct measurements of the wedge's slope and height. The angled surface provides a continuous gradient of heights to ensure accuracy over a greater depth of field in addition to providing a direct comparison to a known real-world surface. Vertical errors vary within ±1 mm between calibration sessions.

The optimal interval of photos to use in stereovision analysis depends on the vertical errors from the validation and the rate of elevation change of the experiment. With stereovision elevation errors of ±1 mm, photos taken in quick succession of a slowly uplifting feature will not resolve the small (<1 mm) changes in elevation between each photo. Within the restraining bend experiment, we see ∼15 mm of total uplift over 48 min. The rate of uplift rate increases in the latter half of the experiment, so the change in elevation between successive pairs of photos exceeds the vertical error of the analysis.

Calculating Incremental Uplift Pattern

The incremental uplift between pairs of photos is calculated by subtracting the topography of the earlier pair from the later pair. However, as the stepper motors drive deformation, the horizontal position of structures in the clay change relative to the fixed field of view of the cameras. As a result, calculating incremental uplift from the difference in elevation between individual time steps can produce artificial uplift due to shifting locations of structures between steps (**Figure 3a**). We correct for this shift by adjusting the horizontal position of points in the DEM using results from the PIV analysis. PIV analysis with the *PIVlab* Matlab® application (Matmon et al., 2006; Mériaux et al., 2009; Haeussler et al., 2017) uses just one photo from each of the stereopairs to produce a grid of incremental horizontal displacements between each step. The grid from the PIV is often at lower resolution than the DEM from stereovision necessitating re-gridding of one or the other datasets. Once the datasets have matching horizontal grids, the incremental horizontal displacements from the PIV can be subtracted from the point locations of the later DEM to shift the later structures to their earlier positions. The resulting difference in elevation between the later and earlier DEM provides the incremental uplift pattern due to active faulting (**Figure 3b**). This approach compensates for the horizontal drift between frames and improves the accuracy of the incremental uplift maps. Around the middle of the experiment, the accuracy of the stereovision elevation is compounded by the relatively low uplift rates (compared to late in the experiment) to reduce the quality of the incremental uplift pattern (**Figure 3c**).

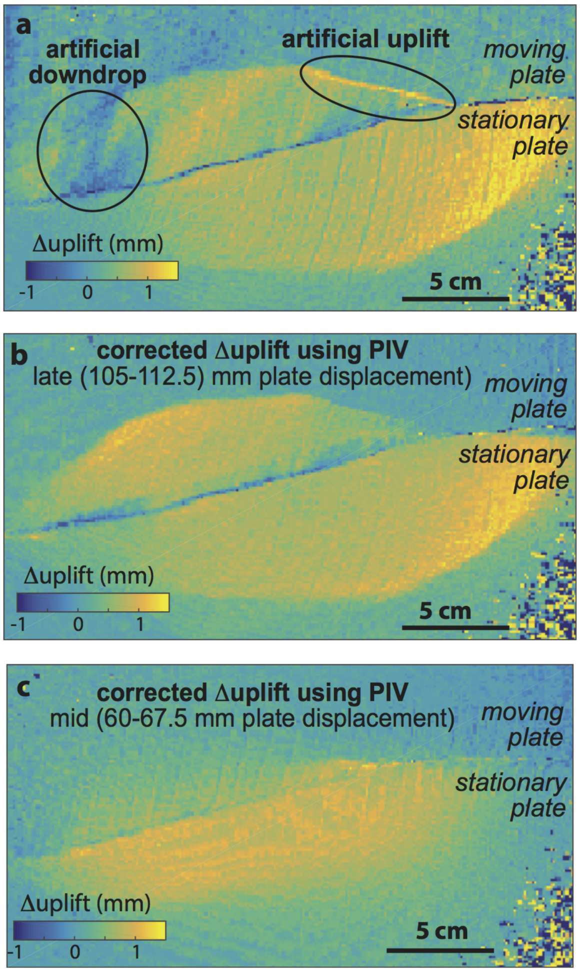

FIGURE 3 | Example incremental uplift maps showing the change in surface elevation over a 7.5 mm increment of applied plate displacement late in the experiment. The lower resolution of the incremental uplift maps compared to the cumulative uplift map reflects the downgrading of the DEM to the resolution of the PIV in order to adjust the horizontal position of migrating structures. **(a)** The differences between elevation at 112.5 and 110 m of plate displacement without PIV correction. The highlighted regions contain artificial down-drop and uplift due to lateral movement of the clay morphology on the moving plate. **(b)** The change in elevation for the same interval of plate displacement as **A** but using the PIV data to correct for the lateral movement. The artificial elevation changes are removed and the resulting change in morphology corresponds to fault activity during this period. **(c)** Incremental uplift for a 7.5 mm stage near the middle of the experiment.

Particle Tracking Velocimetry Methodology

Particle tracking velocimetry is a DIC technique that detects groups of pixels belonging to non-deforming objects/particles and tracks their two-dimensional displacements in successive images. Using a Lagrangian frame of reference, PTV calculates a flow path for each marker, tracking the migration of material throughout an experiment (**Figure 4**). The technique has been used in fluid mechanics research for several decades (e.g., Maas et al., 1993; Ohmi and Li, 2000). Within geoscience applications, PTV has been used to measure water flow and discharge within water sheds (Muste et al., 2008; Patalano et al., 2017). For this study, we use the free Matlab® plug-in, *PTVlab,* developed by Patalano & Wernher and based on *PIVlab Version 1.2 2009* by W. Thielicke. Both *PTVlab* and *PIVlab* rely on the *Image Processing Toolbox* within Matlab®.

The most notable difference between the two-dimensional PTV and PIV techniques is how the images are processed (**Figure 4**). In PIV, pixels within a grid of windows from successive image pairs are cross-correlated to calculate change in displacement between the two photos. The change in displacement from each window contributes to the gridded displacement field. This method provides very precise and complete coverage of the incremental displacement fields. In contrast, PTV identifies individual markers, gives them unique labels, and tracks their migration throughout each subsequent image.

Since PTV relies on being able to detect and correlate unique particles in each image of the experiment, acquiring accurate PTV results requires many of the same setup considerations as stereovision and PIV techniques, such as high-resolution photos and bright non-glare producing lighting. Unlike in stereovision,

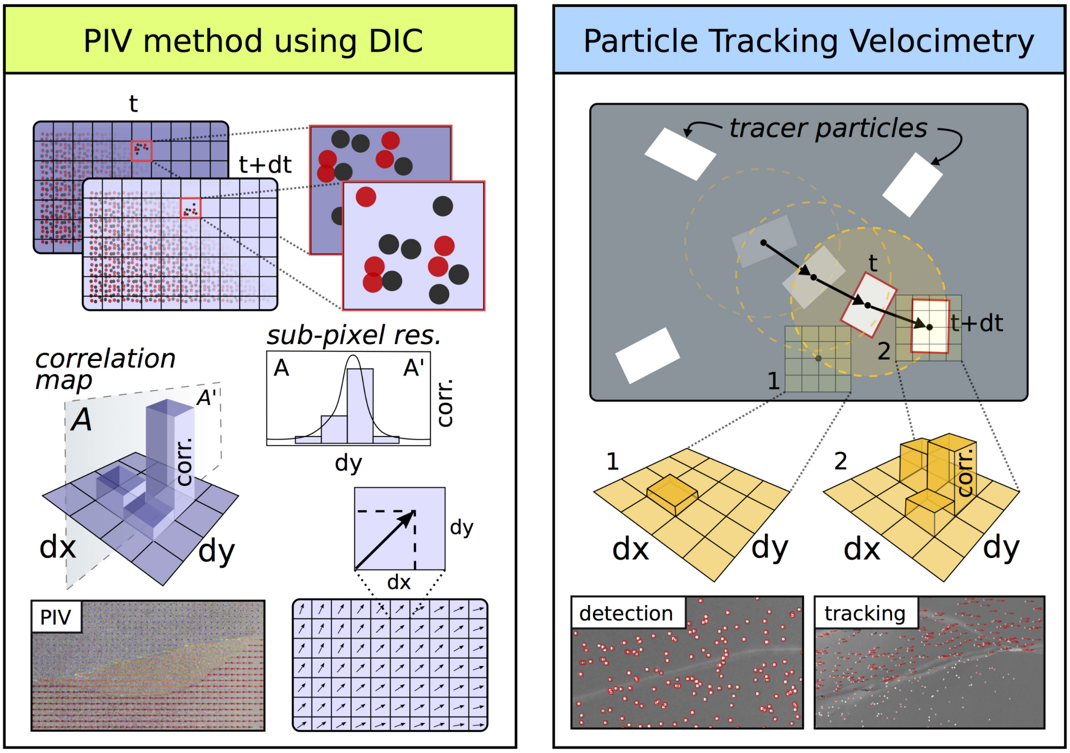

FIGURE 4 | Particle image velocimetry (PIV) method employs digital image correlation (DIC) to measure the change in displacement within each gridded cell for a sequence of images (left panel). The grid remains fixed within a Eularian reference frame with cell size predetermined based on the expected displacement increment and desired spatial resolution. Within each gridded cell, small high-contrast surface markers form a unique pattern that is used to identify each cell's vector of displacement between two sequential frames. A correlation map identifies the grid-locations (*dx*, *dy*) with the strongest match from the previous frame. Fitting the correlation map with a Gaussian curve allows for sub-pixel spatial resolution. PTV, however, employs a non-fixed Lagrangian reference frame to track the displacement and velocity of individual particles. The tracer particles are detected based on size and color contrast with the background image and then given unique identifiers (bottom right). Between frames, the area around each particle is searched using a grid to identify the location with the strongest matching pattern (top right). The radius of the grid search is likewise dependent on the displacement increment and the desired spatial resolution.

however, a single camera can be used to extract the two-dimensional flow paths of the particles. We used the images from one of the two stereovision cameras for PTV analysis collected at 1 min intervals throughout the experiment.

Setting Up Particle Detection

When selecting markers to use for PTV, high color contrast and image resolution should be considered in order ensure that the Gaussian Mask detection algorithm can properly identify the markers at the desired resolution. Since our clay surface is off-white, we chose high contrast black foil pieces (craft glitter) with ∼1 mm^2 area. Because we recorded PTV simultaneously with stereovision, we required the marker's profile on the surface to be undetectable by stereovision—making the thin foil an ideal marker for our application. *PTVlab*'s detection algorithms are designed to detect white particles, so we invert the color in all of the images before loading them into MATLAB® (e.g., **Figure 5A**). Additionally, the *correlation threshold*, *sigma* (number of pixels), and the *intensity thresholds* for the detection algorithm must be adjusted per application to differentiate the white markers from the background surface/noise. For our photos, we used a fixed a minimum correlation of 0.4 and neighbor similarity of 25% to detect the craft glitter in the inverted photographs.

Fine resolution of results requires small interrogation windows for the cross-correlation. Consequently, the displacement increment between photos cannot be larger than the window size since the software searches within the window for the pixel cluster of the object. For fast experiments, this requires frequent photos. We use an interrogation window size of 10 sq-pixels (0.77 mm^2 for our photos) to record the small incremental displacements (0.25 mm/image) in our experiments. The markers used for PTV tracking must be small enough to be detected within the interrogation window. We found that for this interrogation window size, markers with an upper size limit of ∼1 mm^2 yielded the most accurate marker detection. Since the particle tracking algorithms are computationally expensive, greater number of particles can quickly overwhelm your CPU. For our experiment, we continuously tracked several hundred particles randomly distributed across the surface of the experiment.

The results of the PTV analysis are extracted as a MATLAB® cell array. The particle path information can be extracted from PTV results using the *Langranpath* function included with

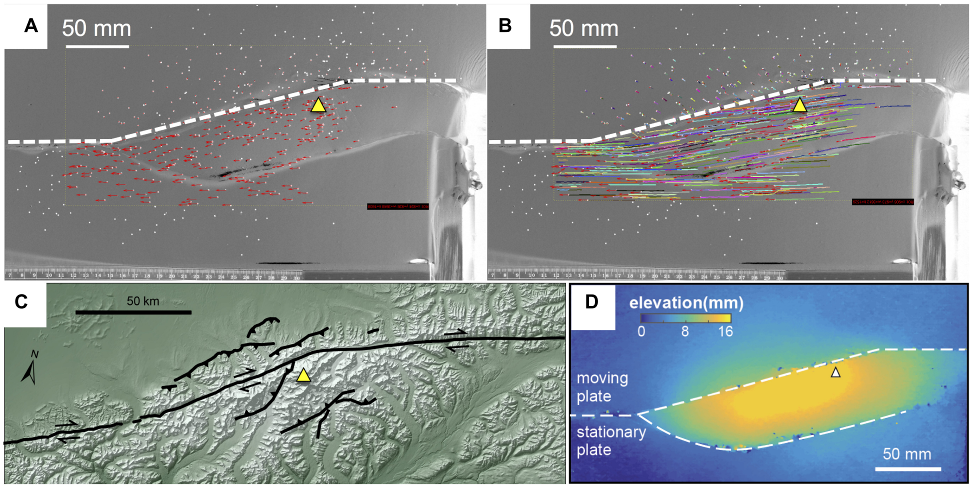

FIGURE 5 | Particle tracking velocimetry (PTV) showing **(A)** incremental and **(B)** cumulative advective transport around a physical model designed to simulate the Mount McKinley restraining bend along the Denali fault zone. **(C)** Digital elevation model of the Denali fault with Denali peak (triangle) and fault trace indicated. **(D)** Cumulative uplift map revealed by stereovision.

PTVlab. This function sorts information from the cell array by the identification numbers that PTVlab assigns to each detected particle and the *Langranpath* function stores the track information in a new *n* by 1 structure, where *n* is the number of particles detected. Each unit of the *n*x1 structure has the *x*- and *y*-positions of the particle through time that can be plotted as a streamline (**Figure 5B**). Not all the particles distributed on the kaolin surface were successfully tracked throughout the experiment. **Figures 6b,c** display the paths from a subset of the 235 particles that were tracked from the start to the end of the experiment. The colors of the streamlines in **Figures 6b,c** indicate the uplift of the particle as it advects along the fault. To assign the uplift information to each particle we co-located the PTV and stereovision datasets. Once co-located, the PTV dataset provides *x*- and *y*-coordinates of the particle throughout the experiment that can be queried from the uplift dataset in order to find the three-dimensional particle path (**Figures 6b,c**). We performed the PTV and PIV analyses over several hours on an Inspiron 660 standard desktop PC built in 2013. This computer is currently out of date; newer computers with faster processors could perform the analysis more quickly and with greater number of particles.

Performing both PIV and PTV on the same experimental photos can be tricky. The fine resolution of the incremental displacement field from PIV requires many more particles that can be reasonably tracked with the PTV analysis. For our investigation of the Mount McKinley restraining bend with homogeneously textured kaolin, we used two different experiments that were each optimized for the different DIC approaches. One experiment had thousands of sand grains sprinkled on the surface of the clay to provide pixel texture for the PIV analysis (**Figures 3**, **5D**) and another experiment had ~250 pieces of glitter for the PTV analysis (**Figure 6**). Photos that contain both thousands of fine particles and hundreds of larger particles could be used for PTV analysis as the fine particles could be filtered out before the analysis. However, using these same photos for PIV may be more problematic. The larger particles will likely create holes in the finer resolution PIV analysis, which would require data conditioning. As long as the markers do not impact the surface topography, uplift data using stereovision tools can be collected from pairs of photos regardless of marker size or spacing.

RESULTS

The cumulative uplift map shows the development of asymmetric high topography around the experimental restraining bend (**Figure 5D**) that resembles the asymmetric topography of the Mt. McKinley restraining bend (**Figure 5C**). The highest topography develops above the stationary plate and is associated with the development of a new thrust fault outboard of the initial 15° restraining segment. This morphology is consistent with that recorded in similarly configured restraining bends experiments that use high-precision laser scanners (e.g., Cooke et al., 2013). Hatem et al. (2015) show that the asymmetry arises from the moving basal plate moving over the stationary plate within the restraining bend. This accounts for why restraining bends that have basal plates that move toward one another (at equal displacement rates), and not one over the other, produce symmetric uplift (McClay and Bonora, 2001; Thielicke and Stamhuis, 2014). Comparisons of the final clay surface elevation (**Figure 7B**) to minimum rock uplift surfaces calculated by thermochronologic data (**Figure 7A**) and modern topography (**Figure 7C**) reveal striking first-order similarity in topographic asymmetry across the Denali fault. In both the experiment and the geologic data, the greatest cumulative uplift occurs adjacent to the restraining segment of the fault and decreases with distance from the fault (**Figures 7A–C**). In contrast, the strike-slip segments of the fault beyond both ends of the restraining segment do not produce a significant uplift signature. The

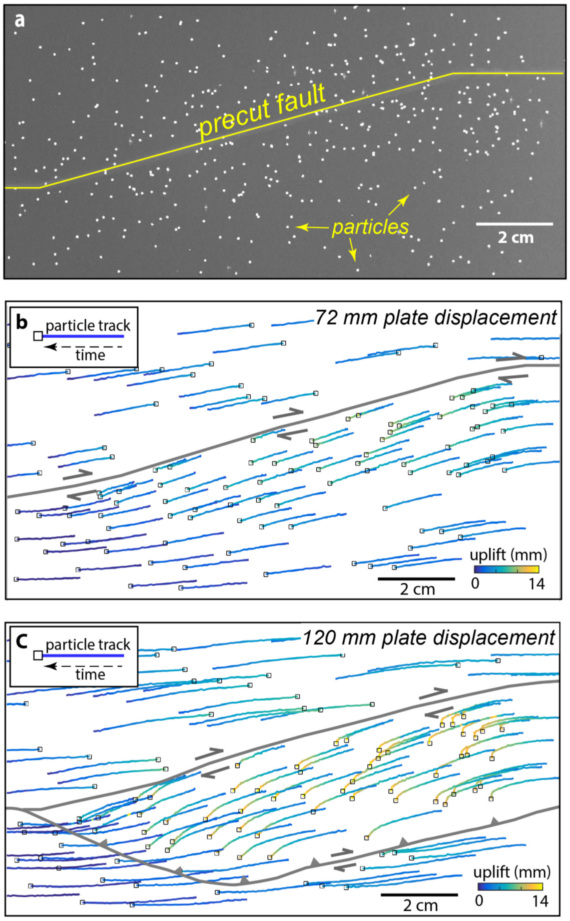

FIGURE 6 | **(a)** Inverted photo used for PTV analysis with black markers on off-white kaolin at the start of the experiment. Flow paths generated from particle tracking velocimetry (PTV) show material migrating through a 15° restraining bend claybox experiment in a fault-fixed reference frame. Color indicates uplift history of each particle. **(b)** Early in the experiment displacement is predominantly parallel to the fault with modest uplift. **(c)** With growth of the new oblique-slip fault, the particles change trajectory and uplift.

mountainous topography along the Denali fault outside of the restraining bend has elevations that are thousands of meters lower than the topography adjacent to the restraining segment (**Figure 7C**), and both the regional geology and preliminary thermochronologic data (Burkett et al., 2016) indicate only limited late Cenozoic exhumation. The development of the new oblique-slip fault outboard of the pre-cut restraining bend in the experiment corresponds to Neogene thrust faults mapped to the south of the of the Denali fault, some of which are noted to exhibit oblique-slip (Haeussler, 2008; **Figure 7**). Similarly, the localized band of uplift and highly oblique particle trajectories on the north side of the restraining segment in the experiment (**Figures 5D**, **6**) is consistent with the occurrence of several active thrust faults that trend sub-parallel to the restraining segment (Burkett et al., 2016; **Figures 1A** and **7C**). While patterns of uplift are remarkably similar, elevation differences between the experiment and geologic constraints (**Figures 7D,E**) highlight the experiment's inability to capture erosion, isostatic response, and differential erodibility of units. Erosion factors into the geologic constraints at two primary scales. First, glacial erosion localized across the higher elevations of the restraining bend drives a crustal isostatic response, producing exhumation values that exceed the scaled experimental uplift on the order of 4–5 km (**Figure 7D**). Second, erosion of broad U-shaped valleys by the major glaciers, particularly along the Denali fault, produce narrow bands where the scaled experimental uplift exceeds the minimum uplift constraints by 2–4 km. Also, the contrast in erodibility between the broadly fractured granitic plutons and the pervasively deformed and fractured Jurassic-Cretaceous sediments of the region (Reed and Nelson, 1980; Haeussler, 2008) likely contributes to the significant topographic relief development illustrated by the two peaks in **Figure 7E** where the minimum uplift surface exceeds the scaled experimental uplift by up to 1.5 km.

Incremental uplift maps show changes in uplift pattern with thrust fault activity (**Figure 3**). During the early activity of the outboard faults (60–67.5 mm of basal plate displacement), off-fault deformation increases uplift rate in the hanging wall of the new thrust fault (**Figure 3c**). At this stage, the greatest uplift rates are adjacent to the precut restraining segment of the fault. Later in the experiment, as the new outboard faults grow and link, the zone of uplift widens to include both hanging walls of the newly created thrust faults (110–112.5 mm basal plate displacement; **Figure 3b**). The greatest uplift rates are then along the traces of the new faults.

Flow paths from PTV analysis show advection of material through the experimental restraining bend (**Figure 6**). Within the experiment, one basal plate moves relative to the other so the faults drift with respect to the overhead stationary camera. In **Figure 6**, we change the reference frame so that the fault remains fixed and markers positioned above the stationary plate appear to move leftward. Prior to the development of the outboard fault, the markers near the fault move parallel to the pre-cut fault segment (**Figure 6b**). Throughout the experiment markers far from the faults move predominantly in the direction of basal plate movement with modest uplift. With the growth of the new fault, the markers above the stationary plate and in the hanging wall of the oblique-slip fault show an abrupt southward change of particle direction and increase in uplift after ~75 mm of total plate displacement (**Figure 6c**). This rapid change in the horizontal trajectory occurs when the uplift pattern suggests growth of the outboard faults.

In this study, we have presented results from two experiments with identical boundary and starting conditions that can be compared to assess repeatability. Aleatory uncertainty due to variable material and experimental conditions naturally occurs within physical experiments so that repeated experiments may give different results (e.g., Schreurs et al., 2016). Both the experiment with sand on the surface of the kaolin (optimal for PIV) and the experiment with glitter distributed on the surface of the clay (optimal for PTV) show development of a new outboard fault that accommodates oblique slip. Both experiments show similar pattern of faulting. One difference between the experiments is the segmented nature of the outboard

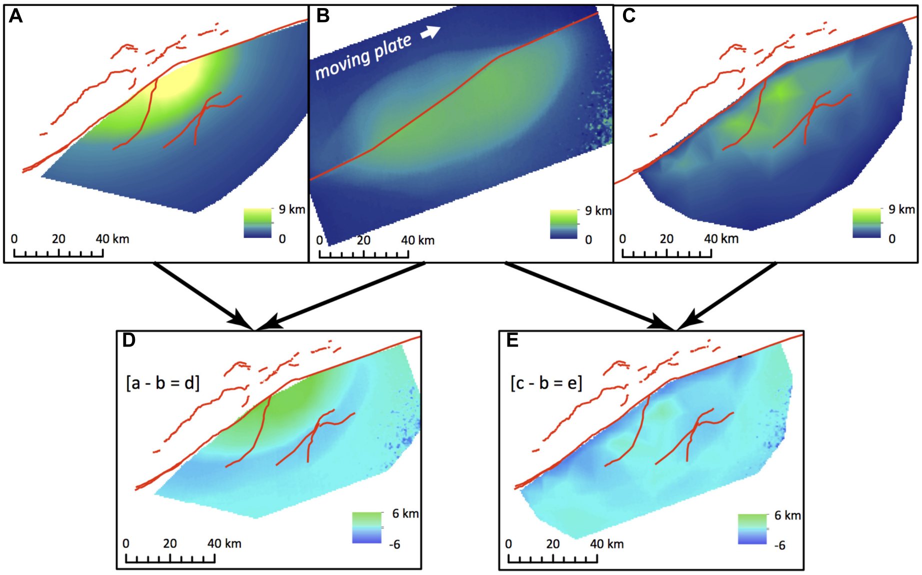

FIGURE 7 | Surfaces representing two geologic constraints on uplift in the Mount McKinley restraining bend **(A,C)** and the surface from the wet kaolin analog experiments **(B)**. Red lines illustrate modern fault traces derived from Reed and Nelson (1980), Haeussler (2008), and Burkett et al. (2016). **(A)** A rock uplift surface derived from low-temperature thermochronology (Fitzgerald et al., 1995). **(B)** Equivalent elevation map of the clay experiment, using the scaling relationships of the experiment to convert into the scale of geologic constraints (Fendick, 2016). **(C)** An approximation of a minimum rock uplift surface derived by extrapolating between modern peak and ridge elevations in the Mount McKinley restraining bend (Fendick, 2016). Surfaces **(D)** and **(E)** are difference maps used to compare the cumulative uplift in the experiment **(B)** to the geologic constraints **(A,C)**. **(D)** The difference between thermochronology-derived uplift **(A)** and the experiment **(B)**. **(E)** The difference between the minimum rock uplift **(C)** and the experiment **(B)**. Positive values (green) represent areas where the experiment did not produce as much uplift as the geologic constraints and negative values (blue) show where the experiment produced more uplift.

fault in the PIV optimized experiment (**Figure 3**) compared to the continuous fault trace in the PTV optimized experiment (**Figure 6**). This difference is not expected to impact the finding of advection through the restraining bend. Repeated restraining bend experiments with the same device and material used in this experiment show variability of fault slip rates of up to 10% of the motor speed (Hatem et al., 2015; **Figure 3b**).

DISCUSSION/CONCLUSION

The stereovision combined with PTV DIC provides a useful approach for tracking advection of several hundred points through the restraining bend. However, the irregular and loose spacing of the PTV particles would not serve well for problems that require high resolution of the displacement or strain fields. For example, mapping active faults and measuring slip rates is better performed with the denser sampling available with PIV DIC.

Other popular techniques exist for extracting 3D topographic data from natural and experimental settings; however, these present challenges for tracking incremental horizontal and vertical displacements through the course of a scaled physical experiment. For example, laser scanners can be used to scan the surface of experiments with comparable resolution. The drawback of laser scanners is that they take several minutes to set up and produce the scan during which the experiment must be stopped. Hatem et al. (2015) show that for time dependent rheology, such as the bi-viscous wet kaolin, stresses within the experiment can dissipate significantly during the time of capturing the laser scan, which impacts the results. Another potential approach is photo-based 3D reconstruction methods (often referred to as structure-from-motion or SfM), which facilitates the creation of a 3D point cloud of a target through the collection of multiple overlapping photographs taken from different viewing angles (e.g., James and Robson, 2012; Westoby et al., 2012; Bemis et al., 2014). The resulting point cloud is effectively the same as those produced through airborne laser swath mapping (ALSM/LIDAR) and lab-based laser scanning tools. Several studies have successfully used these point clouds to measure differential displacements observed in earthquakes and displacements artificially introduced into LIDAR topographic datasets (Nissen et al., 2012, 2014; Scott et al., 2018). However, the iterative-closest-point algorithms employed by these studies rely on a certain degree of topographic complexity to determine unique 3D displacements between the two point clouds. Our experiments exhibit relatively smooth surfaces beyond the localized fault zones; thus, we suspect that iterative-closest-point methods would produce a noisy displacement field at best. Furthermore, this technique requires a windowed/tiled measurement approach (e.g., Nissen et al., 2012), requiring significant processing for a single displacement step. Other algorithms can efficiently calculate differences between point clouds (C2C, M3C2; Lague et al., 2013), but these are unable to account for lateral displacements.

Popular open-source photogrammetry and PIV software MicMac (Galland et al., 2016), TecPIV (Boutelier, 2016), and OpenPIV[1] provide similar functionality to the built-in Matlab® stereovision application and PIVlab plug-in. Open source software does not depend on access to Matlab® though some require Python, which is open source. However, for integration between datasets and further analysis in Matlab®, these programs would create an even more cumbersome workflow. The user-friendly GUI and abundant documentation for both the Matlab® Stereovision App and PIVlab plug-in were important factors in maintaining a practical, in addition to cost-effective, methodology.

While stereovision in combination with DIC can provide both horizontal and vertical displacements of the experiment, the two datasets are not integrated as they would be with the off-the-shelf three-dimensional PIV systems, such as LaVision DaVis StrainMaster®. The extra effort to coordinate between the stereovision uplift dataset and the DIC horizontal displacement dataset, however, is offset by the relative cost savings of using Matlab® based software, available at many institutions. The results of this effort shed insight into the three-dimensional path of material as it advects through the restraining bend.

The calibrated stereovision system reliably produces uplift maps of the clay surface within the experiments with ±1 mm accuracy (∼5% net uplift for a typical experiment). When combined with horizontal displacements, these elevation data describe the three-dimensional deformation within the evolving fault systems, such as advection and uplift of material along restraining bends. In our simulations of the Mt. McKinley restraining bend, we show that the development of outboard thrust faults shifts the trajectory of material advection. The development of the thrust faults also increases the uplift rate of material within the restraining bend, which is revealed from the combination of horizontal and vertical displacements. The uplift/subsidence rate and pattern can be directly calculated by differencing elevation data across sequential time steps. This approach can be used to relate change in fault evolution to changes in uplift rate. Our simulation of the Mount McKinley restraining bend shows that the loci of greatest uplift rate changes during evolution of the fault system from near the strike-slip fault to adjacent to the new thrust fault traces. Uplift rate maps can also provide the dip slip rate along faults with knowledge of the fault dip, which can be estimated by introducing a trench into the analog material. By combining the horizontal displacement field data with elevation data collected with stereovision techniques, geologists have a new inexpensive tool to quantify the three-dimensional structural evolution of crustal systems in scaled physical experiments.

DATA AVAILABILITY

The raw data supporting the conclusions of this manuscript will be made available by the authors, without undue reservation, to any qualified researcher.

AUTHOR CONTRIBUTIONS

KT performed the experiments, collected the data, and wrote first draft of the manuscript. MC, JB, and SB contributed conception and design of the study. KT developed the stereovision workflow and algorithm. MC developed the PTV processing algorithm. KT and MC performed the data analysis. MC and SB wrote sections of the manuscript. SB and JB provided geologic background on Denali fault and motivation for study. AF compiled thermochronology and modern day topographic uplift constraints for the Mount McKinley restraining bend. All authors contributed to manuscript revision, read, and approved the submitted version.

FUNDING

This work was supported partially by the National Science Foundation under Grant No. EAR 1250461 to SB, Grant No. EAR 1550133 to MC, and Grant No. EAR 1249885 to JB.

ACKNOWLEDGMENTS

The authors thank Tim Dooley, Cara Burberry, and a third reviewer for helpful reviews that helped strengthen the paper.

---

[1] www.openpiv.net/

REFERENCES

Adam, J., Urai, J. L., Wieneke, B., Oncken, O., Pfeiffer, K., Kukowski, N., et al. (2005). Shear localisation and strain distribution during tectonic faulting—new insights from granular-flow experiments and high-resolution optical image correlation techniques. *J. Struct. Geol.* 27, 283–301. doi: 10.1016/j.jsg.2004.08.008

Bemis, S. P., Carver, G. A., and Koehler, R. D. (2012). The Quaternary thrust system of the northern Alaska Range. *Geosphere* 8, 196–205. doi: 10.1130/ges00695.1

Bemis, S. P., Micklethwaite, S., Turner, D., James, M. R., Akciz, S., Thiele, S. T., et al. (2014). Ground-based and UAV-Based photogrammetry: a multi-scale, high-resolution mapping tool for structural geology and paleoseismology. *J. Struct. Geol.* 69, 163–178. doi: 10.1016/j.jsg.2014.10.007

Benowitz, J. A., Layer, P. W., Armstrong, P., Perry, S. E., Haeussler, P. J., Fitzgerald, P. G., et al. (2011). Spatial variations in focused exhumation along a continental-scale strike-slip fault: the Denali fault of the eastern Alaska Range. *Geosphere* 7, 455–467. doi: 10.1130/ges00589.1

Benowitz, J. A., Layer, P. W., and Vanlaningham, S. (2013). *Persistent Long-term (c. 24 Ma) Exhumation in the Eastern Alaska Range constrained by stacked thermochronology. Geological Society*. London: Special Publications 378, SP378. 312.

Bonanno, E., Bonini, L., Basili, R., Toscani, G., and Seno, S. (2017). How do horizontal, frictional discontinuities affect reverse fault-propagation folding? *J. Struct. Geol.* 102, 147–167. doi: 10.1016/j.jsg.2017.08.001

Boutelier, D. (2016). TecPIV—A MATLAB-based application for PIV-analysis of experimental tectonics. *Comput. Geosci.* 89, 186–199. doi: 10.1016/j.cageo.2016.02.002

Burkett, C. A., Bemis, S. P., and Benowitz, J. A. (2016). Along-fault migration of the mount mckinley restraining bend of the denali fault defined by late quaternary fault patterns and seismicity, denali national park & preserve, Alaska. *Tectonophysics* 693, 489–506. doi: 10.1016/j.tecto.2016.05.009

Cooke, M. L., Reber, J. E., and Haq, S. (2016). Physical experiments of tectonic deformation and processes: building a strong community. *GSA Today* 26:36. doi: 10.1130/gsatg303gw.1

Cooke, M. L., Schottenfeld, M. T., and Buchanan, S. W. (2013). Evolution of fault efficiency at restraining bends within wet kaolin analog experiments. *J. Struct. Geol.* 51, 180–192. doi: 10.1016/j.jsg.2013.01.010

Cooke, M. L., and van der Elst, N. J. (2012). Rheologic testing of wet kaolin reveals frictional and bi-viscous behavior typical of crustal materials. *Geophys. Res. Lett.* 39:L01308. doi: 10.1029/2011gl050186

Cruz, L., Teyssier, C., Perg, L., Take, A., and Fayon, A. (2008). Deformation, exhumation, and topography of experimental doubly-vergent orogenic wedges subjected to asymmetric erosion. *J. Struct. Geol.* 30, 98–115. doi: 10.1016/j.jsg.2007.10.003

Cunningham, W. D., and Mann, P. (2007). *Tectonics of Strike-Slip Restraining and Releasing Bends: Fig. 1. Geological Society*, Vol. 290. London: Special Publications, 1–12. doi: 10.1144/sp290.1

Dooley, T. P., and Schreurs, G. (2012). Analogue modelling of intraplate strike-slip tectonics: a review and new experimental results. *Tectonophysics* 57, 1–71. doi: 10.1016/j.tecto.2012.05.030

Elliott, A., Oskin, M., Liu-zeng, J., and Shao, Y.-X. (2018). Persistent rupture terminations at a restraining bend from slip rates on the eastern Altyn Tagh fault. *Tectonophysics* 733, 57–72. doi: 10.1016/j.tecto.2018.01.004

Fendick, A. M. (2016). *Denali in a Box: Analog Experiments Modeled After a Natural Setting Provide Insight on Gentle Restraining Bend Deformation*. MS thesis, University of Kentucky, Kentucky.

Fitzgerald, P. G., Roeske, S. M., Benowitz, J. A., Riccio, S. J., Perry, S. E., and Armstrong, P. A. (2014). Alternating asymmetric topography of the Alaska range along the strike-slip Denali fault: strain partitioning and lithospheric control across a terrane suture zone. *Tectonics* 2013:TC003432. doi: 10.1002/2013TC003432

Fitzgerald, P. G., Sorkhabi, R. B., Redfield, T. F., and Stump, E. (1995). Uplift and denudation of the central Alaska Range: a case study in the use of apatite fission track thermochronology to determine absolute uplift parameters. *J. Geophys. Res.* 100, 20175–20191. doi: 10.1029/95JB02150

Galland, O., Bertelsen, H. S., Guldstrand, F., Girod, L., Johannessen, R. F., Bjugger, F., et al. (2016). Application of open-source photogrammetric software MicMac for monitoring surface deformation in laboratory models. *J. Geophys. Res.* 121, 2852–2872. doi: 10.1002/2015JB012564

Haeussler, P. J. (2008). An overview of the neotectonics of interior Alaska: far-field deformation from the Yakutat microplate collision. *Active Tecton. Seismic Potent. Alaska* 179:20080101.

Haeussler, P. J., Matmon, A., Schwartz, D. P., and Seitz, G. G. (2017). Neotectonics of interior Alaska and the late Quaternary slip rate along the Denali fault system. *Geosphere* 13, 1445–1463. doi: 10.1130/GES01447.1

Hatem, A. E., Cooke, M. L., and Madden, E. H. (2015). Evolving efficiency of restraining bends within wet kaolin analog experiments. *J. Geophys. Res.* 120, 1975–1992. doi: 10.1002/2014jb011735

Hatem, A. E., Cooke, M. L., and Toeneboehn, K. (2017). Strain localization and evolving kinematic efficiency of initiating strike-slip faults within wet kaolin experiments. *J. Struct. Geol.* 101, 96–108. doi: 10.1016/j.jsg.2017.06.011

Henza, A. A., Withjack, M. O., and Schlische, R. W. (2010). Normal-fault development during two phases of non-coaxial extension: an experimental study. *J. Struct. Geol.* 32, 1656–1667. doi: 10.1016/j.jsg.2009.07.007

James, M., and Robson, S. (2012). Straightforward reconstruction of 3D surfaces and topography with a camera: accuracy and geoscience application. *J. Geophys. Res.* 117:F03017. doi: 10.1029/2011JF002289

Koehler, R. D., Farrel, R.-E., Burns, P. A. C., and Combellick, R. A. (2012). *Quaternary Faults and Folds in Alaska: A Digital Database*. Alaska Division of Geological & Geophysical Surveys Miscellaneous Publication, 141, 31. doi: 10.14509/23944

Lague, D., Brodu, N., and Leroux, J. (2013). Accurate 3D comparison of complex topography with terrestrial laser scanner: application to the Rangitikei canyon (NZ). *ISPRS J. Photogramm. Remote Sens.* 82, 10–26. doi: 10.1016/j.isprsjprs.2013.04.009

Lease, R. O., Haeussler, P. J., and O'Sullivan, P. (2016). Changing exhumation patterns during Cenozoic growth and glaciation of the Alaska Range: insight from detrital geo- and thermo-chronology. *Tectonics* 2015:TC004067. doi: 10.1002/2015TC004067

Leever, K. A., Gabrielsen, R. H., Sokoutis, D., and Willingshofer, E. (2011). The effect of convergence angle on the kinematic evolution of strain partitioning in transpressional brittle wedges: insight from analog modeling and high-resolution digital image analysis. *Tectonics* 30:F03017. doi: 10.1029/2010tc002823

Maas, H., Gruen, A., and Papantoniou, D. (1993). Particle tracking velocimetry in three-dimensional flows. *Exp. Fluids* 15, 133–146. doi: 10.1007/BF00190953

Matmon, A., Schwartz, D., Haeussler, P., Finkel, R., Lienkaemper, J., Stenner, H. D., et al. (2006). Denali fault slip rates and Holocene–late Pleistocene kinematics of central Alaska. *Geology* 34, 645–648. doi: 10.1130/G22361.1

McClay, K., and Bonora, M. (2001). Analog models of restraining stepovers in strike-slip fault systems. *AAPG Bull.* 85, 233–260.

McGill, S. F., Owen, L. A., Weldon, R. J., and Kendrick, K. J. (2013). Latest Pleistocene and Holocene slip rate for the San Bernardino strand of the San Andreas fault, Plunge Creek, Southern California: implications for strain partitioning within the southern San Andreas fault system for the last 35 k.y. *Geol. Soc. Am. Bull.* 125, 48–72. doi: 10.1130/b30647.1

Mériaux, A. S., Sieh, K., Finkel, R. C., Rubin, C. M., Taylor, M. H., Meltzner, A. J., et al. (2009). Kinematic behavior of southern Alaska constrained by westward decreasing postglacial slip rates on the Denali fault, Alaska. *J. Geophys. Res.* 114:B03404. doi: 10.1029/2007JB005053

Muste, M., Fujita, I., and Hauet, A. (2008). Large-scale particle image velocimetry for measurements in riverine environments. *Water Resour. Res.* 44:W00D19. doi: 10.1029/2008WR006950

Nissen, E., Krishnan, A. K., Arrowsmith, J. R., and Saripalli, S. (2012). Three-dimensional surface displacements and rotations from differencing pre-and post-earthquake LiDAR point clouds. *Geophys. Res. Lett.* 39:16301. doi: 10.1029/2012GL052460

Nissen, E., Maruyama, T., Arrowsmith, J. R., Elliott, J. R., Krishnan, A. K., Oskin, M. E., et al. (2014). Coseismic fault zone deformation revealed with differential lidar: examples from Japanese Mw 7 intraplate earthquakes. *Earth Planet. Sci. Lett.* 405, 244–256. doi: 10.1016/j.epsl.2014.08.031

Ohmi, K., and Li, H.-Y. (2000). Particle-tracking velocimetry with new algorithms. *Measur. Sci. Technol.* 11:603. doi: 10.1088/0957-0233/11/6/303

Patalano, A., García, C. M., and Rodríguez, A. (2017). Rectification of image velocity results (RIVeR): a simple and user-friendly toolbox for large scale water surface particle image velocimetry (PIV) and particle tracking velocimetry (PTV). *Comput. Geosci.* 109, 323–330. doi: 10.1016/J.CAGEO.2017.07.009

Reber, J. E., Dooley, T. P., and Logan, E. (2017). Analog modeling recreates millions of years in a few hours. *EOS* 98, doi: 10.1029/2017EO085753

Reed, B., and Nelson, S. (1980). *Geologic Map of the Talkeetna Quadrangle, Alaska. USGS Misc. Investigations Series, Map I-1174*. Reston, VA: US Geological Survey.

Richard, P., Naylor, M., and Koopman, A. (1995). Experimental models of strike-slip tectonics. *Petrol. Geosci.* 1, 71–80.

Ridgway, K. D., Thoms, E. E., Layer, P. W., Lesh, M. E., White, J. M., and Smith, S. V. (2007). "Neogene transpressional foreland basin development on the north side of the central Alaska Range, Usibelli Group and Nenana Gravel, Tanana basin," in *Tectonic Growth of a Collisional Continental Margin: Crustal Evolution of Southern Alaska Geological Society of America Special Paper*, eds K. D. Ridgway, J. M. Trop, J. M. G. Glen, and J. M. O'Neill (Boulder, CO: Geological Society of America), 507–547.

Ritter, M. C., Santimano, T., Rosenau, M., Leever, K., and Oncken, O. (2018). Sandbox rheometry: co-evolution of stress and strain in Riedel– and Critical

Wedge–experiments. *Tectonophysics* 722, 400–409. doi: 10.1016/j.tecto.2017.11.018

Rosenau, M., Corbi, F., and Dominguez, S. (2017). Analogue earthquakes and seismic cycles: experimental modelling across timescales. *Solid Earth* 8, 597–635. doi: 10.5194/se-8-597-2017

Schreurs, G., Buiter, S. J. H., Boutelier, J., Burberry, C., Callot, J.-P., Cavozzi, C., et al. (2016). Benchmarking analogue models of brittle thrust wedges. *J. Struct. Geol.* 92, 116–139. doi: 10.1016/j.jsg.2016.03.005

Scott, C. P., Arrowsmith, J. R., Nissen, E., Lajoie, L., Maruyama, T., and Chiba, T. (2018). The M 7 2016 Kumamoto, Japan, Earthquake: 3-D Deformation Along the fault and within the damage zone constrained from differential lidar topography. *J. Geophys. Res.* 123, 6138–6155. doi: 10.1029/2018JB015581

Thielicke, W., and Stamhuis, E. (2014). *PIVLab—Time-resolved digital particle image velocimetry tool for MATLAB. PIV ver.* 1.32".).

Turcotte, D., and Schubert, G. (2014). *Geodynamics*. Cambridge: Cambridge University Press. doi: 10.1017/CBO9780511843877

Westoby, M., Brasington, J., Glasser, N., Hambrey, M., and Reynolds, J. (2012). 'Structure-from-Motion'photogrammetry: a low-cost, effective tool for geoscience applications. *Geomorphology* 179, 300–314. doi: 10.1016/j.geomorph.2012.08.021

Conflict of Interest Statement: The authors declare that the research was conducted in the absence of any commercial or financial relationships that could be construed as a potential conflict of interest.

frontiers in Earth Science

CORRECTION
published: 27 September 2019
doi: 10.3389/feart.2019.00253

Corrigendum: Stereovision Combined With Particle Tracking Velocimetry Reveals Advection and Uplift Within a Restraining Bend Simulating the Denali Fault

Kevin Toeneboehn[1]*, Michele L. Cooke[1], Sean P. Bemis[2], Anne M. Fendick[3] and Jeff Benowitz[4]

[1] Geomechanics Laboratory, Department of Geosciences, University of Massachusetts Amherst, Amherst, MA, United States, [2] Global Forum on Urban and Regional Resilience, Virginia Polytechnic Institute and State University, Blacksburg, VA, United States, [3] Department of Earth and Environmental Sciences, University of Kentucky, Lexington, KY, United States, [4] Department of Tectonics and Sedimentation, Geophysical Institute, University of Alaska Fairbanks, Fairbanks, AK, United States

Keywords: stereovision, particle tracking velocimetry, digital image correlation, analog model, restraining bend, Denali fault, computer vision

A Corrigendum on

Stereovision Combined With Particle Tracking Velocimetry Reveals Advection and Uplift Within a Restraining Bend Simulating the Denali Fault
by Toeneboehn, K., Cooke, M. L., Bemis, S. P., Fendick, A. M., and Benowitz, J. (2018). Front. Earth Sci. 6:152. doi: 10.3389/feart.2018.00152

OPEN ACCESS

Approved by:
Frontiers Editorial Office,
Frontiers Media SA, Switzerland

****Correspondence:***
Kevin Toeneboehn
toeneboehn.kevin@gmail.com

Specialty section:
This article was submitted to Structural Geology and Tectonics, a section of the journal Frontiers in Earth Science

Received: *05 September 2019*
Accepted: *12 September 2019*
Published: *27 September 2019*

Citation:
Toeneboehn K, Cooke ML, Bemis SP, Fendick AM and Benowitz J (2019) Corrigendum: Stereovision Combined With Particle Tracking Velocimetry Reveals Advection and Uplift Within a Restraining Bend Simulating the Denali Fault. Front. Earth Sci. 7:253. doi: 10.3389/feart.2019.00253

"Jeff Benowitz" was not included as an author in the published article. The author list has been updated accordingly.

A correction has therefore been made to the ***Author Contributions*** statement appears below.

"KT performed the experiments, collected the data, and wrote first draft of the manuscript. MC, JB, and SB contributed conception and design of the study. KT developed the stereovision workflow and algorithm. MC developed the PTV processing algorithm. KT and MC performed the data analysis. MC and SB wrote sections of the manuscript. SB and JB provided geologic background on Denali fault and motivation for study. AF compiled thermochronology and modern day topographic uplift constraints for the Mount McKinley restraining bend. All authors contributed to manuscript revision, read, and approved the submitted version."

Furthermore, a correction has been made to the ***Funding*** statement:

"This work was supported partially by the National Science Foundation under Grant No. EAR 1250461 to SB and Grant No. EAR 1550133 to MC, and Grant No. EAR 1249885 to JB."

The authors apologize for these error and state that this does not change the scientific conclusions of the article in any way. The original article has been updated.

frontiers in Earth Science

ORIGINAL RESEARCH
published: 23 October 2018
doi: 10.3389/feart.2018.00148

Extending Continental Lithosphere With Lateral Strength Variations: Effects on Deformation Localization and Margin Geometries

Anouk Beniest[1,2]*, *Ernst Willingshofer*[3], *Dimitrios Sokoutis*[3,4] *and William Sassi*[2]

[1] *Sorbonne Université, ISTeP, CNRS-UMR 7193, Paris, France,* [2] *IFP Energies nouvelles, Geosciences Division, Rueil-Malmaison, France,* [3] *Department of Earth Sciences, Utrecht University, Utrecht, Netherlands,* [4] *Department of Geosciences, University of Oslo, Oslo, Norway*

Edited by:
Mélody Philippon,
UMR5243 Géosciences Montpellier,
France

Reviewed by:
Damien Delvaux,
Royal Museum for Central Africa,
Belgium
Lorenzo Bonini,
University of Trieste, Italy

***Correspondence:**
Anouk Beniest
anouk.beniest@etu.upmc.fr

Specialty section:
This article was submitted to
Structural Geology and Tectonics,
a section of the journal
Frontiers in Earth Science

Received: *29 June 2018*
Accepted: *18 September 2018*
Published: *23 October 2018*

Citation:
Beniest A, Willingshofer E, Sokoutis D and Sassi W (2018) Extending Continental Lithosphere With Lateral Strength Variations: Effects on Deformation Localization and Margin Geometries. Front. Earth Sci. 6:148. doi: 10.3389/feart.2018.00148

We investigate the development of margin geometries during extension of a continental lithosphere containing lateral strength variations. These strength variations may originate from the amalgamation of continents with different mechanical properties as was probably the case when Pangea was assembled. Our aim is to infer if localization of deformation is controlled by the boundary between two lithospheres with different mechanical properties (e.g., "weak" and "strong") or not. We ran a series of lithosphere-scale physical analog models in which we vary the strength contrast across equally sized lithospheric domains. The models show that deformation always localizes in the relatively weaker compartment, not at the contact between the two domains because the contact is unfavorably oriented for the applied stress and does not behave as a weak, inherited discontinuity. Wide-rifts develop under coupled conditions when the weak lithosphere consists of a brittle crust, ductile crust and ductile mantle. When a brittle upper mantle layer is included in the weak segment, the rift system develops in two phases. First, a wide rift forms until the mechanically strong upper mantle develops a necking instability after which the weak lower crust and weak upper mantle become a coupled, narrow rift system. The margin geometries that result from this two-phase evolution show asymmetry in terms of crustal thickness and basin distribution. This depends heavily on the locus of failure of the strong part of the upper mantle. The models can explain asymmetric conjugate margin geometries without using weak zones to guide deformation localization.

Keywords: rifting, lithosphere, analog modeling, South Atlantic, deformation localization

INTRODUCTION

The South Atlantic domain resulted from the separation of the African and the South American continents. Prior to rifting and break-up, the supercontinent Pangea (**Figure 1**) consisted of (a) fold and thrust belts, including the Gondwana Fold and Thrust Belt (Cobbold et al., 1992) and the Dom Feliciano Gariep belts, representing inverted back-arc basins (Engelmann de Oliveira et al., 2016; Konopásek et al., 2016; Will and Frimmel, 2017), (b) magmatic provinces of different ages and (c) cratons (Will and Frimmel, 2017). When rifting initiates, the developing rift axes and the locus of

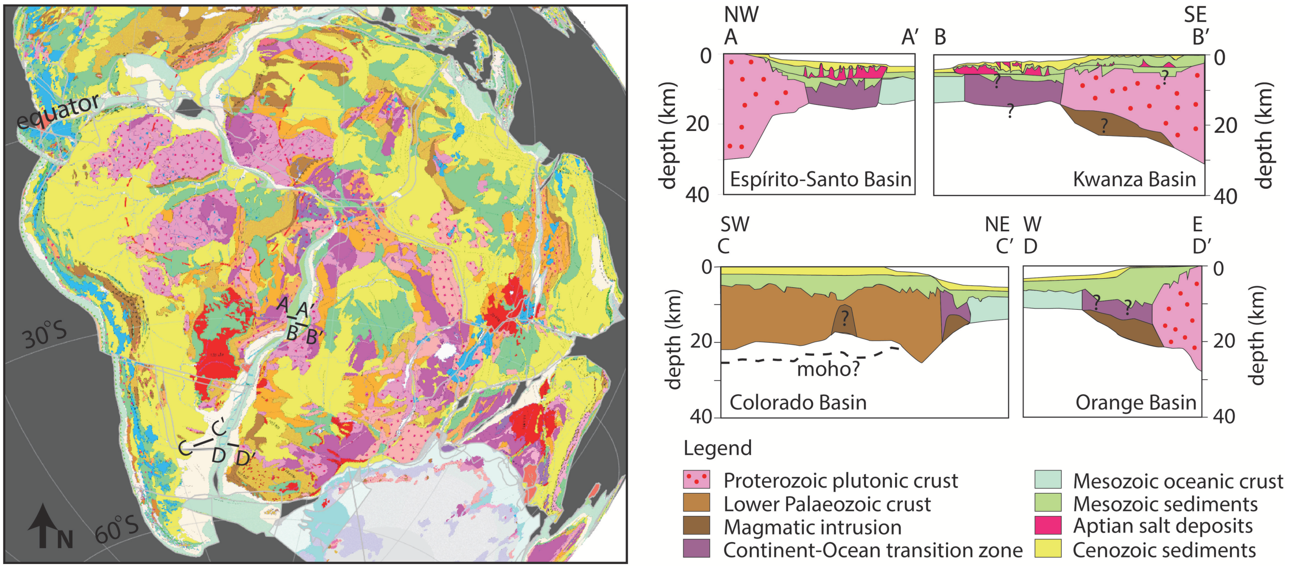

FIGURE 1 | Reconstructed projection of the geological maps of South America and Africa before break-up. Reconstruction has been done using the rotation poles and continental polygons of Seton et al. (2012). The geological map has been extracted from the Geological Map of the World by Bouysse (2014). The cross-sections A-A′, B-B′, C-C′, and D-D′, have been simplified after Blaich et al. (2011) and projected on the reconstruction. The reconstructed geology shows that the continents consist of an amalgamation of different crustal features. This has been adopted for the crustal cross-sections resulting in similar crustal features for the continental part of the Espírit-Santo Basin and Kwanza Basin margins (Proterozoic plutonic crust) and different crustal features for the continental part of Colorado Basin margin (Proterozoic sedimentary crust) and the Orange Basin margin.

the continental break-up sometimes follows the craton's boundary. This is, for example, the case of the western and eastern rift branches of the East African Rift System that surrounds the Tanzanian craton (Ebinger, 1989). In other cases, rifting does not follow these former craton boundaries so strictly, but is distributed over a wide region affecting pre-existing geological features. The Pan-African Araçuai – West Congo orogenic belt is an example where the rift system went through the orogen rather than close to the craton's boundary. At present, roughly two-thirds of this orogen can be found on the South American plate and the rest on the African plate (Pedrosa-Soares et al., 2008). Another example are the remnants of rift features, e.g., horst and graben structures, which are nowadays located on the margins of the southern segment of both the South American and African plates (**Figure 1**, Blaich et al., 2011).

Continental rift initiation and eventual break-up at crustal and lithospheric scale has been studied with physical analog and numerical modeling techniques. Initial setups used in these studies are often simplified with respect to natural cases (Burov and Diament, 1995; Brun and Beslier, 1996; Gueydan and Précigout, 2014; Manatschal et al., 2015; Naliboff et al., 2017). Weak seeds or weak zones representing the inheritance of earlier deformation phases are permitted to achieve strain localization at the desired place or in self consistent ways (Corti et al., 2007; Huismans and Beaumont, 2007; Sokoutis et al., 2007; Brune et al., 2014; Burov and Gerya, 2014; Nestola et al., 2015; Bonini et al., 2016; Zwaan et al., 2016). These studies have been valuable, because they have shown that weak zones in the lower crust have a higher impact on rift localization than weak zones in the lithospheric mantle (Sokoutis et al., 2007) and that strength variations within the lower crust are important for along margin segmentation of the crust (Cappelletti et al., 2013). Apart from weak zones or inherited structures, strain softening mechanisms (Gueydan et al., 2014), complex brittle-ductile stratification and thickness of the lithosphere (Burov and Diament, 1995; Brun and Beslier, 1996) and variations in extension rates (Brune et al., 2016; Naliboff et al., 2017) are important parameters to localize strain.

Few studies have been performed that investigate extension of systems with large, spatial strength variations. Bonini et al. (2007) found that strain preferably localizes in thinner lithosphere in cases where the thickness of the lithosphere varies prior to extension. Koptev et al. (2015, 2016) demonstrated that in lithospheres with a large strength contrast, mantle anomalies migrate along the base of stronger features, breaking the crust in the weaker parts. Beniest et al. (2017a,b) showed that large strength contrasts can result in different break-up styles and final margin geometries, including multiple break-up branches, depending on the location of thermal anomalies.

In this contribution we address the question whether large lateral strength variations within the continental lithosphere by themselves can direct deformation localization and the evolution of rift structures and geometries. Complementary to the studies of e.g., Beniest et al. (2017a,b), Bonini et al. (2007) and Koptev et al. (2015), we use analog modeling techniques that allow the implementation of large strength contrasts across lithospheric segments. Our aim is to understand why, like in the case of the South Atlantic, localization of deformation did not only follow inherited tectonic contacts like suture zones, but also went across old and rigid crustal features. The experimental results increase our understanding of extension affecting amalgamated continents or lithospheres such as Pangea, which was a complex assembly of cratons, fold-and-thrust belts and basins prior to its break-up (Will and Frimmel, 2017).

EXPERIMENTAL SETUP

For our experimental setup we have chosen three different strength profiles that could represent (1) young crust according to the "crème brulée" model, or (2) intermediate strong continental crust and (3) old, cratonic crust, which are variations to the "jelly-sandwich" model (Burov, 2011). Geological observations on the South American and African continents show that these types of crust may occur in the vicinity of one another prior to break-up (**Figure 1**). The model's dimension is 36 × 30 cm (**Figure 2**). The total thickness of the lithosphere was kept the same at 4 cm for all models at the onset of extension, although strength variations may also be associated with thickness variations in nature (Burov and Diament, 1995). Material properties are specified in **Table 1** and scaling laws have been adopted as described in Sokoutis et al. (2005). The models are performed at the Tectonic Laboratory (TecLab) of Utrecht University.

Analog Model Setups

In this study we describe the experimental results of extending lithospheres with lateral strength variations against two reference models, representing weak (M1, **Figure 2A**) and intermediate (M2, **Figure 2A**) strength lithospheres. The strength of these lithospheres has been varied laterally by increasing the thickness of the brittle layers in expense of the ductile layers leading to combinations of weak and strong (model 3, M3, **Figure 2C**) and intermediate and strong lithospheres (model 4, M4, **Figure 2D**). Domains of different strength are equal in size and the separating boundaries are vertical. In our experiments, dry granular materials such as feldspar and quartz sand represent the brittle crust and brittle mantle, whereas mixtures of Rhodorsil Gomme GSIR (RG) silicone with fillers embody the viscous layers (ductile crust and ductile mantle lithosphere). These layers rest on a low viscosity, high density fluid of polytungstate, representing the asthenosphere.

The weakest strength profile (S1, **Figure 2E**) consists of three layers, representing, from bottom to top, the strong part of the lithospheric upper mantle, the ductile lower crust and the brittle upper crust (Bonini et al., 2012). The stronger part of the upper mantle is represented by ductile Rhodorsil-gum layer with a density of 1,503 kg/m3 and an almost Newtonian viscosity and is 2 cm in thickness. A second ductile Rhodorsil-gum layer with a density of 1,407 kg/m3 and an almost Newtonian viscosity represents the ductile lower crust with a thickness of 1.2 cm. A brittle feldspar layer with a density of 1,300 kg/m3 with Mohr-Coulomb behavior represents the upper crust that is 0.8 cm thick. The strength peak of this profile resides in the brittle upper crust. The middle and strongest strength profiles (S2 and S3, **Figures 2F,G**) both consist of four layers, a ductile Rhodorsil-gum layer (1.6 cm thick for S2 and 1.2 cm thick for S3) at the bottom of the model with a density of 1,503 kg/m3. This is covered by a quartz sand layer with Mohr-Coulomb criteria and a density of 1,503 kg/m3 (0.4 cm thick for S2 and 0.8 cm thick for S3). These two layers represent the strong part of the lithospheric mantle. The ductile lower crust is featured by a

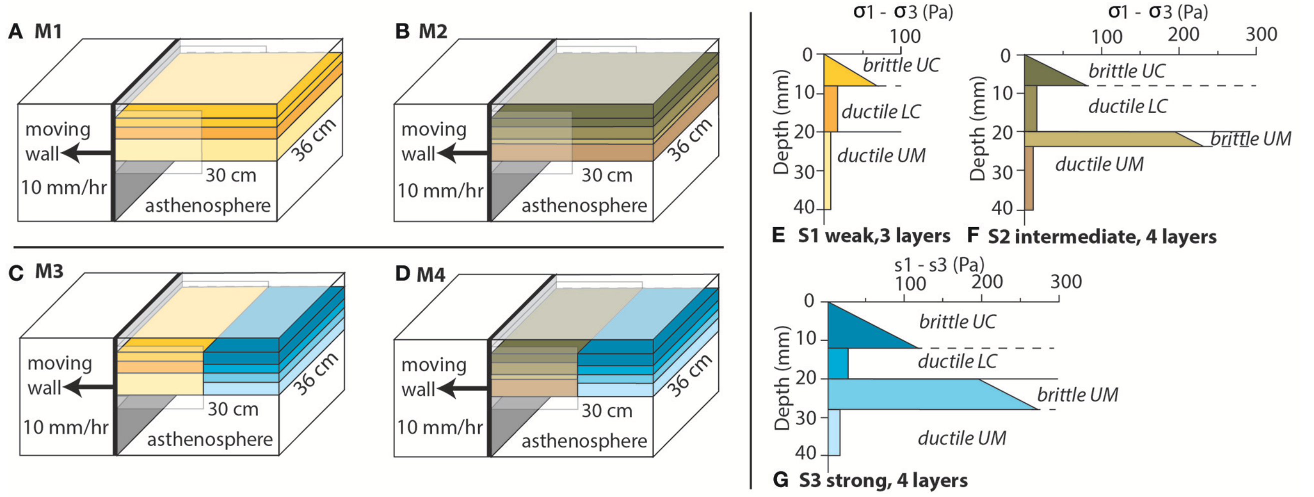

FIGURE 2 | Experimental setup of the four analog models **(A–D)** with rheological strength envelopes **(E–G)**. **(A)** Model 1 (M1), lateral homogeneous stratified strength profile S1 (weak, three layers, **E**). **(B)** Model 2 (M2), lateral homogeneous stratified strength profile S2 (intermediate, four layers, **F**). **(C)** Model 3, lateral variation in strength profile combining vertically stratified strength profile S1 (weak, three layers, **E**) and S3 (strong, four layers, **G,D**) Model 4, lateral variation in strength profile combining vertically stratified strength profile S2 (intermediate, three layers, **E**) and S3 (strong, four layers, (**G**)). The black arrow indicates the direction of the moving wall (10 mm/h, constant rate) that also holds the box-in-box construction. The layered lithosphere floats on a low viscosity high density fluid within the Plexiglas box. *UC, upper crust; LC, lower crust; UM, upper mantle*.

TABLE 1 | Physical properties for experimental material and comparison between nature and experiments.

Layer	Analog material	Density model	Density nature	Layer thickness	Layer thickness	Friction coefficient	Cohesion	Viscosity model	Viscosity nature	Rm model	Rm nature
		ρ (kg/m3)	ρ (kg/m3)	Model (m)	Nature (m)	μ	C (Pa)	η (Pa s)	η (Pa s)		
Upper crust	Feldspar sand	1,300	2,700	0.012	2.20E + 04	0.4–0.7	15–35				
				0.008	1.47E + 04	0.4–0.7	15–35				
				0.006	1.10E + 04	0.4–0.7	15–35				
Lower crust	Rhodorsil gum	1,407	2,900	0.012	2.20E + 04			1.80E + 04	1.60E + 21	9.94	9.78
	mixed with PDMS			0.008	1.47E + 04			1.80E + 04	2.35E + 21	4.42	4.45
Brittle mantle	Quartz sand	1,500	3,300	0.008	1.47E + 04	0.6	30–70				
lithosphere				0.004	7.34E + 03	0.6	30–70				
High viscous mantle	Rhodorsil gum	1,503	3,300	0.02	3.67E + 04			1.66E + 04	3.72E + 22	31.98	31.94
lithosphere	mixed with PDMS			0.016	2.94E + 04			1.66E + 04	4.70E + 22	20.47	20.25
				0.012	2.20E + 04			1.66E + 04	8.40E + 22	11.51	11.33
Asthenosphere	Sodium polytungstate	1,600	3,200					1.2	1.00E+23		

second Rhodorsil-gum layer with a density of 1,407 kg/m3 and an almost Newtonian viscosity (thickness of 1.2 cm for S2 and 0.8 cm thickness for S3). The top layer depicts the upper crust and consists of feldspar sand with Mohr-Coulomb behavior and a density of 1,300 kg/m3, the thickness being 0.8 cm for S2 and 1.2 cm for S3. The intermediate and strong strength profiles have two strength peaks, one in the brittle crust and another in the brittle mantle lithosphere (e.g., Brun, 1999).

All models float on a heavy liquid of polytungstate-glycerol mixture, with a low viscosity and a density of 1600 kg/m^3 and to avoid the model from subducting. This fluid represents the asthenosphere as well as the very weak part, with the least strength of the lithospheric mantle (Willingshofer et al., 2005). The models are subjected to extensional forces through gravity spreading upon moving one Plexiglas wall away from the experimental lithosphere at a constant rate of 1.0 cm/h, which scales to 1.4 cm/yr in nature. In this study we aim to capture the (first) deformational response of the continental lithosphere with lateral strength variations prior to break-up. As a consequence, the total amount of extension is not the same in all models and depends on the rheological setup of the experiments. Following Allemand and Brun (1991), extension of the lithosphere was implemented by a box-in-box construction. A small box that measured half of the model box' width was attached to the moving wall creating a velocity discontinuity at the long sides of the Plexiglas box (**Figure 2**). One half of the box was attached to the moving wall perpendicular to the contact between the lithosphere segments of variable strength (**Figure 2**). During the experiments, top view photos were taken every 10 min. Models ran for a variety of time (3 to 8.5 h).

Analog Model Scaling

Analog models are comparable with natural examples on various grounds. One is the rheological similarity between the silicon layers that behave in a ductile manner and the sand layers that behave in a brittle way that compare to the viscous and plastic behavior of rocks on geological time scales. Also geometric, dynamic and kinematic criteria need to be met. For geometric scaling the modeled length ratios need to be equal in all directions (x (length), y (width) and z (depth), i.e., $\frac{X_m}{X_n} = \frac{Y_m}{Y_n} = \frac{Z_m}{Z_n}$). The reference models M1 and M2 consist of a lateral homogeneous setup of 36 × 30 × 4 cm. M3 and M4 consist of two types of strength profiles, with equal thicknesses (4 cm), widths (36 cm), and lengths (16 cm). With a scale-factor of 6.67 e-7, this would represent 540 km × 480 km × 60 km in nature, or 1 cm is 15 km. Dynamic scaling of the model with a natural example can be accomplished by respecting the stress-scale factor which includes stress distribution, rheologies and densities (Hubbert, 1937; Ramberg, 1981; Brun, 1999; Sokoutis et al., 2005), $\frac{\sigma^*}{L^*} + \rho^* g^* - \rho^* \left(\frac{\varepsilon^*}{t^*}\right) = 0$, when conserving mass. The following conditions apply for the model:

$$\sigma^* = L^* \rho^* g^* \quad (1)$$

$$\varepsilon^* = g^* (t^*)^2 \quad (2)$$

where σ refers to stress, L to length, ρ to density, g to gravitational acceleration, ε to strain and t to time. The asterisk indicates that the number is unit-less, representing the ratio between the model and nature.

Experiments are carried out under normal gravity and therefore the gravity ratio (g^*) is equal to 1. The densities for the model and the natural example are in the same order of magnitude (e.g., 1,300 kg/m^3 for the model and 2,800 kg/m^3 for the natural example), hence the density ratio (ρ^*) is more or less equal to 1. This simplifies Equation. 1 to:

$$\sigma^* = L^* \tag{3}$$

or in other words, the ratio between the stresses and the length of the model and natural example need to be roughly equal (Davy and Cobbold, 1991; Brun, 1999). For kinematic scaling, the model and the natural example abide a timescale that is proportional to the changes in shape and/or position in both the model and natural example (so $\frac{t_m}{t_n} = \frac{t_{m2}}{t_{n2}} = \frac{t_{mx}}{t_{nx}}$ etc.). Since velocity is given by length/time, the model can be scaled with respect to the prototype with the following equation:

$$V_n = V_m{}^* \frac{L_n^* t_m^*}{L_m^* t_n^*} \tag{4}$$

where V_n is velocity in nature, V_m is velocity in the model, L_n is length in nature, L_m is length in the model, t_n is time in nature and t_{tm} is time of the model. With a modeled 1 cm/h extension rate (V_m) the natural velocity is 1.4 cm/yr, which is comparable to the average diverging rate in the South Atlantic domain (Müller et al., 2008).

The Reynolds number (Equation 5) for these kind of experiments is rather low for both the model and the natural example (Re = 10^{-8} and Re = 10^{-24}).

$$Re = \frac{(\rho v l)}{\eta} \tag{5}$$

where ρ stands for the density, v is the extension velocity, l the extended length and η the viscosity. Therefore inertial forces can be neglected compared to the viscous ones and this allows time and length ratios to be seen as separate variables (Ramberg, 1981; Dombrádi et al., 2010). The time ratio is thus calculated using the length ratios and corresponding velocities and results in a time ratio $t^* = 3.17^{-10}$ between the duration of the model and the geological time scale.

The Ramberg number (Rm, Equation 6) was calculated to test dynamic and kinematic similarities between the ductile layers assuming a background strain rate of 1.0E−16 for the

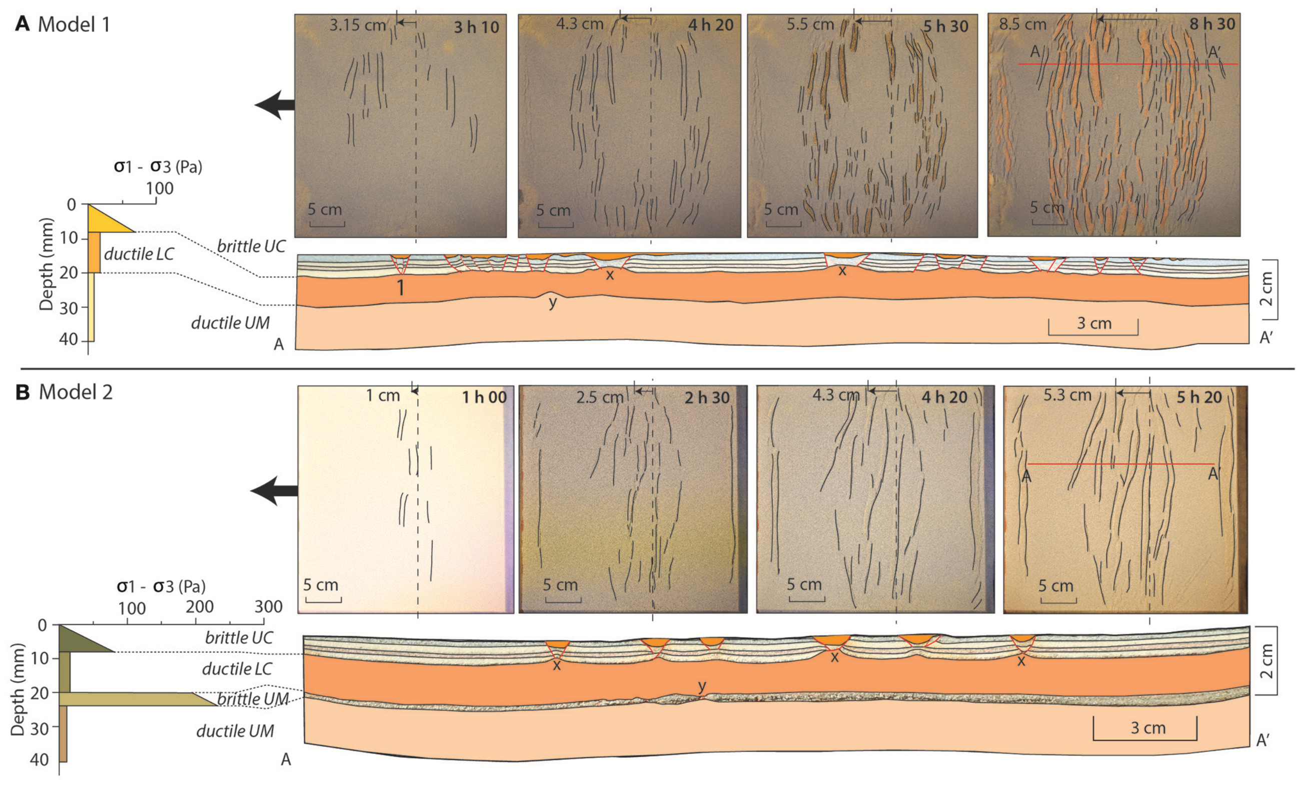

FIGURE 3 | Experimental results of models with one type of lithosphere **(A)** Model 1 (M1) and **(B)** Model 2 (M2). Wide rifts form in both models, M2 being 25% less wide than M1 due to the presence of a stronger sub-Moho mantle. Ductile lower crust is exhumed (locations x, M1, and M2). Moho topography shows subtle long wavelength undulations, generally not in phase with the graben structures indicating the flow of material. Pinch and swell structures form in the brittle lithospheric mantle of M2 (location y). The bracketed line on the top-view images represents the contact between the two lithospheric segments. *BC, brittle crust; DC, ductile crust; BM, brittle mantle; DM, ductile mantle*.

natural prototype. This yielded viscosities between 9.5E+22 and 2.0E+23, which is within the range expected for natural systems (Burov, 2011).

$$Rm = \frac{\rho z g}{(\sigma_1 - \sigma_3)} \tag{6}$$

where ρ is the density of the material, *z* the thickness of the layer, *g* the gravitational acceleration and $\sigma_1 - \sigma_3$ refers to the ductile strength of the material (Bonini et al., 2012).

Model Results

The models with laterally uniform strength have been extended for 8.5 cm (127.5 km in nature, M1, **Figure 3A**) and 5.3 cm (79.5 km in nature, M2, **Figure 3B**). Both experiments show that the brittle crust accommodates extension through normal faulting that outline horst and graben, half-graben, and tilted fault block structures. Faults grow either through laterally propagating graben structures or by coalescence of individually developed fault segments to form structures that span the entire width of the models (map views, **Figures 3A,B**). In cross-sections, these graben structures where lower crust is being exhumed, are shown by location x (**Figures 3A,B**). Asymmetric structures such as tilted blocks, half grabens or slightly asymmetric grabens exist on the scale of the brittle crust, but the overall deformation is symmetric, both on the scale of the individual layers as well as the entire lithosphere. With reference to the moving wall, the extensional structures develop randomly, not in sequence. This shows that deformation is evenly distributed. None of the structures developed into a major rift that would eventually lead to a break-up system. At deeper levels, the ductile upper mantle penetrates into the ductile lower crust at location y (**Figures 3A,B**). In M2, the brittle upper mantle develops pinch and swell structures where the ductile mantle rises (location y, **Figure 3B**). The most important difference observed on the cross-sections between the above described experiments is that grabens in M1 are distributed over a distinctly wider area as opposed to M2 (compare **Figures 3A,B**).

The model with combined weak and strong lithospheres, M3, accommodated 3.2 cm of extension (48 km in nature, **Figure 4A**). This model develops deformation structures exclusively in the weak lithosphere. The structural style is similar to M1 with graben and half graben in the brittle crust and flow dominated deformation in the ductile layers. The more pronounced exhumation of the lower crust to shallow levels (location x, **Figure 4A**) and a more distinct Moho topography are the consequence of extension being focused within a less wide segment of lithosphere compared to M1. The final lithosphere-scale geometry of the model is asymmetric as a consequence of thinning of the weak lithosphere from 4.0 to 2.6 cm (35% thickness decrease). The combined intermediate and strong lithosphere, M4, has accommodated 6.2 cm of extension (93 km in nature, **Figure 4B**). The deformation appears to be distributed less randomly than in the other models and closer located toward the contact between the different rheological segments. Nevertheless deformation only occurs in the relatively weaker segment. Deformation in the brittle crust is symmetric with a series of grabens that exhume lower crust material. Faulting affects the brittle layers in M4 until the boundary between the two lithosphere segments (**Figure 4B**, position x). Different to M3, extension in M4 led to necking of the mantle lithosphere and exhumation of the ductile mantle layer where the brittle mantle broke and got separated (**Figure 4B**, position y). This region of maximum thinning of the mantle lithosphere is only matched by the location of one of the grabens within the crust that developed later in the evolutionary sequence (graben a, **Figure 4B**). Overall, narrow and localized deformation within the mantle lithosphere is compensated by distributed deformation within the crust. Besides thinning at the area of necking (4.0 to 2.6 cm, 35% thickness decrease), minor thickness change occurred within the mantle lithosphere of the intermediate-strength lithosphere (4.0 to 3.6 cm, 10% thickness decrease). For both M3 and M4 the strong segment kept its original thickness.

DISCUSSION

Rheological Control on the Locus of Extension and Style of Deformation in Continental Lithosphere With Lateral Strength Variations

Our experiments consistently predict that extension of continental lithosphere with lateral strength variations will lead to stretching of the relatively weaker lithosphere (**Figure 4**, M3 and M4). Unexpectedly, deformation never initiates at the location where the rheological contrast is largest (at the transition of the weaker to the stronger lithosphere) but almost always starts within the weaker segment and never propagates into the stronger one. The only exception is M4 where one normal fault formed at the contact between the two different lithospheres very early in the rift evolution. Deformation eventually localizes somewhere in the weak domain and thus this small normal fault ceases to accommodate extension. One reason for this could be that the perpendicular orientation of the contact with respect to the extension direction might not be favorable for deformation localisation. Our results are therefore consistent with the analog modeling study of Bonini et al. (2007), who investigated lithosphere extension with laterally changing mechanical properties related to rifting in West Antarctica. In their models, deformation solely concentrated within the weak lithosphere, but compared to our models they differ on the aspect of strain localization. Bonini et al. (2007) show that the transition from strong to weak lithosphere can turn into the locus of the main boundary fault confining the evolving rift under initial conditions of having a stress gradient from the strong to the weak lithosphere in response to significant thickness variations. The impact of this stress gradient is probably enhanced through the application of the centrifuge technique. Additionally, there is in our experiments no predefined fault or zone of weakness that cuts across layers at the transition from the strong to the weak lithospheric domain that would facilitate strain localisation at the onset of deformation there. The continuity of brittle and ductile layers in our experiments, yet subject to thickness

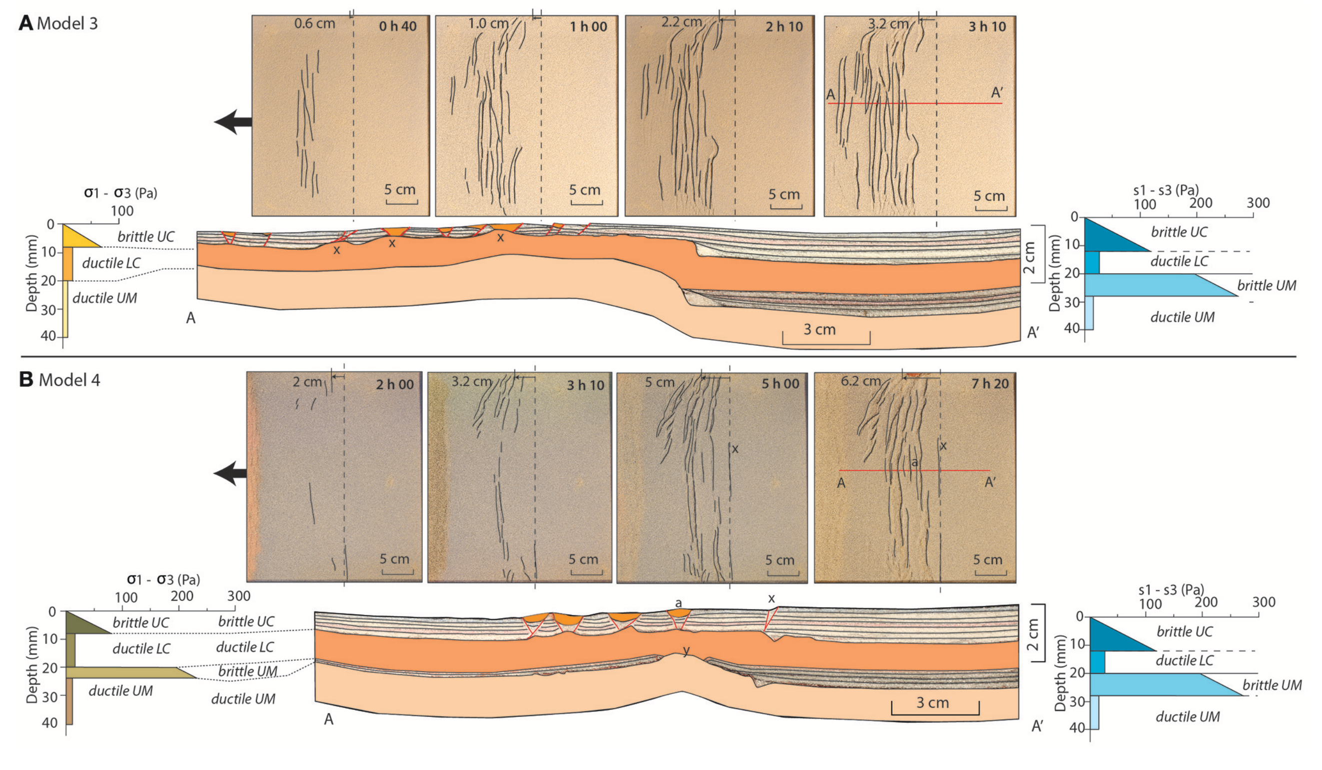

FIGURE 4 | Experimental results of homogeneous lithospheric setup **(A)** Model 3 (M3) and **(B)** Model 4 (M4). M3 and M4 show that all extension is accommodated in the weak segment. The thickness of the weak segment of M3 decreases with 35% in a distributed fashion. In the weak segment of M4 the sub-Moho mantle has lost its strength and thickness decreases with 35% at the necking domain (**B**, location y). The original thickness of the strong domains of both models remains. The bracketed line on the top-view images represents the contact between the two lithospheric segments. *BC, brittle crust; DC, ductile crust; BM, brittle mantle; DM, ductile mantle*.

changes to produce the stronger and weaker domains, seems to render the actual rheological contrast insignificant for localizing deformation. This behavior is different to convergent settings where deformation tends to localize at transitions from stronger to weaker and vice versa crust or lithosphere (e.g., Willingshofer et al., 2005; Munteanu et al., 2014; Calignano et al., 2015). This emphasizes the sensitivity of the localization of deformation at strength contrasts to the orientation of that strength contrast with respect to the applied stress, i.e., to the tectonic regime (extensional vs. compressional). As shown by our experiments, the locus of deformation may thus significantly deviate from the position of rheological heterogeneities in the system in cases where no inherited weak structures exist at the contact of weak and strong domains.

Numerical models that have tested the influence of inherited structures on rift localisation clearly underline the importance of these structures for the early phases of rift evolution (e.g., Manatschal et al., 2015; Naliboff et al., 2017). After strain and structural softening, also the thermal and rheological structure control the break-up location (Huismans and Beaumont, 2007; Manatschal et al., 2015; Duretz et al., 2016). With the models presented here, we show that large strength contrasts in the lithosphere by itself are in-sufficient to localize deformation.

In our experiments extension affects large parts of the weaker lithosphere, whereby the width of deformation is regulated by the degree of coupling among the layers that constitute the lithosphere. The width of the deformed zone is wider when layers are coupled (M1, **Figure 3A**, and M3, **Figure 4A**) and narrower by 40–50% when layers are less well coupled (M2, **Figure 3B**, and M4, **Figure 4B**). This behavior is consistent with previous analog modeling studies that emphasize the importance of the mechanical coupling between the layers on width and style of deformation (Brun, 1999; Nestola et al., 2015; Gabrielsen et al., 2016; Brun et al., 2018). During distributed extension the ductile mantle rises below the larger grabens, leading to significant exhumation of the mantle lithosphere (Brun and Beslier, 1996; Corti et al., 2011; Brun et al., 2018) as often observed along passive margins (Manatschal et al., 2015). From the early stages of rifting to spreading, the style and architecture of the evolving rift system is in a first instance controlled by the thermal and mechanical structure of the extending crust and lithosphere, the presence of inherited heterogeneities (Buck, 1991; Manatschal et al., 2015; e.g., Brun et al., 2018). However, parameters like the extension rate may regulate the strength of the ductile layers as it affects the dynamics of the rifted domain (Bassi, 1995) and thus the degree of coupling amongst layers. Changes in extension rate may lead to a switch from distributed to localized deformation or

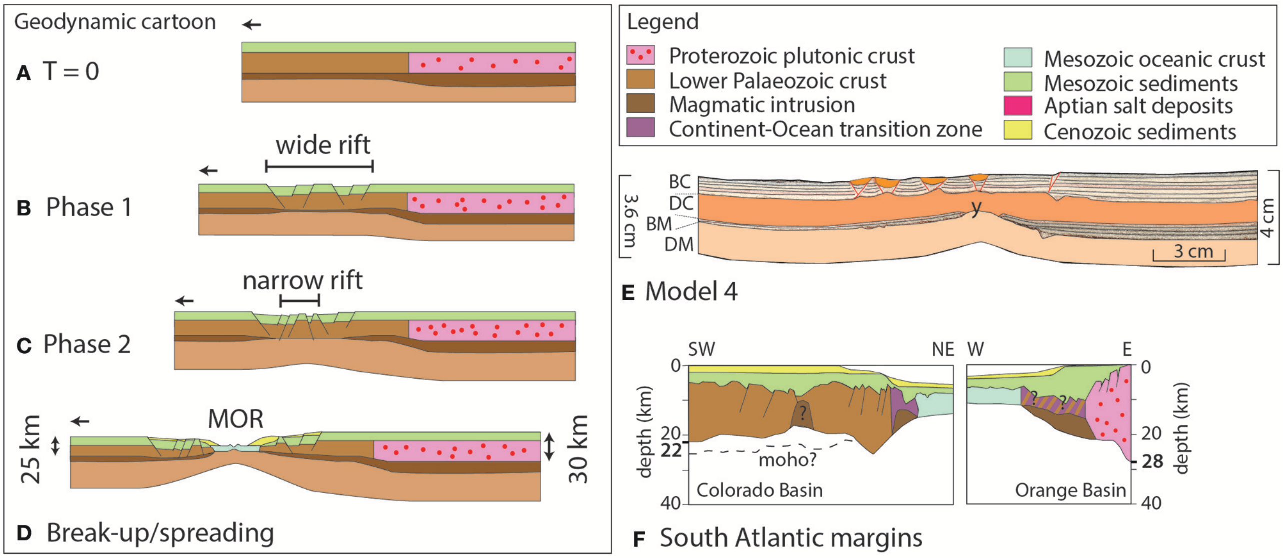

FIGURE 5 | Cartoon showing the two-phased conceptual evolution of continental break-up in a system **(A)** consisting of two large lithosphere segments, T = 0. **(B)** Phase 1 shows the distributed or wide rift formation, with normal faulting occurring in the weak segment. **(C)** Phase 2 shows localized or narrow deformation that occurs directly above the location where the upper mantle has failed and the weak lower crust and the weak part of the upper mantle are in direct contact. **(D)** Continuous extension will eventually lead to breakup above the necking point that formed during the second phase, resulting in asymmetric margins in terms of crustal thickness and basin positioning. **(E)** M4, with two lithospheric segments of different strength shows a small decrease in thickness for the weak segment (right side) and a very. **(F)** The simplified cross-section of the South Segment continental margin of the South Atlantic shows that the crustal thickness of both margins is not equal, being thinner on the South American side also the transition zones have different thicknesses and more horst and graben structures are located on the margin of the South American continent.

vice versa (Brun et al., 2016; Naliboff et al., 2017). Additionally, we infer that the switch from distributed to localized deformation through time is also controlled by the strength of the sub-Moho mantle. This strength decreases during the initial distributed rifting phase (phase 1, wide-rift, **Figure 5B**) when pinch-and-swell structures develop (e.g., location y, **Figure 3B**). Once the ductile crust and ductile mantle are in direct contact (location y, **Figures 4B**, **5E**), a localized weaker zone emerges (phase 2, narrow rift, **Figure 5C**) that develops into the necking domain. Such structural softening, following the necking of competent layers, has been described by Duretz et al. (2016) and we argue that the locus of necking in the mantle will control where maximum exhumation of the lower crust and mantle will take place and where the formation of a mid-oceanic ridge or spreading center will occur (**Figure 5D**).

The analog models presented here compare well to the numerical studies of Beniest et al. (2017a,b). The numerical experiments investigate the effect of thermal anomalies on the style of continental break-up of lithosphere consisting large domains with different strength. The mantle anomaly simulates the presence of the Tristan plume in the South Atlantic domain (Torsvik et al., 2006). The numerical results show that depending on the initial location of the mantle anomaly with respect to the contact between the different strength segments, several modes of continental break-up may develop. In other words, even though our analog models show that no thermal anomaly is needed to create a potential break-up locus, including thermal processes increases the variety of break-up styles that may occur in a setting consisting of multiple lithospheric domains with different strength. The numerical models are better at explaining high density/high velocity bodies as being underplated material or partial melts that result from migrating plume material at the base of the lithosphere (Beniest et al., 2017a,b) than the analog models, but asymmetric margin geometries can be reproduced by both analog and numerical experiments.

Relevance for Natural Systems

Our models are built to investigate the effect of extension on large strength contrast in (super)continents. The crustal strength of the South American plate is assumed to be weaker than the African crust due to a previous extensional deformation phase that has affected the Argentinian and Uruguayan margin (Autin et al., 2013), forming the E-W trending basins that are nowadays located along the margins of the South Segment of the South Atlantic. This deformation phase might have led to thinning of the lithosphere on the South American side, which is currently 120 km thick (Heit et al., 2007). In comparison, the continental lithosphere on the African side is currently up to 200 km thick (Fishwick, 2010). Also the occurrence of different types of outcrops on either side of the margin [Precambrian sediments on the South American side (**Figure 1**) and Precambrian volcanic rocks on the African side (Bouysse, 2014)] suggest different strengths on either side of the margin prior to break-up. Our models only show the first two phases of rifting in which a wide rift develops first and a narrow rift forms during a second phase when the strong upper mantle has failed and the weaker lower crust and weaker part of the upper mantle are in direct contact, representing the main softening mechanism. If extension would continue, continental separation is expected above this necking point (**Figure 5D**). This final geometry is comparable to the present day margins of the South Atlantic in various ways.

Firstly, it is comparable in terms of crustal thicknesses. As it is unknown what the crustal thickness was prior to break-up, it can be assumed that lithosphere thickness was different on both sides as a result of the first deformation phase that formed the roughly E-W trending basins and only affected the South American continent as pointed out by Autin et al. (2013). It can also be assumed that the crustal thicknesses were more equal despite this previous extension phase as the crustal thicknesses of the Brazilian and African cratons are currently within the same order of magnitude [42 km for the South American São Francisco craton (Van Der Meijde et al., 2013) and between 38 and 45 km for the southern African crust (Stankiewicz et al., 2002)]. Both cases of crustal thicknesses are justified. Our analog models presented here assume the latter case, where crustal thicknesses would be more equal. M4 shows that extending a system with two crustal segments with different strengths but similar thicknesses can produce thinning all over the weak segment, leaving the strong segment undeformed. The differences in crustal thicknesses can therefore also be explained just due to strength variations in the crust, without needing a previous deformation phase. The results are again comparable to the South Atlantic margins (**Figure 5F**), where the continental side of the South American margin is roughly 22 km thick and can be as thick as 25–30 km (Schnabel et al., 2008), compared to 28 on the African side (Blaich et al., 2011), which can be as thick as 40 km (Maystrenko et al., 2013).

Secondly, the models can be compared to nature in terms of basin distribution along the margins. The first phase of our M4 model (**Figure 5E**) produces a wide rift with basins distributed over a large part of the basin (**Figures 4B**, **5B**). The localized rift that follows this first phase produces a necking zone that will eventually break the crust above this necking point, leaving an uneven basin distribution. In this case more basins reside on the right side than on the left side, which is comparable to the higher amount of small basins within the Colorado basin observed on the South American side below the sediments cover than on the African side (**Figure 5F**, Blaich et al., 2011). The distribution of the basins depends largely on the location where the resistant upper mantle fails, which does not have to be exactly in the center of the initial distributed rift (see section Rheological Control on the Locus of Extension and Style of Deformation in Continental Lithosphere With Lateral Strength Variations).

The width of the margins is a third comparison that can be made between the models and the natural case. If we consider the point of break-up to be directly above the necking point as formed in model M4, a sliver of weak lithosphere will become detached from the weak segment and remains attached to the strong segment. The margin that forms on the weak segment, will be thinner and wider for a large area, whereas the margin that develops on the strong segment will show a sharp decrease in thickness from the continent to the margin as the small, thin sliver of weak lithosphere will remain attached to the strong, thick continental lithosphere. On the cross-sections of Blaich et al. (2011) the upper limit of the Continent-Ocean-Transition is unsure. A hypothesis could be that a thin sliver of weaker material remained attached to the African continent after break-up, leading to asymmetric widths and geometries between both margins. In this case, the continent would not have been broken at the contact between the two segments but rather through a former back arc basin, which could have been the case for parts of the South Atlantic (Will and Frimmel, 2017).

CONCLUSION

We investigated the deformational response to extensional forces on continental lithosphere with lateral strength variations. Deformation structures that lead to significant rifting are only developed in the weaker lithosphere segment, not at the contact between the two segments, suggesting that in the absence of a weak zone at the contact, the rheological heterogeneity may be unfavorable oriented with respect to the applied stresses to facilitate strain localization at that point. The weaker segment thins, whereas the strong segment preserves its original thickness. Models including a strong sub-Moho mantle develop a necking zone once the strong part of the upper mantle has failed. The evolution of these models is two-phased with (1) a distributed or wide rift phase with normal fault systems throughout the weak segment and (2) a localized or narrow rift phase that forms once the strong upper mantle suffers strength failure and develops a necking zone. We have shown with these models that it is possible to break a continent at a different location than at a pre-existing heterogeneity, without the influence of thermal processes or by including inherited weak zones. This two phase evolution forms asymmetric margins that can be compared to a natural case, the South Atlantic domain, in terms of crustal thicknesses, basin distribution and margin widths. We state therefore that large-scale lateral strength variations in the lithosphere are an important factor controlling both the location of deformation localisation within the weak domain and the architecture of the rift system. We also argue that the strong part of the upper mantle plays a major role in determining the location of necking and future break-up.

AUTHOR CONTRIBUTIONS

AB, EW, and DS conducted the experiments in the laboratory. AB provided the figures of the manuscript. AB, EW, DS, and WS participated in model setup discussions. AB, EW, DS, and WS wrote and edited the manuscript.

ACKNOWLEDGMENTS

EW and DS thank the Netherlands Research Centre for Integrated Solid Earth Sciences for supporting the infrastructure relevant for this study. AB thanks Antoine Auzemery for his indispensable help in the lab. This work has been included in the thesis of Beniest (2017).

REFERENCES

Allemand, P., and Brun, J. P. (1991). Width of continental rifts and rheogical layering of the lithosphere. *Tectonophysics* 188, 63–69.

Autin, J., Scheck-Wenderoth, M., Loegering, M. J., Anka, Z., Vallejo, E., Rodriguez, J. F., et al. (2013). Colorado Basin 3D structure and evolution, Argentine passive margin. *Tectonophysics* 604, 264–279. doi: 10.1016/j.tecto.2013.05.019

Bassi, G. (1995). Relative importance of strain rate and rheology for the mode of continental extension. *Geophys. J. Int.* 122, 195–210.

Beniest, A. (2017). *From Continental Rifting to Conjugate Margins: Insights From Analogue and Numerical Modelling*. Paris IV : Université Pierre et Marie Curie -.

Beniest, A., Koptev, A., and Burov, E. (2017a). Numerical models for continental break-up: implications for the South Atlantic. *Earth Planet. Sci. Lett*. 461, 176–189. doi: 10.1016/j.epsl.2016.12.034

Beniest, A., Koptev, A., Leroy, S., Sassi, W., and Guichet, X. (2017b). Two-branch break-up systems by a single mantle plume : insights from numerical modeling. *Geophys. Res. Lett*. 44, 1–9. doi: 10.1002/2017GL074866

Blaich, O. A., Faleide, J. I., and Tsikalas, F. (2011). Crustal breakup and continent-ocean transition at South Atlantic conjugate margins. *J. Geophys. Res*. 116, 1–38. doi: 10.1029/2010JB007686

Bonini, L., Basili, R., Toscani, G., Burrato, P., Seno, S., and Valensise, G. (2016). The effects of pre-existing discontinuities on the surface expression of normal faults: insights from wet-clay analogue modelling. *Tectonophysics* 684, 157–175. doi: 10.1016/j.tecto.2015.12.015

Bonini, M., Corti, G., Del Ventisette, C., Manetti, P., Mulugeta, G., and Sokoutis, D. (2007). Modelling the lithospheric rheology control on the Cretaceous rifting in West Antarctica. *Terra Nova* 19, 360–366. doi: 10.1111/j.1365-3121.2007.00760.x

Bonini, M., Sane, F., and Antonielli, B. (2012). Basin inversion and contractional reactivation of inherited normal faults: a review based on previous and new experimental models. *Tectonophysics* 522–523, 55–88. doi: 10.1016/j.tecto.2011.11.014

Bouysse, P. (2014). *Geological Map of the World at 1:35 000 000.* Paris: CCGM-CGMW.

Brun, J.-P., Faccenna, C., Gueydan, F., Sokoutis, D., Philippon, M., Kydonakis, K., et al. (2016). The two-stage Aegean extension, from localized to distributed, a result of slab rollback acceleration. *Can. J. Earth Sci*. 53, 1142–1157. doi: 10.1139/cjes-2015-0203

Brun, J. P. (1999). Narrow rifts versus wide rifts : inferences for the mechanics of rifting from laboratory experiments [and discussion]. *Philos. Trans. R. Soc. Lond. Ser. A Math. Phys. Eng. Sci.* 357, 695–712.

Brun, J. P., and Beslier, M. O. (1996). Mantle exhumation at passive margins. *Earth Planet. Sci. Lett*. 142, 161–173. doi: 10.1016/0012-821X. (96).00080-5

Brun, J. P., Sokoutis, D., Tirel, C., Gueydan, F., Van Den Driessche, J., and Beslier, M.-O. (2018). Crustal versus mantle core complexes. *Tectonophysics*. doi: 10.1016/j.tecto.2017.09.017

Brune, S., Heine, C., Pérez-Gussinyé, M., and Sobolev, S. V. (2014). Rift migration explains continental margin asymmetry and crustal hyper-extension. *Nat. Commun*. 5, 1–9. doi: 10.1038/ncomms5014

Brune, S., Williams, S. E., Butterworth, N. P., and Müller, R. D. (2016). Abrupt plate accelerations shape rifted continental margins. *Nat. Publ. Gr*. 536, 201–204. doi: 10.1038/nature18319

Buck, W. R. (1991). Modes of continental lithospheric extension. *J. Geophys. Res.* 96, 20161–20178. doi: 10.1029/91JB01485

Burov, E., and Gerya, T. (2014). Asymmetric three-dimensional topography over mantle plumes. *Nature* 513, 85–89. doi: 10.1038/nature13703

Burov, E. B. (2011). Rheology and strength of the lithosphere. *Mar. Pet. Geol*. 28, 1402–1443. doi: 10.1016/j.marpetgeo.2011.05.008

Burov, E. B., and Diament, M. (1995). The effective elastic thickness. (Te). of continental lithosphere: what does it really mean? *J. Geophys. Res*. 100, 3905–3927. doi: 10.1029/94JB02770

Calignano, E., Sokoutis, D., Willingshofer, E., Gueydan, F., and Cloetingh, S. (2015). Strain localization at the margins of strong lithospheric domains: insights from analog models. *Tectonics* 34, 396–412. doi: 10.1002/2014TC003756.Received

Cappelletti, A., Tsikalas, F., Nestola, Y., Cavozzi, C., Argnani, A., Meda, M., et al. (2013). Impact of lithospheric heterogeneities on continental rifting evolution: constraints from analogue modelling on South Atlantic margins. *Tectonophysics* 608, 30–50. doi: 10.1016/j.tecto.2013.09.026

Cobbold, P. R., Gapais, D., Rossello, E. A., Milani, E. J., and Szatmari, P. (1992). "Permo-Triassic intracontinental deformation," in *Inversion Tectonics of the Cape Fold Belt, Karoo and Cretaceous Basins of South Africa*, ed S. W. Gondwana (Rotterdam: Balkema), 23–26.

Corti, G., Bonini, M., Innocenti, F., Manetti, P., Piccardo, G. B., and Ranalli, G. (2007). Experimental models of extension of continental lithosphere weakened by percolation of asthenospheric melts. *J. Geodyn*. 43, 465–483. doi: 10.1016/j.jog.2006.11.002

Corti, G., Calignano, E., Petit, C., and Sani, F. (2011). Controls of lithospheric structure and plate kinematics on rift architecture and evolution: an experimental modeling of the Baikal rift. *Tectonics* 30, 1–16. doi: 10.1029/2011TC002871

Davy, P., and Cobbold, P. R. (1991). Experiments on shortening of a 4-layer model of the continental lithosphere. *Tectonophysics* 188, 1–25. doi: 10.1016/0040-1951. (91).90311-F

Dombrádi, E., Sokoutis, D., Bada, G., Cloetingh, S., and Horváth, F. (2010). Modelling recent deformation of the pannonian lithosphere: lithospheric folding and tectonic topography. *Tectonophysics* 484, 103–118. doi: 10.1016/j.tecto.2009.09.014

Duretz, T., Petri, B., Mohn, G., Schmalholz, S. M., Schenker, F. L., and Müntener, O. (2016). The importance of structural softening for the evolution and architecture of passive margins. *Nat. Publ. Gr*. 6, 1–7. doi: 10.1038/srep38704

Ebinger, C. J. (1989). Tectonic development of the western branch of the East African rift system. *Geol. Soc. Am. Bull*. 101, 885–903.

Engelmann de Oliveira, C. H., Jelinek, A. R., and Chemale, F Jr., Bernet, M. (2016). Evidence of post-Gondwana breakup in Southern Brazilian Shield : insights from apatite and zircon fission track thermochronology. *Tectonophysics* 666, 173–187. doi: 10.1016/j.tecto.2015.11.005

Fishwick, S. (2010). Surface wave tomography: imaging of the lithosphere – asthenosphere boundary beneath central and southern Africa? *Lithos* 120, 63–73. doi: 10.1016/j.lithos.2010.05.011

Gabrielsen, R. H., Sokoutis, D., Willingshofer, E., and Faleide, J. I. (2016). Fault linkage across weak layers during extension : an experimental approach with reference to the Hoop Fault Complex of the SW Barents Sea. *Pet. Geosci*. 22, 123–135. doi: 10.1144/petgeo2015-029

Gueydan, F., and Précigout, J. (2014). Modes of continental rifting as a function of ductile strain localization in the lithospheric mantle. *Tectonophysics* 612–613, 18–25. doi: 10.1016/j.tecto.2013.11.029

Gueydan, F., Précigout, J., and Montési, L. G. J. (2014). Strain weakening enables continental plate tectonics. *Tectonophysics* 631, 189–196. doi: 10.1016/j.tecto.2014.02.005

Heit, B., Sodoudi, F., Yuan, X., Bianchi, M., and Kind, R. (2007). An S receiver function analysis of the lithospheric structure in South America. *Geophys. Res. Lett*. 34, 1–5. doi: 10.1029/2007GL030317

Hubbert, M. K. (1937). Theory of scale models as applied to the study of geologic structures. *Bull. Geol. Soc. Am*. 48, 1459–1520.

Huismans, R. S., and Beaumont, C. (2007). Roles of lithospheric strain softening and heterogeneity in determining the geometry of rifts and continental margins. *Geol. Soc. Lond. Spec. Publ*. 282, 111–138. doi: 10.1144/SP282.6

Konopásek, J., Sláma, J., and Kosler, J. (2016). Linking the basement geology along the Africa-South America coasts in the South Atlantic. *Precambrian Res*. 280, 221–230. doi: 10.1016/j.precamres.2016.05.011

Koptev, A., Burov, E., Calais, E., Leroy, S., Gerya, T., Guillou-Frottier, L., et al. (2016). Contrasted continental rifting via plume-craton interaction: applications to Central East African Rift. *Geosci. Front*. 7, 221–236. doi: 10.1016/j.gsf.2015.11.002

Koptev, A., Calais, E., Burov, E., Leroy, S., and Gerya, T. (2015). Dual continental rift systems generated by plume – lithosphere interaction. *Nat. Geosci*. 8, 388–392. doi: 10.1038/NGEO2401

Manatschal, G., Lavier, L., and Chenin, P. (2015). The role of inheritance in structuring hyperextended rift systems: some considerations based on observations and numerical modeling. *Gondwana Res*. 27, 140–164. doi: 10.1016/j.gr.2014.08.006

Maystrenko, Y. P., Scheck-Wenderoth, M., Hartwig, A., Anka, Z., Watts, A. B., Hirsch, K. K., et al. (2013). Structural features of the Southwest African continental margin according to results of lithosphere-scale 3D gravity and thermal modelling. *Tectonophysics* 604, 104–121. doi: 10.1016/j.tecto.2013.04.014

Müller, R. D., Sdrolias, M., Gaina, C., Steinberger, B., and Heine, C. (2008). Long-term sea-level fluctuations driven by ocean basin dynamics. *Science* 319, 1357–1362. doi: 10.1126/science.1151540

Munteanu, I., Willingshofer, E., Matenco, L., Sokoutis, D., and Cloetingh, S. (2014). Far-field contractional polarity changes in models and nature. *Earth Planet. Sci. Lett*. 395, 101–115. doi: 10.1016/j.epsl.2014.03.036

Naliboff, J. B., Buiter, S. J. H., Péron-Pinvidic, G., Osmundsen, P. T., and Tetreault, J. (2017). Complex fault interaction controls continental rifting. *Nat. Commun*. 8, 1–9. doi: 10.1038/s41467-017-00904-x

Nestola, Y., Storti, F., and Cavozzi, C. (2015). Strain rate-dependent lithosphere rifting and necking architectures in analog experiments. *J. Geophys. Res. Solid Earth* 120, 584–594. doi: 10.1002/2014JB011623.Received

Pedrosa-Soares, A. C., Alkmim, F. F., Tack, L., Noce, C. M., Babinski, M., Silva, L. C., et al. (2008). Similarities and differences between the Brazilian and African counterparts of the Neoproterozoic Araçuaí – West Congo. *Geol. Soc. Lond. Spec. Publ*. 294, 153–172. doi: 10.1144/SP294.9

Ramberg, H. (1981). *Gravity, Deformation, and the Earth's Crust in Theory, Experiments Ad Geological Application*. (London: Academic Press)

Schnabel, M., Franke, D., Engels, M., Hinz, K., Neben, S., Damm, V., et al. (2008). The structure of the lower crust at the Argentine continental margin, South Atlantic at 44°S. *Tectonophysics* 454, 14–22. doi: 10.1016/j.tecto.2008.01.019

Seton, M., Müller, R. D., Zahirovic, S., Gaina, C., Torsvik, T., Shephard, G., et al. (2012). Earth-science reviews global continental and ocean basin reconstructions since 200 Ma. *Earth Sci. Rev*. 113, 212–270. doi: 10.1016/j.earscirev.2012.03.002

Sokoutis, D., Burg, J., Bonini, M., Corti, G., and Cloetingh, S. (2005). Lithospheric-scale structures from the perspective of analogue continental collision. *Tectonophysics* 406, 1–15. doi: 10.1016/j.tecto.2005.05.025

Sokoutis, D., Corti, G., Bonini, M., Pierre Brun, J., Cloetingh, S., Mauduit, T., et al. (2007). Modelling the extension of heterogeneous hot lithosphere. *Tectonophysics* 444, 63–79. doi: 10.1016/j.tecto.2007.08.012

Stankiewicz, J., Chevrot, S., Van Der Hilst, R. D., and De Wit, M. J. (2002). Crustal thickness, discontinuity depth, and upper mantle structure beneath southern Africa: constraints from body wave conversions. *Phys. Earth Planet. Inter*. 130, 235–251. doi: 10.1016/S0031-9201.(02).00012-2

Torsvik, T. H., Smethurst, M. A., Burke, K., and Steinberger, B. (2006). Large igneous provinces generated from the margins of the large low-velocity provinces in the deep mantle. *Geophys. J. Int*. 167, 1447–1460. doi: 10.1111/j.1365-246X.2006.03158.x

Van Der Meijde, M., Julià, J., and Assumpção, M. (2013). Gravity derived Moho for South America. *Tectonophysics* 609, 456–467. doi: 10.1016/j.tecto.2013.03.023

Will, T. M., and Frimmel, H. E. (2017). Where does a continent prefer to break up? Some lessons from the South Atlantic margins. *Gondwana Res*. 53, 9–19. doi: 10.1016/j.gr.2017.04.014

Willingshofer, E., Sokoutis, D., and Burg, J.-P. (2005). Lithospheric-scale analogue modelling of collision zones with a pre-existing weak zone. *Geol. Soc. London, Spec. Publ*. 243, 277–294. doi: 10.1144/GSL.SP.2005.243.01.18

Zwaan, F., Schreurs, G., Naliboff, J., and Buiter, S. J. H. (2016). Insights into the effects of oblique extension on continental rift interaction from 3D analogue and numerical models. *Tectonophysics* 693, 239–260. doi: 10.1016/j.tecto.2016.02.036

Conflict of Interest Statement: The authors declare that the research was conducted in the absence of any commercial or financial relationships that could be construed as a potential conflict of interest.

frontiers
in Earth Science

ORIGINAL RESEARCH
published: 15 November 2018
doi: 10.3389/feart.2018.00199

Laboratory Modeling of Coeval Brittle and Ductile Deformation During Magma Emplacement Into Viscoelastic Rocks

Håvard Svanes Bertelsen[1], Benjamin D. Rogers[1], Olivier Galland[1], Guillaume Dumazer[2] and Alexandre Abbana Benanni[3]*

[1] *Physics of Geological Processes, Department of Geosciences, The NJORD Center, University of Oslo, Oslo, Norway,* [2] *PoreLab, Physics Department, The NJORD Center, University of Oslo, Oslo, Norway,* [3] *Ecole Normale Supérieure de Lyon, Lyon, France*

OPEN ACCESS

Edited by:
Mélody Philippon,
UMR5243 Géosciences Montpellier,
France

Reviewed by:
Ben Matthew Kennedy,
University of Canterbury, New Zealand
Mimmo Palano,
Istituto Nazionale di Geofisica e
Vulcanologia, Italy

***Correspondence:**
Håvard Svanes Bertelsen
h.s.bertelsen@geo.uio.no

Specialty section:
This article was submitted to
Volcanology,
a section of the journal
Frontiers in Earth Science

Received: *02 July 2018*
Accepted: *26 October 2018*
Published: *15 November 2018*

Citation:
Bertelsen HS, Rogers BD, Galland O,
Dumazer G and Abbana Benanni A
(2018) Laboratory Modeling of Coeval
Brittle and Ductile Deformation During
Magma Emplacement Into
Viscoelastic Rocks.
Front. Earth Sci. 6:199.
doi: 10.3389/feart.2018.00199

The mechanics of magma emplacement in the Earth's crust corresponds to the flow of a viscous fluid into a deforming solid. The Earth's crust through which magma is emplaced is visco-elasto-plastic, and field observations show that most intrusions are likely to be accommodated by combined brittle and ductile deformation of their host. However, mechanical models of magma emplacement account for either purely elastic, plastic or viscous end-member rheology of the host rock, therefore they cannot simulate the natural diversity of magma intrusion shapes and magma emplacement mechanisms. Thus they are of limited use to constrain under which conditions intrusions of contrasting shapes form. Here we present a series of 2D experiments where a viscous fluid (oil) was injected into a host matrix (laponite gel), the visco-elasto-plastic rheology of which is varied from dominantly viscous to dominantly elastic. The oil intrusion in the elastic gel is a thin conduit with a sharp tip, like magmatic dykes, whereas the oil intrusion in the viscous gel is rounded, like diapirs. In addition, the oil intrusion in gels of intermediate properties exhibits complex, hybrid shapes. The experiments were run in a polariscope, which highlighted birefringence patterns related to deformation structures within the gel. Our experiments show a strong correlation between intrusion shapes and host matrix deformation modes: (1) thin intrusions dominantly propagate by tensile failure and elastic deformation of the host, (2) rounded "diapiric" intrusions dominantly propagate by viscous flow of the host, and (3) irregular "hybrid" intrusions propagate by coeval brittle (tensile and shear) and ductile deformation of the host. Our novel experiments are the first able to produce the natural diversity of intrusion shapes and host deformation mechanisms. In addition, our results show that the use of a polariscope in gel experiments is essential to unravel the mechanics of magma emplacement within a host of realistic visco-elasto-plastic rheology.

Keywords: magma emplacement, laponite gel, visco-elasto-plastic experiments, 2D laboratory models, polariscopic imaging

1. INTRODUCTION

The mechanics of magma transport and emplacement in the Earth's crust generally corresponds to the flow of a viscous fluid into a solid, which deforms to accommodate the incoming volume of magma. In volcanic systems, however, the simplicity of this statement is challenged by the complexity of geological materials. The viscosity of magma varies over many orders of magnitude, depending on, e.g., temperature, volatile content and composition (e.g., Dingwell et al., 1993; Scaillet et al., 1997), while crustal rocks exhibit a wide range of visco-elasto-plastic rheologies (e.g., Ranalli, 1995). Consequently, depending on magma viscosity and host rock rheology, the magma/host mechanical systems can exhibit distinct and/or mixed physical behaviors, which lead to (1) intrusions of significantly diverse shapes (e.g., sheets to "blobs") and (2) contrasting deformation patterns in the host (Galland et al., 2018).

Currently, models of magma emplacement mainly account for end-member mechanical behaviors of crustal rocks.

1. A popular model for the emplacement of high-viscosity magma in the lower ductile crust addresses the host rock as a viscous fluid. In these models, the magma intrusions are considered as diapirs (e.g., Ramberg, 1981; Miller and Paterson, 1999; Burov et al., 2003; Gerya and Burg, 2007) (**Figure 1A**).
2. Models accounting for the emplacement of thick, so-called "punched laccoliths" in the brittle crust address the host rock as a Coulomb brittle (plastic) material (e.g., Román-Berdiel et al., 1995; Galland et al., 2006; Abdelmalak et al., 2012; Montanari et al., 2017; Schmiedel et al., 2017). In these models, magma intrusions are emplaced by pushing their host rock, which is displaced along fault planes (**Figure 1B**).
3. Most models of emplacement of igneous sheet intrusions (i.e., dykes, sills, cone sheets, thin laccoliths) in the brittle crust address the host rock as an elastic solid (e.g., Rubin, 1995; Menand et al., 2010; Galland and Scheibert, 2013; Kavanagh et al., 2015; Rivalta et al., 2015). In these models, magma intrusions are addressed as idealized tensile hydraulic fractures, the thickening of which is accommodated by elastic bending of the host rock (**Figure 1C**).

However, the Earth's crust is neither purely viscous, plastic, nor elastic, but, as stated, visco-elasto-plastic. Therefore, even if purely viscous diapiric rise, plastic faulting, or elastic hydraulic fracturing may happen, most intrusions are likely to be accommodated by hybrid viscous, plastic, and elastic deformations of the host (Rubin, 1993; Vachon and Hieronymus, 2016; Scheibert et al., 2017).

This statement is corroborated by field observations of igneous sills emplaced in shale-carbonate rocks, which exhibit complex brittle-ductile deformation that accommodated the emplacement of the magma (Schofield et al., 2012; Duffield et al., 2016; Spacapan et al., 2017) (**Figure 1D**). Moreover, field observations in the host rock of thin laccoliths in the Henry Mountains, Utah, evidence significant plastic shear failure and ductile deformation of the overburden (Román-Berdiel et al., 1995; de Saint Blanquat et al., 2006; Wilson et al., 2016), in contrast to the elastic assumptions of the theoretical models (e.g., Pollard, 1973; Bunger and Cruden, 2011).

Seismicity monitored in active volcanoes also highlights the complex mechanical behavior of the crust during dyke emplacement. While dyke emplacement models assume tensile propagation in purely elastic host rock, earthquake swarms monitored during dyke propagation exhibit numerous, if not most dominant, double-couple focal mechanisms interpreted as shear faulting (e.g., Borandsdottir and Einarsson, 1979; Ukawa and Tsukahara, 1996; Battaglia et al., 2005; Roman and Cashman, 2006; White et al., 2011; Ágústsdóttir et al., 2016). These geophysical observations suggest that shear failure can significantly accommodate dyke propagation, and that the plastic Coulomb properties of the crust are likely at work during dyke propagation, in contrast to the established theories.

Finally, the sheet morphologies of sills and saucer-shaped sills were used to argue that they result from tensile hydraulic fracturing (e.g., Bunger and Cruden, 2011; Galland and Scheibert, 2013; Kavanagh et al., 2015), similar to dykes. Recent models, however, show that the emplacement of saucer-shaped sills is likely controlled by the shear failure of their brittle overburden (Haug et al., 2017, 2018). These models show that the Coulomb plastic properties of the crust likely play an important role in the emplacement of sheet intrusions, again in contradiction to the tensile elastic assumptions of established models of sheet intrusion emplacement.

These observations highlight that the end-member rheological assumptions of the current theoretical, laboratory, and numerical models of magma emplacement have limited physical validity because the host-magma interaction is too simplified. In addition, because the models assume rheological end-members, they cannot simulate the natural diversity of magma intrusion shapes and magma emplacement mechanisms, and so they are of limited use to predict under which conditions intrusions of contrasting shapes form. Such limitation lead to the heated debates in the 80-90's that opposed the diapiric vs. hydraulic fracturing models for granite emplacement, whereas field evidences supported both mechanisms (e.g., Rubin, 1993; Petford, 1996; Miller and Paterson, 1999; Petford and Clemens, 2000). These limitations lead to the following questions, as highlighted by Rubin (1993):

1. How does combined viscous, plastic, and elastic (subsequently referred to as "hybrid") deformation of the host control the emplacement of magma?
2. What properties govern the transition between brittle and ductile intrusion mechanisms, and under which conditions might hybrid behaviors occur?
3. What are the characteristic patterns of hybrid deformation during magma emplacement, and how do we identify the end-member intrusion mechanisms?

Answering these questions requires the design of a model able to simulate the injection of a viscous fluid into a matrix of controllable and variable rheological properties. Several laboratory studies in the physics community implemented such an approach to constrain the dynamics of viscous fingering vs. viscoelastic fracturing (e.g., Lemaire et al., 1991; Hirata, 1998; Nase et al., 2008; Sumita and Ota, 2011). However, these models

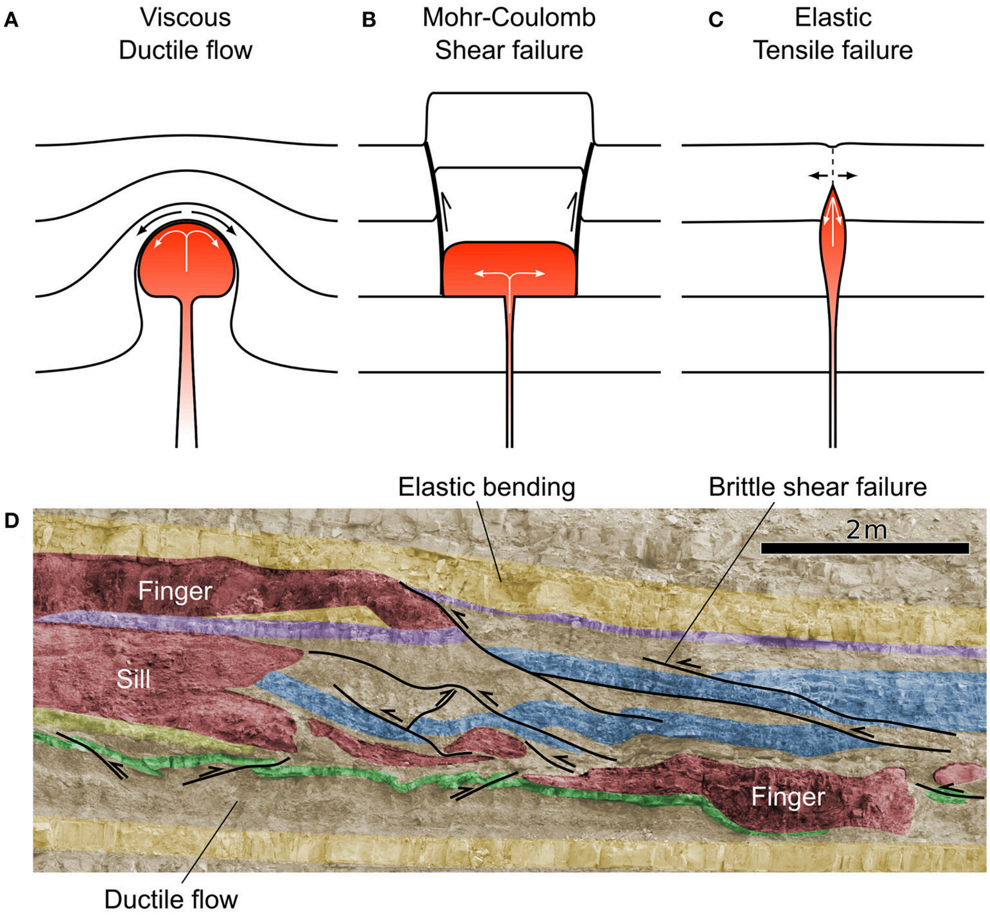

FIGURE 1 | Diagram of idealized end-member cases of magma ascent. **(A)** A diapir (viscous end-member) indents and displaces the surrounding host rock extensively, making the host rock viscosity a fundamental parameter for governing ascent rate. **(B)** A punched laccolith (brittle shear failure end-member) indents and displaces the overburden, which fails along plastic, brittle faults. **(C)** A dyke (elastic end-member) fractures and intrudes the host rock with negligible host rock displacement, thus, the ascent rate is primarily controlled by host rock fracture strength and magma viscosity. Adapted from Rubin (1993). **(D)** Interpreted field photograph of outcrop exposing a sheet-like sill, magmatic fingers, and the associated structures in the shale-carbonate host rock, Cuesta del Chihuido, Mendoza Province, Argentina (Spacapan et al., 2017). The outcrop shows that the sill tip is round or blunt, and that both ductile deformation of the shale layers, brittle shear faulting of thin carbonate layers and elastic bending of thick carbonate layers accommodate the emplacement and propagation of the sill. Detailed descriptions of the structures and associated mechanisms can be found in Spacapan et al. (2017).

focused on the morphology of the intruding fluid only, such that the complex deformation happening within the host matrix was not observed, and so not understood. In this paper, we present exploratory laboratory models designed to constrain the deformation mechanisms accommodating viscous fluid injection into a viscoelastic host. To achieve this, we used a polariscope to monitor birefringence patterns corresponding to deformation of the viscoelastic host matrix. Our exploratory experiments highlight contrasting ductile and brittle deformation patterns accommodating the emplacement of, among others, viscous fingers, hydraulic fractures and hybrid intrusions.

2. MATERIALS AND METHODS

In our model, the host rock is represented by a colloidal aqueous gel of laponite RD, a synthetic smectite clay produced by BYK Altana. The laponite gel can display a wide range of viscoelastic behaviors for different concentration, salt content, pH, and curing time (Ruzicka and Zaccarelli, 2011a; Ruzicka et al., 2011b). A major rheological trait of laponite gel is that it shows shear-thinning and thixotropy (e.g., Pignon et al., 1997; Bonn et al., 2002). The magma is represented by dyed olive oil with a Newton viscosity measured at $\mu = 99 \pm 0.1$ mPa s using a VEB MLW falling ball viscosimeter (Bertelsen, 2014).

Our experiments are prepared by filling a rectangular Hele-Shaw cell of width × height = 520 ×570 mm, gap = 5 mm) with an aqueous laponite mixture (**Figure 2**). The depth of the injection inlet is *ca.* 30 cm. After controlled curing at room temperature, the mixture becomes a viscoelastic gel. When the gel is ready, a syringe pump injects the viscous magma analog into the viscoelastic gel at constant flow rate. We followed the rigorous laponite gel preparation protocol described by

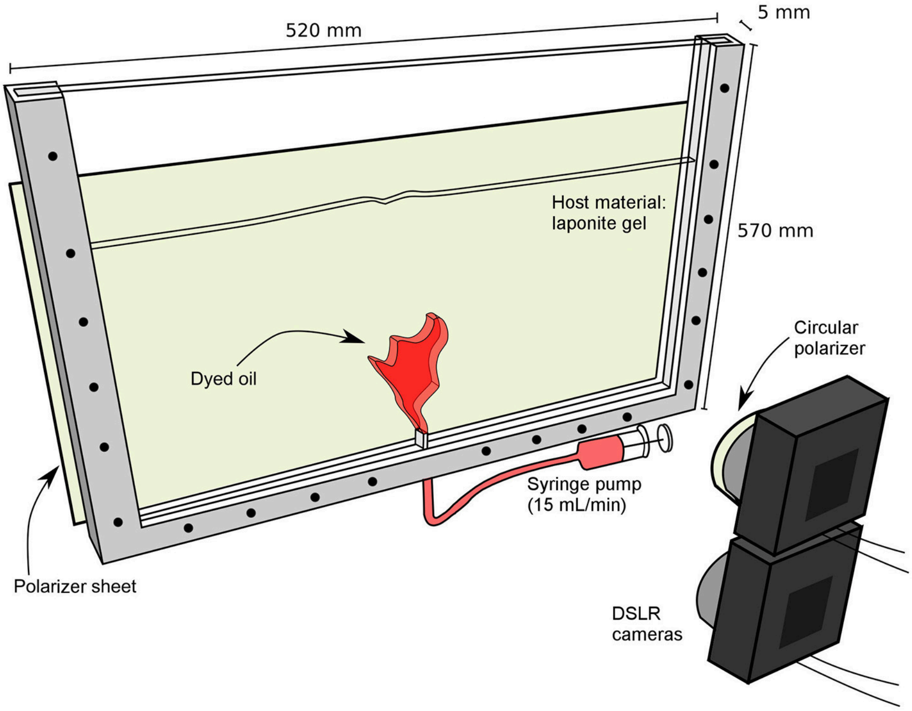

FIGURE 2 | Drawing of the experimental setup. A Hele-Shaw cell filled with a viscoelastic laponite gel is intruded by dyed olive oil. The cell is backlit with a diffused white light source. Intrusion flow rate is controlled with a syringe pump. The cell stands between a polarizer sheet and a circular polarizer mounted on the camera lense: strain-induced birefringence in the gel, as well as the gel/oil interface, is captured by the camera because the polarizers are crossed.

Ruzicka and Zaccarelli (2011a) and Ruzicka et al. (2011b), which is necessary to ensure reproducible mechanical properties of the laponite gel (see detailed procedure description by Bertelsen, 2014).

With the laponite concentration used in this study, the laponite gel is optically isotropic when not strained or when only viscous deformation accommodates strain. When the gel exhibits elastic strain, it becomes birefringent (e.g., Mourchid et al., 1998). To image the strain patterns associated with the propagating oil intrusion, the cell is placed in a polariscope composed of a polarizer sheet placed behind the cell and a DSLR camera holding a circular polarizer (**Figure 2**). During the experiments, our setup allows monitoring simultaneously both the evolution of the shape of the intruding fluid and a birefringence map within the viscoelastic gel (**Figure 3**). Another DSLR camera also monitors the experiments with natural light, i.e., without a circular polarizer. The cameras shot pictures with frequency of 1 Hz.

In this paper we present a series of seven exploratory experiments for testing the influence of the visco-elasto-plastic host rheology on the fluid emplacement (**Table 1**). The laponite concentration was constant (laponite to water mass fraction: $w_i = 3.3 \pm 0.1$ wt. %), while the curing time was varied from 0 min to 240 min. Short curing time corresponds to weak, dominantly viscous gel, whereas long curing time corresponds to stiff, dominantly elastic gel (Kaushal and Joshi, 2014). In all experiments, olive oil was injected at the same flow rate (15 mL min^{-1}).

It is important to constrain the rheological properties of the laponite gel matrix. We qualitatively estimated the mechanical behaviors of the laponite used in this study from the data of Kaushal and Joshi (2014), who measured the creep compliance and stress relaxation moduli for laponite gels at different curing times. The creep compliance expresses the ability of a material to creep; high values of creep compliance implies that the material flows easily, therefore the material behaves more as a viscous fluid than an elastic solid. The stress relaxation modulus, on the other hand, expresses how much a material releases stress due to non-reversible flow; high stress relaxation modulus implies limited stress relaxation ability, therefore the material behaves more elastic and hardly flows. Kaushal and Joshi (2014) showed a decrease of creep compliance and an increase of stress relaxation moduli with increasing curing time. This means that short curing times lead to low viscosity and dominantly inelastic gels, whereas long curing times lead to higher viscosity and more elastic gels. Note that the laponite concentration in the study of Kaushal and Joshi (2014) (3.5%) is slightly higher than in our experiments (3.3%). However, we expect that the trends measured in the gels of Kaushal and Joshi (2014) are similar to those of our gels, albeit with shorter curing times and stiffer gels (see also Ruzicka and Zaccarelli, 2011a; Ruzicka et al., 2011b), as subsequently confirmed by our results.

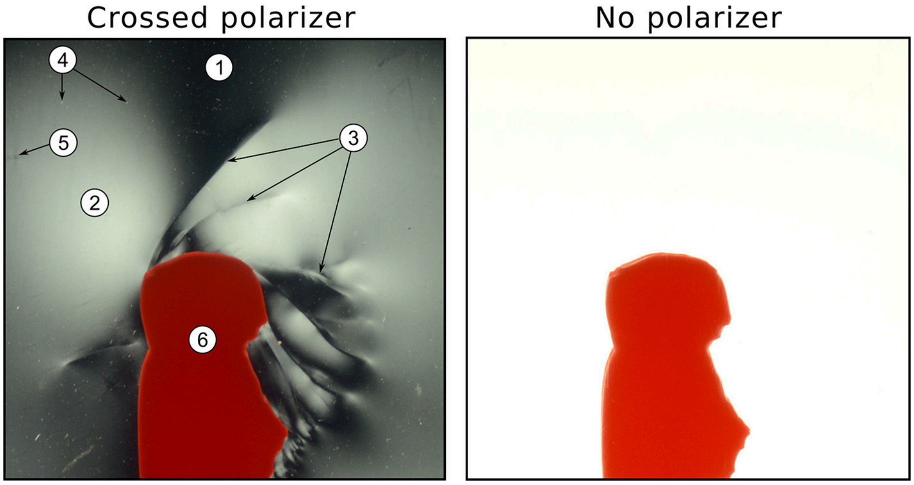

FIGURE 3 | Left: Characteristic polarized photograph displaying birefringence patterns in the laponite gel. (1) Dark, unstrained gel. (2) Diffused birefringence lobe. (3) Hairline birefringence jumps. (4) White patches of laponite particle clusters. (5) Crossed patterns of birefringence around a rigid impurity in the gel. (6) Red oil. **Right:** photograph (same area/time) without polarizer. Note the lack of features shown in the gel in the unpolarized photograph as compared to the polarized photograph.

TABLE 1 | List of experiments and experimental parameters.

Number	Curing time T_w (min)	Injected fluid	Flow rate (mL min^{-1})	Injected volume (mL)
E1	0	Oil	15	48
E2	40	Oil	15	40
E3	60	Oil	15	134
E4	90	Oil	15	122
E5	120	Oil	15	196
E6	150	Oil	15	149
E7	240	Oil	15	104

3. EXPERIMENTAL RESULTS

Before describing the evolution of the seven experiments presented in this paper, we will describe the main characteristics of the observed birefringence patterns (**Figure 3**). We observe two main types of birefringence features: distributed birefringence zones with gradual lateral variations (2 in **Figure 3**) and hairline abrupt birefringence jumps within the matrix (3 in **Figure 3**). These hairline features are concentrated around the irregular inflating parts of the intrusion; they are visible from the start and are maintained until the end of the experiments once they are formed. In the polarized images, one also observes small white spots (4 in **Figure 3**), interpreted as clusters of laponite particles, as well as dark blur crosses (5 in **Figure 3**), interpreted as strain shadows around more rigid heterogeneities. Large dark areas also indicate no birefringence of the gel (1 in **Figure 3**).

In all experiments, the oil propagate upward toward the surface. The oil injection systematically triggers uplift of the gel surface, forming a dome, with the exception of experiment E1 (**Figure 4**).

In experiment E1 ($T_w = 0$ min, low gel strength), the oil intrusion initiates as a rounded blobby body (**Figure 4**, left). It subsequently develops an inverted tear drop shape, with an upward migrating upper head connected to the injection inlet by a thin channel. The leading head is systematically wider than the lower thin channel. The shape of the intrusion is rounded and smooth, until it reaches the surface of the gel (**Figure 4**, left). Note that we do not observe any birefringence in the gel.

In experiment E2 ($T_w = 40$ min), the oil intrusion starts as a rounded blob (**Figure 5**, left), similarly to experiment E1. Subsequently, the oil intrusion develops a subvertical conduit that propagates upward. The tip of the conduit is relatively rounded, but the degree of curvature is higher than that of the intrusion in experiment E1 (**Figure 4**). Polarized photographs display a weak distributed birefringence pattern, which is significantly more prominent close to the propagating tip of the intrusion. The birefringence is symmetrical on both sides of the intrusion. At $t = 40$s, weak and distributed birefringence lobes seem to connect the intrusion tip to the edges of the uplifted dome at the surface. This birefringence lobe also spreads downward, parallel to the sub-vertical walls of the intrusion.

In contrast to experiments E1 and E2, the shapes of the oil intrusions in experiments E3 ($T_w = 60$ min) to E5 ($T_w = 120$ min) are irregular, with alternating wide and thinner domains (**Figures 6–8**). One can observe some straight segments of the intrusion walls, separated by relatively sharp angles. The birefringence intensities are higher than in experiments E1 and E2 and concentrate near the main thickening irregularities of the oil intrusions. We also systematically observe hairline birefringence jumps nucleating at the acute angle irregularities of the oil intrusions. These hairline birefringence jumps are more

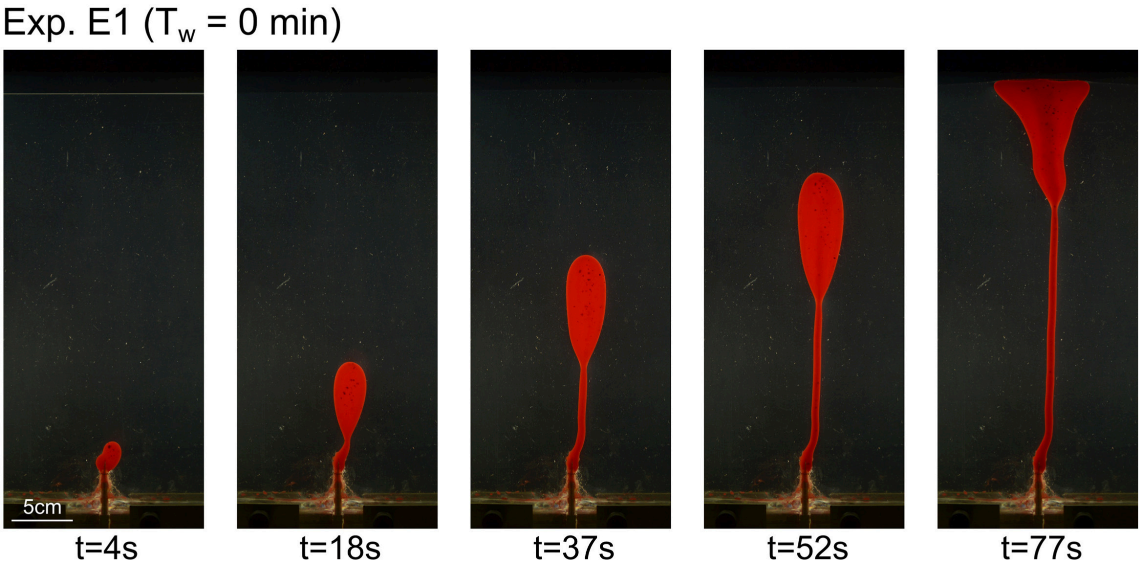

FIGURE 4 | Time series of polarized light photographs of Experiment E1 ($T_W = 0$ min).

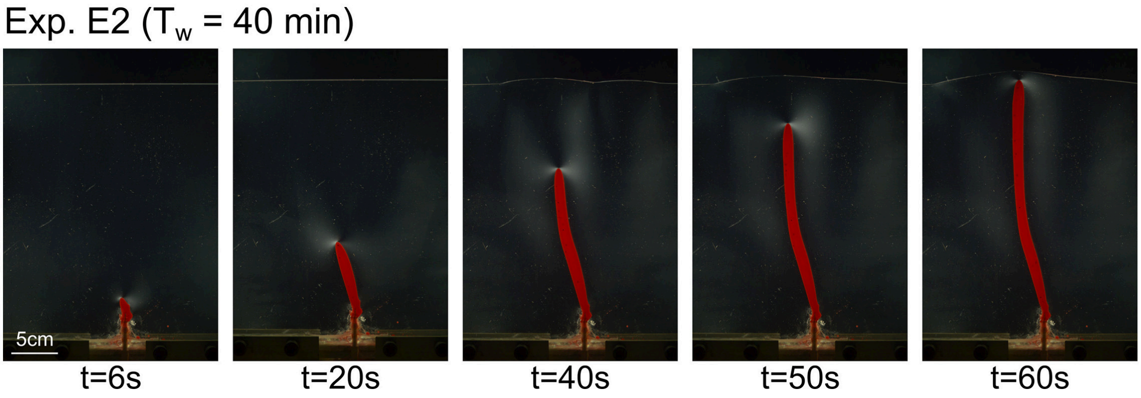

FIGURE 5 | Time series of polarized light photographs of Experiment E2 ($T_W = 40$ min).

numerous and longer from experiment E3 to experiment E5 (**Figures 6–8**). These structures appear sharper in experiment E5 than in experiments E3 and E4.

The intrusion in experiment E6 develops in two stages. The first stage extends until $t \approx 50$ s, where the intrusion grows as a thin irregular conduit (**Figure 9**). During this stage, birefringence patterns exhibit continuous lobes, without hairline birefringent jumps. From $t \approx 50$ s, the upper tip of the intrusion thickens while propagating. During this thickening stage, prominent hairline birefringent jumps nucleate from the angular irregularities of the intrusion walls (**Figure 9**).

The evolution of the intrusion in experiment E7 develops in three main stages. During the first stage until $t \approx 30$ s, the intrusion grows as a regular, thin oblique conduit (**Figure 10**). During this stage, the main birefringence exhibits small continuous lobes concentrated at the sharp tip of the intrusion. During the second stage, the tip of the intrusion thickens and develops an irregular, blobby shape. During this second phase, wide birefringence lobes exhibit sharp jumps (**Figure 10**). At $t \approx 90$ s, the third stage starts with the initiation of a thin oil conduit that follows a hairline birefringence jump formed during the second stage (**Figure 12E**). From then, the intrusion grows as thin, regular conduits with very sharp tips. Intense, continuous birefringence lobes concentrate at the propagating sharp tips of the intrusion (**Figure 10**).

Figure 11A displays the time evolutions of the intrusions' contours during all experiments. The time gap between the grey contours is 4 s, while the time gap between the black contours is 20 s. The distance between the contours provides a graphic indication of the evolution of the displacement velocity of the intrusions' walls in all directions: the closer the contours are, the slower the intrusions' walls move. The

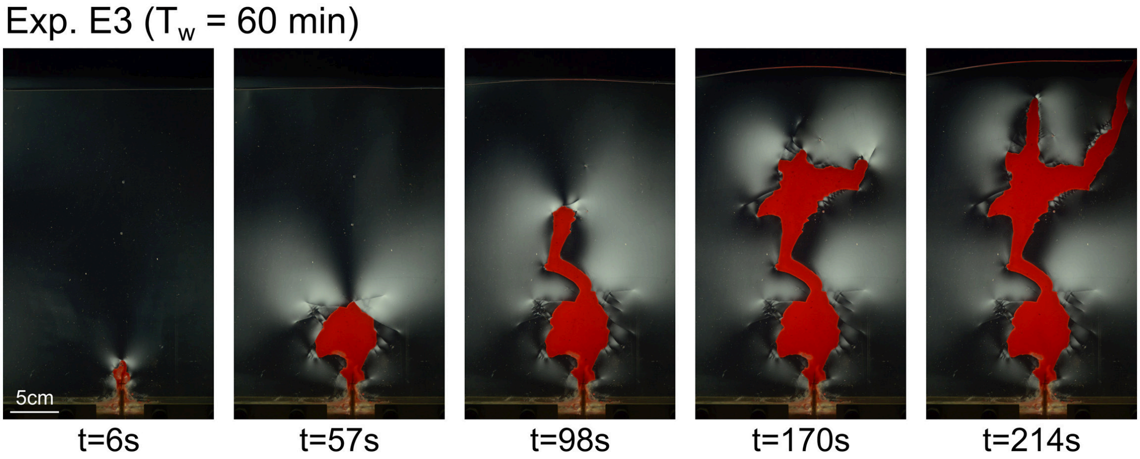

FIGURE 6 | Time series of polarized light photographs of Experiment E3 ($T_W = 60$ min).

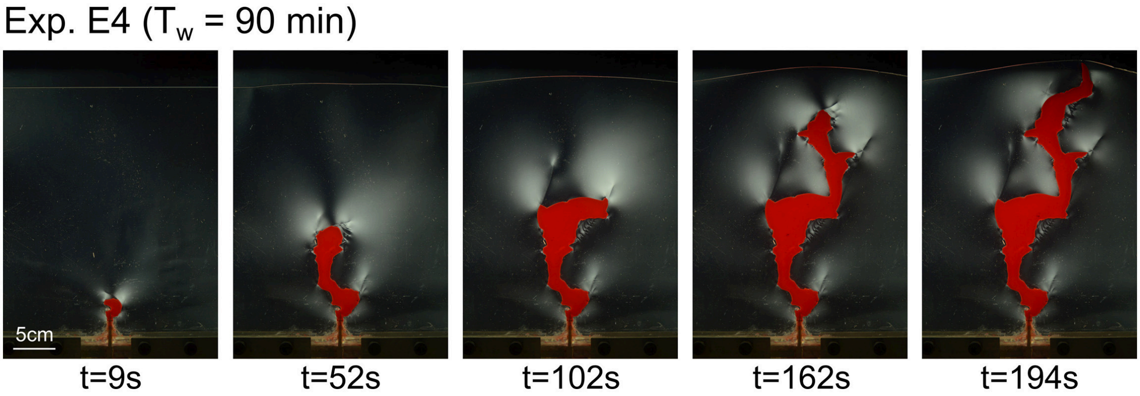

FIGURE 7 | Time series of polarized light photographs of Experiment E4 ($T_W = 90$ min).

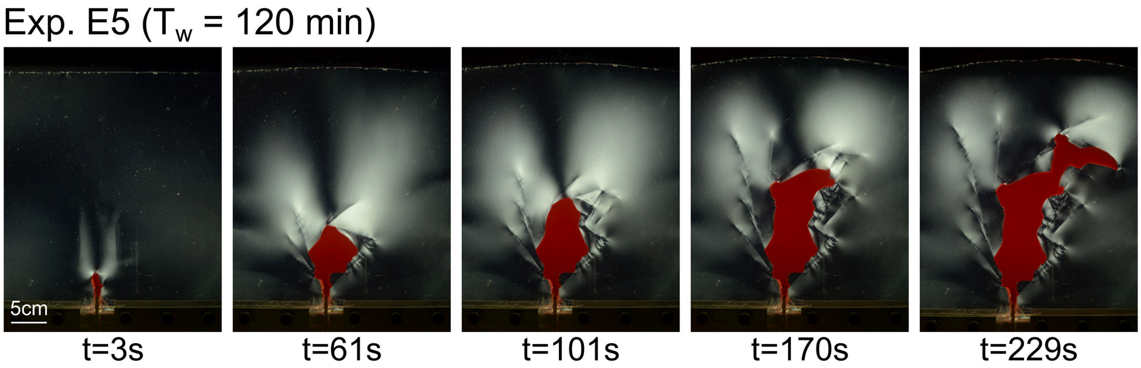

FIGURE 8 | Time series of polarized light photographs of Experiment E5 ($T_W = 120$ min).

comparison between the contours evolutions of experiments E2 and E7 is essential to highlight subtle, but essential, differences. In experiment E2, the subvertical walls of the conduit are almost perfectly parallel, defining a finger-shape. The thickness of the intrusion is set almost from the beginning of the experiment; subsequently, only the tip propagates upward, while the thickness of the underlying conduit remains constant during the whole experiment (**Figure 11A**, E2, $t \approx 40$ s). Conversely,

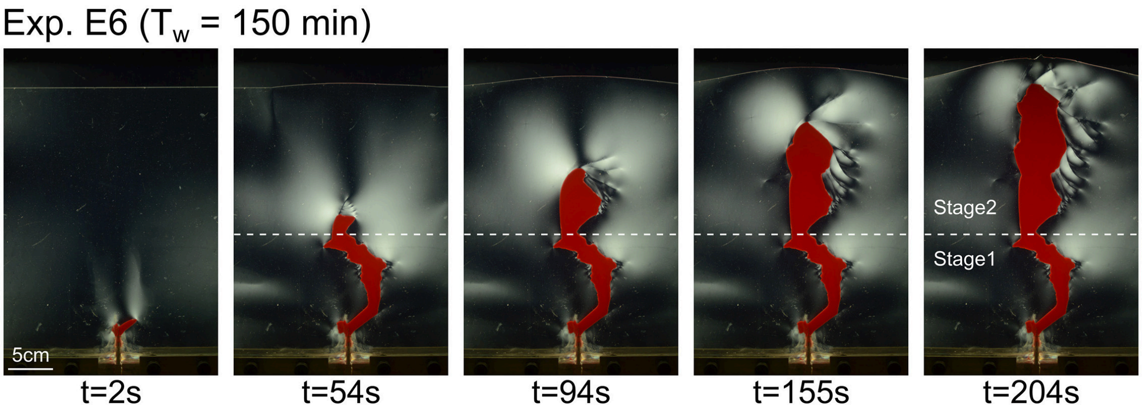

FIGURE 9 | Time series of polarized light photographs of Experiment E6 ($T_W = 150$ min).

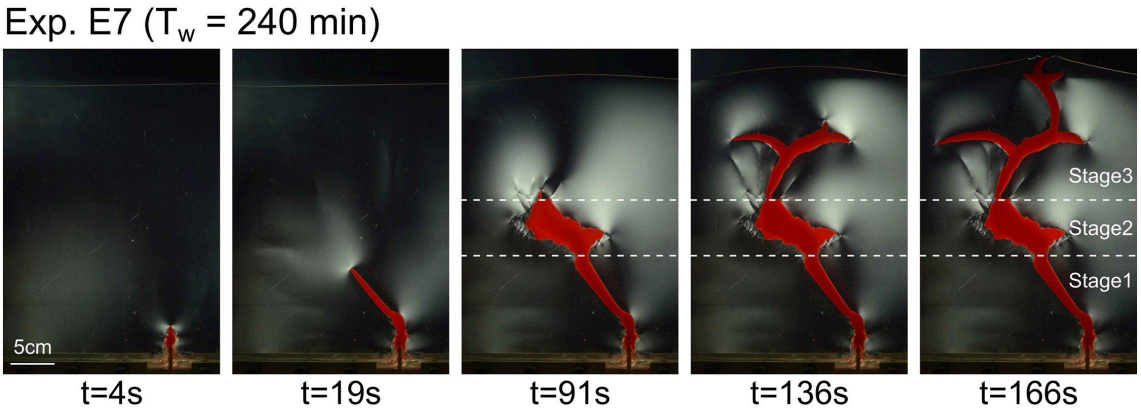

FIGURE 10 | Time series of polarized light photographs of Experiment E7 ($T_W = 240$ min).

during experiment E7, the shape of the thin conduit emplaced during the first stage is that of a thin wedge pointing toward the intrusion tip (**Figure 11A**, E7, $t \approx 240$ s). In addition, the fourth to sixth contours of **Figure 11A** (E7, $t \approx 240$ s) show that the growth of the conduit during this first stage occurs by both tip propagation and thickening of the thin wedge-shape conduit.

Figure 11B displays the evolution of the dimensionless position h/h_{max} of the uppermost tip of the intrusions; here h_{max} corresponds to the distance between the tip of the inlet and the initial gel surface. **Figures 11A,B** evidences a time correlation between the morphological evolutions of the intrusions and their propagation velocity. In experiments E1 and E2, i.e., those with shorter curing times, intrusions keep their shapes during the entire experiments, while their propagation velocity remains constant. In experiment E2, the contour map shows that the thickness of the conduit remains constant during the whole experiment (**Figure 11**, E2, $t \approx 40$ s). The evolution of intrusion in Experiment E3 is more complex, and we identify three morphological transitions. Transition 1 (**Figure 11**, E3, $t \approx 60$ s) corresponds to a sudden shift from a massive blob to a narrower conduit, and corresponds to an acceleration of the intrusion tip. Transition 2 (**Figure 11**, E3, $t \approx 90$ s) is the opposite, such that it marks a sudden widening of the intrusion head along with a deceleration of the intrusion tip. Finally, transition 3 (**Figure 11**, E3, $t \approx 180$ s) marks again a sudden narrowing of the intrusion and an acceleration of the intrusion tip. Similar correlation is visible in Experiment E4, during which transition 1 (**Figure 11**, E4, $t \approx 25$ s) marks a sudden widening of the intrusion head along with a deceleration of the intrusion tip. In addition, transition 2 (**Figure 11**, E4, $t \approx 100$ s) marks the sharp transition from a wide intrusion head to the initiation of a thin conduit, along with a sharp acceleration of the intrusion tip. In Experiment E6, we identify one transition only (**Figure 11**, E6, $t \approx 40$ s), but it is not as sharp as those identified in Experiments E3 and E4. Finally, we identify four clear and sharp transitions during experiment E7 (**Figure 10**). Transition 1 (**Figure 11**, E7, $t \approx 25$ s) marks the sudden widening of the intrusion head along with a sudden deceleration of the intrusion tip; Transition 2 (**Figure 11**, E7, $t \approx 90$ s) marks the initiation of a thin sub-vertical conduit along with the sudden acceleration of the intrusion tip; Transition 3 (**Figure 11**, E3, $t \approx 100$ s) marks the sudden splitting and lateral spreading of the intrusion

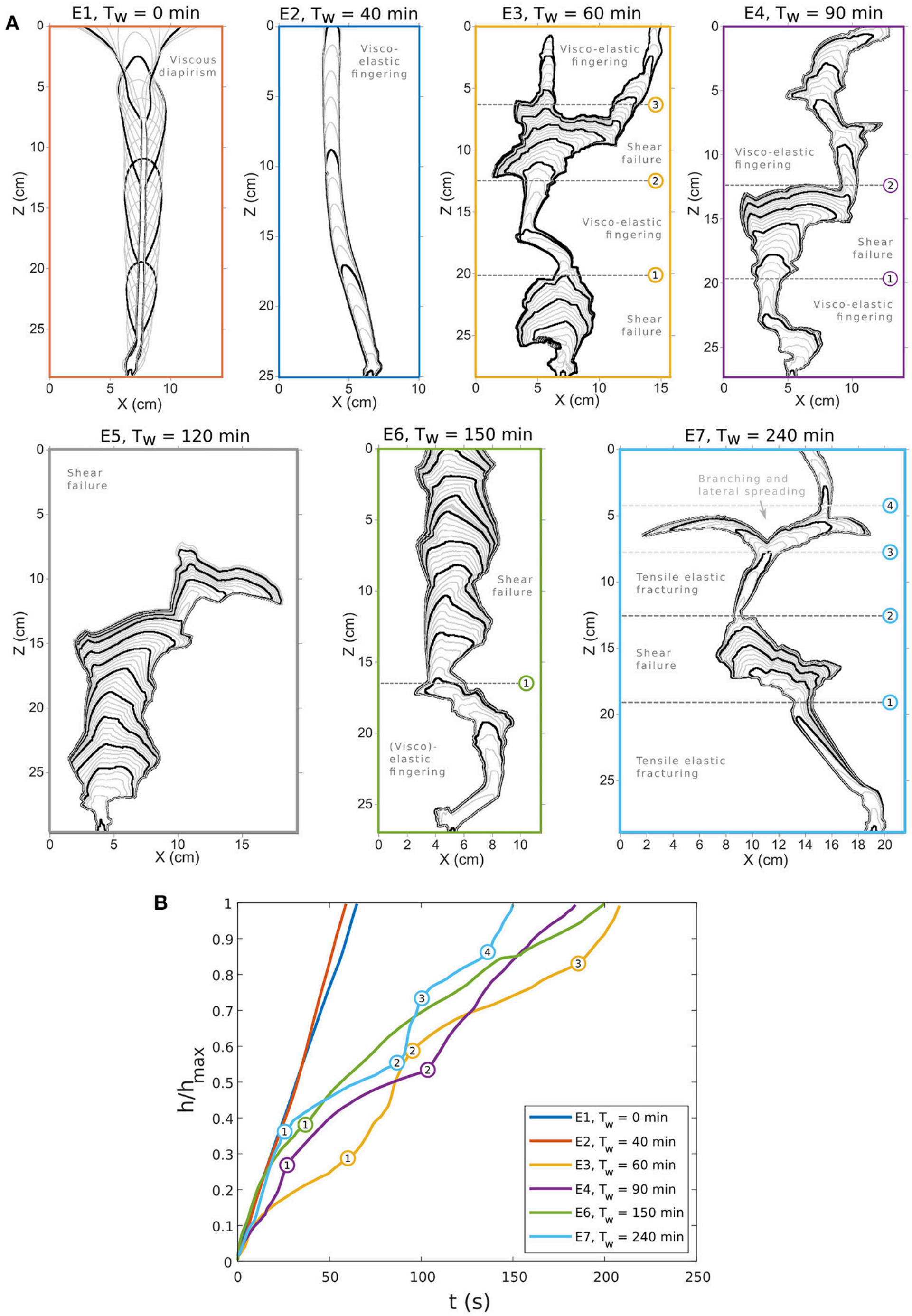

FIGURE 11 | (A) Maps of time evolutions of intrusions' contours calculated with image analysis. The time gap between the gray contours is 4 s, while the time gap between the black contours is 20 s. Numbers indicate the position of the intrusion tips when morphological transitions occur during intrusion evolution. The labeling of the emplacement modes for the identified stages refers to interpretation in section 4.2 and in **Figure 12**. **(B)** Plot of scaled position of the uppermost tip of the intrusions (h/h_{max}) as a function of time for all experiments but E5. The numbers correspond to the morphological transitions identified on intrusion shape maps in **(A)**. Note that these morphological transitions coincide with sharp kinks of propagation velocity.

along with a sudden deceleration of the intrusion tip; finally transition 4 (**Figure 11**, E3, $t \approx 140$ s) marks the sudden initiation of a new sub-vertical thin conduit along with a sharp acceleration of the intrusion tip. Note that the initial propagation velocities in Experiments E1, E2, E6, and E7 are almost equal, even if the initial conditions strongly differ. In addition, the shapes of the early oil conduits in Experiments E2 and E7 are very similar, i.e., thin conduits with tips of low angles of curvature.

4. INTERPRETATION

4.1. Deformation Mechanisms in the Gel

The birefringence patterns observed in the laponite gel in the experiments qualitatively highlight where deformation in the gel occurs. In this section, we will interpret which deformation mechanisms can be inferred from such birefringence patterns. In experiment E1 ($T_w = 0$ min), we observe no birefringence in the gel, while it deforms to accommodate the flow of the oil (**Figure 4**). In this experiment, the curing time T_w is so short that the laponite mixture does not have the time to build a gel structure in the solution, so we infer that it dominantly flows viscously. In experiments E2 to E7, i.e., with increasing curing times, it appears that the amount of birefringence increases (**Figures 5–10**). Correlating this observation with the results of Kaushal and Joshi (2014), which show that increasing curing time T_w leads to more elastic laponite gel, we infer that the birefringence observed in our experiments is a proxy for elastic deformation of the gel. In experiment E2 ($T_w = 40$ min), the birefringence is weak (**Figure 5**), suggesting that a small fraction of the gel deformation is elastic, while the rest is viscous.

In experiments E2 to E7, one can observe both birefringence within the gel and uplift of the surface of the gel (**Figures 5–10**). The uplift of the laponite gel occurs as a domed surface, at the apex of which outer-arc elastic stretching is expected (e.g., Pollard and Johnson, 1973; Galland and Scheibert, 2013; Galland et al., 2016). However, no birefringence is observed where significant elastic stretching is expected (**Figures 7–10**). We infer from this observation that birefringence in the laponite gel is a proxy for elastic shear strain, not normal strain.

The hairline birefringence jumps (**Figure 3**) are only observed in experiments E3 to E7 (**Figures 6–10**), i.e., those with the longest curing time T_w. We interpret such birefringence discontinuities as fractures within the gel. Given that these fractures do not appear to accommodate space opening, we interpret these fractures to result from shear failure, i.e., faulting. This deformation mechanism is neither elastic nor viscous, but brittle. In the following sections, we will refer to this brittle behavior as plastic, as opposed to elastic and viscous.

To summarize, we infer that the laponite gels in our experiments deform by either viscous flow, elastic strain or plastic shear failure, or a combination of them, according to the curing time of the gel.

4.2. Emplacement Mechanisms of the Oil

The understanding of the gel deformation mechanisms combined with the oil intrusion shapes reveals diverse oil emplacement mechanisms in our experiments.

In experiment E1 ($T_w = 0$ min; **Figure 4**), the lack of birefringence strongly suggests that the gel flows in a viscous manner. In addition, the shape of the oil intrusion, with a propagating head that is wider than the lower tail, strongly suggests that part of the oil emplacement is driven by buoyancy, similar to a Rayleigh-Taylor instability (**Figure 12A**). In addition, the forceful injection of the oil phenomenologically corresponds to the injection of a fluid within a fluid of different viscosity, similarly to a Saffman-Taylor instability (Saffman and Taylor, 1958; Saffman, 1986), or viscous fingering (Lemaire et al., 1991; Hirata, 1998). Because our experimental cells are vertical, gravity and resulting buoyancy forces contribute to oil propagation, in contrast to the experiments of Saffman and Taylor (1958), Lemaire et al. (1991), and Hirata (1998), where the cells were horizontal. Nevertheless, we cannot rule out that surface tension between the aqueous gel and the intruding oil is significant enough to control the formation of the inverted drop shape of the intrusion, similarly to a Rayleigh-Plateau instability (e.g., de Gennes et al., 2004).

In experiments E3 to E7 (**Figures 6–10**), the development of hairline birefringence jumps accompanied the growth of irregular and relatively thick inflating parts of oil intrusion. We infer from section 4.1 that the oil emplacement occurs by plastic shear failure of the gel (**Figure 12C**). In this mechanism, the oil pushes the gel, the displacement of which is accommodated along shear fractures, i.e., faults. This mechanism accommodates the emplacement of relatively wide intrusions. In addition, the development of several shear fractures control the angular irregularities of the intrusion walls. This mechanism is very similar to the fault-assisted emplacement of punched-laccoliths (e.g., Corry, 1988; Schmiedel et al., 2017).

In most experiments exhibiting hairline birefringence jumps, the oil does not flow along the shear fractures induced by its propagation. In experiment E7, however, one can see that the initiation of the third underwater stage of emplacement corresponds to the initiation of a thin sheet, which follows a shear fracture that accommodated the earlier growth and thickening of the intrusion during the second stage of emplacement (**Figure 12D**). This mechanism of damage-controlled flow is in good agreement with the laboratory models of Abdelmalak et al. (2012) and Schmiedel et al. (2017), and the numerical models of Haug et al. (2017) and Haug et al. (2018).

Finally, in experiment E7, the oil intrusion during the stages 1 and 3 described in section 3 exhibits a regular sheet-like shape with a sharp tip (**Figures 10**, **12E**). In addition, the birefringence pattern exhibits localized concentration at the tip (**Figure 12E**). In this experiment, the gel is expected to be stiffer than in all the other experiments. We infer from these observations that the oil propagates by a mechanism that is close to elastic tensile fracturing. This mechanism is one of the most established to account for the emplacement of sheet intrusions, such as dykes and sills (e.g., Pollard and Johnson, 1973; Rubin, 1993; Rivalta et al., 2015; Galland et al., 2018).

The intrusions in experiment E2 and in the first stage of experiment E7 look rather similar, such that their morphologies are not sufficient to discriminate between their emplacement mechanisms. However, several subtle differences allow us to interpret distinct emplacement mechanisms. First, the birefringence signal in experiment E2 (**Figure 5**) is much weaker than that in experiment E7 (**Figure 10**). This suggests that substantial elastic deformation of the gel is at work in experiment E7, whereas a significant part of the gel deformation

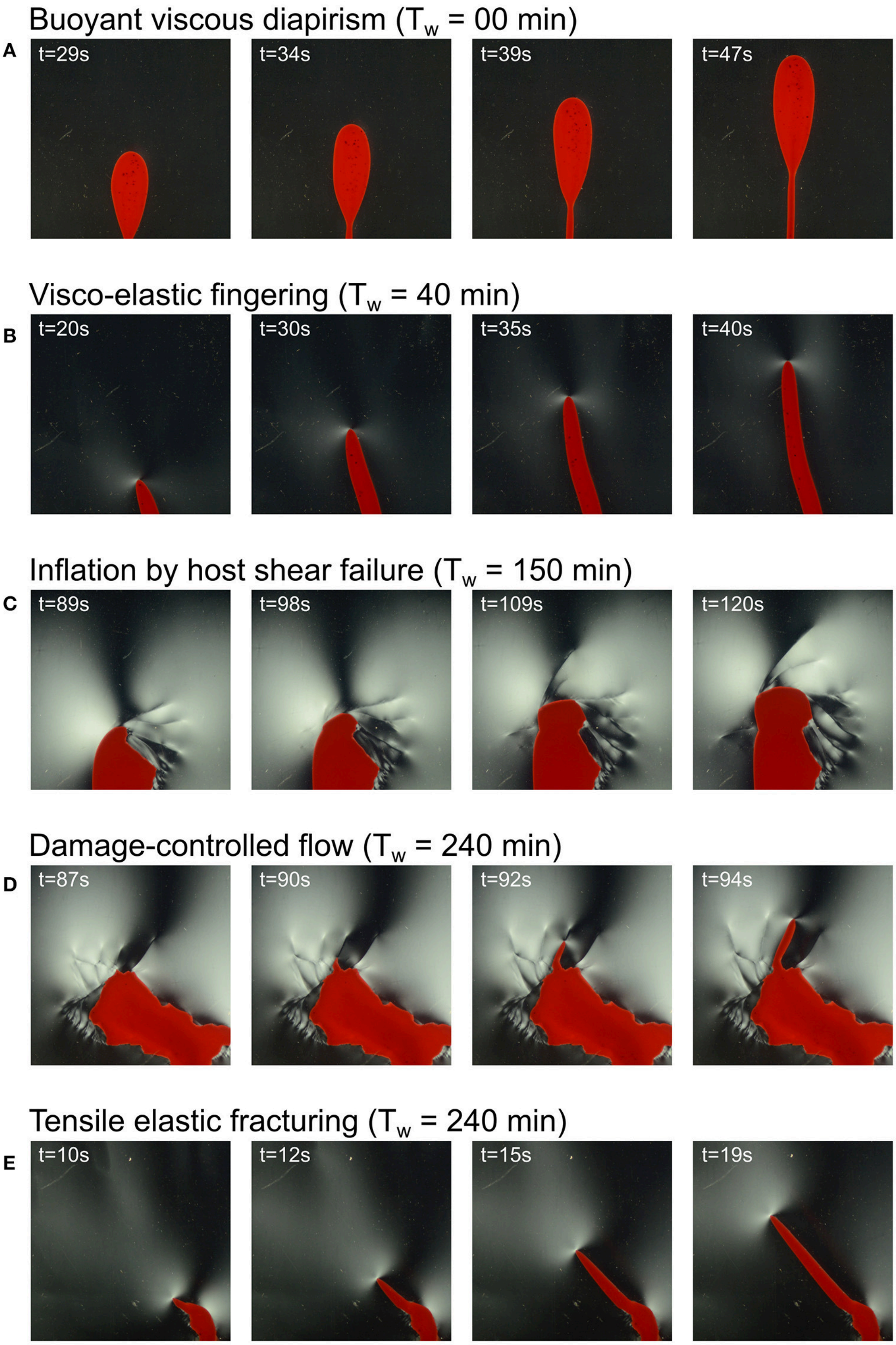

FIGURE 12 | Time series of polarized photographs illustrating characteristic mechanisms of oil emplacement. **(A)** Viscous diapirism in Experiment E1 ($T_W = 0$ min). **(B)** Viscoelastic fingering in Experiment E2 ($T_W = 40$ min). **(C)** Intrusion inflation by shear failure of the host in Experiment E6 ($T_W = 150$ min). **(D)** Intrusion of sheet intrusion along damage/fault produced during earlier steps of oil intrusions in Experiment E7 ($T_W = 240$ min). **(E)** Hydraulic fracturing of sheet intrusion in Experiment E7 ($T_W = 240$ min).

in experiment E2 is accommodated by inelastic flow (see also interpretation in section 4.1). Second, the shapes and growth behaviors of the intrusions in both experiments differ. In experiment E7, the intrusion during the first stage exhibits a thin wedge, which thickens while its tip propagates (**Figure 11A**, $T_w = 240$ min). Such behavior is in good agreement with the propagation of a fluid-filled fracture, the thickness of which is expected to be proportional to the length (e.g., Pollard, 1973, 1987; Rubin, 1993; Galland and Scheibert, 2013). We thus infer that the thin intrusion of the first stage of experiment E7 is likely a tensile fracture in a dominantly elastic host matrix. Conversely, in experiment E2, the oil intrusion exhibits a finger shape with parallel walls [**Figure 11A** ($T_w = 40$ min) and **Figure 12B**]. In addition, the growth of the intrusion occurs only through tip propagation, but without thickening of the early parts of the intrusion (**Figure 11A**; $T_w = 40$ min). This growth behavior is incompatible with a mechanism of fracture propagation through an elastic medium. In contrast, such behavior is very similar to a Saffman-Taylor instability (Saffman and Taylor, 1958; Saffman, 1986), i.e., the viscous fingering of a low viscosity fluid into a fluid of higher viscosity. In addition, such viscous fingering has also been observed in a non-Newtonian, including sheart-thinning, viscoelastic host matrix (Nase et al., 2008). Given that the laponite gel is shear-thinning, and the weak birefringent pattern in experiment E2 showing some component of elastic strain, it is likely that such complex visco-elastic fingering controls the emplacement of the oil in this experiment. Nevertheless, a firm interpretation would require more data.

The plot of **Figure 11B** shows that the propagation velocities of the intrusion tips exhibit significant differences with respect to different curing times T_w. The constant propagation velocities in experiments E1 and E2, i.e., those with shorter curing times, are compatible with a deformation that is distributed within the gel matrix. This is in good agreement with a dominantly viscous deformation of the laponite gel. In contrast, the variable propagation velocities of the intrusions' tips suggest that another mechanism accommodates the emplacement of the oil. The abrupt velocity changes visible during experiments E3 to E7 (**Figure 11B**) are compatible with discrete deformational events. This is in good agreement with fracturing of the gel matrix, which is corroborated by the occurrence of the shear fractures in the gel (**Figures 6–10**). Note that the data plotted on **Figure 11B** correspond to one point only of the growing intrusions, i.e., the uppermost tip. The contour maps displayed in **Figure 11A** shows that the propagation velocity of the intrusions is variable at all points and in all directions. A quantitative analysis of the complex propagation of the intrusions' walls might provide valuable insights on the emplacement dynamics of the oil with respect to the visco-elasto-plastic behavior of the gel matrix.

To summarize, our experiments show how the shapes of the oil intrusions are controlled by the deformation mechanism of the gel matrix: the rounded shape in experiment E1 dominantly results from viscous flow of the gel, the regular finger in experiment E2 dominantly results from viscoelastic fracturing of the gel, the angular and irregular shapes in experiments E3 to E7 dominantly result from shear faulting of the gel, and the sharp-tipped thin sheet in experiment E7 dominantly results from elastic tensile fracturing. Our experiments are thus able to model – for the first time – most mechanisms of magma emplacement inferred from geological observations.

5. DISCUSSION

5.1. Laboratory Method

A strong assumption of our experimental apparatus is that it has 2-dimensional geometry, whereas igneous intrusions in nature are 3-dimensional structures. Such geometry implies potential severe boundary effects on the results. However, the laponite gel is shear thinning, i.e., it weakens when strained, such that it self-lubricates against the acrylic glass walls of the cell, and so reduces the boundary effects. The boundary conditions of our model system are therefore close to plane strain. For more details, Bertelsen (2014) discusses in detail the limitations of the 2D Hele-Shaw cell on the results. In our apparatus we chose a gap of 5 mm between the acrylic glass plates. This ensures that the gel layer is thick enough to produce visible and interpretable birefringence patterns through the polariscope; if the gap were smaller, the gel layer would be too thin, given that the amount of birefringence through a gel layer is proportional to the thickness of the layer (e.g., Fuller, 1995).

The birefringence patterns visible on **Figures 4–12** provide invaluable insights about the deformation mechanisms of the gel. Such information is absolutely not reachable on photographs taken with natural light; actually, close direct observations of the gel during experiments show that it looks perfectly homogeneous in natural light, and even the fractures highlighted by the hairline birefringence jumps are invisible. Without polariscope, Lemaire et al. (1991) and Hirata (1998) based their physical analyses of the fluid injection in viscoelastic gels on the shapes of the intruding fluid. Our study shows that the mechanical information provided by the use of a polariscope is invaluable for revealing the complex deformation regimes in the deforming visco-elasto-plastic gel. It shows that the use of a polariscope is essential for revealing the deformation mechanisms in experiments using birefringent gels, such as laponite and gelatine.

The observed birefringent signals is integrated over the full thickness of the models. In our 2-dimensional cell, given that the structures are dominantly perpendicular to the walls, the polarized light crosses the gel perpendicular to the structures in the gel, so that each structure is well visible on the observed birefringence patterns. In addition, the use of a high-resolution DSLR camera allows imaging fractures in the gel evidenced by the sharp hairline birefringence jumps (**Figure 3**). In 3-dimensional gel models, resolving each fracture with polariscopy would be impossible because (1) structures can be out-of-plane with respect to the light source and (2) the light can cross several structures (e.g., Taisne and Tait, 2009). Another method used to image deformation in 3-dimensional gel experiments implements the tracking of particles in suspension in the gel and illuminated by a laser sheet (e.g., Kavanagh et al., 2015, 2018). Nevertheless, the resolution of the digital image correlation for particle tracking is not enough to image sharp structures like the fractures we observe.

5.2. Geological Implications

Our experiments simulate several mechanisms of emplacement of a viscous fluid into a visco-elasto-plastic matrix: (1) emplacement by viscous flow, (2) emplacement by shear brittle failure, i.e., faulting, and (3) emplacement by tensile failure, i.e., hydraulic fracturing. These three emplacement mechanisms have been inferred to govern magma emplacement at diverse levels of the Earth's crust (e.g., Corry, 1988; Rubin, 1993; de Saint Blanquat et al., 2006). Our experiments are the first able to account, in the same model system, for most of the main magma emplacement mechanisms documented in nature. Our models are thus of great potential for revealing the complex physics governing magma emplacement in the visco-elasto-plastic crust. In addition, they offer a unique tool to constrain the physical conditions that are favourable for each dominant emplacement mechanism.

In all our experiments, the gel exhibits both viscous, plastic and elastic properties, but depending on T_w, one property is dominant with respect to the others. For example, in experiment E1 viscous flow of the gel is dominant, whereas elastic deformation is likely dominant in experiment E7. In the other experiments, however, it is likely that several mechanisms of gel deformation are at work at the same time. For example, the emplacement of the intrusion in experiment E3 (**Figure 6**) likely results from a complex combination of viscous flow, elastic strain and shear fracturing of the gel matrix, i.e., hybrid emplacement mechanism. In these experiments, the complex shapes of the intrusions reflect the complex magma intrusion shapes observed in nature (e.g., Bartley et al., 2012; Burchardt et al., 2012; Spacapan et al., 2016). This suggests that such hybrid emplacement mechanisms, i.e., involving coeval viscous, plastic (brittle) and /or elastic deformation of the host rock, is likely at work during the emplacement of magma intrusions in nature (Pollard, 1973; Spacapan et al., 2017). This shows that magma emplacement models based on end-member host rock rheology (viscous, plastic, or elastic) are too simplistic to address the complex emplacement of magma in the Earth's crust, as already demonstrated by Rubin (1993), Vachon and Hieronymus (2016), and Scheibert et al. (2017). Our models, on the other hand, have the potential to address such complexity.

The structures in our experiments are in good agreement with geological and geophysical observations. For example, the shear fractures visible in our experiments can be related to the numerous structures accommodating the emplacement of intrusions of diverse sizes and shapes, such as large laccoliths (de Saint Blanquat et al., 2006; Wilson et al., 2016) and igneous sills (Pollard, 1973; Pollard and Johnson, 1973; Spacapan et al., 2017) (**Figure 1**). In addition, seismological measurements evidence dominant shear failure associated dyke emplacement (White et al., 2011; Ágústsdóttir et al., 2016) and cryptodome emplacement (e.g., Okada et al., 1981; Merle and Donnadieu, 2000), suggesting again more complex propagation mechanisms than tensile failure are at work in geological systems. Finally, the shear fractures in our experiments E3 to E7 are in good agreement with laboratory models of magma emplacement in dry granular materials (Merle and Donnadieu, 2000; Guldstrand et al., 2007; Mathieu et al., 2008; Abdelmalak et al., 2012; Schmiedel et al., 2017), in which the magma propagates by pushing its host until shear failure, i.e., the so-called viscous indenter model.

The oil intrusions in experiment E2 (**Figure 5**) and during the first stage of experiment E7 (**Figure 10**) exhibit very similar shapes. However, we discussed in section 4.2 that the intrusion in experiment E2 is likely emplaced by viscoelastic fingering with dominant viscous flow of the gel, whereas the intrusion in experiment E7 is likely emplaced by tensile fracturing, with dominant elastic deformation of the gel. We conclude that the morphology of an intrusion alone is not a sufficient proxy for inferring its emplacement mechanism. This implies that intrusions exhibiting sheet morphology do not systematically result from tensile fracturing, as they can also result from viscoelastic fingering. This conclusion is unambiguously supported by the detailed field study of Spacapan et al. (2017), who demonstrate that the propagation of a sheet-shaped sill was accommodated by significant ductile, compressional deformation of the host rock, in agreement with the viscoelastic fingering mechanism. Such a result is in disagreement with most of the literature, which assumes that the sheet shapes of, e.g., dykes and sills are systematic proxies of tensile fracturing of a dominantly elastic host (e.g., Pollard, 1987; Rubin, 1995; Rivalta et al., 2015, and references therein). This result can also have significant implications for geodetic modeling, given that most geodetic models used to invert geodetic data associated with the emplacement of dykes or sills are based on the assumption that these intrusions formed by tensile opening within a purely elastic host rock (e.g., Sigmundsson et al., 2010; Wright et al., 2012), even when field observations contradict these assumptions. To summarize, even if sheet intrusions resemble simple tensile fractures, their emplacement can be governed by other, more complex processes. We conclude that, in order to reveal the emplacement mechanisms of sheet intrusions, among others, it is essential to investigate both (1) the intrusion shapes and (2) the deformational structures in the host accommodating magma emplacement (see e.g., Spacapan et al., 2017).

The intrusions modeled in experiments E3 to E7, as well as the deformational structures in the gel, exhibit very complex and discrete structures, which are typical of brittle behavior. Interestingly, the initial conditions of our experiments are simple, with gels that are prepared to be as homogeneous as possible. The occurrence of the observed complex, discrete structures in our experiments show that complex brittle structures occur spontaneously from a macroscopically homogeneous solid. Such behavior suggests that the gel exhibits numerous, very small-scale heterogeneities that control the stochastic properties of brittle fracturing, similarly to flaws in natural rocks. Stochastic fracturing processes have, for example, been inferred to control the nucleation and the thickness of dykes (Krumbholz et al., 2014). In addition, the variable intrusion propagation velocities observed in experiments E3 to E7, i.e., in experiments with brittle shear deformation, show that the propagation occurs through successive stages of fast propagation and accumulation, each stage corresponding to distinct emplacement mechanisms associated with distinct mechanical behavior of the host rock. Such stepwise behavior has been observed e.g., during propagation of dykes (White et al., 2011; Ágústsdóttir et al., 2016), suggesting that sudden dyke acceleration and deceleration are associated with distinct deformation modes of the crust. The behavior of the laponite gel therefore seems to reproduce the stochastic properties of the brittle crust.

5.3. Future Challenges

We discussed in the former sections that the laponite gel in our experiments exhibits complex visco-elasto-plastic behaviors, which reproduce phenomenologically the mechanical behaviors of the Earth crust. A challenge, however, is to discuss the physical similarity between the mechanical behaviors of the laponite gel and those of natural rocks (Barenblatt, 2003). This requires systematic measurements of the mechanical properties (e.g., elastic modulus, yield stress, viscosity) of the gel, and a robust quantification of the relative contributions of the distinct end member properties. Nevertheless, discussing the physical similarity between our models and geological systems also requires a robust understanding of the visco-elasto-plastic rheology of the Earth's crust. Currently, even if the individual end member mechanical behaviors of the crust are relatively well- known (e.g., Ranalli, 1995; Boutonnet et al., 2013), its overall visco-elasto-plastic rheology remains poorly constrained. Our models thus should be viewed as physical experiments aiming at understanding a complex physical system instead of so-called "analogue" experiments that intend to reproduce geological systems (Galland et al., 2018).

Our laboratory experiments show that the laponite gel can deform by viscous flow, brittle (plastic) shear failure, and elastic. We discussed above that the three deformation mechanisms are likely at work at the same time during the experiments. In addition, even if the intrusions in experiments E2 and E7 exhibit similar shapes, we interpret their emplacement mechanisms to be different, i.e., viscoelastic fingering vs. fracturing, but so far we have no means to estimate the relative contributions of elastic and viscous deformation. A challenge will be to quantify the relative viscous, plastic and elastic strains in the complex deformation patterns in the gel. We are confident that this is feasible with new modern and available imaging techniques (e.g., Galland et al., 2016). In addition, the dynamics of magma emplacement is not only governed by the mechanical behavior of the host rock, but greatly depends on the viscosity of the magma, which can span over more than 10 orders of magnitude. Testing the effects of the viscosity of the injected fluid in our experiments will also be of great interest. Therefore, even if our experiments bring challenges, we feel that they open a new niche for revealing the complex dynamics of magma emplacement in the Earth's crust.

6. CONCLUSIONS

This paper describes the results of exploratory 2-dimensional laboratory experiments of magma emplacement within the Earth's crust of complex visco-elasto-plastic rheology. The model magma is dyed olive oil and the model rock is laponite gel of variable visco-elasto-plastic properties. We performed a parameter study to test the effect of the rheology of the host matrix on the emplacement of model magma. The main results of our studies are the following.

1. Our experiments reproduce a broad diversity of intrusion shapes, ranging from diapirs, viscoelastic fingers, hydraulic fractures, and complex, angular intrusions. This is the first time that such a diversity of intrusion shapes is simulated in a single experimental apparatus.
2. The laponite gels in our experiments exhibit coeval viscous, elastic and plastic deformation patterns to accommodate the intruding oil. In addition, we observe coeval tensile and shear brittle failure accommodating the propagation of the oil.
3. The use of a polariscope during 2-dimensional gel experiments reveals essential to image and study the complex gel matrix deformation that accommodates magma emplacement, thanks to the birefringent properties of the gel. The high-resolution of the technique allows mapping both continuous, viscoelastic strain fields and discrete structures, such as plastic shear fractures.
4. Our experiments reproduce several magma emplacement mechanisms in the same experimental apparatus. This is the first time an experimental technique is able to catch the broad complexity of magma emplacement in the Earth's crust.
5. Qualitatively, laponite gels appear to be relevant crustal rock analogs. Significant additional effort is required to constrain their mechanical properties, in order to discuss their physical similarity to natural rocks.
6. Our experiments are able to account for the stochastic behavior of the Earth's brittle crust, showing how small-scale heterogeneities within the laponite matrix control the large-scale deformation.
7. Finally, we our experiments show that revealing magma emplacement necessitates analysing both the shape of intrusions and the deformation mechanisms in the host rock.

Overall, our exploratory experiments show that it is essential to account for the visco-elasto-plastic rheology of the Earth's crust to fully understand magma emplacement processes. Overall, our models suggest that emplacement mechanisms accounting for end member rheologies of the host rock may be uncommon in nature, as supported by field and geophysical observations. Our models imply fundamental new thinking of our physical approach of magma emplacement models.

AUTHOR CONTRIBUTIONS

HB designed experimental setup. Main writer of the manuscript. BR performed the presented experiments. Second writer of the manuscript. OG initiated the project, supervised the work, and wrote parts of the manuscript. GD and AA performed shape analysis by coding image analysis programs. They read and corrected the manuscript.

ACKNOWLEDGMENTS

This study was supported by the Faculty of Mathematics and Natural Sciences at the University of Oslo through doctoral fellowship grants to HB and BR. We acknowledge fruitful and constructive discussions with the Oslo Volcano Plumbing System Group at the Physics of Geological Processes and the Njord center.

REFERENCES

Abdelmalak, M., Mourgues, R., Galland, O., and Bureau, D. (2012). Fracture mode analysis and related surface deformation during dike intrusion: Results from 2D experimental modeling. *Earth Planet. Sci. Lett.* 359, 93–105. doi: 10.1016/j.epsl.2012.10.008

Ágústsdóttir, T., Woods, J., Greenfield, T., Green, R. D., White, R. S., Winder, T. et al. (2016). Strike-slip faulting during the 2014 Bárðarbunga-Holuhraun dike intrusion, central Iceland. *Geophys. Res. Lett.* 43, 1495–1503. doi: 10.1002/2015GL067423

Barenblatt, G. I. (2003). *Scaling*. Cambridge, MA: Cambridge University Press.

Bartley, J.M., Glazner, A. F., and Mahan, K. H. (2012). Formation of pluton roofs, floors, and walls by crack opening at Split Mountain, Sierra Nevada, California. *Geosphere* 8, 1086–1103. doi: 10.1130/GES00722.1

Battaglia, J., Ferrazzini, V., Staudacher, T., Aki, K., and Cheminée, J. (2005). Pre-eruptive migration of earthquakes at the Piton de la Fournaise volcano (Réunion Island). *Geophys. J. Int.* 16, 549–558. doi: 10.1111/j.1365-246X.2005.02606.x

Bertelsen, H. S. (2014). *Blowing the Viscoelastic Trumpet - Experiment Design for Mapping Stress-Strain Patterns in Viscoelastic Hydrofracture*. MSc thesis. Available online at: http://urn.nb.no/URN:NBN:no-45994

Bonn, D., Tanase, S., Abou, B., Tanaka, H., and Meunier, J. (2002). Laponite: aging and Shear Rejuvenation of a Colloidal Glass. *Phys. Rev. Lett.* 89:015701. doi: 10.1103/PhysRevLett.89.015701

Boutonnet, E., Leloup, P. H., Sassier, C., Gardien, V., and Ricard, Y. (2013). Ductile strain rate measurements document long-term strain localization in the continental crust. *Geology* 41, 819–822. doi: 10.1130/G33723.1

Brandsdóttir, B., and Einarsson, P. (1979). Seismic activity associated with the September 1977 deflation of the Krafla central volcano in northeastern Iceland. *J. Volcanol. Geother. Res.* 6, 197–212.

Bunger, A. P., and Cruden, A. R. (2011). Modeling the growth of laccoliths and large mafic sills: role of magma body forces. *J. Geophys. Res. Solid Earth* 116:B02203. doi: 10.1029/2010JB007648

Burchardt, S., Tenner, D. C., and Krumbholz, M. (2012). The Slaufrudalur pluton, southeast Iceland-An example of shallow magma emplacement by coupled cauldron subsidence and magmatic stoping. *Geol. Soc. Am. Bull.* 124, 213–227. doi: 10.1130/B30430.1

Burov, E., Jaupart, C., and Guillou-Frottier, L. (2003). Ascent and emplacement of buoyant magma bodies in brittle-ductile upper crust. *J. Geophys. Res.* 108. doi: 10.1029/2002JB001904

Corry, C. (1988). Laccoliths; mechanisms of emplacement and growth. *Geol. Soc. Am. Spec. Pap.* 11, 48–51, 59–62 doi: 10.1130/SPE220-p1

de Gennes, P.G., Brochard-Wyart, F., and Quéré, D. (2004). *Capillarity and Wetting Phenomena.* New York, NY: Springer.

de Saint-Blanquat, M., Habert, G., Horsman, E., Morgan, S. S., Tikoff, B., Launeau, P., et al. (2006). Mechanisms and duration of non-tectonically assisted magma emplacement in the upper crust: the Black Mesa pluton, Henry Mountains, Utah. *Tectonophysics* 428, 1–31. doi: 10.1016/j.tecto.2006.07.014

Dingwell, D. B., Bagdassarov, N. S., Bussov, G. Y., and Webb, S. L. (1993). "Magma rheology," in *Experiments at High Pressure and Applications to the Earth's Mantle*, eds R. W. Luth. (Edmonton, AB: Mineralogical Association of Canada), 21, 131–196.

Duffield, W.A., Bacon, C. R., and Delaney, P. T. (2016). Deformation of poorly consolidated sediment during shallow emplacement of a basalt sill, Coso Range, California. *Bull. Volcanol.* 48, 97–107. doi: 10.1007/BF01046545

Fuller, G. G. (1995). *Optical Rheometry of Complex Fluids*. New York, NY: Oxford University Press.

Galland, O., Bertelsen, H. S., Guldstrand, F., Girod, L., Johannessen, R. F., Bjugger, F., et al. (2016). Application of open-source photogrammetric software MicMac for monitoring surface deformation in laboratory models. *J. Geophys. Res. Solid Earth* 121, 2852–2872. doi: 10.1002/2015JB012564

Galland, O., Cobbold, P. R., Hallot, E., de Bremond d'Ars, J., and Delavaud, G. (2006). Use of vegetable oil and silica powder for scale modelling of magmatic intrusion in a deforming brittle crust. *Earth Planet. Sci. Lett.* 243, 786–804. doi: 10.1016/j.epsl.2006.01.014

Galland, O., Holohan, E., van Wyk de Vries, B., and Burchardt, S. (2018). "Laboratory modelling of volcano plumbing systems: a review," in *Physical Geology of Shallow Magmatic Systems. Advances in Volcanology (An Official Book Series of the International Association of Volcanology and Chemistry of the Earth's Interior)*, eds C. Breitkreuz and S. Rocchi (Cham: Springer), 147–214. doi: 10.1007/11157_2015_9

Galland, O. and Scheibert, J. (2013). Analytical model of surface uplift above axisymmetric flat-lying magma intrusions: implications for sill emplacement and geodesy. *J. Volcanol. Geotherm. Res.* 253, 114–130. doi: 10.1016/j.jvolgeores.2012.12.006

Gerya, T. V. and Burg, J.-P. (2007). Intrusion of ultramafic magmatic bodies into the continental crust: numerical simulation. *Phys. Earth Planet. Interiors* 160, 124–142. doi: 10.1016/j.pepi.2006.10.004

Gerya, T. V. and Burg, J.-P. (2007). Dynamics of surface deformation induced by dikes and cone sheets in a cohesive Coulomb brittle crust. *J. Geophys. Res. Solid Earth* 122, 8511–8524. doi: 10.1002/2017JB014346

Haug, Ø. T., Galland, O., Souloumiac, P., Souche, A., Guldstrand, F., and Schmiedel, T. (2017). Inelastic damage as a mechanical precursor for the emplacement of saucer-shaped intrusions. *Geology* 45, 1099–1102. doi: 10.1130/G39361.1

Haug, Ø. T., Galland, O., Souloumiac, P., Souche, A., Guldstrand, F., Schmiedel, T., et al. (2018). Shear versus tensile failure mechanisms induced by sill intrusions – Implications for emplacement of conical and saucer-shaped intrusions. *J. Geophys. Res. Solid Earth* 123. 3430–3449. doi: 10.1002/2017JB015196

Hirata, T. (1998). Fracturing due to fluid intrusion into viscoelastic materials. *Phys. Rev. E* 57:1772.

Kaushal, M. and Joshi, Y. M. (2014). Linear viscoelasticity of soft glassy materials. *Soft Matter* 10, 1891–1894. doi: 10.1039/C3SM52978A

Kavanagh, J. L., Boutelier, D., and A. R. Cruden (2015), The mechanics of sill inception, propagation and growth: experimental evidence for rapid reduction in magmatic overpressure. *Earth Planet. Sci. Lett.* 421:052801. doi: 10.1016/j.epsl.2015.03.038

Kavanagh, J. L., Burns, A. J., Hilmi Hazim, S., Wood, E. P., Martin, S. A., Hignett, S., et al. (2018). Challenging dyke ascent models using novel laboratory experiments: implications for reinterpreting evidence of magma ascent and volcanism. *J. Volcanol. Geother. Res.* 354, 87–101. doi: 10.1016/j.jvolgeores.2018.01.002

Krumbholz, M., Hieronymus, C. F., Burchardt, S., Troll, V. R., Tanner, D. C., and Friese, N. (2014). Weibull-distributed dyke thickness reflects probabilistic character of host-rock strength. *Nat. Commun.* 5:3272. doi: 10.1038/ncomms4272

Lemaire, E., Levitz, P., Daccord, G., and Van Damme, H. (1991). From viscous fingering to viscoelastic fracturing in colloidal fluids. *Phys. Rev. Lett.* 67, 2009–2012.

Mathieu, L., van Wyk de Vries, B., Holohan, E. P., and Troll, V. R. (2008). Dykes, cups, saucers and sills: analogue experiments on magma intrusion into brittle rocks. *Earth Planet. Sci. Lett.* 270, 1–13. doi: 10.1016/j.epsl.2008.02.020

Menand, T., Daniels, K. A., and Benghiat, P. (2010). Dyke propagation and sill formation in a compressive tectonic environment. *J. Geophys. Res. Solid Earth* 115. doi: 10.1029/2009JB006791

Merle, O. and Donnadieu, F. (2000). Indentation of volcanic edifices by the ascending magma. *Geol. Soc. Lond.* 174, 43–53. doi: 10.1144/GSL.SP.1999.174.01.03

Miller, R. B. and Paterson, S. R. (1999). In defense of magmatic diapirs. *J. Struct. Geol.* 21, 1161–1173.

Montanari, D., Bonini, M., Corti, G., Agostini, A., and Del Ventisette, C. (2017). Forced folding above shallow magma intrusions: Insights on supercritical fluid flow from analogue modelling. *J. Volcanol. Geother. Res.* 345, 67–80. doi: 10.1016/j.jvolgeores.2017.07.022

Mourchid, A., Lécolier, E., Van Damme, H., and Levitz, P. (1998). On viscoelastic, birefringent, and swelling properties of Laponite clay suspensions: revisited phase diagram, *Langmuir* 14, 4718–4723.

Nase, J., Lindner, A., and Creton, C. (2008). Pattern formation during deformation of a confined viscoelastic layer: from a viscous liquid to a soft elastic solid. *Phys. Rev. Lett.* 101:074503. doi: 10.1103/PhysRevLett.101.074503

Okada, H., Watanabe, H., Yamashita, H., and Yokoyama, I. (1981). Seismological significance of the 1977–1978 eruptions and the magma intrusion process of Usu volcano, Hokkaido, *J. Volcanol. Geother. Res.* 9, 311–334.

Petford, N. (1996). Dykes or diapirs? *Geol. Today* 16, 180–184.

Petford, N. and Clemens, J. D. (2000). Granites are not diapiric! *Geol. Today* 16, 180–184. doi: 10.1111/j.1365-2451.2000.00008.x

Pignon, F., Magnin, A., Piau, J.-M., Cabane, B., Lindner, P. and Diat, O. (1997). Yield stress thixotropic clay suspension: investigations of structure by light, neutron, and x-ray scattering. *Phys. Rev. E* 56, 3281–3289.

Pollard, D. D. (1973). Derivation and evaluation of a mechanical model for sheet intrusions. *Tectonophysics* 19, 233–269.

Pollard, D. D. (1987). "Elementary fracture mechanics applied to the structural interpretation of dikes," in *Mafic Dyke Swarms*, eds H. C. Halls and W. F. Fahrig (Toronto, ON: Geological Society of Canada Special Papers), 5–24.

Pollard, D. D. and Johnson, A. M. (1973). Mechanics of growth of some laccolithic intrusions in the Henry Mountains, Utah, II. Bending and failure of overburden layers and sill formation. *Tectonophysics* 18, 311–354.

Ramberg, H. (1981), *Gravity, Deformation and the Earth's Crust.* London: Academic Press.

Ranalli, G. (1995), *Rheology of the Earth.* London: Chapman and Hall.

Rivalta, E., Taisne, B., Bunger, A. P., and Katz, R. F. (2015). A review of mechanical models of dike propagation: schools of thought, results and future directions. *Tectonophysics* 638, 1–42. doi: 10.1016/j.tecto.2014.10.003

Roman, D. C., and Cashman, K. V. (2006). The origin of volcano-tectonics earthquake swarms. *Geology* 34, 457–460. doi: 10.1130/G22269.1

Román-Berdiel, T., Gapais, D., and Brun, J. P. (1995). Analogue models of laccolith formation. *J. Struct. Geol.* 17, 1337–1346.

Rubin, A. (1993). Dikes vs. diapirs in viscoelastic rock. *Earth Planet. Sci. Lett.* 119, 641–659.

Rubin, A. (1995). Propagation of magma-filled cracks. *Annu. Rev. Earth Planet. Sci.* 23, 287–336.

Ruzicka, B., and Zaccarelli, E. (2011a). A fresh look at the Laponite phase diagram. *Soft Matter* 7, 1268–1286. doi: 10.1039/C0SM00590H

Ruzicka, B., Zaccarelli, E., and Zulian, L. (2011b). Observation of empty liquids and equilibrium gels in a colloidal clay. *Nat. Mater.* 10, 56–50. doi: 10.1038/nmat2921

Saffman, P. G. (1986). Viscous fingering in Hele-Shaw cells. *J. Fluid Mech.* 173, 73–94.

Saffman, P. G. and Taylor, G. (1958). The penetration of a fluid into a porous medium or Hele-Shaw cell containing a more viscous liquid. *Proc. R. Soc. Lond. A* 245, 312–329.

Scaillet, B., Holtz, F., and Pichavant, M. (1997). "Rheological properties of granitic magmas in their crystallization range," in *Granite: From Segregation of Melt to Emplacement Fabrics*, eds J. L. Bouchez, D. H. W. Hutton, and W. E. Stephens (Dordrecht: Springer-Verlag), 11–29.

Scheibert, J., Galland, O., and Hafver, A. (2017). Inelastic deformation during sill and laccolith emplacement: insights from an analytic elasto-plastic model. *J. Geophys. Res. Solid Earth* 122, 923–945. doi: 10.1002/2016JB013754

Schmiedel, T., Galland, O., and Breitkreuz, C. (2017). Dynamics of sill and laccolith emplacement in the brittle crust: role of host rock strength and deformation mode. *J. Geophys. Res. Solid Earth* 122, 8625–9484. doi: 10.1002/2017JB014468

Schofield, N., Brown, D. J., Magee, C., and Stevenson, C. T. (2012). Sill morphology and comparison of brittle and non-brittle emplacement mechanisms. *J. Geol. Soc.* 169, 127–141. doi: 10.1144/0016-76492011-078

Sigmundsson, F., Hreinsdóttir, S., Hooper, A., Arnadóttir, R. Pedersen, M. J. Roberts, N. et al. (2010). Intrusion triggering of the 2010 Eyjafjallajökull explosive eruption. *Nature* 468, 426–430. doi: 10.1038/nature09558

Spacapan, J., Galland, O., Leanza, H. A., and Planke, S. (2016). Control of strike-slip fault on dyke emplacement and morphology *J. Geol. Soc.* 173, 573–576. doi: 10.1144/jgs2015-166

Spacapan, J., Galland, O., Leanza, H. A., and Planke, S. (2017). Igneous sill emplacement mechanism in shale-dominated formations: a field study at Cuesta del Chihuido, Neuquén basin, Argentina. *J. Geol. Soc.* 174, 422–433. doi: 10.1144/jgs2016-056

Sumita, I., and Ota, Y. (2011). Experiments on buoyancy-driven crack around the brittle-ductile transition. *Earth Planet. Sci. Lett.* 304, 337–346. doi: 10.1016/j.epsl.2011.01.032

Taisne, B., and Tait, S. (2009). Eruption versus intrusion? Arrest of propagation of constant volume, buoyant, liquid-filled cracks in an elastic, brittle host. *J. Geophys. Res. Solid Earth* 114. doi: 10.1029/2009JB006297

Ukawa, M., and Tsukahara, H. (1996). Earthquake swarms and dike intrusions off the east coast of Izu Peninsula, central Japan. *Tectonophysics* 253, 285–303.

Vachon, R., and Hieronymus, C. F. (2016). Effect of host-rock rheology on dike shape, thickness, and magma overpressure. *Geophys. J. Int.* 208, 1414–1429. doi: 10.1093/gji/ggw448

White, R. S., Drew, J., Martens, H. R., Key, J., Soosalu, H., and Jakobsdóttir, S. S. (2011). Dynamics of dyke intrusion in the mid-crust of Iceland. *Earth Planet. Sci. Lett.* 304, 300–312. doi: 10.1016/j.epsl.2011.02.038

Wilson, P. I. R., McCaffrey, K. J. W., Wilson, R. W., Jarvis, I., and Holdsworth, R. E. (2016). Deformation structures associated with the Trachyte Mesa intrusion, Henry Mountains, Utah: implications for sill and laccolith emplacement mechanisms. *J. Struct. Geol.* 87, 30–46. doi: 10.1016/j.jsg.2016.04.001

Wright, T. J., Sigmundsson, F., Pagli, C., Belachew, M., Hamling, I. J., Brandsdóttir, B., et al.(2012). Geophysical constraints on the dynamics of spreading centres from rifting episodes on land. *Nat. Geosci.* 5, 242–250. doi: 10.1038/ngeo1428

Conflict of Interest Statement: The authors declare that the research was conducted in the absence of any commercial or financial relationships that could be construed as a potential conflict of interest.

ORIGINAL RESEARCH
published: 19 November 2018
doi: 10.3389/feart.2018.00209

Growth of Continental Shelves at Salt Margins

Jean-Pierre Brun[1]* *and Xavier Fort*[2]

[1] *Univ Rennes, CNRS, Géosciences Rennes-UMR 6118, Rennes, France,* [2] *g. o. Logical Consulting, Cesson-Sévigné, France*

Whereas, salt margins are rather common, the growth of continental shelves on top of salt margins is a topic that has seldom been considered. In such settings, the sediments coming from the nearby continental areas are deposited on a viscous substratum and therefore a continental shelf can form and stabilize only if the salt layer underlying sediments does not flow or stops flowing. The present study that combines evidence from the northern Gulf of Mexico and laboratory modeling concerns more particularly those salt tectonic settings where the direction of sediment supply is oblique to the direction of salt flow because this allows to decipher between the relative effects of sedimentation and salt flow. It is shown, in both northern Gulf of Mexico and experiment, that: (i) shelf growth is controlled by an association of normal faults and transfer zones, (ii) shelf breaks, controlled by normal faults, and transfer zones trend perpendicular and parallel to salt flow, respectively, (iii) the rate of shelf break migration is faster in areas of higher sedimentation rates, (iv) even at late stages of shelf growth, when the role of salt flow tends to decrease, transfer zones still remain controlled by the direction of salt flow, and (v) transfer zones that participated to the shaping of a continental shelf provide a precious tool to map the direction of salt flow and its variations in space and time. The interaction between salt flow and sediment supply controls the trend of the shelf envelope during shelf growth. Because the rate of salt flow decreases with time, a constant or increasing rate of sediment supply results in a rotation of the shelf envelope trend from perpendicular to salt flow direction at early stages toward perpendicular to sediment supply direction at the late stages.

Keywords: continental shelf, salt margin, salt tectonics, laboratory modeling, Gulf of Mexico

Edited by:
Christoph Von Hagke,
RWTH Aachen Universität, Germany

Reviewed by:
Frank Strozyk,
RWTH Aachen Universität, Germany
Luis E. Lara,
Sernageomin, Chile

***Correspondence:**
Jean-Pierre Brun
jean-pierre.brun@univ-rennes1.fr

Specialty section:
This article was submitted to Structural Geology and Tectonics, a section of the journal Frontiers in Earth Science

Received: *29 June 2018*
Accepted: *31 October 2018*
Published: *19 November 2018*

Citation:
Brun J-P and Fort X (2018) Growth of Continental Shelves at Salt Margins. Front. Earth Sci. 6:209. doi: 10.3389/feart.2018.00209

INTRODUCTION

Continental shelves of passive margins correspond to shallow water and very low dipping surfaces, located between the coastline and the slope, and underlain by shallow marine sequences (Swift and Thorne, 1991). The growth of continental shelves as documented by subsurface data results from repeated regressive-transgressive transits of deltas and other shoreline systems down to the edge of a pre-existing shelf that are controlled by sea level changes (Posamentier et al., 1988; Steckler et al., 1999; Galloway, 2001; Steel et al., 2008) and sediment supply (Carvajal et al., 2009). Growth processes in action at shelf break are either purely sedimentary or result from interactions between sedimentary and deformation processes (Helland-Hansen et al., 2012). A particular example of the latter occurs at passive margins where salt tectonics is active (Brun and Fort, 2011; Fort and Brun, 2012) because the sediments coming from the nearby continental areas are deposited on flowing evaporites.

The present paper is devoted to the deformation patterns related to continental shelf growth in salt tectonic environments, a topic that has seldom been considered. Our study focuses more particularly on those salt passive margins where the direction of sediment supply is oblique to the direction of salt flow as this allows deciphering of structural and dynamic effects related to sediment supply and salt flow, respectively. The northern Gulf of Mexico that is one of the largest salt basin worldwide provides a remarkable and well-documented example of a large migration of the shelf break (i.e., several hundred km) during the Neogene (Galloway et al., 2000; Galloway, 2001), in association with the development of transfer zones (Fort and Brun, 2012). Laboratory analogue modeling is used to illustrate the mechanisms of deformation involved in the continental shelf growth when, like in the northern Gulf of Mexico, the direction of sedimentary supply trends at 60° to the regional direction of salt flow. Simple rules governing the deformation patterns that control the growth of continental shelves in a salt tectonic setting are deduced from experimental evidence and comparison with the northern Gulf of Mexico.

SHELF BREAK MIGRATION IN ACTIVE SALT TECTONIC SETTINGS

In a salt basin, a continental shelf can form and stabilize only if the underlying salt layer is not flowing or flows at very low rate. In most passive margins, sediments coming from the onshore domain are transported almost parallel to margin dip. On the other hand, gravity gliding of the salt and the overlying sediments down margin dip generates extensional structures in the salt margin landward part with normal faults trending approximately perpendicular to the direction of salt flow, parallel to margin dip (see review by Brun and Fort, 2011). In other words, salt flow and sediment transport most often trend nearly parallel.

As long as the salt layer is thick enough to allow easy flow, the overlying sedimentary layers undergo extensional faulting and fault blocks are transported seaward (**Figure 1A**). The shelf first forms on the landward side of the salt layer pinch-out and progressively extends seaward as a function of the interaction between (i) the input of sediments and (ii) the salt flow rate. Gravity driven salt tectonics at passive margins is a process whose rate does not vary strongly (strain rates in the range 10^{-15} to 10^{-16} s^{-1}). Laboratory experiments (Mauduit et al., 1997; Fort et al., 2004b) show that the gliding rate increases with the thickness of the sediments deposited on top of the salt. On the contrary, sedimentation rates at passive margins can vary over several orders of magnitude with the highest values generally corresponding to delta-type environments. Therefore, the dynamics of continental shelf growth in a salt margin depends on the rate of sedimentary supply. In salt margins with low rates of sedimentary input, the seaward migration of the boundary between non-flowing and still flowing salt domains can be faster than shelf break migration. In such a situation, the continental shelf growth interacts with salt tectonics but only at very early stages of development. In salt margins with high rates of sediment supply, the shelf break corresponds to the boundary between an updip domain of non-flowing salt (or salt flowing at very low rate) and a seaward domain where salt is flowing more vigorously. In terms of sediment deformation, the shelf break separates a landward domain with no or very weak (i.e., the shelf) faulting from a seaward domain where stronger faulting controls the deposition of incoming sediments.

With ongoing seaward displacement of faulted sedimentary blocks, the salt layer progressively thins, thus allowing the continental shelf to stabilize and the shelf break to migrate seaward (**Figure 1B**). The strongly thinned basal salt layer can still flow below the continental shelf but at very low rate. This is illustrated in the north margin of the northern Gulf of Mexico where the very flat seafloor indicates that any fault-induced irregularity is rapidly smoothed by sedimentation whereas, in neighboring onshore areas, active ground deformations can be observed and measured (e.g., Dokka et al., 2006; Engelkemeir et al., 2010).

In summary, in an active salt tectonics environment, the shelf break corresponds to a mechanical boundary between low and high strain rates in the deforming basal salt layer.

If the direction of sediment supply trends oblique to margin dip, sediment thickness is not constant in a direction perpendicular to the salt flow direction. Consequently, the gliding rate varies along strike, resulting in a segmentation of the extensional domain by transfer zones parallel to the salt flow direction (**Figure 1C**). Where sediments are thicker, the gliding rate is faster and salt layer thinning is stronger. Consequently, the rate of shelf break migration is faster. Across several neighboring extensional domains with different gliding rates, the map contour of the shelf break then becomes undulated (**Figure 1C**).

Remark: In **Figure 1**, we represented the extension affecting the sediments above salt only as series of normal faults and related block tilting. Note that this is done for the sake of simplicity and that, in nature, other types of salt tectonics structures, like rollovers, horsts and grabens or diapirs, can contribute as well to salt layer thinning and shelf stabilization.

CONTINENTAL SHELF GROWTH IN THE NORTHERN GULF OF MEXICO

To produce a detailed map of the Cenozoic continental shelf at whole Gulf of Mexico (GoM) scale, Galloway et al. (2000) have compiled in a Geographic Information System (GIS) the following data sources: (i) 241 publications and theses, (ii) 800 well data sets, and (iii) deep-basin seismic lines of UTIG (University of Texas Institute for Geophysics). This database allowed the identification of 18 major depositional episodes and the differentiation of 31 depositional facies associations used to construct paleogeographic maps. Then, the Cenozoic history of the GoM sedimentary filling was summarized by a map pattern of shelf-margin migration, based on 25 depositional systems.

For the purpose of the present paper, only the map part concerning the northern GoM salt basin is redrawn showing each depositional system with an arbitrary color (**Figure 2**). The terminations of depositional episodes represent the successive positions of the shelf break. They are identified by their age (in

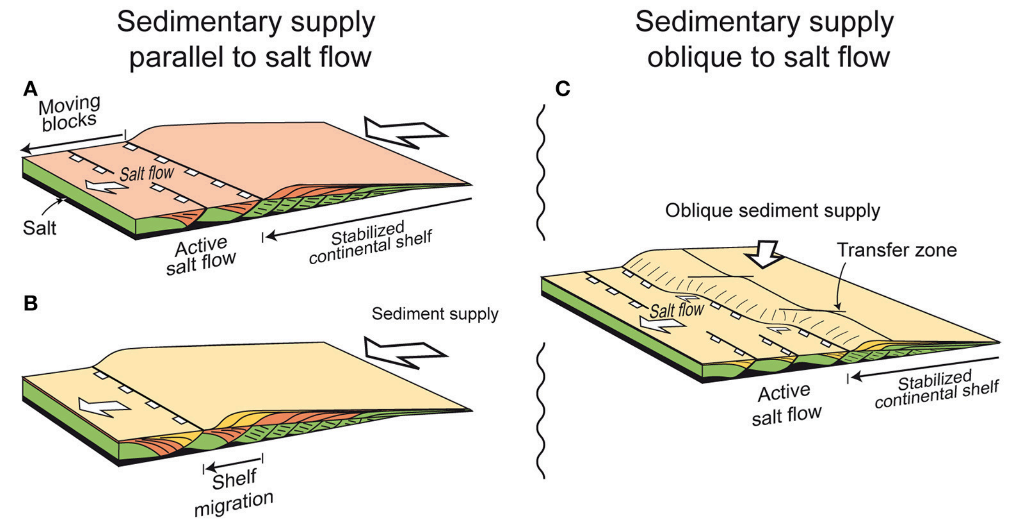

FIGURE 1 | Conceptual models for the development of a continental shelf at a passive margin involving active salt tectonics [Modified after (Fort and Brun, 2012)]: **(A)** and **(B)** show two successive stages of shelf break migration at a passive margin where sediment supply (Thick arrows) is parallel to salt flow (Thin arrows). Green, orange and yellow: successive depositional episodes. Normal faults trend parallel to the direction of salt flow. The position of shelf break for each episode is controlled by an active normal fault. Each new depositional episode seals the faults that were active during a previous depositional episode on the landward side of the shelf break. Below the stabilized continental shelf salt stopped flowing. Sediments deposited on the seaward side of the shelf break contribute to the growth of fault blocks that displace seaward on top of the flowing salt. **(C)** Tri-dimensional structure of a passive margin where sediment supply is oblique to salt flow. The shelf break is, like in **(A)** and **(B)**, controlled by normal faulting but it is offset by transfer zones trending parallel to the salt flow.

My) according to the time scale of Berggren et al. (1995). For an easier appraisal of the progressive growth of the continental shelf, each depositional episode is shown separately in **Figure 3**.

Throughout the Cenozoic, the bulk of the sediments that filled the northern GoM margins have been provided by five main extrabasinal axes (**Figure 2**): the palaeo Rio Grande (RD), Houston (HN), Red (RD), Central Mississippi (CM), and East Mississippi (EM). For more details see Galloway (2001).

Shelf Break Migration

Between Cretaceous (65 Ma) and base Oligocene (33 Ma), the mean shelf break trend was stable, from SW-NE in Texas (Northwest margin) to E-W in Louisiana (North margin) (**Figure 2**). During this time interval, the shelf break migrated ~150 km, on average, toward the S or SE in Northwest margin (blue curve in insert of **Figure 2**).

Since Oligocene, the shelf has displayed a 2 fold evolution. In the Northwest margin, it continued to migrate toward the SE with almost the same SW-NE trend. In the North margin, its evolution became rather complex. A major change in the orientation and position of the shelf break occurred in the Middle Miocene (from 16 to 12 Ma in **Figures 2**, **3**). To the East, the shelf break trend rotated from an E-W to a WNW-ESE trend. To the West, the shelf break jumped close to its present-day position, keeping its SW-NE trend.

Amounts and rates of shelf break migration have varied in space and time (red curve in insert of **Figure 2**). In the Northwest margin, the overall displacement reached approximately 230 km and the migration history alternated between accelerations and decelerations, with a mean rate of 0.35 cm y^{-1}. Low rates of shelf migration occurred in Early to Middle Eocene, Late Oligocene to Early-Miocene and since Middle Miocene. The highest rate of shelf migration occurred from Late Eocene to Early Oligocene. In the North margin, the overall displacement reached approximately 400 km. The rate of shelf migration has slowly increased from Late Eocene to Lower Miocene. A strong and sudden acceleration occurred in early middle Miocene. Since Middle Miocene (16 Ma), the mean migration rate has remained almost constant at approximately 1.8 cm y^{-1}–i.e., more than five times faster than in the West margin.

Transfer Zones

During the Neogene, the shelf break contours became meandering, defining numerous NE-SW trending transfer zones (Dashed lines in **Figure 2**) (Fort and Brun, 2012). In **Figure 3**, solid black lines represent the transfer zones that were active during each depositional episode and dashed lines the trace of those that were active in previous episodes. The whole trajectories (2.3–0.0 Ma in **Figure 3**) are curved showing a NE-SW trends prior to 16 Ma and after 6 Ma and an ENE-WSW trend between 16 and 6 Ma. This temporal anomaly, from Middle Miocene to Late Miocene, corresponds to the period during which the shelf break migration reached its maximum rate. Since the end of Oligocene-Lower Miocene (26-18 Ma), the North margin shelf break has migrated as a mean in a SW direction, almost parallel to the Northwest margin shelf and even along it since the end of Middle Miocene (12 Ma).

Fort and Brun (2012), used the structures displayed by digital bathymetry maps of slope and deep margin basin, located South of present day shelf break, to carry out a kinematic analysis

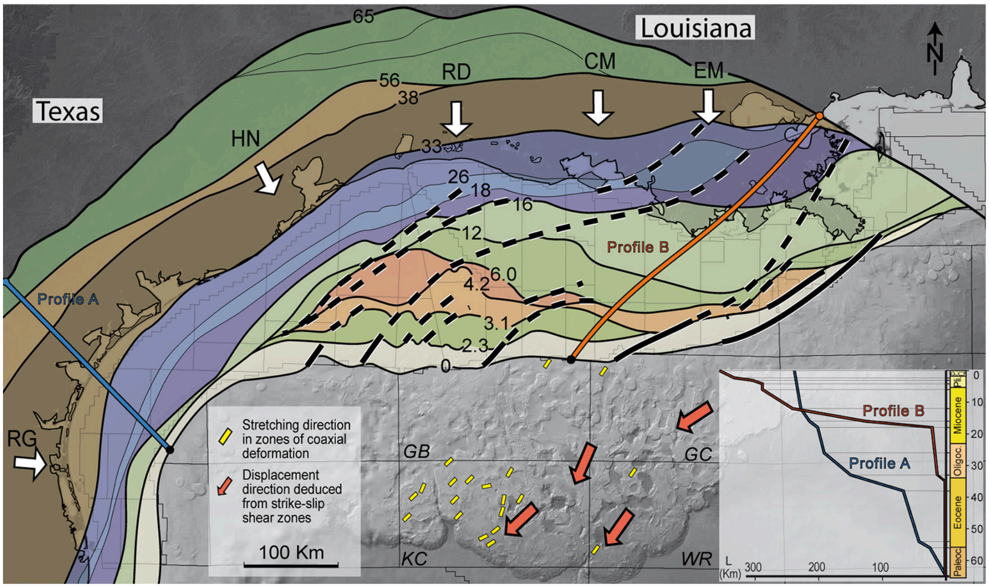

FIGURE 2 | Kinematics of continental shelf growth in the northern Gulf of Mexico [Modified after (Fort and Brun, 2012)]. Contours and ages (in My) of depositional episodes and main axes of sediment supply (White arrows) after Galloway et al. (2000). Solid black lines: Recent transfer zones (see **Figure 1C**). Dashed lines: trace of previous transfer zones. The five main extrabasinal axes from which sediments filled the northern GoM margins are: RG, palaeo Rio Grande; HN, Houston; RD, Red; CM, Central Mississippi; EM, East Mississippi. Lower right insert: Curves of shelf break migration in the Northwestern margin (Profile A) and North margin (Profile B).

of deformation zones between minibasins. Both stretching directions in zones of co-axial deformation (yellow bars in **Figure 2**) and mean direction of displacement obtained from a statistical analysis of senses of strike-slip shear (Red arrows in **Figure 2**) trend in a mean NE-SW direction, almost parallel to the mean trend of transfer zones in the continental shelf. This strongly supports the use of transfer zones as a kinematic indicator for the direction of salt flow during the of shelf break migration (**Figure 1C**), as proposed by Fort and Brun (2012).

In summary, the location, geometry and kinematics of shelf break migration show that the North and West margins have strikingly different histories. Two diachronic major changes occurred, in Late Eocene-Early Oligocene in the West margin and in Middle-Miocene in the North margin. Since Middle Miocene, the North margin shelf break has migrated toward the SW. This indicates that salt was flowing toward the SW at the scale of the northern GoM domain with an obliquity of around 60° with the mean direction of sediment supply (**Figure 2**).

LABORATORY MODELING

As argued above, the transfer zones involved in the migration of the shelf break as well as kinematic indicators from the slope domain and deep basin indicate that, in the northern Gulf of Mexico, salt flow trends at regional scale in a mean NE-SW direction with an obliquity of around 60° to the mean N-S direction of sediment supply. Therefore, the laboratory experiment presented here has been carried out to test the effects of a sedimentation oblique to the salt flow direction and more particularly: (i) the growth of a continental shelf and (ii) the development of transfer zones, in relation with the bulk dynamic evolution of the salt basin. In other words, this experiment does not aim at modeling the complexities of salt tectonics in the Gulf of Mexico but simply at testing the processes at work during the growth of a shelf in an active salt basin. Results should be applicable to other salt basins elsewhere in the world.

Experimental Procedure

The experimental procedure used in the present work is similar to the one currently used for the study of salt tectonic processes in various laboratories (e.g., Austin: Dooley et al., 2007; London: Adam et al., 2012; Rennes: Fort et al., 2004a; Lille: Lymer et al., 2018) using silicone putties and sand to represent salt and sediments, respectively. However, whereas a large number of experiments of salt tectonics type have been carried out, since about four decades, none has been dedicated to the formation of continental shelves in salt basins.

Scaling

The model is scaled using the classical principles defined for the modeling of brittle-ductile systems using sand and silicone putties. For a small-scale model to be representative of a natural example (a prototype), a dynamic similarity in terms of distribution of stresses, rheologies, and densities between the model and the prototype is required (Hubbert, 1937; Ramberg, 1981). Following these principles, it can be shown that in sand-silicone models, the dynamic similarity is respected when the ratios of stresses and lengths are nearly equal (Brun, 1999).

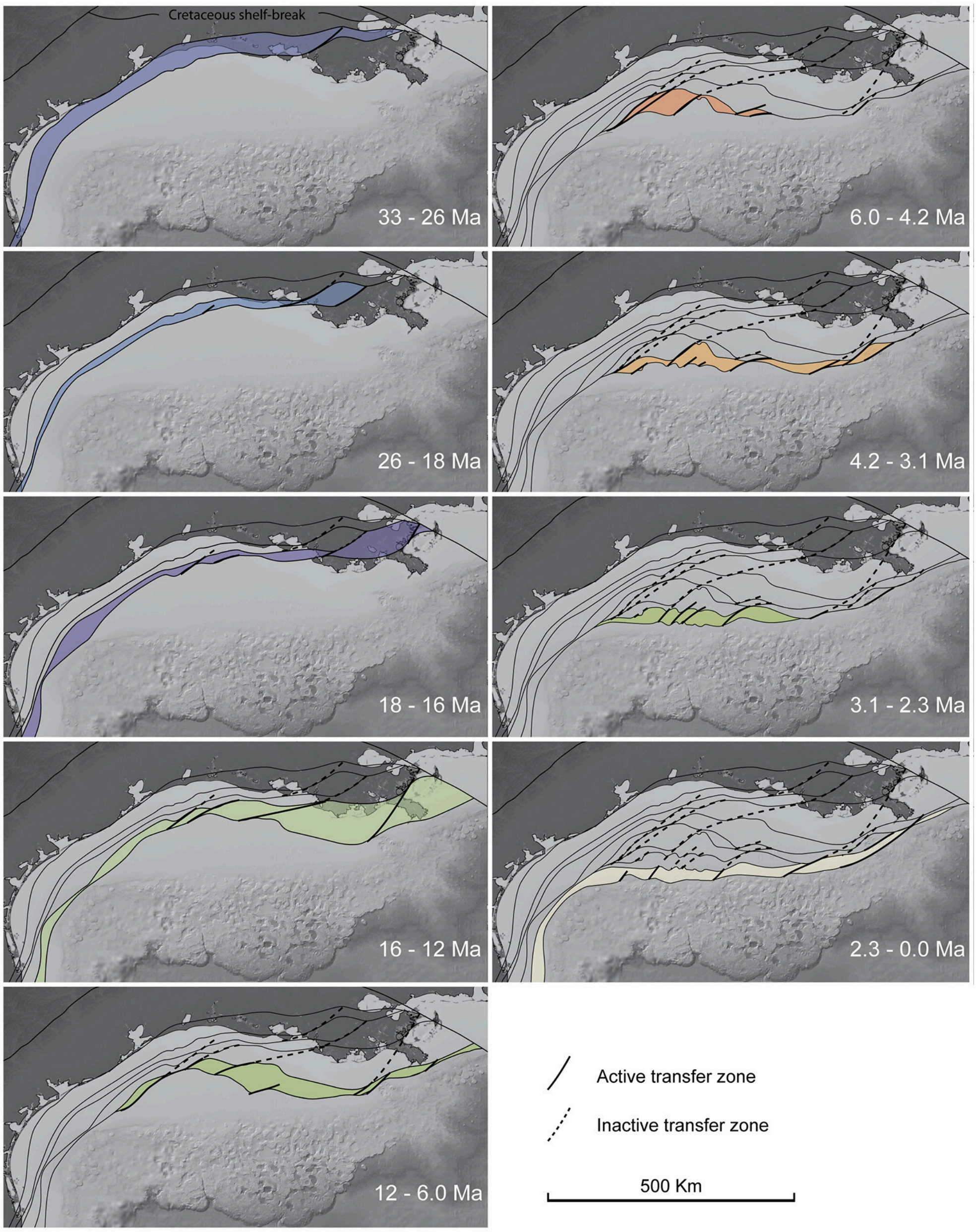

FIGURE 3 | Step-by-step growth of the continental shelf in the northern Gulf of Mexico. Shelf break contours, colors of depositional episodes (growth increments) and ages like in **Figure 2**. Solid black lines: Transfer zones active during a shelf growth increment; dashed lines: trace of transfer zones that developed during previous shelf growth increments.

Materials

Sediments are represented by Fontainebleau sand with a density ρ of about 1,400 kg/m^3 and an angle of friction ϕ in the range 30–33°, but without significant cohesion C. Salt is represented by a transparent silicone putty (XM RBG-0901 GUM, Dow Corning) with a Newtonian viscosity $\mu = 10^4$ Pa s and a density $\rho = 1{,}000$ kg/m3. The density contrast between silicone putty and sand ($\Delta\rho_m = 1.4$) is slightly higher than might be expected between salt and sediments in nature ($\Delta\rho_p = 1.05$–1.18; according to Weijermars et al., 1993). However, as pointed out by Weijermars et al. (1993) this disparity is acceptable because the density contrast between salt and sediments is not the primary factor responsible for the rise of diapirs.

Model Building

The **Figure 4** summarizes the experimental setting. The silicone layer (i.e., salt) has a double wedge shape to simulate salt layer pinch-out at basin edges. Its dimensions are: length: 150 cm, width: 100 cm and maximum thickness: 2 cm. A 0.6 cm thick sand

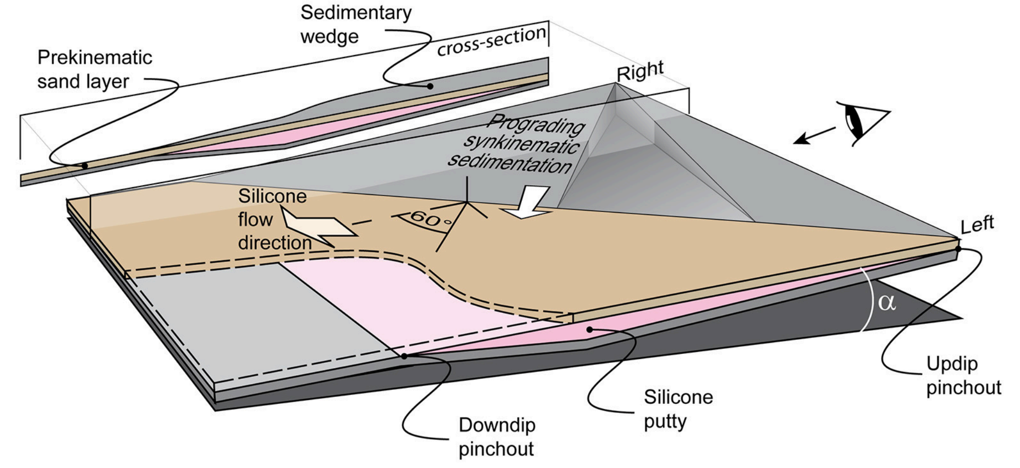

FIGURE 4 | Tri-dimensional sketch of the experimental setting used to study the growth of a continental shelf in a salt tectonic environment where the sediment supply (white arrow) is oblique to salt flow. The basal layer of silicone putty (pink) is double-wedge shaped to simulate salt pinch-out at the updip and downdip ends of the salt basin. A thin sand layer is deposited on top of the silicone layer before the onset of experiment. The direction of salt flow is obtained in inclining the model by an angle α. The obliquity between sediment supply and salt flow is 60°.

layer (so-called pre-kinematic layer) is deposited on top of the silicone layer prior to the onset of experiment.

Model Run

The experiment duration was 9 days. At the onset of experiment the model was inclined by an angle $\alpha = 0.8^\circ$. Then this angle was increased once per day to reach an angle $\alpha = 2.7^\circ$ after 7 days. A wedge-shape sand layer, with a thickness of around 1.0 cm at the back and regularly thinning frontward (**Figure 4**), was deposited with a funnel once per day to simulate a sediment progradation in a direction trending at 60° to basin tilt. Surface photographs were taken at regular time intervals during the experiment.

Results

For the purpose of the present paper, which primarily concerns the development of a continental shelf, the results are summarized in three figures: (i) A selection of top views between 72 and 215 h (**Figure 5**) showing the progressive deformation at model surface and the progressive growth of a continental shelf in the updip part of the model, (ii) a tracking of surface displacements reported on the last model top view (**Figure 6**), and (iii) three cross sections to illustrate the style of structures that developed at different places within the model (**Figure 7**).

DEFORMATION, DISPLACEMENTS AND STRUCTURES

Deformation History

The observation of model top views (**Figure 5**) shows that two main stages can be distinguished, prior and after a frontal rupture that occurred at 144 h.

Prior to frontal rupture, a domain of extension developed in the updip part of the model that progressively enlarged to occupy two thirds of the distance between the two salt (silicone putty) pinch-outs (From 72 to 144 h; **Figure 5**). Simultaneously, a domain of shortening developed close to the down-dip salt pinch-out (144 h; **Figure 5**). The width of the domain of shortening, which was initially made of several folds and thrusts, progressively decreased to form a single thrust zone that evolved into a frontal rupture.

After rupture, a frontal salt nappe formed whose very fast displacement reached 20 cm (nearly 1/8 of the initial salt basin length) in 67 h (around 1/3 of the total model duration). Soon after the initiation of the salt nappe, lateral salt extrusion occurred on both sides of the model giving a bulk lobate shape to the salt nappe front. Simultaneously, extension started to develop in the whole downdip part of the model that was previously undeformed (i.e., backward extension).

Displacement Pattern

The tracking of material points located along two cross-lines in the updip extensional domain (**Figure 6**) illustrates the two-stage evolution described above, in terms of displacement history.

Before frontal rupture (blue arrows in **Figure 6**), the displacements slightly decreased laterally from right to left– i.e., from thicker to synkinematic thinner sediment deposits– in the updip part of the extensional domain. Note that the terms right and left here refer to model sides when looking in the salt flow direction. In direct relation with the variation of displacement rate, extensional structures are more numerous to the right than to the left (compare 72 and 96 h in **Figure 5**). Conversely, a lateral variation of the displacements in not observed in the downdip part of the extensional domain. In this area, new extensional structures, which participate to an enlargement of the extensional domain, develop parallel to the downdip salt pinch-out and to the domain of frontal shortening. This indicates that, prior to frontal rupture, the downdip part of the extensional domain was less sensible

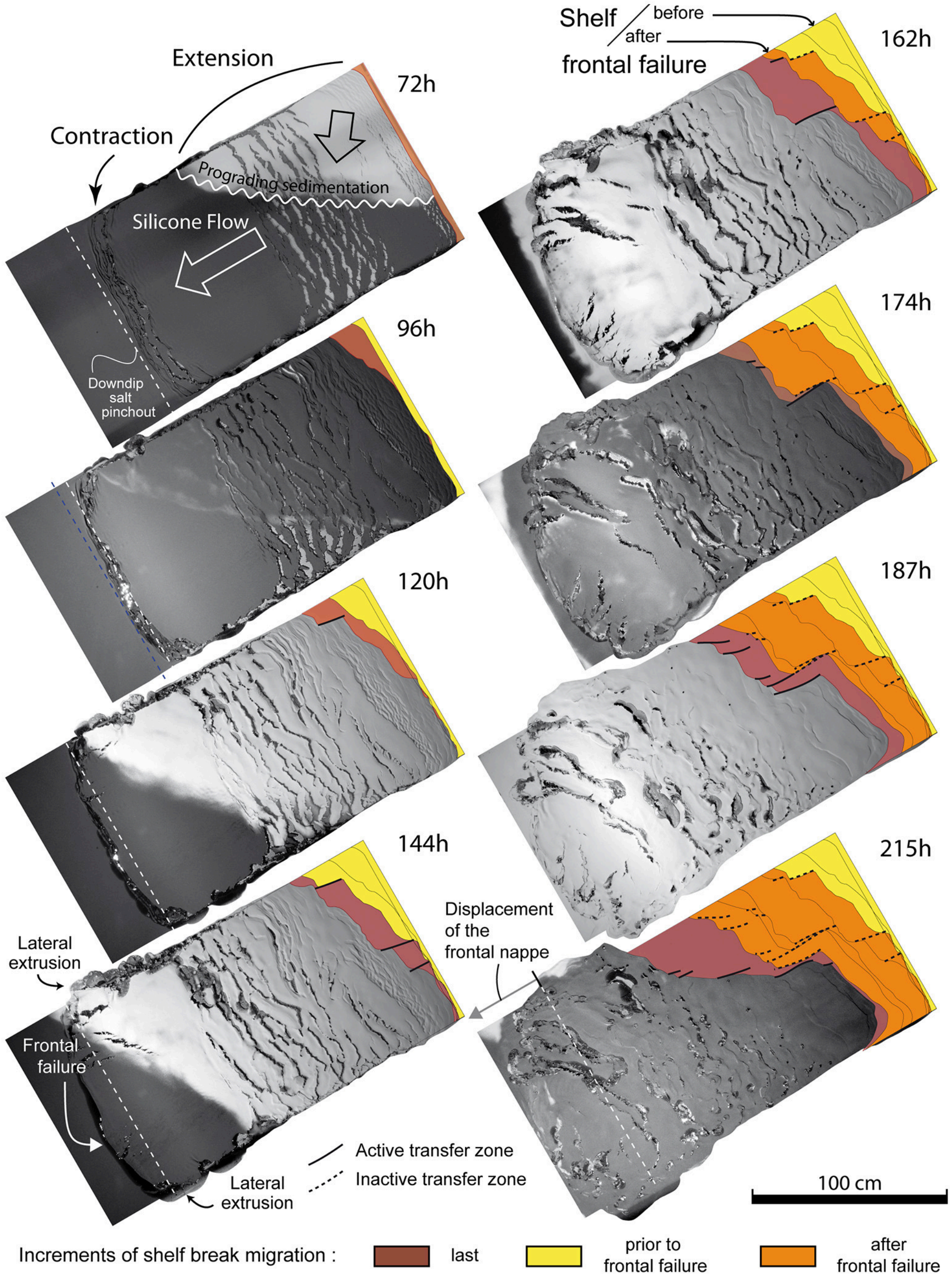

FIGURE 5 | Selection of model top views showing the progressive evolution of surface deformation and growth of the continental shelf. The duration since experiment onset is indicated for each snapshot. White arrows (at 72 h): Directions of silicone (salt) flow and sediment supply.

to lateral variations of synkinematic sediment thickness than the updip part and, reciprocally, more sensible to frontal shortening.

After frontal rupture (Red arrows in **Figure 6**), the reverse effect occurred. In both the updip and downdip parts of the extensional domain, the displacement increased from right to left. In fact, this is due to synkinematic sedimentation at salt nappe front in the right part of the model. The tip of the synkinematic sedimentary wedge reached the right end of the frontal zone of shortening almost simultaneous with frontal rupture. Consequently, further synkinematic sediment deposits occurred to the right part of the salt nappe reducing its rate of displacement with reference to the left part (see 162 to 187 h in **Figure 5**).

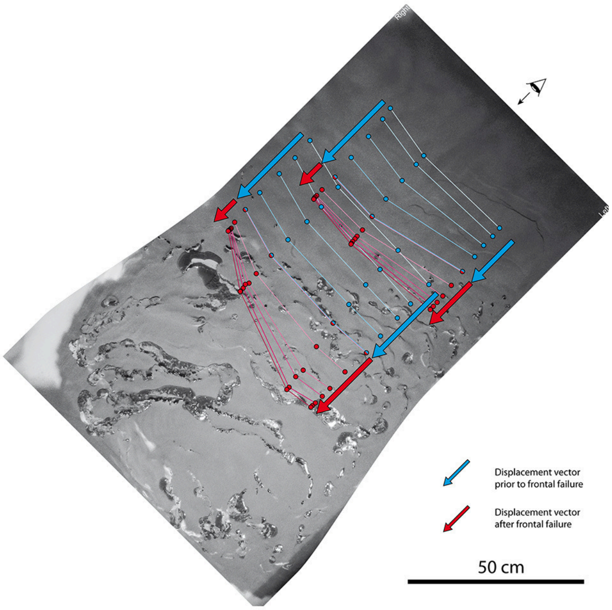

FIGURE 6 | Model top view at the end of experiment (215 h/9 days) with tracking of two series of material points initially located in the updip and downdip parts of the updip extensional domain (See 72 h top view in **Figure 5**).

Structures

The thickness to length ratio is too small to allow a single model cross-section parallel to salt flow direction to display all significant structures. Therefore, three smaller cross-sections are shown to illustrate the structures that characterize the main deformation domains and their evolution in time.

The shelf domain (**Figure 7a**) shows a sequence of normal faulting that progressively accommodated the stabilization of the model updip part leading to a downdip shelf migration. The five top layers (from top to base black, yellow, white, black, and white) successively sealed normal faults in a downdip sense, controlling the successive locations SB1–SB4 of the shelf break. Fault sealing occurred when the basal salt layer became too thin to allow further downdip displacement of the hanging-wall fault block. During the sequential sealing of fault blocks, fault spacing and therefore fault block width increased from right to left as a function of shelf thickness. This syn-sedimentary deformation pattern illustrates the mechanism of continental shelf growth and downdip migration of shelf break.

The updip extensional domain (**Figure 7b**; see surface views 72 h—144 h in **Figure 5**) shows the segmentation of sedimentary cover by normal faulting and the formation of rafts on top of the autochthonous salt. Raft separation allowed the formation of diapirs and subsequent sub-horizontal spreading of salt on top of the rafts, forming an irregular allochthonous salt layer. Sediments deposited on top of the allochthonous salt correspond to minibasins.

The frontal salt nappe and the backward extensional domain (**Figure 7c**) formed after frontal rupture (144 h in **Figure 5**). The section shows the advance of the salt nappe with reference to the downdip pinch-out. The salt nappe has transported a raft whose basal layer is the pre-kinematic layer deposited on top of salt prior to the onset of experiment. To the right of the salt nappe, the sedimentary cover was not previously submitted to extension (up to 144 h in **Figure 5**). Extension occurred in an updip direction (i.e., backward) as a result of frontal rupture and emplacement of the salt nappe. This downdip extensional domain displays rafts with a prekinematic layer at the base above the autochthonous salt, an allochthonous salt layer, and minibasins above the allochthonous salt. Folds that formed prior to frontal rupture in the downdip domain of contraction (72 h in **Figure 5**), close to the salt pinch-out, were disrupted by thrust faults and encapsulated in the salt layer (**Figure 7c**).

SHELF GROWTH

The updip domain that progressively stabilized illustrates the progressive shelf growth in map view (**Figure 5**) and in cross-section (**Figure 7a**). Thin black lines (in **Figure 5**) correspond to successive map contours of the shelf. Three colors display the growth history of the continental shelf: (i) brown corresponds to the last depositional episode in each snapshot, (ii) yellow and orange represent the two main growth periods prior and after frontal rupture, respectively.

Shelf Breaks and Transfer Zones

The shelf contours show two main trends. One is almost parallel to the extensional structures and corresponds to the shelf break strictly speaking (i.e., normal faults; see **Figure 7a**). The other one is almost parallel to the direction of salt flow and corresponds to a lateral offset of the shelf break. To the right side of contours trending parallel to salt flow, the shelf is stabilized as demonstrated by the absence of normal faults at surface indicating that the underlying salt stopped flowing. The left side displays normal faults indicating that underlying salt is still flowing. Therefore, these contours parallel to the displacement correspond to transfer zones–i.e., zones that connect two shelf breaks and that transfer extension from one to the other. It is noteworthy that at whole model-scale they trend parallel or nearly parallel to the direction of salt flow.

History of Shelf Growth

Figure 8 shows shelf break migration along two profiles (red and yellow dots) and advance of the deforming system front (blue dots), including frontal rupture.

Prior to frontal rupture, the sand layer at deforming system front underwent thrusting and folding, giving a complex imbrication of sand and silicone (72 h in **Figure 5**). This frontal shortening ultimately lead to the emergence at surface of a continuous silicone layer that allowed acceleration of the process (i.e., "Frontal rupture" at 144 h in **Figure 5**). During this first period shelf break migration was faster where sedimentation rate was higher (red dots a1 to a4 in **Figure 8B**). An acceleration of shelf break migration in both model sides (red and yellow dots) occurs during frontal rupture.

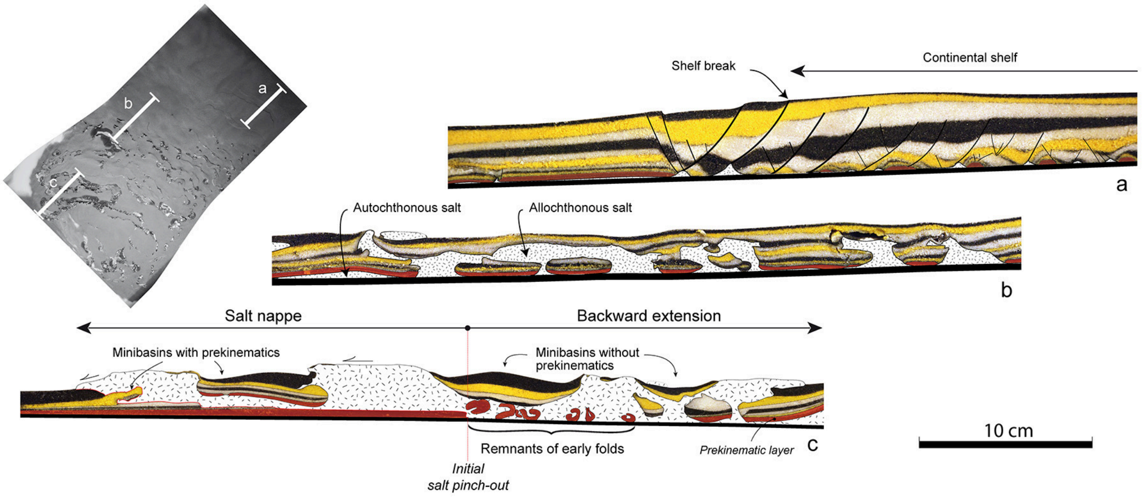

FIGURE 7 | Cross-sections showing the structures that characterize the main deformation domains in the model (See location in the insert: 215 h top view in **Figure 5**). **(a)** Growth structure of the continental shelf. SB1 to SB4 correspond to successive shelf break locations. **(b)** Rafts and salt diapirs in the updip extensional domain. **(c)** Frontal salt nappe and neighboring backward extensional domain. Red: prekinematic sand layer. White: Silicone putty (salt). Yellow, black, and white: synkinematic sand layers.

Frontal displacement being limited by the apparatus length, it is unfortunately not possible to follow shelf growth long after frontal rupture. However, on model right side (red dots) shelf break continued to migrate, even faster than before frontal rupture. This intriguing effect results from the interaction between high sedimentation rate and stop of model front displacement that inhibits silicone flow (see last sub-section of section Deformation History). Interestingly, this shows that if salt is still present but unable to flow due to boundary conditions a shelf can stabilize and grow.

Progressive Rotation of the Overall Shelf Envelope

The shelf started to develop prior to frontal rupture (96 h −144 h in **Figure 5**) but it is only after this major change in the system dynamics that shelf growth became really significant. The overall shelf envelope that integrates both normal faults and transfer zones displays a trend that started parallel to the mean trend of normal faults and that progressively rotated counter-clockwise to become almost perpendicular to the direction of sediment supply–i.e., parallel to the front of synkinematic sedimentary wedge (see the progressive evolution from 144 to 215 h in **Figure 5**). This indicates (i) that deformation played a major role on shelf development at early stages when the gravity potential driving salt tectonics was maximum and (ii) that, as the gravity potential progressively reduced, salt flow velocity progressive decreased, whereas the rate of sedimentation remained constant. In other words, the shelf envelope trend became progressively more influenced by the direction of sediment supply. However, even at the latest stages (e.g., 187–215 h in **Figure 5**), when the influence of sedimentation became stronger, transfer faults still remained parallel to salt flow direction.

TRANSFER ZONES: A TOOL FOR KINEMATIC ANALYSIS IN SALT TECTONICS

The laboratory experiment presented in this paper provides, for the first time, a mechanical basis to explain how transfer zones develop during the growth of a continental shelf at a salt margin. The experimental model confirmed the conceptual model of Fort and Brun (2012) that was developed only from available data sets in the northern Gulf of Mexico (**Figure 1C**).

It is interesting to compare the transfer zones that develop during shelf growth in a salt basin to transform faults that offset oceanic spreading centers (**Figure 9**). At a spreading center, the transform fault whose active part is located between two oceanic rifts provides the direction of displacement between the two separating plates (Wilson, 1965; Morgan, 1968). The segments of transform faults that became inactive are recorded in the oceanic crust outside the active ridge. Their changes of direction are records of previous directions of plate displacement. Similarly, in salt tectonics, the transfer zones offset the shelf break that separates an active domain where salt is still flowing from a stable shelf domain below which salt has stopped flowing. Like transform faults in plate tectonics, the transfer zones that develop during shelf growth give the direction of displacement between the inactive and active domains–i.e., the direction of salt flow. The transfer zones that became inactive are fossilized in the continental shelf and therefore provide a record of changes in the direction of salt flow during shelf break migration.

In conclusion, the transfer zones that participate to the shaping of a continental shelf provide a precious tool for mapping the direction of salt flow and its variations in space and time at basin scale.

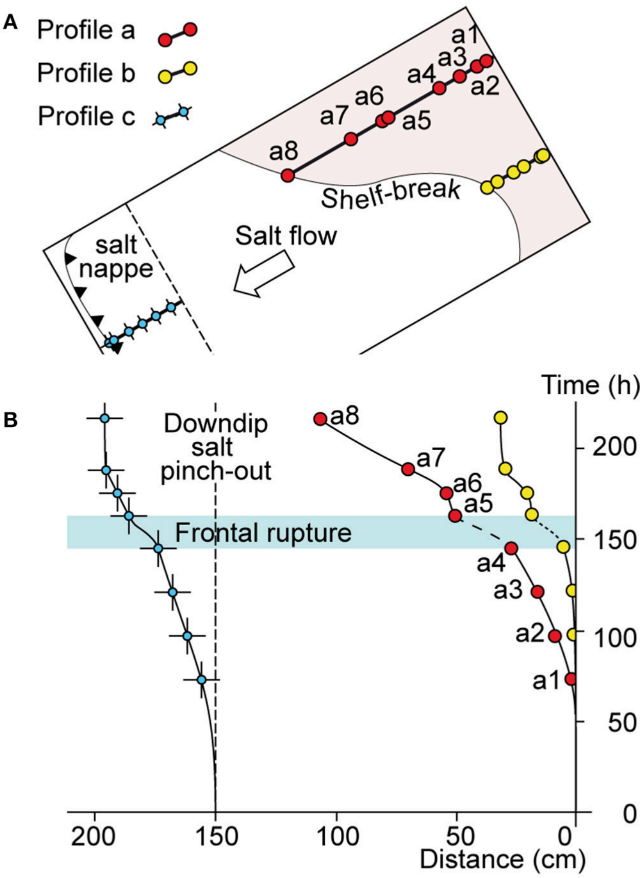

FIGURE 8 | Relation between shelf break migration along two profiles (red and yellow dots) and advance of the deforming system front (blue dots) in the model. **(A)** Model top view with location of profiles. **(B)** Shelf migration profiles and displacement of deforming system front.

DISCUSSION: COMPARISON BETWEEN MODEL AND NORTHERN GULF OF MEXICO

Whereas, the model presented above did not intend to directly model the northern Gulf of Mexico, several structural and kinematic features of the model are directly comparable to the tectonic evolution of the northern Gulf of Mexico. They can be summarized in three main points.

Transfer Zones in the Shelf as Markers of the Salt Flow Direction

As exemplified by the model and already mentioned in the previous section, transfer zones that develop during shelf growth are excellent markers of the salt flow direction that can be used for kinematic analysis in salt tectonics.

Fort and Brun (2012) interpreted the irregular contours of the depositional episodes mapped in the continental shelf of the northern GoM (Galloway et al., 2000) as a shelf break offset by transfer zones indicating a regional NE-SW trending direction of salt flow (**Figures 1**, **2**). This interpretation is supported by the similar NE-SW trend of the stretching directions deduced from the kinematic analysis of structures observed on the bathymetric map in the nearby slope and deep basin.

Frontal Rupture at Salt Basin Edge and Onset of Fast Shelf Growth

The model exemplifies that fast shelf growth started after frontal rupture and subsequent formation of a salt nappe close to the downdip salt pinchout (**Figures 5**, **7c**, **8**). With the release of salt flow at basin front, the whole salt basin became submitted to extension creating favorable conditions, through salt flow and thinning, to stabilize synkinematic sediments and shelf growth.

A very similar sequence of events occurred in the northern GoM. The onset of fast shelf break migration that occurred around the Oligocene-Miocene boundary (**Figure 3**) was contemporaneous to the formation of a salt nappe (in Keathley Canyon; KC in **Figure 2**) displacing toward the SW (Fort and Brun, 2012).

Interaction Between Sedimentation and Salt Flow

The model shows that the migration rate of the shelf break is a direct function of synkinematic sediment accumulation: faster in areas of thick sedimentation than in areas of thin sedimentation. As a direct consequence, the overall envelope of the shelf contour underwent a counterclockwise rotation from perpendicular to strongly oblique to the direction of salt flow at early stages toward perpendicular to the direction of sediment supply at late stages (**Figure 5**).

The step-by-step evolution of the shelf break migration in the GoM displays a comparable kinematic pattern (**Figure 3**). The overall envelope of the shelf contour that was trending WNW-ESE trend, strongly oblique to the mean NE-SW salt flow direction, at 12 Ma progressively rotated toward an EW trend, almost perpendicular to the direction of sediment supply at 3.1 Ma (**Figure 10**). In the GoM, like in the model and like in almost all salt tectonic systems, the gravity potential progressively reduced with time. But, at variance with the model, the flux of sediments in the GoM did not remain constant but even significantly increased since late Miocene-Pliocene (Galloway et al., 2000) increasing the effect of sediment supply in the observed rotation of the shelf break envelope.

In both model and GoM, even at late stages of shelf growth, the transfer zones are still controlled by the direction of salt flow. This indicates that in the GoM like in the model, even if the accumulation of sediments strongly influences the system response, the main driving force remains the salt flow.

Applicability to Other Salt Margins

It is the obliquity between trends of salt flow and sediment supply observed in the GoM (Fort and Brun, 2012) that motivated the experimental approach presented here. In other salt margins of our knowledge, salt flow and sediment supply are in general parallel or close to parallel as in salt margins of South Atlantic (e.g., Angola: Fort et al., 2004a; Hudec and Jackson, 2004; Brazil:

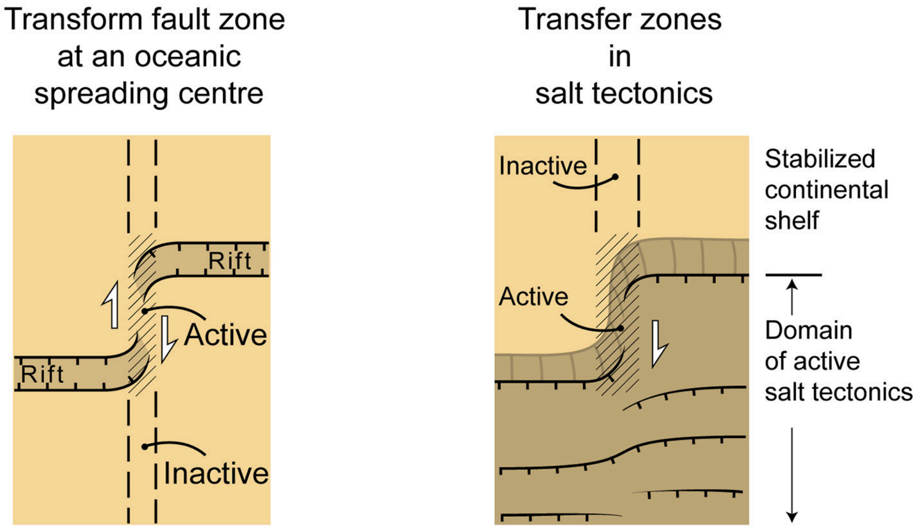

FIGURE 9 | Comparison between the offset (i) of an oceanic spreading ridge by a transform fault **(left)** and (ii) of a shelf break by a transfer zone in salt tectonics **(right)**.

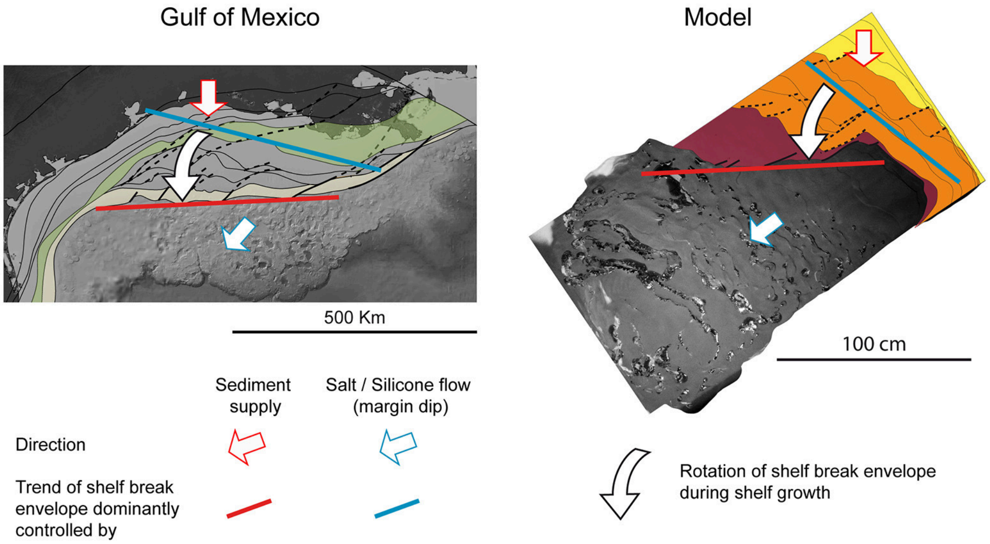

FIGURE 10 | Counterclockwise rotation of the shelf envelope in the Gulf of Mexico and in the model. The rotation results from the interaction between salt flow whose rate reduces with time and sediment supply whose rate is either constant (model) or increasing with time (Gulf of Mexico). Whereas, the role of salt flow decreases with time, transfer zones remain parallel to salt flow.

Mohriak et al., 2012; Kukla et al., 2018). In these margins, some geological features indicate significant amounts of shelf break migration controlled by salt tectonics but no specific study of shelf growth in relation with salt tectonics is available. The inner Kwanza basin of Angolan margin shows that the coastline displaced seaward of up to 130 km (see map of Figure 1, Hudec and Jackson, 2004) since middle Miocene (see cross-section restoration in Figures 9F–I, Hudec and Jackson, 2004) during an extreme thinning of the basal salt layer. Along the Brasil margin, cross sections (Figure 6 in Kukla et al., 2018) show that in the North, in the Espirito Santo Basin, the shelf break, whose location is controlled by a basement fault, has not migrated whereas southward, in the southern Campos Basin and central Santos Basin, the shelf break has migrated between 50 and 100 km.

Even if salt flow and sediment supply are parallel, it cannot be excluded that in such margins transfer zones could develop during shelf migration due lateral variations in the rock pile like, for example, variations of salt thickness along margin strike that can be responsible for lateral differences in rates of salt flow. But this remains to be documented.

To our knowledge the dynamics of shelf growth in salt basins has never been considered to bring an additional understanding of salt tectonics. The GoM as well as the above lines of evidence suggest that it could be extremely informative to systematically carry out an analysis of shelf growth in salt margins as it provides a fine recording of the history of salt basin dynamics.

CONCLUSIONS

Laboratory modeling of shelf growth at a salt margin and comparison with the northern Gulf of Mexico leads to the following conclusions:

1. In a basin affected by salt tectonics, the growth of a continental shelf is controlled by salt layer thinning that strongly reduces with ongoing basin updip extension and can even stop further salt flow.
2. The shelf break corresponds to a normal fault or a series of normal faults trending perpendicular to the direction of salt flow. It separates an updip domain in which salt has stopped flowing, or that still flows but at very low strain rates, from a downdip domain of active salt tectonics. The migration of a shelf break records the overall downdip flow of salt at basin scale.
3. In salt tectonic systems, in which the direction of sediment supply is oblique to the salt flow direction, the shelf break is offset by transfer zones parallel or close to parallel to salt flow. Therefore, transfer zones that participated to the shaping of a continental shelf provide a precious tool to map the direction of salt flow and its variations in space and time.
4. During long-term growth of a continental shelf, in a basin where sediment supply is oblique to salt flow, the overall shelf envelope undergoes a rotation from almost perpendicular to the direction of salt flow at early stages toward perpendicular to the direction of sediment supply at late stages. This rotation occurs because with time (i) the potential of gravity driven salt tectonics decreases (i.e., salt flow) and (ii) the sediment supply either remains constant or increases. However, even at late stages of shelf growth, transfer zones are still controlled by the direction of salt flow. In other words, whereas the accumulation of sediments strongly influences the system response, salt flow remains the dominant driving force.

From a general point of view, it is worth emphasizing that both model experiment and natural system, studied in this work, exemplify for the first time that continental shelves developing at salt margins provide a fine recording of basin-scale salt tectonics events, in terms of timing and bulk kinematics.

AUTHOR CONTRIBUTIONS

J-PB and XF conceived the modeling procedure and ran the experiments, discussed the results, and shared the writing of the paper.

FUNDING

This work has been carried out in the frame of a consulting contract between g.o. logical consulting and Equinor (previously Statoil).

ACKNOWLEDGMENTS

We are extremely grateful to Equinor (previously Statoil) for support throughout the years, freedom of action, access to data and positive interactions with numerous people in Houston and Oslo. We address our special thanks to R. Hunsdale and E. Blanc for numerous discussions and help at various stages of this work. Great thanks to the two reviewers Luis E. Lara and Frank Strozyk whose remarks and suggestions help improve the paper.

REFERENCES

Adam, J., Ge, Z., and Sanchez, M. (2012). Post-rift salt tectonic evolution and key control factors of the Jequitinhonha deepwater fold belt, central Brazil passive margin: insights from scaled physical experiments. *Mar. Petrol. Geol.* 37, 70–100. doi: 10.1016/j.marpetgeo.2012.06.008

Berggren, W. A., Kent, D. V., Swisher, C. C., and Aubry, M. P. (1995). "A revised Cenozoic geochronology and chronostratigraphy," in *Geochronology, Time Scales and Global Stratigraphic Correlation*, eds W. A. Berggren, D. V. Kent, M. P. Aubry, and J. Hardenbol (Tulsa, OK: Society for Sedimentary Geology, Special Publications), 129–212.

Brun, J. P. (1999). Narrow rifts versus wide rifts: inferences for the mechanics of rifting from laboratory experiments. *Philos. Transact. R. Soc.* 357, 695–712. doi: 10.1098/rsta.1999.0349

Brun, J. P., and Fort, X. (2011). Salt tectonics at passive margins: geology versus models. *Mar. Petrol. Geol.* 28, 1123–1145. doi: 10.1016/j.marpetgeo.2011.03.004

Carvajal, C., Steel, R. J., and Petter, A. (2009). Sediment supply: the main driver of shelf margin growth. *Earth Sci. Rev.* 96, 221–248. doi: 10.1016/j.earscirev.2009.06.008

Dokka, R. K., Sella, G. F., and Dixon, T. H. (2006). Tectonic control of subsidence and southward displacement of southeast Louisiana with respect to stable North America. *Geophys. Res. Lett.* 33:L23308. doi: 10.1029/2006GL027250

Dooley, T. P., Jackson, M. P. A., and Hudec, M. R. (2007). Initiation and growth of salt-based thrust belts on passive margins: results from physical models. *Basin Res.* 19, 165–177. doi: 10.1111/j.1365-2117.2007.00317.x

Engelkemeir, R., Khan, S. D., and Burke, K. (2010). Surface deformation in Houston, Texas using GPS. *Tectonophysics* 490, 47–54. doi: 10.1016/j.tecto.2010.04.016

Fort, X., and Brun, J. P. (2012). "Kinematics of regional salt flow in the northern Gulf of Mexico," in *Salt Tectonics, Sediments and Prospectivity*, eds G. I. Alsop, S. G. Archer, A. J. Hartley, N. T. Grant, and R. Hodgkinson (London: Geological Society; Special Publication), 265–287. doi: 10.1144/SP363.12

Fort, X., Brun, J. P., and Chauvel, F. (2004a). Salt tectonics on the Angolan margin, synsedimentary deformation processes. *Bull. Amer. Assoc. Petrol. Geol.* 88, 1523–1544. doi: 10.1306/06010403012

Fort, X., Brun, J. P., and Chauvel, F. (2004b). Contraction induced by block rotation above salt. *Mar. Petrol. Geol.* 21, 1281–1294. doi: 10.1016/j.marpetgeo.2004.09.006

Galloway, W. E. (2001). Cenozoic evolution of sediment accumulation in deltaic and shore-zone depositional systems, northern Gulf of Mexico Basin. *Mar. Petrol. Geol.* 18, 1031–1040. doi: 10.1016/S0264-8172(01)00045-9

Galloway, W. E., Ganey-Curry, P. E., Li, X., and Buffler, R. T. (2000). Cenozoic depositional history of the Gulf of Mexico basin. *Bull. Amer. Assoc. Petrol. Geol.* 84,1743–1774. doi: 10.1306/8626C37F-173B-11D7-8645000102C1865D

Helland-Hansen, W., Steel, R. J., and Sømme, T. O. (2012). Shelf genesis revisited. *J. Sediment. Res.* 82, 133–148. doi: 10.2110/jsr.2012.15

Hubbert, M. K. (1937). Theory of scale models as applied to the study of geologic structures. *Bull. Geol. Soc. Am*. 48, 1459–1520. doi: 10.1130/GSAB-48-1459

Hudec, M., and Jackson, M. P. A. (2004). Regional restoration across the Kwanza Basin, AngolaSalt tectonics triggered. *Bull. Amer. Assoc. Petrol. Geol.* 88, 971–990. doi: 10.1306/02050403061

Kukla, P. A., Strozyk, F., and Mohriak, W. U. (2018). South Atlantic salt basins–witnesses of complex passive margin evolution. *Gondwana Res.* 53, 41–57. doi: 10.1016/j.gr.2017.03.012

Lymer, G., Vendeville, B. C., Gaullier, V., Chanier, F., and Gaillard, M. (2018). Using salt tectonic structures as proxies to reveal post-rift crustal tectonics: the example of the Eastern Sardinian margin (Western Tyrrhenian Sea). *Mar. Petrol. Geol.* 96, 214–231. doi: 10.1016/j.marpetgeo.2018.05.037

Mauduit, T., Guerin, G., Brun, J. P., and Lecanu, H. (1997). Raft tectonics: the effects of basal slope value and sedimentation rate on progressive extension. *J. Struct. Geol.* 19, 1219–1230. doi: 10.1016/S0191-8141(97)00037-0

Mohriak, W. U., Szatmari, P., and Anjos, S. (2012). "Salt: geology and tectonics of selected Brazilian basins in their global context," in *Salt Tectonics, Sediments and Prospectivity,* Vol. 363, eds G. I. Alsop, S. G. Archer, A. J. Hartley, N. T. Grant, and R. Hodgkinson (London: Geological Society; Special Publication), 131–158. doi: 10.1144/SP363.7

Morgan, W. J. (1968). Rises, trenches, great faults, and crustal blocks. *J. Geophys. Res.* 73, 1959–1982. doi: 10.1029/JB073i006p01959

Posamentier, H. W., Jervey, M. T., and Vail, P. R. (1988). "Eustatic controls on clastic deposition: I, conceptual framework," in *Sea-Level Changes: An Integrated Approach*, eds C. K. Wilgus, B. S. Hastings, C. A. Ross, H. W. Posamentier, J. Van Wagoner, and C. G. St.C. (Kendall, FL: Special Publication), 109–124. doi: 10.2110/pec.88.01.0109

Ramberg, H. (1981). *Gravity, Deformation and the Earth's Crust*. London: Academic Press Inc.

Steckler, M. S., Mountain, G. S., Miller, K. G., and Christie-Blick, N. (1999). Reconstruction of tertiary progradation and clinoform development on the New Jersey passive margin by 2-D backstripping. *Mar. Geol.* 154, 399–420. doi:10.1016/S0025-3227(98)00126-1

Steel, R. J., Carvajal, C., Petter, A., and Uroza, C. (2008). "The growth of shelves and shelf margins," in *Recent Advances in Shallow-Marine Stratigraphy; Perspectives and Applications*, eds G. J. Hampson, R. J. Steel, P. M. Burgess, and R. W. Dalrymple (Tulsa, OK: SEPM, Special Publication), 47–71.

Swift, D. J. P., and Thorne, J. A. (1991). "Sedimentation on continental margins l: a general model for shelf sedimentation," in *Shelf Sand and Sandstone Bodies*, eds D. J. P. Swift, G. F. Oertel, R. W. Tillman, and J. A. Thorne (Oxford: International Association of Sedimentologists; Special Publication), 199–219.

Weijermars, R., Jackson, M. P. A., and Vendeville, B. (1993). Rheological and tectonic modeling of salt provinces. *Tectonophysics* 217, 143–174. doi: 10.1016/0040-1951(93)90208-2

Wilson, J. T. (1965). A new class of faults and their bearing on continental drift. *Nature* 207:343, 343–347

Conflict of Interest Statement: The authors declare that the research was conducted in the absence of any commercial or financial relationships that could be construed as a potential conflict of interest.

frontiers in Earth Science

ORIGINAL RESEARCH
published: 27 November 2018
doi: 10.3389/feart.2018.00204

Initiation of Subduction Along Oceanic Transform Faults: Insights From Three-Dimensional Analog Modeling Experiments

David Boutelier and David Beckett*

School of Environmental and Life sciences, University of Newcastle, Newcastle, NSW, Australia

Three-dimensional analog experiments are employed to explore how self-sustaining subduction may initiate along an oceanic transform fault. The models include a realistic spatial distribution of plate thickness, strength, and buoyancy of the lithosphere near an oceanic transform fault characteristic of the spreading rate. Convergence is imposed across the transform fault and strain in the model lithosphere is quantified using a surface Particle Imaging Velocimetry system. A force sensor is employed to defined when a self-sustaining subduction regime is generated. Cylindrical experiments reveal that subduction polarity is controlled by the buoyancy gradient and the strengths of the plates. With no inclined weak zones, imposed orthogonal compression results in the nucleation of a new fault in the weakest plate leading to the young and positively buoyant plate subducting. However, with an inclined weak zone, the buoyancy contrast controls subduction polarity with the most negatively buoyant plate subducting and a self-sustaining subduction regime obtained after ~300 km of imposed shortening. This situation is obtained when including an inverted triangular weak zone on top of the transform fault associated with the serpentinization of the crust and mantle. In non-cylindrical experiments, taking into account the change along strike of plate strength and buoyancy, the capacity of the transform fault to generate a self-sustaining subduction regime is greatly reduced. Subduction initiates simultaneously with opposite polarity at the two extremities of the transform segment and, at depth, a lithospheric tear is produced that separates the two subducting slabs. In the center of the transform fault, the lack of buoyancy or strength contrast between the two plates leads to multiple thrusts with variable polarities, overlapping each other, and each accommodating too little shortening to become the new plate boundary. This indicates that additional mechanical work is required in the center of the transform fault which prevents the establishment of a self-sustaining subduction regime.

Keywords: analog modeling, subduction, subduction initiation, oceanic fault, serpentinization, buoyancy, lithosphere

Edited by:
Mélody Philippon,
UMR5243 Géosciences Montpellier,
France

Reviewed by:
Diane Arcay,
Centre National de la Recherche
Scientifique (CNRS), France
Andres Folguera,
Universidad de Buenos Aires,
Argentina

***Correspondence:**
David Boutelier
david.boutelier@newcastle.edu.au
orcid.org/0000-0002-9383-4156

Specialty section:
This article was submitted to
Structural Geology and Tectonics,
a section of the journal
Frontiers in Earth Science

Received: *14 June 2018*
Accepted: *30 October 2018*
Published: *27 November 2018*

Citation:
Boutelier D and Beckett D (2018)
Initiation of Subduction Along Oceanic
Transform Faults: Insights From
Three-Dimensional Analog Modeling
Experiments. Front. Earth Sci. 6:204.
doi: 10.3389/feart.2018.00204

1. INTRODUCTION

Subduction initiation is a fundamental component of the plate tectonic theory, yet how subduction starts remains controversial (e.g., Stern, 2002, 2004; Gerya, 2011a,b, and references therein).

The gravitational instability of the oceanic lithosphere is generally thought to be the main driving force of subduction (e.g., Vlaar and Wortel, 1976). Due to surface cooling, the oceanic lithosphere becomes denser than the underlying asthenospheric mantle some 10–50 Ma after its formation at a mid-ocean ridge (Oxburgh and Parmentier, 1977; Cloos, 1993; Afonso et al., 2007). Because continental passive margins contain the oldest and thus presumably the most gravitationally unstable seafloor, they were first proposed as preferred sites of spontaneous subduction initiation (Dewey, 1969; Karig, 1982). However, despite the abundance of active and passive margins, no conclusive evidence for a transition from passive to active have been identified. This lack of evidence for initiation of subduction at a passive margin is explained by the fact that the bending and shear strength of the lithosphere, particularly where it is old and thick, is generally thought to be too high to permit spontaneous subduction initiation (Mueller and Phillips, 1991; Regenauer-Lieb et al., 2001; Mart et al., 2005; Nikolaeva et al., 2010).

Oceanic transform faults and fracture zones have then been proposed as alternative sites for spontaneous subduction nucleation because they are thought to be mechanically much weaker than passive margins and the large buoyancy gradient across these faults because of the difference in the age of the lithosphere, was thought to facilitate foundering (e.g., Stern, 2002, 2004). However, even across weak oceanic transform faults, the strength of the lithosphere has been shown to be still too large to permit spontaneous collapse (Mueller and Phillips, 1991; Toth and Gurnis, 1998). Self-sustaining subduction, defined as subduction driven by the negative buoyancy of the sinking lithosphere, may however be achieved if at least ∼100 to 150 km of convergence can be imposed on an oceanic fracture zone with sufficient buoyancy gradient across the fault (Hall et al., 2003; Gurnis et al., 2004). This is because a minimum length of negatively buoyant lithosphere must be subducted in order to generate sufficient downward slab pull force to overcome the shear strength of the fault zone and the bending resistance of the lithosphere. These interesting results however did not take into account the fact that the age of the lithosphere and therefore its strength and buoyancy not only varies across the oceanic fault zone, but also along the strike of the fault since many oceanic transform fault link segments of spreading ridges.

Here we investigate using three-dimensional analog models how the spatial distribution of strength and buoyancy along and across an oceanic transform fault zone affects the polarity of subduction and whether self-sustaining subduction can be obtained. We designed three-dimensional analog experiments in which two oceanic lithospheric plates are separated by a weak transform fault and convergence is imposed in the horizontal direction perpendicular to the strike of the fault. The spatial distribution of plate thickness and buoyancy are varied along and across the strike of the transform fault, and whether self-sustaining subduction is obtained is assessed using a force sensor.

2. BUOYANCY DISTRIBUTION

The lithospheric plate thickness can be estimated from the age of seafloor (Müller et al., 1997, 2008) using the half-space cooling equation (Turcotte and Schubert, 1982):

$$\frac{T - T_0}{T_m - T_0} = erf\left(\frac{z}{2\sqrt{\kappa t}}\right) \tag{1}$$

where T is the temperature at depth z and time t, T_0 is the surface temperature, T_m is the temperature of the mantle, and κ is the thermal diffusivity.

Using the temperature at the base of the lithosphere, this equation yields the thickness of the plate $z_l \simeq \sqrt{\kappa t}$ where z_l is the depth of the base of the lithosphere (m). With $\kappa = 1 \times 10^{-6}$ $\mathrm{m^2\,s^{-1}}$, a simple relationship between plate thickness H (km) and age A (Ma) can be obtained:

$$H \simeq 10\sqrt{A} \tag{2}$$

Assuming an oceanic crust with thickness $H_c = 7\,\mathrm{km}$ and density $\rho_c = 2,800\,\mathrm{kg\,m^{-3}}$, a mantle lithosphere of variable thickness with density $\rho_l = 3,330\,\mathrm{kg\,m^{-3}}$, a sub-lithospheric mantle with density $\rho_l = 3,250\,\mathrm{kg\,m^{-3}}$, the average density ($\bar{\rho}_p$) and dimensionless relative buoyancy (b) of the lithospheric plate can then be calculated:

$$\bar{\rho}_p = \frac{\rho_c H_c + \rho_l (H - H_c)}{H}. \tag{3}$$

and

$$b = \frac{\rho_a - \bar{\rho}_p}{\rho_a} \times 100. \tag{4}$$

with ρ_a the density of the underlying mantle (asthenosphere). Since we are interested in the spatial distribution of thickness and buoyancy along and across oceanic transform faults for the purpose of informing the design of three-dimensional analog models, we calculated average density and buoyancy profiles along and across transform fault zones linking fast or slow spreading ridges (**Figure 1**).

The maps demonstrate that, regardless of the spreading rate, a buoyancy gradient do exist across the oceanic transform fault when considering plate segments in the vicinity of the boundary ($< 100\,\mathrm{km}$). The profiles (**Figure 2**) reveal that on one side of the transform fault the buoyancy is positive, indicating that the plate is more buoyant than the underlying mantle, while on the other side of the transform fault the buoyancy of the lithosphere is negative, the plate is less buoyant than the underlaying mantle. The maps (**Figure 1**) and profiles (**Figure 2**) also demonstrate that the sign of the gradient, indicating on which side the negatively buoyant and positively buoyant plates are, changes along the strike of the transform. For example along the transform segment of the plate boundary separating the Africa and Antarctica plates, the most negatively buoyant lithosphere is on the Africa side of the transform near the northern end of the transform segment. However the most negatively buoyant plate is on the Antarctica side near the southern end the same transform

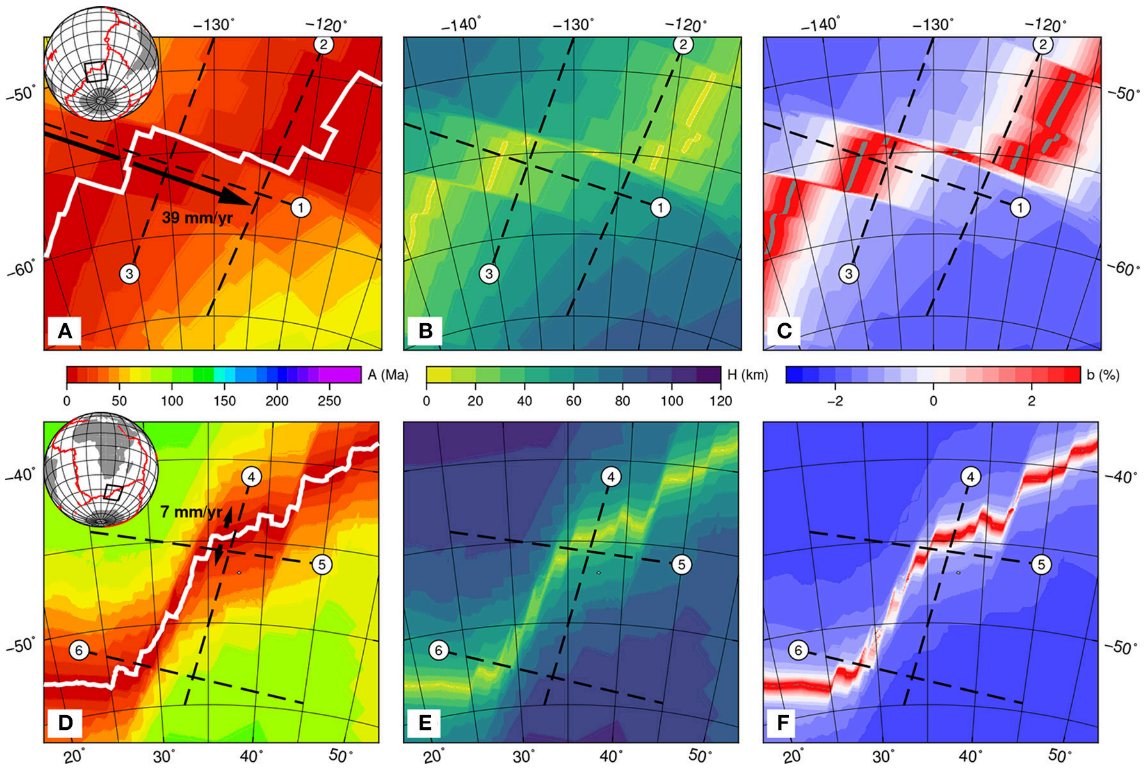

FIGURE 1 | Maps of seafloor age (Müller et al., 1997, 2008), plate thickness and buoyancy relative to underlying mantle for fast spreading ridge separating the Pacific and Antarctic plates **(A–C)**, or slow spreading ridge separating the Africa and Antarctic plates **(C,E,F)**. Half spreading rates from GSRM (Kreemer et al., 2003, 2014). Points labeled 1–6 refer to profiles in **Figure 2**. Plate thickness and relative buoyancy are calculated using the half-space cooling model and the simple plate structure discussed in the text.

segment. A similar reversal of the sign of the buoyancy gradient is observed for the transform segment linking the fast spreading ridges separating the Pacific and Antarctica plates.

Furthermore, with faster spreading the plates are significantly younger on both side of the transform fault. Because the rate of plate cooling and thickening reduces with the plate age, the thickness, and buoyancy differences associated with small age differences across the fast transform are amplified. The difference in buoyancy across the fault is more important for a fast spreading ($\sim 2\%$ for the fast segment vs. $\sim 0.5 - 1.0\%$ for the slow segment).

If one assumes that the polarity of a subduction zone initiated along a transform fault is a function of the buoyancy gradient, one should expect that subduction initiates with opposite polarity at the two extremities of each transform segment. How would these hypothetical subduction zones connect and how this affects the establishment of a self-sustaining subduction remain open questions.

3. MODEL SET-UP

3.1. General Modeling Scheme

We employ a simplified kinematic framework whereby the effect of the shear traction caused by the drag of the asthenosphere on the lithosphere (Funiciello et al., 2003a,b; Royden and Husson, 2006) is replaced by a piston that imposes a constant-rate convergence (Boutelier and Oncken, 2011).

An important characteristic of the large strain deformation of the lithosphere is its ability to produce and maintain lithospheric-scale shear zone. In the brittle layers of the lithosphere strain localization is well described by a Mohr-Coulomb rheology. However, strain localization also occurs in the ductile regime, and may be promoted by strain softening mechanisms such as dynamic recrystallization and development of crystallographic preferred orientations (e.g., Hansen et al., 2012a,b; Montési, 2013), and/or shear heating (e.g., Poirier, 1980; Montési, 2002; Regenauer-Lieb et al., 2008). However, the softening functions associated with these mechanisms are still debated (Rutter, 1999; De Bresser et al., 2001; Montési and Hirth, 2003; Oncken et al., 2012). In our model lithosphere, an equivalent strain localization process is employed using specially designed ductile strain-softening elasto-plastic materials (Boutelier and Oncken, 2011). The materials are composed of various quantities of paraffin wax, vaseline, and paraffin oil held together with a highly branched alpha-olefin polymer. The density is adjusted with the addition of a clay powder, which binds with the oil-based matrix via a water-in-oil surfactant (phosphatidylcholine). The compositions of the materials employed in this study are provided in **Table 1**.

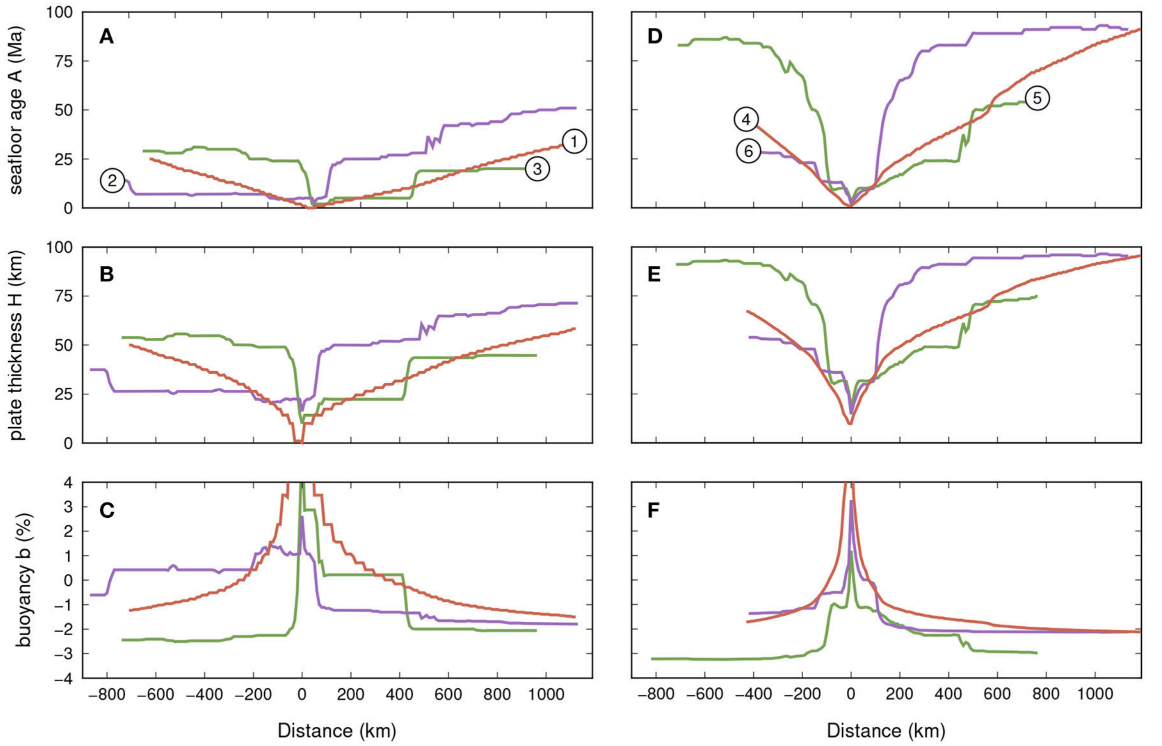

FIGURE 2 | Profiles of seafloor age, plate thickness, and plate buoyancy relative to the underlying mantle for the examples of the fast spreading ridge **(A–C)** and slow spreading ridge **(D–F)**. The numbers in white circles are the points plotted in **Figure 1** to locate the end of the profile.

TABLE 1 | Compositions of the employed analog materials (weight %).

Ingredient	*C*	M_1	M_2
Paraffin wax	8.37	6.30	6.44
Microcrystalline wax	1.99	1.50	1.53
Alpha-olefin polymer	5.58	4.07	4.15
Vaseline	42.03	31.20	32.21
Mineral oil	42.03	31.20	32.21
Clay powder	0	25.30	23.0
Phosphatidylcholine	0	0.35	0.32

C is crustal analog, M_1 and M_2 and employed for the lithospheric mantle.

TABLE 2 | Parameter values employed in the models, corresponding values in Nature, and scaling factors.

Parameter	Model	Nature	Scaling factor
Lithosphere thickness, H_l (m)	$0.5 - 2.5 \times 10^{-2}$	$17.5 - 87.5 \times 10^{-3}$	2.86×10^{-7}
Crust thickness, H_C (m)	2.0×10^{-3}	7.0×10^{3}	2.86×10^{-7}
Upper mantle thickness, H_m (m)	1.9×10^{-2}	6.6×10^{5}	2.86×10^{-7}
Lithosphere density, ρ_l (kg m^{-3})	1,030	3,347	3.08×10^{-1}
Upper mantle density, ρ_m (kg m^{-3})	1,000	3,250	3.08×10^{-1}
Lithosphere plastic strength, σ_l (Pa)	25	250×10^{6}	8.79×10^{-8}
Lithosphere thermal diffusivity, κ (m^2 s^{-1})	2.8×10^{-8}	1×10^{-6}	2.8×10^{-2}
Convergence rate, V (m s^{-1})	8.7×10^{-5}	8.87×10^{-10}	9.8×10^{4}
Time, t (s)	92	3.15×10^{13}	2.9×10^{-13}

3.2. Scaling

We adopt a length scaling factor $L^* = L_m/L_n = 2.86 \times 10^{-7}$ (subscript m and n refer to model and nature respectively) that means that 1 cm in the model represents 35 km in nature. The scaling factor for densities is $\rho^* = 3.08 \times 10^{-1}$ and 1,000 kg m^{-3} represents 3,250 kg m^{-3}. Hydrostatic pressure, $\rho g z$, where depth z scales with length, sets the scaling factor for stress σ^* (Buckingham, 1914). Since the experiments are carried out under normal gravitational acceleration (i.e., $g^* = 1$ and $g_m = g_n = 9.81$ m.s^{-2}), $\sigma^* = \rho^* \times L^* = 8.79 \times 10^{-8}$. Consequently, a flow stress of 10 MPa at the bottom of the lithosphere is 0.879 Pa in the model, while a flow stress of 500 MPa in the stronger parts of the lithosphere corresponds to 43.95 Pa in the model. Since strength decreases with depth within each layer because of the imposed temperature gradient, we use the strength averaged over the layer thickness for scaling of stress (see **Table 2**).

The time scale factor is chosen in order to scale the relative temperature variations associated with deformation (Chemenda et al., 2000; Boutelier et al., 2002). The imposed velocity controls the advection of heat in the model. In order to maintain the balance between advection and diffusion of heat, the dimensionless ratio VL/κ (i.e., Peclet number) must be the same in the model and nature, where V is the convergence velocity and κ is the thermal diffusivity. Time is then simply defined in a kinematic sense using the dimensionless ratio Vt/L. Our hydrocarbon compounds have a thermal diffusivity of $2.8 \times 10^{-8}\,\mathrm{m^2\,s^{-1}}$ (Boutelier and Oncken, 2011). Assuming that rocks have a thermal diffusivity of $1 \times 10^{-6}\,\mathrm{m^2\,s^{-1}}$ (Turcotte and Schubert, 1982), $\kappa^* = 2.8 \times 10^{-2}$ and $V^* = \kappa^*/L^* = 9.8 \times 10^4$. This scaling factor means that a natural subduction velocity of $2.8\,\mathrm{cm\,yr^{-1}}$ (i.e., $8.87 \times 10^{-10}\,\mathrm{m\,s^{-1}}$) is $8.7 \times 10^{-5}\,\mathrm{m\,s^{-1}}$ in the model. The scaling factor for time is $t^* = L^*/V^* = 2.92 \times 10^{-12}$, which means that 1 Ma in nature (i.e., 3.15×10^{13} s) is 92 s in the model. The parameter values adopted for the experiments, scaled to nature and the scaling factors are listed in **Table 2**.

3.3. Model Setup

The model includes two lithospheric plates resting on a low-viscosity asthenosphere (**Figure 3**). Both plates are made of temperature-sensitive elasto-plastic materials with strain softening described above and are subjected to a constant vertical

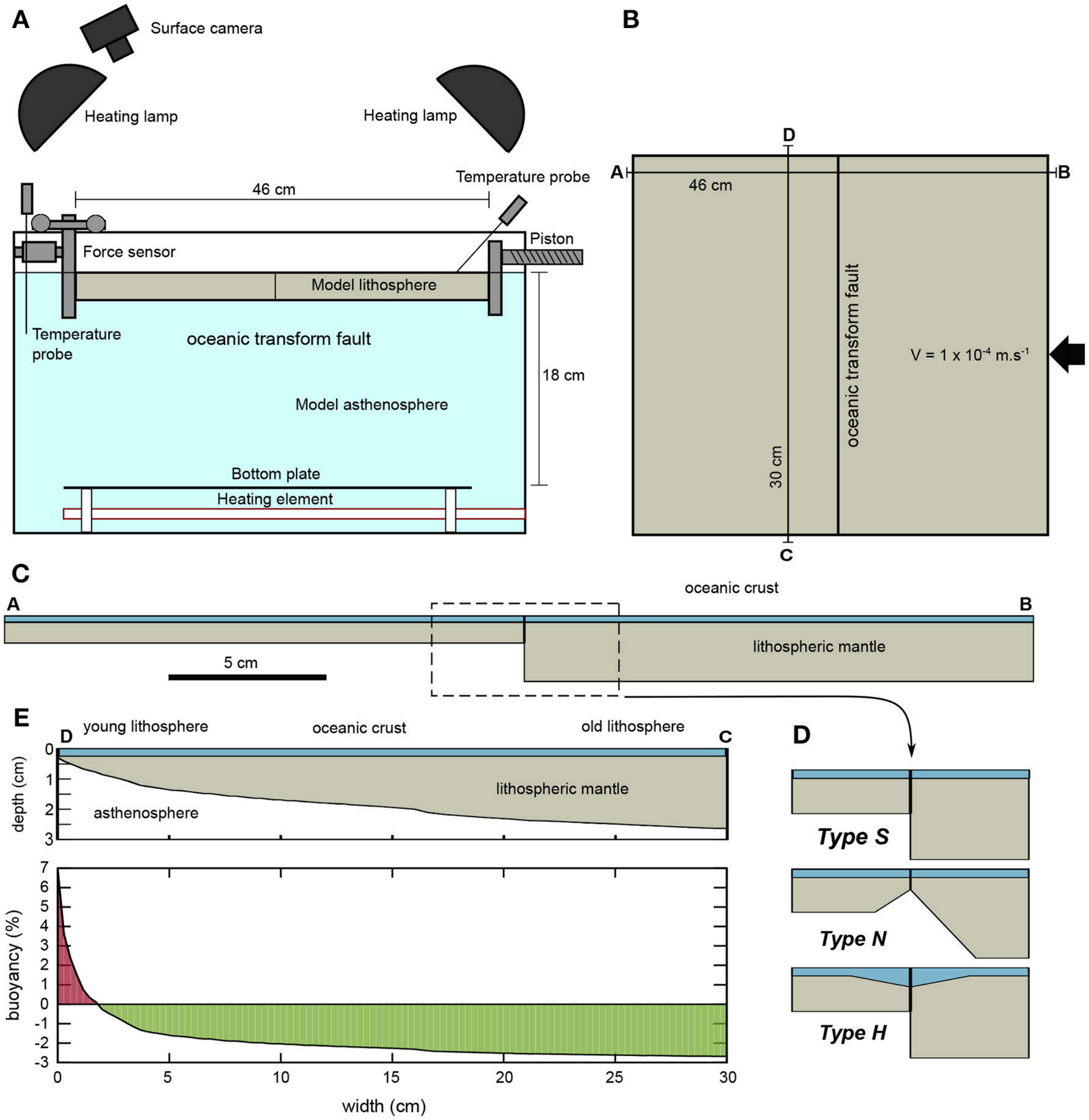

FIGURE 3 | Sketches of the model setup. **(A)** vertical cross-section of the experimental apparatus. **(B)** map view of the model. The two plates are separated by a vertical cut representing the oceanic transform fault. **(C)** vertical cross-section of the model lithosphere perpendicular to the transform fault near the edges of the model. One plate is young and thin whereas the other is old and thick. **(E)** vertical cross-section parallel to the transform fault. The age of the plate and its thickness vary along strike. The thickness of the oceanic crust remains constant, it is the lithospheric mantle thickness which changes, leading to the appropriate spatial distribution of buoyancy. **(D)** the transform fault may be or three different types. Type-S: the transform is a straight vertical cut. Type-N: the transform has a notch, the lithospheric thickness is locally reduced under the fault. Type-H: the crust is hydrothermally altered around the fault zone leading to a triangular zone of weak, low-density serpentinite.

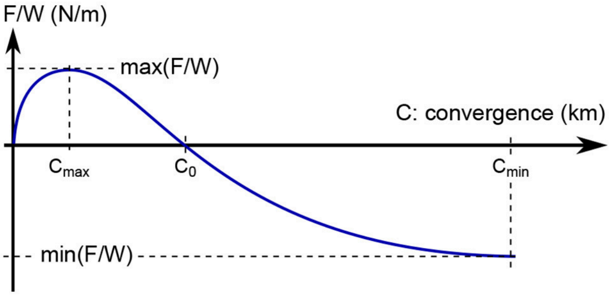

FIGURE 4 | Sketch of the parameters characterizing the force evolution in the experiments, reported in **Table 4**.

thermal gradient resulting in a reduction of strength with depth (Boutelier and Oncken, 2011).

Four infrared emitters equipped with large diffusers are placed above the four corners of the experimental tank and are oriented toward the center of the model surface. The duration of the heat pulses generated by the infrared emitters is calculated by a thermo-regulator that receives a reading of the surface temperature T_s from a thermal probe (**Figure 3A**). Thermal imaging has demonstrated that this configuration provides a surface temperature field that is relatively constant (±0.1°C) in time and homogeneous (±0.2°C) in space (Boutelier and Oncken, 2011). Furthermore the infrared emitters do not produce any visible light and the cameras monitoring the model deformation do not detect the emitted infrared waves. The light required to obtain sufficiently contrasted images of the model surface for Particle Imaging Velocimetry processing (Adam et al., 2005; Boutelier, 2016) is produced by 5 W LEDs, which do not contribute to the surface heating. The temperature of the sub-lithospheric mantle (T_a) is maintained and controlled using an electrical heating element at the bottom of the experimental tank, a thermal probe and a second thermo-regulator.

The model includes two plates separated by a transform fault zone, which at it simplest is a vertical cut (**Figures 3B–D**). The spatial distribution of buoyancy is modeled using two layers for the oceanic lithosphere (**Figure 3E**). The oceanic crust is 2 mm (equivalent to 7 km in nature) and 870 $\mathrm{kg\,m^{-3}}$, while the lithospheric mantle underneath is of variable thickness and has density of either 1,030 or 1,040 $\mathrm{kg\,m^{-3}}$. The mature oceanic lithosphere is 2 to 3 cm-thick (70–100 km) and its average density is thus 1,019–1,029 $\mathrm{kg\,m^{-3}}$. Its buoyancy relative to the underlaying mantle is thus −1.9 to −2.9% (Cloos, 1993). However, a young oceanic lithosphere with a thickness of only 1 cm (35 km) has an average density of 998 to 1,006 $\mathrm{kg\,m^{-3}}$ and the buoyancy relative to the underlaying mantle is +0.2 to −0.6%. Younger lithosphere, closer to the spreading ridge is even thinner and more positively buoyant (**Figure 3E**). This setup thus allows varying simulatenously the bending strength and negative buoyancy of the plate as a function of its thickness which in nature is a function of the age (**Figure 3E**). In addition the use of two lithospheric mantle materials with nearly identical composition (see **Table 1**) allows us to vary independently the plate strength, buoyancy, and thickness, although in nature both plate strength and buoyancy are linked to plate thickness and age. Rheological tests indicate that the two mantle materials have statistically indistinguishable plastic strengths, but a significant density difference of 10 $\mathrm{kg\,m^{-3}}$. This is because only the amount of clay powder was varied between the lithospheric mantle analog materials and the change was small (only 2%). This change has a significant impact on the density because density is mostly controlled by the relative amount of clay with respect to all other ingredients combined, while the strength is more impacted by the relative amounts of the waxes, oil, and polymers.

Two series of experiments are presented. In the first series, the models are cylindrical. A thickness and buoyancy gradient is implemented across the transform fault zone, but it does not vary along the strike of the fault. This series was design to test the validity of the assumption that subduction polarity can be estimated from the sign of the buoyancy gradient. In the second series, the buoyancy gradient changes along and across the transform fault.

3.4. Particle Imaging Velocimetry

Precise spatio-temporal strain monitoring is obtained using the Particle Imaging Velocimetry (PIV) technique, a non-intrusive method for accurate measurement of instantaneous velocity fields using digital image correlation (Adam et al., 2005; Boutelier, 2016). We employ a PIV system equipped with a 36-megapixel DSLR camera enabling spatial resolution of the displacement of <0.1 mm with a temporal resolution of 10 s. The surface views of the model are precisely corrected and calibrated using a checkerboard pattern on a calibration board with 900 control points distributed across the image space. The corrected views are further enhanced before correlation. The background value is removed using a gaussian filter and the intensities of the particles placed at the surface of the model are normalized. The FFT (Fast Fourier Transform) algorithm is used to transform the sub-areas of two successive images into the frequency domain (Smith, 1999). Multiplying the real and imaginary parts of the first image with the real and imaginary parts of the second image generates the real and imaginary parts of the correlation map in the frequency domain. The Inverse FFT completes the operation and yields the correlation map in the spatial domain, where the value of each pixel is the measure of how well the two images match when shifted by the coordinates of the point. The sub-pixel position of the correlation peak is measured by fitting a gaussian curve (Nobach and Honkanen, 2005). A multipass approach with progressively decreasing interrogation window size, and window deformation is employed to yield dense vector fields together with sub-pixel precision on displacement vectors (Adam et al., 2005; Boutelier, 2016). The produced vector field are filtered out using minimum and maximum values of the velocity components, maximum standard deviation for each velocity component as well as a universal outlier (Westerweel and Scarano, 2005). Discarded vectors are interpolated using a diffusion/Laplacian model solved using a finite difference scheme with boundary values (Boutelier, 2016).

The velocity field obtained from PIV makes the computation of horizontal strain-rate components ($E_{xx}/\Delta t$, $E_{yy}/\Delta t$, $E_{xy}/\Delta t$) straightforward. E_{ij} is the incremental strain component (with i, j being x or y coordinate vectors), defined as the gradient of the i component of the vector displacement D in the direction j (i.e., $E_{ij} = \Delta D_i/\Delta j$). Δt is the time increment between correlated images. The topography generated in the models is generally below 2 mm while the top camera is placed 100 cm above the model surface, therefore topography does not interfere significantly with the calculation of horizontal strain using a simple 2D PIV technique (Adam et al., 2005; Boutelier, 2016).

4. RESULTS

23 experiments have been performed varying multiple parameters (**Table 3**). Here we detail 4 representative experiments and summarize the insights from the other experiments. **Table 4** provides a quantification of the force evolution in each experiment. The parameters employed for this quantification are illustrated in **Figure 4**, and scaled-up values are provided in **Table 4** for comparison with previous work.

4.1. Cylindrical Models

In the first series of experiments, the buoyancy of the plates varies across the transform fault but not along its strike. This series investigate how the difference in thickness and buoyancy across the fault determines the polarity of the subduction when convergence is imposed perpendicular to the fault.

4.1.1. Experiment 11

On the right hand side of the transform fault, the lithospheric plate is 20 mm thick and the average density is 1,015 kg m^{-3}. The relative buoyancy to the underlaying mantle is therefore −1.5%. On the other side of the transform fault, the lithospheric plate is 15 mm and the average density is 1,009 kg m^{-3}. The relative buoyancy to the underlaying mantle is therefore −0.9%. Shortening is accommodated by two oppositely dipping fault zones nucleating from the base of the pre-existing vertical cut representing the transform fault (**Figure 5A**). Shortening was also accommodated in a third fault zone near the trailing edge of the thin plate (**Figures 5B,C**). From the begining of the experiment, the fault dipping toward the thick plate accomodated more shortening than its conjugate. At about 400 s most of the imposed shortening is accomodated in a single thrust resulting in

TABLE 3 | List of experiments.

Exp.	H_1	ρ_1	S_1	H_2	ρ_2	S_2	T_s-T_a	TF	ΔH	Outcome
1	25	1,040	M_1	10	1,040	M_1	38–41	S	none	P2 subducts at fault. P1 subducts at piston
2	20	1,040	M_1	20	1,015	M_2	38–41	S	none	P1 and P2 subduct at both walls, not self-sustaining
3	20	1,040	M_1	20	1,015	M_2	38–41	S	b +1 cm	P2 subducts at wall, not self-sustaining
4	20	1,040	M_1	10	1,015	M_2	38–41	S	b +1 cm	P2 subducts, not self-sustaining
5	10	1,013	C/M_2	20	1,040	M_1	38–41	N	b +1 cm	P2 folded
6	15	1,025	C/M_1	15	996	C/M_2	38-41	N	none	Plate 2 underplated, no self-sustaining subduction
7	15	1,031	M_1	15	1,010	M_2	38–41	N	t: 15–20	P2 subducts, not self-sustaining
8	15	1,031	M_1	15	1,010	M_2	38–41	N	t: 15–20	P2 subducts, not self-sustaining
9	15	1,009	C/M_1	15	1,009	C/M_1	38–41	N	none	Thrusts with opposing polarity, not self-sustaining
10	13	1,012	C/M_1	17	1,012	C/M_1	38–41	N	none	Thrusts with opposing polarity, not self-sustaining
11	15	1,009	C/M_1	20	1,015	C/M_1	39–42	N	none	P1 subducts, no self-sustaining subduction
12	15	1,009	C/M_1	20	1,015	C/M_1	39-42	N	none	P1 subducts, no self-sustaining subduction
13	15	1,031	M_1	15	1,010	M_2	39-42	N	t: 15–20	P2 underplated, no self-sustaining s
14	20	1,015	C/M_1	12	1,004	C/M_1	39–42	-	none	P1 subducts, self-sustaining.
15	10	999	C/M_1	20	1,015	C/M_1	39–42	H+N	t (P1): 10–20	P2 subducts, self-sustaining.
16	15	1,009	C/M_1	12	1,004	C/M_1	39-42	H+N	none	Thrusts with opposing polarity, not self-sustaining
17	27	1,019	C/M_1	10	999	C/M_1	39-42	H+N	none	P2 subducts, not self-sustaining
18	30	1,020	C/M_1	10	999	C/M_1	39-42	H	t (P2): 10-20	P1 subducts, self-sustaining.
19	30–5	1,020–967	C/M_1	5–30	967–1,020	C/M_1	39–42	H	none	Thrusts with opposing polarity, not self-sustaining
20	30-5	1,020–967	C/M_1	5–30	967–1,020	C/M_1	39-42	H	none	Thrusts with opposing polarity, not self-sustaining
21	30–5	1,020–967	C/M_1	5–30	967–1,020	C/M_1	39–42	H	b	Thrusts with opposing polarity, not self-sustaining
22	30-5	1,020–967	C/M_1	5-30	967–1,020	C/M_1	39–42	H	b	Thrusts with opposing polarity, not self-sustaining
23	30-5	1,020–967	C/M_1	5–30	967–1,020	C/M_1	39–42	H	b	Thrusts with opposing polarity, not self-sustaining

*H_1 and H_2 are the thicknesses of plates 1 and 2 respectively (in mm). ρ_1 and ρ_2 are the average densities of plates 1 and 2 (in kg m^{-3}). Plate 1 (P1) is on the left-hand side on photographs of the models, while plate 2 (P2) is on the right hand side. Plate 2 is pushed at constant rate by the piston. T_s and T_a are the imposed temperatures at the surface and in the asthenosphere. S, N and H denote the geometry of the transform fault in vertical cross section (see **Figure 3**). ΔH denotes across strike plate thickness variation. b (bolster) indicates that the model edge in contact with the moving piston and back wall has been locally thickened . t (taper) indicates a linear thickness increase over the length of the plate from a minima value near the transform fault to maximum value near the trailing edge. S_1 and S_2 are keys refering to the structure of plate 1 and 2. C indictates crust, M_1 and M_2 indicate the two compositions employed for the lithospheric mantle.*

TABLE 4 | Force measured in experiments.

Exp.	max(F/W) $(\mathrm{N\,m^{-1}})$		c_{max} (m)		min(F/W) $(\mathrm{N\,m^{-1}})$		c_{min} (m)		c_0 (m)	
	m	**n**	**m**	**n**	**m**	**n**	**m**	**n**	**m**	**n**
1	6.75×10^{-1}	2.69×10^{13}	1.08×10^{-1}	3.78×10^{5}	5.00×10^{-1}	1.99×10^{13}	1.28×10^{-1}	4.48×10^{5}	–	–
2	7.50×10^{-1}	2.99×10^{13}	6.80×10^{-2}	2.38×10^{5}	-6.75×10^{-1}	-2.69×10^{13}	1.55×10^{-1}	5.43×10^{5}	1.47×10^{-1}	5.15×10^{5}
3	2.12×10^{0}	8.47×10^{13}	6.40×10^{-2}	2.24×10^{5}	1.25×10^{-1}	4.98×10^{12}	1.90×10^{-1}	6.64×10^{5}	–	–
4	1.05×10^{0}	4.18×10^{13}	1.00×10^{-2}	3.50×10^{4}	5.00×10^{-1}	1.99×10^{13}	1.16×10^{-1}	4.06×10^{5}	–	–
5	–	–	–	–	–	–	–	–	–	–
6	1.00×10^{0}	3.98×10^{13}	1.00×10^{-1}	3.50×10^{5}	5.50×10^{-1}	2.19×10^{13}	1.40×10^{-1}	4.90×10^{5}	–	–
7	7.00×10^{-1}	2.79×10^{13}	1.52×10^{-2}	5.31×10^{4}	2.50×10^{-1}	9.96×10^{12}	1.48×10^{-1}	5.17×10^{5}	–	–
8	7.00×10^{-1}	2.79×10^{13}	5.20×10^{-2}	1.82×10^{5}	3.25×10^{-1}	1.29×10^{13}	2.00×10^{-1}	6.99×10^{5}	–	–
9	6.50×10^{-1}	2.59×10^{13}	2.80×10^{-2}	9.79×10^{4}	2.00×10^{-1}	7.97×10^{12}	1.40×10^{-1}	4.90×10^{5}	–	–
10	1.05×10^{0}	4.18×10^{13}	1.20×10^{-1}	4.20×10^{5}	9.25×10^{-1}	3.69×10^{13}	1.48×10^{-1}	5.17×10^{5}	–	–
11	2.75×10^{-1}	1.10×10^{13}	4.60×10^{-2}	1.61×10^{5}	1.00×10^{-1}	3.98×10^{12}	1.92×10^{-1}	6.71×10^{5}	–	–
12	6.25×10^{-1}	2.49×10^{13}	6.80×10^{-2}	2.38×10^{5}	4.25×10^{-1}	1.69×10^{13}	1.28×10^{-1}	4.48×10^{5}	–	–
13	8.50×10^{-1}	3.39×10^{13}	1.76×10^{-1}	6.15×10^{5}	8.50×10^{-1}	3.39×10^{13}	1.76×10^{-1}	6.15×10^{5}	–	–
14	1.50×10^{-1}	5.98×10^{12}	4.00×10^{-2}	1.40×10^{5}	-1.37×10^{-1}	-5.48×10^{12}	2.00×10^{-1}	6.99×10^{5}	9.60×10^{-2}	3.36×10^{5}
15	2.12×10^{-1}	8.47×10^{12}	4.00×10^{-2}	1.40×10^{5}	-2.00×10^{-1}	-7.97×10^{12}	1.60×10^{-1}	5.59×10^{5}	7.60×10^{-2}	2.66×10^{5}
16	5.25×10^{-1}	2.09×10^{13}	1.24×10^{-1}	4.34×10^{5}	3.25×10^{-1}	1.29×10^{13}	2.00×10^{-1}	6.99×10^{5}	–	–
17	4.50×10^{-1}	1.79×10^{13}	7.20×10^{-2}	2.52×10^{5}	3.25×10^{-1}	1.29×10^{13}	1.56×10^{-1}	5.45×10^{5}	–	–
18	2.50×10^{-1}	9.96×10^{12}	3.20×10^{-2}	1.12×10^{5}	0.00×10^{0}	0.00×10^{00}	1.00×10^{-1}	3.50×10^{5}	1.00×10^{-1}	3.50×10^{5}
19	6.25×10^{-1}	2.49×10^{13}	6.00×10^{-2}	2.10×10^{5}	5.50×10^{-1}	2.19×10^{13}	1.44×10^{-1}	5.03×10^{5}	–	–
20	3.75×10^{-1}	1.49×10^{13}	4.80×10^{-2}	1.68×10^{5}	1.25×10^{-1}	4.98×10^{12}	8.00×10^{-2}	2.80×10^{5}	–	–
21	2.87×10^{-1}	1.15×10^{13}	6.00×10^{-2}	2.10×10^{5}	8.75×10^{-2}	3.49×10^{12}	1.44×10^{-1}	5.03×10^{5}	–	–
22	1.05×10^{0}	4.18×10^{13}	5.20×10^{-2}	1.82×10^{5}	7.50×10^{-1}	2.99×10^{13}	1.16×10^{-1}	4.06×10^{5}	–	–
23	5.50×10^{-1}	2.19×10^{13}	8.80×10^{-2}	3.08×10^{5}	4.50×10^{-1}	1.79×10^{13}	1.12×10^{-1}	3.92×10^{5}	–	–

min(F/W) and max(F/W) are the minimum and maximum horizontal force measured by the sensor and divided by the model width respectively. c_{max} and c_{min} are the amount of convergence at the maximum and minimum force respectively. c_0 is the amount of convergence for which the force becomes zero. This parameter is measured only after the peak force. m indicates values from the model, while n indicates scaled up values (nature). In experiment 5 a technical failure prevented the force data to be recorded.

the subduction of the thin, less negatively buoyant plate under the thick, more negatively buoyant plate (**Figures 5D,E**). The record of the horizontal force shows a positive (compressional) and increasing value until about 600 s. The force value remained at the peak (11×10^{-2} N) until ∼1,000 s then steadily decreased until the end of the experiment but remained positive (**Figure 5F**).

4.1.2. Experiment 14

This model includes not two but three plates separated by inclined, rounded, and lubricated fault zones. The model is designed to test the polarity of subduction when convergence does not require the formation of new inclined thrust faults but can employ pre-existing weak zones. Two oceanic lithospheric plates with different thicknesses and buoyancies are placed with the third plate in between which includes two oppositely dipping, lubricated, round cuts. The right-hand plate is 12 mm thick and its density is 1,004 $\mathrm{kg\,m^{-3}}$ (i.e., $b = -0.4\%$), while the left-hand plate is 20 mm thick and its density is 1,015 $\mathrm{kg\,m^{-3}}$ (i.e., $b = -1.5\%$). The center plate is up to 15 mm thick in the center but tapers owing to two curved weak zones. The curvature radius of the weak zones is 7-cm as in previous subduction experiments performed by Boutelier and Cruden (2016). The density of the center plate is 1,004 $\mathrm{kg\,m^{-3}}$. The center plate is 100 mm long and like all other plates 40 cm wide. Imposed convergence is initially accommodated in both inclined cuts (**Figures 6A,B**), but the fault allowing the subduction of the thicker and more negatively buoyant plate accommodates more shortening. At 700 s convergence becomes exclusively accommodated by the fault allowing the burial of the thicker plate (**Figures 6C–E**). At 500 s, the horizontal force reaches a peak value (6×10^{-2} N), and then decreases steadily until 1,500 s (**Figure 6F**). At about 1,200 s the recorded force becomes negative, indicating that the pull generated by the negative buoyancy of the subducted slab now overcomes the bending strength and shear along the plate boundary. Following Gurnis et al. (2004) we interpret this signature as subduction become self-sustaining, being driven by the negative buoyancy of the slab. At 1,500 s, the force goes back up to zero (**Figure 6F**), while the tip of the subducted slab touches the rigid plate simulating the high viscosity lower mantle. The force then decreases again, as the slab rolls over (Boutelier and Cruden, 2016).

4.1.3. Experiment 15

This experiment is similar to Experiment 14, but the two oppositely dipping weak zones are now collapsed into a small triangular zone sitting across and on top of the transform fault zone. This setup attempts to simulate the mechanical effect of hydrothermal alteration of the oceanic lithosphere

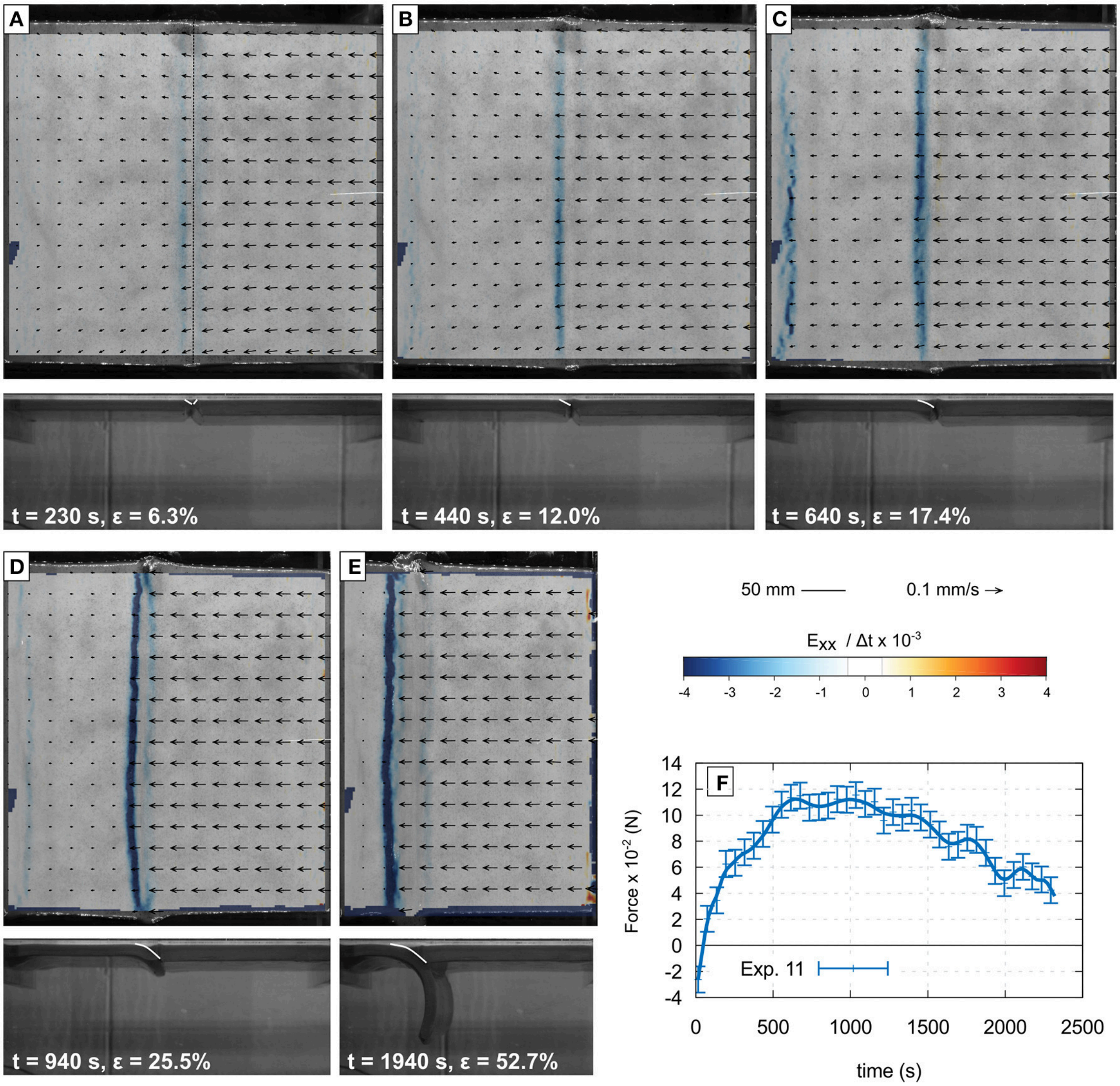

FIGURE 5 | Successive stages of Exp. 11. Panels **(A–E)** show the surface view of the deformed model with PIV vectors, and convergence-parallel horizontal shortening rate. Panel **(F)** shows the evolution of the force measured at the trailing edge of the plate on the left-hand side. Despite being more negatively buoyant, the thicker right-hand side plate becomes the overriding plate. White lines on side views delineate the active faults. ϵ is the bulk shortening.

around the fault zone. At the fault zone, fluids can percolate to some 10–15 km-depth causing deep mechanical weakening via serpentinization, whereas only 10–20 km away from the oceanic transform fault the maximum depth that alteration can reach decreases (Roland et al., 2010). We simplified this spatial distribution of hydrothermal alteration and employed two half triangles made of the oceanic crust material, separated from the rest of the plates by a weak inclined interface (i.e., lubricated with paraffin oil during the making of the model). The depth of the inverted triangle was 4 mm (equivalent 14 km), and the half width of the inverted triangle was 5 mm (equivalent to 17.5 km). While both plates have the same weak triangular zone atop the transform zone, the right-hand plate is 20 mm thick and its buoyancy is 1,015 kg m^{-3} (i.e., $b = -1.5\%$), while the left-hand plate is only 10 mm thick and its density is 999 kg m^{-3} (i.e., $b = +0.1\%$). Convergence is accommodated in the weak zones surrounding the transform fault, and rapidly a new fault propagate from the alteration triangle allowing the subduction of the thicker and more negatively buoyant lithosphere (**Figures 7A–E**). The peak force (8×10^{-2} N) is measured at 500 s, and decreases rapidly after to reach zero at 1,000 s. The force remains near zero until about 1,400 s, and then decreases rapidly again (**Figure 7F**).

4.1.4. Type-N Models

In theses experiments (Exp. 5–13) the lithosphere is thinned below the transform fault. The maps of the age of the

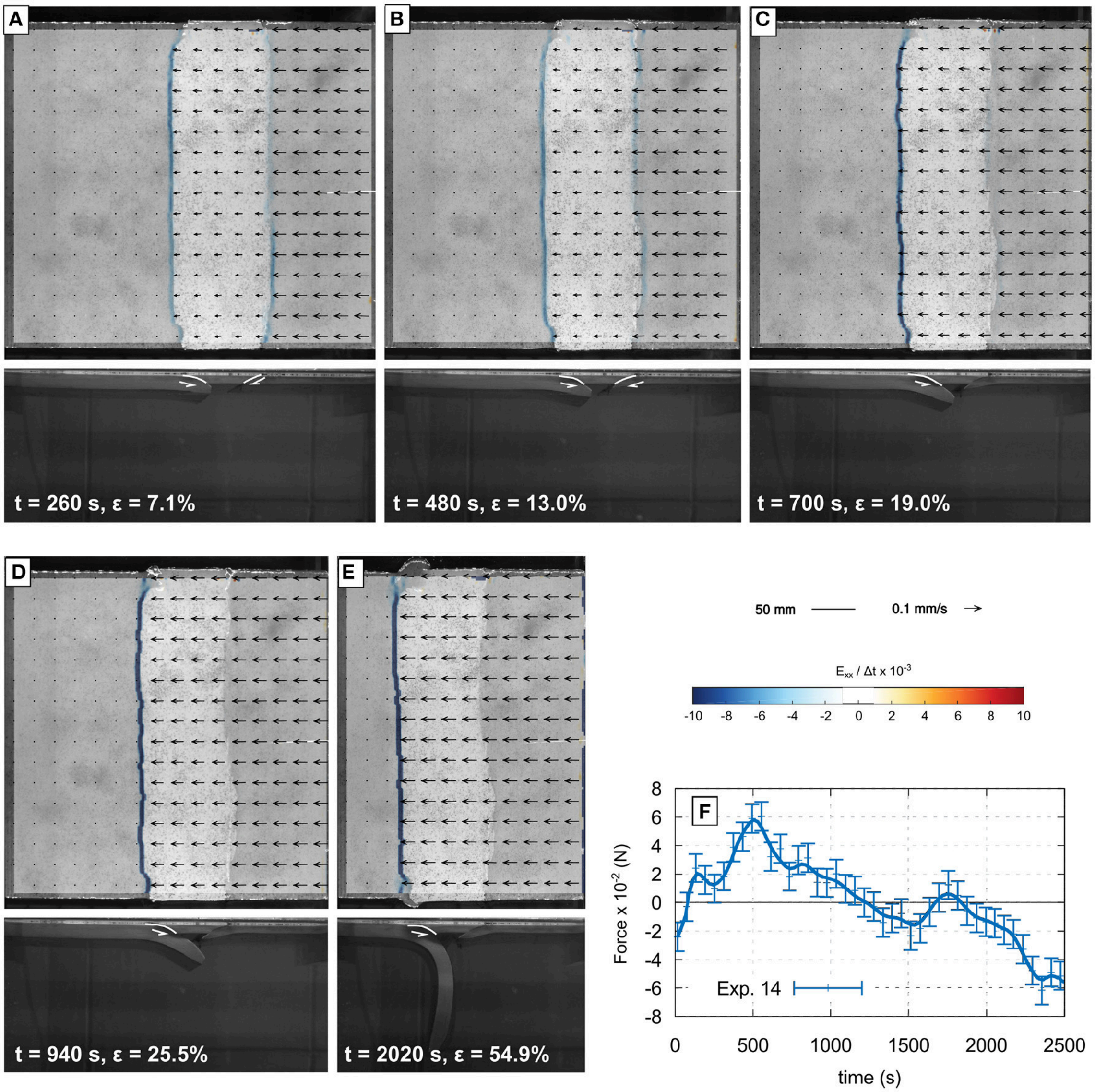

FIGURE 6 | Successive stages of Exp. 14. Panels **(A–E)** show the surface view of the deformed model with PIV vectors, and convergence-parallel horizontal shortening rate. Panel **(F)** shows the evolution of the force measured at the trailing edge of the plate on the left-hand side. This unique three-plates experiment shows that when weak inclined faults pre-exist, the thick and most negatively buoyant plate subducts.

seafloor show that the transform segment is not always perfectly perpendicular to the spreading segment. Therefore, some transform segments may actually be bounded by very young lithosphere near the transform fault. Accounting for this observation, we thinned the lithosphere and created a steep transition from very young at the plate boundary to much older a few ten km away from the fault (**Figure 3D**). In experiment 5 the plate thickness was 5 mm within a 1 cm wide notch with vertical sides. In all other experiments with a notch the plate thickness increased linearly away from the transform fault where the tickness was 5 mm. The sides of the notch were inclined at 60°. No other parameter of the notch structure were varied. The notch resulted in focusing the deformation into the transform fault and away from the trailing edges of both plates. In a number of experiments the thin plate failed first and often it failed near its trailing edge. The thinning of the mantle lithosphere below the transform prevented this undesired effect. However, around the transform faults, two oppositely dipping faults nucleated and the thinnest and weakest plate generally failed first thus becoming the lower plate. We therefore concluded that implementing a notch below the transform fault did not affect the polarity of subduction initiation but only focused deformation in the transform zone, and therefore away from the trailing edge. Another possibility to achieve the same outcome was to progressively increase the plate thickness away from the transform.

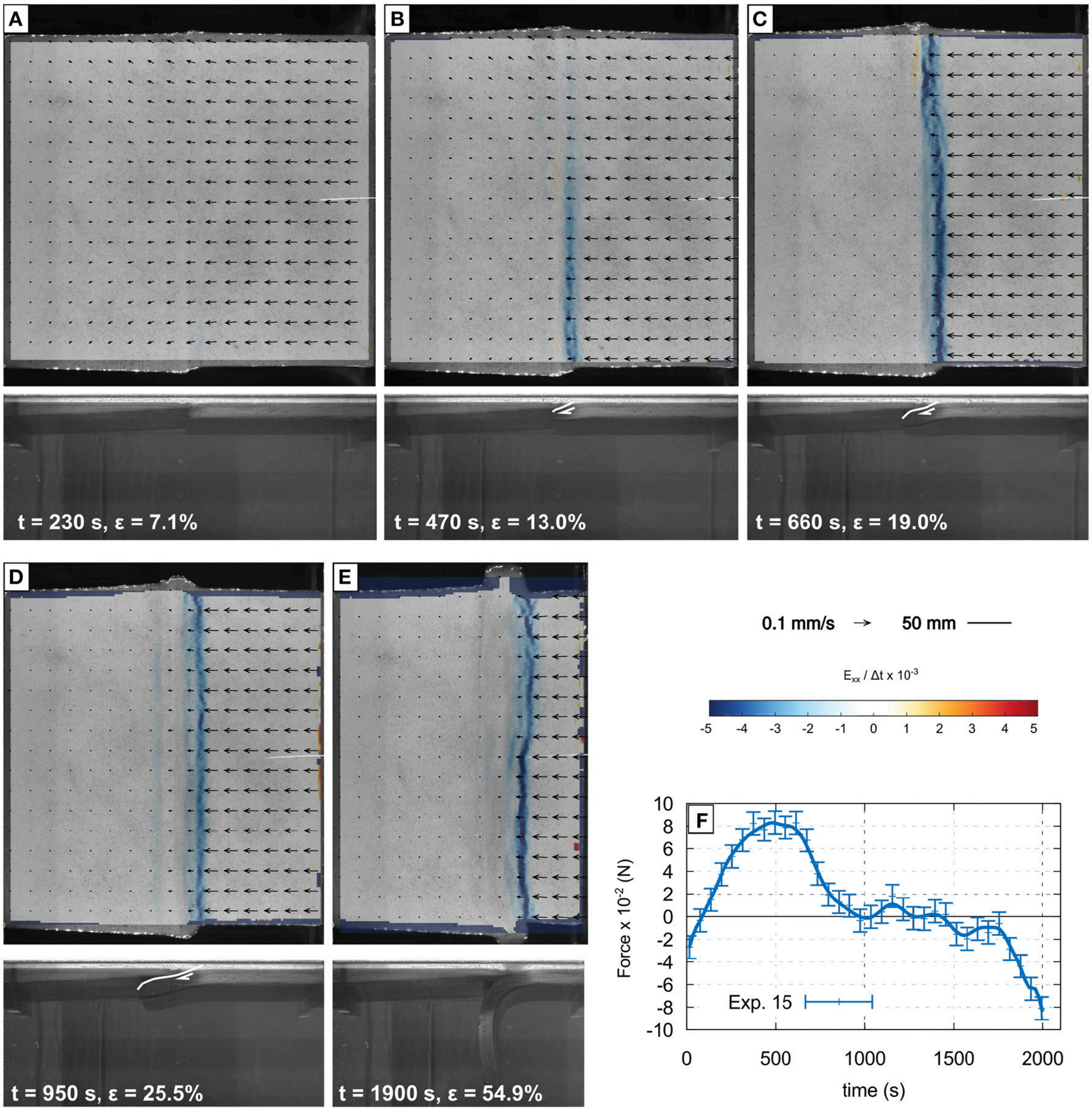

FIGURE 7 | Successive stages of Exp. 15. Panels **(A–E)** show the surface view of the deformed model with PIV vectors, and convergence-parallel horizontal shortening rate. Panel **(F)** shows the evolution of the force measured at the trailing edge of the plate on the left-hand side. Owing to the weak inverted triangle atop the transform fault, the control on the polarity of subduction exerted by plate strength is diminshed and the thick and most negatively buoyant plate becomes the subducting plate.

4.1.5. Surface Temperature

As the first experiments (Exp. 1–10) revealed that the thin plate, despite being positively buoyant, generally failed first and became the lower plate, we decreased the relative importance of the plate mechanical strength by increasing the surface temperature. This leads to an important reduction in strength, while maintaining buoyancy gradient across the boundary. However, the same outcome was systematically obtained: the thin plate breaks first and becomes the lower plate despite the buoyancy gradient. We concluded that the outcome of the experiments did not derive from excessive plate strength relative to buoyancy, but because of the strength difference between the thin and thick plates. Adding a weak oceanic crust layer at the model surface provided a more realistic strength profile, but did not change the situation.

4.1.6. Type-H Models

These models are similar to detailed Experiment 15 (**Figure 7**). An inverted triangle of oceanic crust is implemented on top of the transform zone simulating the hydrothermal alteration of crust and mantle causing mechanical weakening which extended further away from the faut zone near the surface than at depth. With inclined weak zones, the relative strength of the thin or thick plates did not matter as much since both are equally weak along the inverted triangular zone. Therefore the strength control over subduction polarity is lessened and it is the thick plate which becomes the lower plate because it is more negatively buoyant. We note that the triangular zone only affect the formation of the inclined thrust, not the bending of the plate itself. Therefore our results suggest that it is not the plate bending strength which controlled the polarity in experiments without the inclined weak zones, but the plastic shear strength which must be overcome to generate a new thrust.

4.2. Non-cylindrical Models

The non-cylindrical models include a plate thickness and buoyancy variation in the horizontal direction parallel to the transform fault (**Figure 3**). The thickness and buoyancy variations are mirrored across the fault such that the buoyancy contrast across the fault changes sign along the fault.

The experiment was reproduced four times with similar parameters and obtained slightly different behaviors. However, the recorded horizontal force is systematically higher than obtained in cylindrical models at the same stage and the force did not become negative, indicating that self-sustaining subduction regime was not obtained.

In all non-cylindrical experiments, imposed convergence produced two oppositely dipping thrusts at the ends of the transform fault, where the relative buoyancy contrast was largest (**Figure 8**). The thrusts initiated near the edges of the model and propagated laterally along the transform fault toward the model interior. The thrusts then connected near the middle of the model width via a tear.

Experiment 21 (**Figure 8**) had a third thrust initiated near the center of the model width but further away from the transform fault than the two thrusts formed near the model edges. As the three thrust faults propagated laterally the central fault overlapped and then connected with the side thrust with the same polarity. This created a long thrust fault accross most of the model width. However, it never resulted in a single structure accomodating all the convergence as obtained in the cylindrical models, but a network of faults accomodating the shortening, and causing block rotation and distributed horizontal shear (**Figure 8**). Although Exp. 21 provided the lowest horizontal force of all the non-cylindrical experiments, the measured force never became negative. The collapse of the model associated with the retreat of one of the thrust (**Figure 8e**) does indicate that the subducted slab is locally generating a large downward pull and driving retreat. However, near the center of the model, subduction is not yet self-sustaining and several thrusts with the same polarity are active, indicating that there is a large compressional horizontal stress.

The non-cylindrical experiments generally display several thrust faults accomodating shortening near the center of the model. In Experiment 21 these thrusts are dipping in the same direction but in the others, the thrusts are dipping in opposite direction, facing the former transform fault. Only near the edges of the model, is the shortening generally accommodated by a single thrust achieving sufficient cumulated shortening to produce a sufficiently long subducted slab to generate a significant downward pull.

5. DISCUSSION

5.1. Polarity of Subduction

Our scaled analog experiments demonstrate that in the absence of a suitably oriented weak zone, induced subduction initiation at a transform fault by orthogonal convergence at constant rate requires the nucleation of a new thrust near the transform fault. This indicates that the transform fault zone could be preserved and former transform fault zone could be in the forearc basement of induced subduction zones. This possibility of paleo transform fault parallel to the trench in the forearc domain might constitute a major weak zone if the convergence in the subduction zone later becomes oblique. Such feature could localize strain partitioning in the forearc instead of the arc during the formation of a sliver such as in Sumatra-Java (Beck, 1991; Cochran, 2010; Haq and Davis, 2010; Lallemand, 2014).

Another important consequence of the mentionned-above experimental observations is that without a suitably oriented weak zone, plastic failure and the nucleation of the new plate boundary systematically occurs in the weakest plate, which is the younger and thinner plate. Our experiments thus confirm the previous findings of Gurnis et al. (2004), that deformation concentrates within the young plate. In our cases this deformation led to the young and weak plate systematically becoming the lower plate. An inclined thrust initiates preferentially from the bottom of the transform fault through the thin plate, allowing the underthrusting of the thin plate. This prefered polarity is similar to previous shortening experiments of single layer (Boutelier and Oncken, 2011), and is due to the fact that the opposite polarity of a thrust through the thin plate would either build a large topographic high above the thick plate or require its bending downward or a combination of both (**Figure 9**). During incipient failure the plastic fault dipping toward the thick plate is thus favored because the opposite polarity requires additional mechanical work. When the thin plate is subducted, the monitored horizontal force in the plates never became negative, and therefore we conclude that the self-sustaining subduction regime was not achieved.

Experiments 6, 7, and 8 suggest that without a plate thickness variation, the less negatively buoyant plate subduct because of a strength contrast between the plates (**Table 3**). This strength difference could be due to the different compositions employed for the mantle lithosphere to cause a negative buoyancy difference. An increase in strength associated with an increase in density is indeed likely, as adding filler tends to increase both the density and the plastic strength. However rheological tests indicate that the two employed materials have indistinguishable plastic yield stresses. We therefore acknowledge a bias in the experimental results that may be associated with the low repetition number. The strength difference between the plates associated exclusively with plate thickness change is evident in experiments 11, 12, and 15–23, since the same materials were employed for both plates (see **Table 3**). Then, in the absence of a pre-existing inclined weak zone, deformation occured systematically in the thin plate because it is weaker, and led to its subduction underneath the thick plate. Without any possible strength difference between the plates, when the same

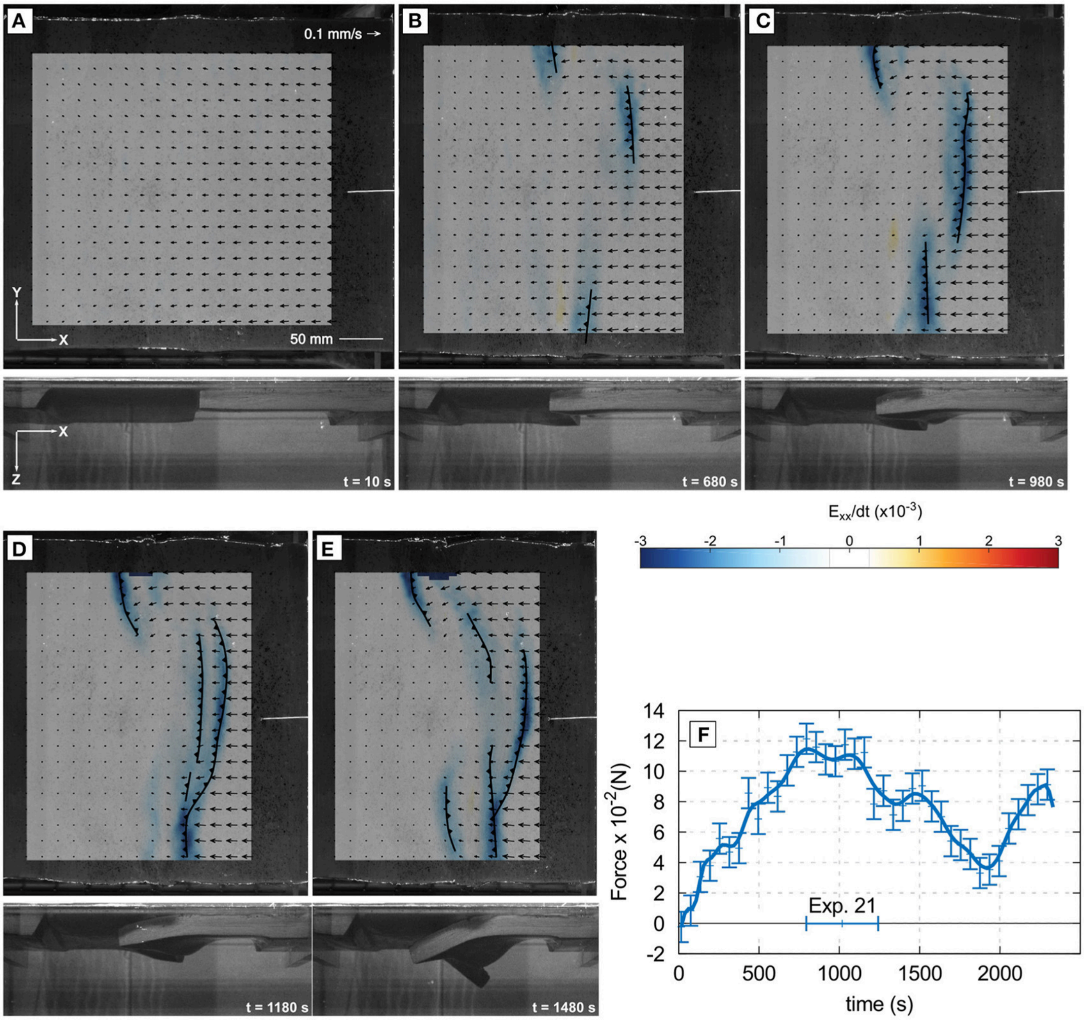

FIGURE 8 | Successive stages of Exp. 21. Panels **(A–E)** show the surface view of the deformed model with PIV vectors, and convergence-parallel horizontal shortening rate. Panel **(F)** shows the evolution of the force measured at the trailing edge of the plate on the left-hand side. The variation of plate thickness and buoyancy along teh strike of the transform fault resuslted in generation of multiple faults.

materials were employed for both plates and the same constant thickness was employed for both plates, many thrusts were formed simulatenously and self-sustaining subduction regime could not be achieved (e.g., exp. 9 and 16, **Tables 3, 4**).

Following Gurnis et al. (2004), we implemented pre-existing dipping weak zones to determine the polarity of the created thrust and also confirm that in this case the most negatively buoyant plate generally does become the lower plate despite also having the largest bending strength. We collapsed the weak zones into a narrow inverted triangle on top of the transform fault zone simulating the mechanical effect of hydrothermal alteration around the transform fault. Aqueous fluids penetrate the crust and the lithosphere around the transform fault, and the maximum depth which the fluid and therefore alteration reaction can reach decreases away from the transform fault. The hydrothermal alteration weakens the crust and mantle and therefore two weak zones may exist on either side of the transform that dip toward the fault. Our experiments show that this approximate spatial distribution of strength around the transform fault associated with hydrothermal alteration is sufficient to remove the need to create a new thrust through undeformed lithosphere material and therefore the polarity of subduction becomes primarily controlled by the buoyancy gradient across the transform fault. The fault dipping toward the thin plate (red in **Figure 10**) requires the bending of the thick plate but cuts through the hot and hence weak bottom part of the thin plate, while the fault dipping toward the thick plate requires cutting through the colder and stronger thicker plate. Our models indicate that both faults form at the surface of the model, but the fault dipping toward the thin plate rapidly becomes dominant and therefore must require the least mechanical work. This allows the thick negatively buoyant plate to subduct and the slab pull force to increase with time and shortening, eventually leading to self sustaining subduction in the case of cylindrical models.

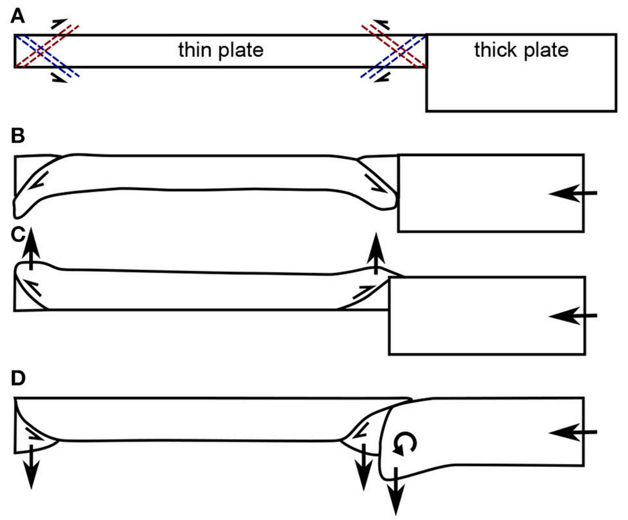

FIGURE 9 | Plastic failure initiation in the thin plate. **(A)** plastic failure may initiate simulatenously at both ends of the thin plate, and two conjugate thrusts may be formed originating from either the top or bottom of the plate end. **(B)** prefered polarity allows the subduction of the tin plate from both ends. Conjugate thrusts lead to build-up of topographic highs **(C)** and/or bending down of the thick plate **(D)**.

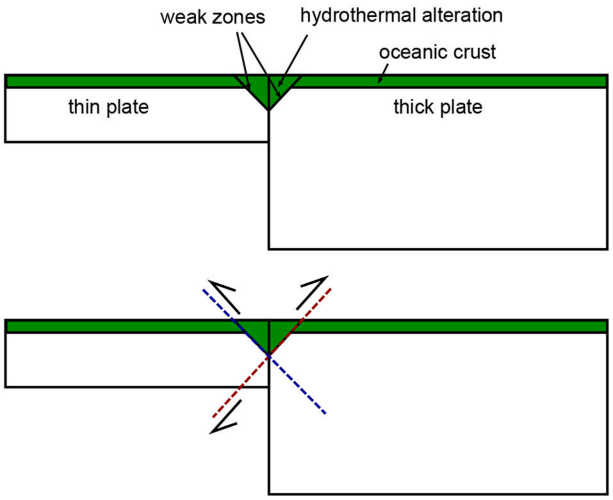

FIGURE 10 | Plastic failure initiation around hydrothermally altered transform fault. **Top**: simplified model structure around the transform fault. **Bottom**: two conjugate faults created along the pre-existing weak zones consitituting the limits of the hydrothermally altered crust and mantle.

5.2. Forced Initiation and Self-Sustaining Subduction

Like in previous numerical simulations by Gurnis et al. (2004), self-sustaining subduction, or subduction driven by the negative buoyancy of the subducted slab, has been obtained in our analog experiments after a critical amount of convergence is imposed (**Table 4**). The simulations of Gurnis et al. (2004) employed a visco-elasto-plastic rheological model of the lithosphere and viscous upper mantle that can not be reproduced in our analog setup. Instead we employed an elasto-plastic with strain softening rheology for the lithosphere and an inviscid asthenosphere. The rate-independant rheological model for the lithosphere in the analog experiments is required for the rate of advection associated with deformation to be scaled with the rate of heat diffusion via the Peclet number. The viscosity of the asthenosphere was shown to not be a controlling parameter of the investigated process in the simulations of Gurnis et al. (2004), but the parametrization of the ductile softening is important and poorly constrained. The convergence rate was shown to be an important factor for nucleation of self-sustaining subduction throughout an homogeneous plate by Gurnis et al. (2004). However, the differences between our models and the simulations by Gurnis et al. (2004) are not simply due to the rate since we have used rates equivalent to 2.8 cm/year while Gurnis et al. (2004) employed a similar convergence rate of 2.0 cm/year.

In several of our analog experiments the peak stress is reached after some $\sim$500 s and $\sim$4.25 cm of imposed convergence, which scales to $\sim$5.4 Ma and $\sim$150 km (**Table 4**) and fits very well with the previous results of Gurnis et al. (2004). The magnitude of the peak force in our cylindrical models is $\sim 1 \times 10^{-2}$ N, which gives $\sim 2.75 \times 10^{-2}\,\mathrm{N\,m^{-1}}$ and scales up to $\sim 1.1 \times 10^{12}\,\mathrm{N\,m^{-1}}$ (**Table 4**). This magnitude of the force per linear length of trench compares well with the previous values of Gurnis et al. (2004) ($\sim 2 - 4 \times 10^{12}\,\mathrm{N\,m^{-1}}$), but are significantly lower than the values obtained by Bonnardot et al. (2008), Hassani et al. (1997), or Martinod et al. (2016) (up to $\sim 2 \times 10^{13}\,\mathrm{N\,m^{-1}}$).

However, in our analog experiments, the compressive horizontal force in the model lithosphere did not decrease as rapidly as in some of the simulations of Gurnis et al. (2004), and therefore the force in the model did not become negative before some 1,000 s and 85 mm of imposed convergence which scales up to 10.8 Ma and 297 km (Exp. 15, **Figure 7**). Therefore we conclude that with our strain softening analog materials (see Boutelier and Cruden, 2016), self-sustaining subduction does not start with only 100 to 150 km of imposed convergence but requires at least $\sim$300 km.

A shorter minimal length of imposed shortening would be obtained for a more efficient softening mechanism in the lithosphere, or if the downward pull is enhanced. This could result from metamorphic reactions (eclogitization) causing the negative buoyancy of the subducted slab to increase (e.g., Doin and Henry, 2001) or flow in the mantle assisting the downward movement of the slab instead of resisting it (e.g., Boutelier and Cruden, 2008; Baes and Sobolev, 2017).

5.3. Buoyancy Gradient Along the Fault

Our experiments indicate that the buoyancy gradient along the transform fault causes the formation of at least two oppositely-dipping thrust faults at the ends of the transform segment. In several experiments the two thrusts propagated toward the model interior and connected via a tear of the subducted slabs at depth. Since both slabs are continuously subducted the tear must propagate in both directions at the same rate as convergence. At the model surface a broad area of shear and vertical axis rotation is observed between the subduction zones. This behavior was obtained for age differences of up to 25 Myr across the transform fault. If the age difference across the fault is larger, for example when the spreading rate was lower, the plate thickness difference may be larger but the buoyancy difference lower because the thickness and buoyancy change with age rapidly when the plate is young, slowly when the plate is old (**Figure 2**). It is therefore unclear whether large mega transform faults associated with protracted slow spreading such as observed in the central Atlantic or Indian ocean would facilitate subduction where the age difference is larger. However, regardless of the rate of spreading and associated spatial distribution of lithospheric plate ages, the across-strike buoyancy gradient must change sign along the strike of the transform fault. Therefore we suggest that the observed formation of two thrusts at the edges of the transform fault, with opposite polarities and propagating toward the center of the transform will occur regardless of the rate of spreading prior to the inversion of the trasnform. This is because the pattern of changing the sign of the buoyancy gradient across the fault exist regardless of the spreading rate and it is the controlling parameter leading to the formation of the two thrusts with opposite polarities.

In our non-cylindrical experiments the horizontal force measured at the trailing edge of the left-hand plate was generally higher than obtained in the cylindrical experiments and never became negative. The retreat of the trench in parts of the models, in particular near the edges, demonstrates that the slab locally pulls downward and therefore one would expect to measure a horizontal tension in the plates (Boutelier and Oncken, 2011; Boutelier and Cruden, 2013). However, in the center of the model where there is little thickness and buoyancy contrast between the two plates across the transform fault, several thrusts faults may be created and active, demonstrating that the system is in a strongly compressional stress state. As several thrusts are formed, each accomodates a fraction of the total convergence and none produce a sufficiently long subducted slab to generate a downward pull. The side views show two developping slabs and therefore at least one tear allowing these to lengthen. We postulate that the slab tear and the central compressional domain in the model prevent the model from becoming self-sustaining. Although the slab pull increases at the edges of the model, in the center the plate deformation including the tears require mechanical work and therefore external forcing to continue.

6. CONCLUDING REMARKS

We have modeled the most simple geometrical configuration for a transform fault zone to become a subduction zone. We have confirmed that in the absence of a suitably oriented weak zone, imposed convergence results in deformation of the thinner, younger plate. This deformation manifests itself in a inclined thrust initiated from the bottom of the transform fault through the thin plate, and allowing the underthrusting of the thin plate.

We have demonstrated that the buoyancy gradient and plate thickness or strength gradient across the fault associated with the age difference does control the polarity if a suitably oriented weak zone can be employed to thrust the young, thin and positively buoyant plate over the old, thick and negatively buoyant plate. We have shown that the buoyancy gradient across the fault appear to depend on the rate of spreading prior to inversion, but even with a significant buoyancy gradient, a weak zone is required.

Then we have demonstrated that the simple fact that the buoyancy gradient changes sign along the strike of the fault prevent the establishement of a self-sustaining subduction zone because two subduction zones with opposite polarity are created from both ends of the transform segment and a broad zone of lithospheric deformation, including several thrusts is formed in the center which resist spontaneous subduction. It appears that the idea of a transform fault zone becoming a major self-sustaining subduction zone is flawed because the three-dimensional nature of the object was not sufficiently taken into account. However, we must acknowledge that there are other geometrical characteristics of transform faults and subduction zones that must be investigated such as relative scale of the transform and spreading segments, as well as obliquity and diachronicity of convergence.

We conclude that subduction is more likely to be initiated at transform faults that do not link segments of a spreading ridge but separate a continental and oceanic plate or constitute the transform edge of a retreating back-arc basin. For example, the Hunter fault zone marks the south-eastern edge of the North-Fidji basin and formed because of the retreat of the New Hebrides subduction hinge (Charvis and Pelletier, 1989; Schellart et al., 2006; Patriat et al., 2015). However, this fault now separates the young lithosphere of the North-Fidji back-arc basin from the significantly older oceanic lithosphere of the South-Fidji basin. There could therefore be a suitable buoyancy gradient, which however does not vary along strike in the manner described in this study. Another example, is the western termination of the Aleutian subduction zone in a transform fault separating the old pacific oceanic lithosphere from the stretched north-american continental lithosphere.

Finally, the magmatic arc may also be considered as a more favorable site of subduction initiation. Collision of the Ontong-Java plateau with the Vitiaz trench resulted in the initiation of the New-Hebrides subduction zone in the back of the arc (e.g., Mann and Taira, 2004). A similar scenario has been proposed for the initiation of the Carribean subduction zone. The collision of an oceanic plateau with an “andean” east-dipping subduction caused the nucleation of a new subduction with reversed polarity in the magmatic arc, which accomodated the eastward movement of the caribbean plate (Pindell et al., 2005; Pindell and Kennan, 2009). As the magmatic arc often rifts to open backarc basins, they can rapidly shorten when a buoyant object arrives in the trench causing a new subduction via subduction polarity reversal (Boutelier et al., 2003).

AUTHOR CONTRIBUTIONS

DBo designed the project, developed the methods, analyzed the results and wrote the manuscript. DBe built the models, and ran the experiments.

ACKNOWLEDGMENTS

We acknowledge support by the University of Newcastle.

REFERENCES

Adam, J., Urai, J., Wieneke, B., Oncken, O., Pfeiffer, K., Kukowski, N., et al. (2005). Shear localisation and strain distribution during tectonic faulting-new insights from granular-flow experiments and high-resolution optical image correlation techniques. *J. Struct. Geol.* 27, 283–301. doi: 10.1016/j.jsg.2004.08.008

Afonso, J.-C., Ranalli, G., and Fernàndez, M. (2007). Density structure and buoyancy of the oceanic lithosphere revisited. *Geophys. Res. Lett.* 34:L10302. doi: 10.1029/2007GL029515

Baes, M., and Sobolev, S. V. (2017). Mantle flow as a trigger for subduction initiation: a missing element of the Wilson cycle concept. *Geochem. Geophys. Geosyst.* 18, 4469–4486. doi: 10.1002/2017GC006962

Beck, M. E. (1991). Coastwise transport reconsidered: lateral displacements in oblique subduction zones, and tectonic consequences. *Phys. Earth Planet. Interiors* 68, 1–8. doi: 10.1016/0031-9201(91)90002-Y

Bonnardot, M.-A., Hassani, R., and Tric, E. (2008). Numerical modelling of lithosphere-asthenosphere interaction in a subduction zone. *Earth Planet. Sci. Lett.* 272, 698–708. doi: 10.1016/j.epsl.2008.06.009

Boutelier, D. (2016). TecPIV - A MATLAB-based application for PIV-analysis of experimental tectonics. *Comput. Geosci.* 89, 186–199. doi: 10.1016/j.cageo.2016.02.002

Boutelier, D., Chemenda, A., and Burg, J.-P. (2003). Subduction versus accretion of intra-oceanic volcanic arcs: insight from thermo-mechanical analogue experiments. *Earth Planet. Sci. Lett.* 212, 31–45. doi: 10.1016/S0012-821X(03)00239-5

Boutelier, D., Chemenda, A., and Jorand, C. (2002). Thermo-mechanical laboratory modelling of continental subduction: first experiments. *J. Virt. Explorer* 6, 61–65.

Boutelier, D., and Cruden, A. (2008). Impact of regional mantle flow on subducting plate geometry and interplate stress: insights from physical modelling. *Geophys. J. Int.* 174, 719–732. doi: 10.1111/j.1365-246X.2008.03826.x

Boutelier, D., and Cruden, A. (2013). Slab rollback rate and trench curvature controlled by arc deformation. *Geology* 41, 911–914. doi: 10.1130/G34338.1

Boutelier, D., and Cruden, A. (2016). Slab breakoff: insights from 3D thermo-mechanical analogue modelling experiments. *Tectonophysics* 694, 197–213. doi: 10.1016/j.tecto.2016.10.020

Boutelier, D., and Oncken, O. (2011). 3-D thermo-mechanical laboratory modeling of plate-tectonics: modeling scheme, technique and first experiments. *Solid Earth* 2, 35–51. doi: 10.5194/se-2-35-2011

Buckingham, E. (1914). On physically similar systems; illustrations of the use of dimensional equations. *Phys. Rev.* 4, 345–376. doi: 10.1103/PhysRev.4.345

Charvis, P., and Pelletier, B. (1989). The northern New Hebrides back-arc troughs: history and relation with the North Fiji basin. *Tectonophysics* 170, 259–277. doi: 10.1016/0040-1951(89)90275-8

Chemenda, A. I., Burg, J.-p., and Mattauer, M. (2000). Evolutionary model of the Himalaya-Tibet system: geopoem. *Earth Planet. Sci. Lett.* 174, 397–409. doi: 10.1016/S0012-821X(99)00277-0

Cloos, M. (1993). Lithospheric buoyancy and collisional orogenesis: subduction of oceanic plateaus, continental margins, island arcs, spreading ridges, and seamounts. *Geol. Soc. Am. Bull.* 105, 715–737. doi: 10.1130/0016-7606(1993)105<0715:LBACOS>2.3.CO;2

Cochran, J. R. (2010). Morphology and tectonics of the Andaman Forearc, northeastern Indian Ocean. *Geophys. J. Int.* 182, 631–651. doi: 10.1111/j.1365-246X.2010.04663.x

De Bresser, J. H. P., Ter Heege, J. H., and Spiers, C. J. (2001). Grain size reduction by dynamic recrystallization: can it result in major rheological weakening? *Int. J. Earth Sci.* 90, 28–45. doi: 10.1007/s005310000149

Dewey, J. F. (1969). Continental margins: a model for conversion of Atlantic type to Andean type. *Earth Planet. Sci. Lett.* 6, 189–197. doi: 10.1016/0012-821X(69)90089-2

Doin, M. P., and Henry, P. (2001). Subduction initiation and continental crust recycling: The roles of rheology and eclogitization. *Tectonophysics* 342, 163–191. doi: 10.1016/S0040-1951(01)00161-5

Funiciello, F., Faccenna, C., Giardini, D., and Regenauer-Lieb, K. (2003a). Dynamics of retreating slabs: 2. Insights from three-dimensional laboratory experiments. *J. Geophys. Res.* 108:2207. doi: 10.1029/2001JB000896

Funiciello, F., Morra, G., Regenauer-Lieb, K., and Giardini, D. (2003b). Dynamics of retreating slabs: 1. Insights from two-dimensional numerical experiments. *J. Geophys. Res.* 108:2206. doi: 10.1029/2001JB000898

Gerya, T. (2011a). Future directions in subduction modeling. *J. Geodyn.* 52, 344–378. doi: 10.1016/j.jog.2011.06.005

Gerya, T. (2011b). "Intra-oceanic subduction zones," in *Arc-Continent Collision,* eds D. Brown and P. D. Ryan (Berlin; Heidelberg: Springer Verlag), 23–51.

Gurnis, M., Hall, C., and Lavier, L. (2004). Evolving force balance during incipient subduction. *Geochem. Geophys. Geosyst.* 5:Q07001. doi: 10.1029/2003GC000681

Hall, C. E., Gurnis, M., Sdrolias, M., Lavier, L. L., and Müller, R. (2003). Catastrophic initiation of subduction following forced convergence across fracture zones. *Earth Planet. Sci. Lett.* 212, 15–30. doi: 10.1016/S0012-821X(03)00242-5

Hansen, L. N., Zimmerman, M. E., Dillman, A. M., and Kohlstedt, D. L. (2012a). Strain localization in olivine aggregates at high temperature: a laboratory comparison of constant-strain-rate and constant-stress boundary conditions. *Earth Planet. Sci. Lett.* 333–334, 134–145. doi: 10.1016/j.epsl.2012.04.016

Hansen, L. N., Zimmerman, M. E., and Kohlstedt, D. L. (2012b). The influence of microstructure on deformation of olivine in the grain-boundary sliding regime. *J. Geophys. Res. Solid Earth* 117, 1–17. doi: 10.1029/2012JB009305

Haq, S. S. B., and Davis, D. M. (2010). Mechanics of fore-arc slivers: insights from simple analog models. *Tectonics* 29, 1–14. doi: 10.1029/2009TC002583

Hassani, R., Jongmans, D., and Chéry, J. (1997). Study of plate deformation and stress in subduction processes using two-dimensional numerical models. *J. Geophys. Res. B Solid Earth* 102, 17951–17965. doi: 10.1029/97JB01354

Karig, D. E. (1982). Initiation of subduction zones: implications for arc evolution and ophiolite development. *Geol. Soc. Lond.* 10, 563–576. doi: 10.1144/GSL.SP.1982.010.01.37

Kreemer, C., Holt, W. E., and Haines, A. J. (2003). An integrated global model of present-day plate motions and plate boundary deformation. *Geophys. J. Int.* 154, 8–34. doi: 10.1046/j.1365-246X.2003.01917.x

Kreemer, C., Klein, E., Shen, Z.-K., Wang, M., Estey, L., Wier, S., and Boler, F. (2014). A geodetic plate motion and Global Strain Rate Model. *Geochem. Geophys. Geosyst.* 15, 3849–3889. doi: 10.1002/2014GC005407

Lallemand, S. (2014). Strain modes within the forearc, arc and back-arc domains in the Izu (Japan) and Taiwan arc-continent collisional settings. *J. Asian Earth Sci.* 86, 1–11. doi: 10.1016/j.jseaes.2013.07.043

Mann, P., and Taira, A. (2004). Global tectonic significance of the Solomon Islands and Ontong Java Plateau convergent zone. *Tectonophysics* 389, 137–190. doi: 10.1016/j.tecto.2003.10.024

Mart, Y., Aharonov, E., Mulugeta, G., Ryan, W., Tentler, T., and Goren, L. (2005). Analogue modelling of the initiation of subduction. *Geophys. J. Int.* 160, 1081–1091. doi: 10.1111/j.1365-246X.2005.02544.x

Martinod, J., Regard, V., Letourmy, Y., Henry, H., Hassani, R., Baratchart, S., et al. (2016). How do subduction processes contribute to forearc Andean uplift? Insights from numerical models. *J. Geodyn.* 96, 6–18. doi: 10.1016/j.jog.2015.04.001

Montési, L. G. (2013). Fabric development as the key for forming ductile shear zones and enabling plate tectonics. *J. Struct. Geol.* 50, 254–266. doi: 10.1016/j.jsg.2012.12.011

Montési, L. G. and Hirth, G. (2003). Grain size evolution and the rheology of ductile shear zones: from laboratory experiments to postseismic creep. *Earth Planet. Sci. Lett.* 211, 97–110. doi: 10.1016/S0012-821X(03)00196-1

Montési, L. G. J. (2002). A unified description of localization for application to large-scale tectonics. *J. Geophys. Res.* 107:2045. doi: 10.1029/2001JB000465

Mueller, S., and Phillips, R. (1991). On the initiation of subduction. *J. Geophys. Res.* 96, 651–665. doi: 10.1029/90JB02237

Müller, R. D., Roest, W. R., Royer, J. Y., Gahagan, L. M., and Sclater, J. G. (1997). Digital isochrons of the world's ocean floor. *J. Geophys. Res.* 102, 3211–3214. doi: 10.1029/96JB01781

Müller, R. D., Sdrolias, M., Gaina, C., and Roest, W. R. (2008). Age, spreading rates, and spreading asymmetry of the world's ocean crust. *Geochem. Geophys. Geosyst.* 9, 1–19. doi: 10.1029/2007GC001743

Nikolaeva, K., Gerya, T. V., and Marques, F. O. (2010). Subduction initiation at passive margins: numerical modeling. *J. Geophys. Res.* 115:B03406. doi: 10.1029/2009JB006549

Nobach, H., and Honkanen, M. (2005). Two-dimensional Gaussian regression for sub-pixel displacement estimation in particle image velocimetry or particle position estimation in particle tracking velocimetry. *Exp. Fluids* 38, 511–515. doi: 10.1007/s00348-005-0942-3

Oncken, O., Boutelier, D., Dresen, G., and Schemmann, K. (2012). Strain accumulation controls failure of a plate boundary zone: linking deformation of the Central Andes and lithosphere mechanics. *Geochem. Geophys. Geosyst.* 13:Q12007. doi: 10.1029/2012GC004280

Oxburgh, E. R., and Parmentier, E. M. (1977). Compositional and density stratification in oceanic lithosphere-causes and consequences. *J. Geol. Soc.* 133, 343–355. doi: 10.1144/gsjgs.133.4.0343

Patriat, M., Collot, J., Danyushevsky, L., Fabre, M., Meffre, S., Falloon, T., et al. (2015). Propagation of back-arc extension into the arc lithosphere in the southern New Hebrides volcanic arc. *Geochem. Geophys. Geosyst.* 16, 3142–3159. doi: 10.1002/2015GC005717

Pindell, J., Kennan, L., Maresch, W. V., Stanek, K.-P., Draper, G., and Higgs, R. (2005). Plate-kinematics and crustal dynamics of circum-Caribbean arc-continent interactions: tectonic controls on basin development in Proto-Caribbean margins.*Geol. Soc. Spec. Pap.* 394, 7–52. doi: 10.1130/0-8137-2394-9.7

Pindell, J. L. and Kennan, L. (2009). Tectonic evolution of the Gulf of Mexico, Caribbean and northern South America in the mantle reference frame: an update. *Geol. Soc. Lond.* 328, 1–55. doi: 10.1144/SP328.1

Poirier, J. (1980). Shear localization and shear instability in materials in the ductile field. *J. Struct. Geol.* 2, 135–142. doi: 10.1016/0191-8141(80)90043-7

Regenauer-Lieb, K., Rosenbaum, G., and Weinberg, R. F. (2008). Strain localisation and weakening of the lithosphere during extension. *Tectonophysics* 458, 96–104. doi: 10.1016/j.tecto.2008.02.014

Regenauer-Lieb, K., Yuen, D. a., and Branlund, J. (2001). The initiation of subduction: criticality by addition of water? *Science* 294, 578–580. doi: 10.1126/science.1063891

Roland, E., Behn, M. D., and Hirth, G. (2010). Thermal-mechanical behavior of oceanic transform faults: implications for the spatial distribution of seismicity. *Geochem. Geophys. Geosyst.* 11:Q07001. doi: 10.1029/2010GC003034

Royden, L. H. and Husson, L. (2006). Trench motion, slab geometry and viscous stresses in subduction systems. *Geophys. J. Int.* 167, 881–905. doi: 10.1111/j.1365-246X.2006.03079.x

Rutter, E. (1999). On the relationship between the formation of shear zones and the form of the flow law for rocks undergoing dynamic recrystallization. *Tectonophysics* 303, 147–158. doi: 10.1016/S0040-1951(98)00261-3

Schellart, W., Lister, G., and Toy, V. (2006). A Late Cretaceous and Cenozoic reconstruction of the Southwest Pacific region: Tectonics controlled by subduction and slab rollback processes. *Earth Sci. Rev.* 76, 191–233. doi: 10.1016/j.earscirev.2006.01.002

Smith, S. (1999). *The Scientist and Engineer's Guide to Digital Signal Processing*. San Diego,CA: California Technical Publishing.

Stern, R. (2002). Subduction zones. *Rev. Geophys.* 40:1012. doi: 10.1029/2001RG000108

Stern, R. J. (2004). Subduction initiation: spontaneous and induced. *Earth Planet. Sci. Lett.* 226, 275–292. doi: 10.1016/S0012-821X(04)00498-4

Toth, J., and Gurnis, M. (1998). Dynamics of subduction initiation at preexisting fault zones. *J. Geophys. Res.* 103, 18053–18067. doi: 10.1029/98JB01076

Turcotte, D., and Schubert, G. (1982). *Geodynamics: Applications of Continuum Physics to Geological Problems*. New York, NY: John Wiley and Sons.

Vlaar, N., and Wortel, M. (1976). Lithospheric aging, instability and subduction. *Tectonophysics* 32, 331–351. doi: 10.1016/0040-1951(76)90068-8

Westerweel, J., and Scarano, F. (2005). Universal outlier detection for PIV data. *Exp. Fluids* 39, 1096–1100. doi: 10.1007/s00348-005-0016-6

Conflict of Interest Statement: The authors declare that the research was conducted in the absence of any commercial or financial relationships that could be construed as a potential conflict of interest.

frontiers
in Earth Science

ORIGINAL RESEARCH
published: 24 January 2019
doi: 10.3389/feart.2018.00248

Smart Speed Imaging in Digital Image Correlation: Application to Seismotectonic Scale Modeling

Michael Rudolf[1]*, *Matthias Rosenau*[1], *Thomas Ziegenhagen*[1], *Volker Ludwikowski*[2], *Torsten Schucht*[2], *Horst Nagel*[2] and *Onno Oncken*[1]

[1] Lithosphere Dynamics, Helmholtz Centre Potsdam, German Research Centre for Geosciences (GFZ), Potsdam, Germany,
[2] LaVision GmbH, Göttingen, Germany

Edited by:
Christoph Von Hagke,
RWTH Aachen Universität, Germany

Reviewed by:
Yuntao Ji,
Utrecht University, Netherlands
Olivier Galland,
University of Oslo, Norway

***Correspondence:**
Michael Rudolf
michael.rudolf@gfz-potsdam.de

Specialty section:
This article was submitted to
Structural Geology and Tectonics,
a section of the journal
Frontiers in Earth Science

Received: 30 June 2018
Accepted: 19 December 2018
Published: 24 January 2019

Citation:
Rudolf M, Rosenau M, Ziegenhagen T, Ludwikowski V, Schucht T, Nagel H and Oncken O (2019) Smart Speed Imaging in Digital Image Correlation: Application to Seismotectonic Scale Modeling. Front. Earth Sci. 6:248. doi: 10.3389/feart.2018.00248

Analog models of earthquakes and seismic cycles are characterized by strong variations in strain rate: from slow interseismic loading to fast coseismic release of elastic energy. Deformation rates vary accordingly from micrometer per second (e.g., plate tectonic motion) to meter per second (e.g., rupture propagation). Deformation values are very small over one seismic cycle, in the order of a few tens of micrometer, because of the scaled nature of such models. This cross-scale behavior poses a major challenge to effectively monitor the experiments by means of digital image correlation techniques, i.e., at high resolution (>100 Hz) during the coseismic period but without dramatically oversampling the interseismic period. We developed a smart speed imaging tool which allows on-the-fly scaling of imaging frequency with strain rate, based on an external trigger signal and a buffer. The external trigger signal comes from a force sensor that independently detects stress drops associated with analog earthquakes which triggers storage of a short high frequency image sequence from the buffer. After the event has passed, the system returns to a low speed mode in which image data is downsampled until the next event trigger. Here we introduce the concept of smart speed imaging and document the necessary hard- and soft-ware. We test the algorithms in generic and real applications. A new analog earthquake setup based on a modification of the Schulze ring-shear tester is used to verify the technique and discuss alternative trigger systems.

Keywords: analog modeling, digital image correlation, seismotectonics, data analysis, monitoring

1. INTRODUCTION

During earthquakes elastic stress and strain is suddenly released in the lithosphere, causing abrupt relative motion of two adjacent crustal blocks. Earthquakes are usually bound spatially to a discontinuity (e.g., fault, or fault zone) and often occur in a quasiperiodic manner over geological timescales (ka to Ma) (Hyndman and Hyndman, 2016). According to the elastic rebound theory, each earthquake is preceeded by a period of seismic quiescence, followed by the earthquake and associated postseismic deformation (Reid, 1910). This cyclic behavior is termed "seismic cycle" and is the basis for assessing the geologic evolution of a seismogenic fault and the seismic hazard associated with it (Scholz, 2010). It is characterized by strongly contrasting strain rates in the interseismic and coseismic phase. During the interseismic period the system is frictionally locked, loaded at low rates (mm/a) and elastic strain gradually builds up (Tse et al., 1985; Schurr et al., 2014). In some cases the fault is not completely locked and shows slow creep deformation, e.g., in the form of slow slip events (Ide et al., 2007; Bürgmann, 2018). If the accumulated strain leads to stresses that exceed the frictional strength of the locked patch, a slip event nucleates and results in an earthquake with slip velocities in the range of m/s.

Although the recurrence behavior of earthquakes on a single fault is quasiperiodic, under the assumption of constant loading rates and frictional parameters, it is not possible to predict the onset of seismic slip (Ben-Zion et al., 2003). Therefore, numerical simulations and physical experiments have been designed to model fault slip and the seismic cycle (Rosenau et al., 2017). Because of the multiscale nature of fault slip, many numerical simulations are limited to either short (e.g., rupture models) (Heinecke et al., 2014) or long timescales (e.g., geodynamic models) (Dinther et al., 2013). Only few numerical techniques allow the combination of short term and long term processes, and frequently the parametrization and implementation of the non-linear, multiscale interactions between the long and short timescales remains difficult (Avouac, 2015). Seismotectonic analog experiments allow to address the multiscale nature of slip on a laboratory scale and may provide additional insight into the deformation over multiple seismic cycles (Rosenau et al., 2017). Even though the analog experiments are strong simplifications of a seismogenic fault system, they inherently show stick-slip dynamics without the need of a complex integration scheme (Caruso et al., 2007; Marković and Gros, 2014).

The strong variation of slip rate during the interseismic and coseismic period is the main challenge for monitoring the physical experiment (**Figure 1**). To capture the full rupture and associated coseismic deformation, the camera has to run at high image rates. Usually, there are two modes of recording a slip event. Either the camera is always running at high frame rate, and the images are only stored after a trigger is send (typical for very high speed cameras $F > 1kHz$). This only captures one rupture at a time, and does not provide constant monitoring over the complete seismic cycle. The other possibility is to monitor at a constant frame rate and storing all the images. This provides a constant monitoring but requires large amounts of data to be stored during an experiment which either is limited by the total amount of storage available (e.g., on the harddrive) or by the maximum rate of data transfer (e.g., memory to harddrive). Although, some cameras allow a change in recording frequency during the recording, this is not possible for experiments with non-predictable and very short events ($t_d < 3s$), because the event is over before the frame rate can be adjusted manually.

The images taken during the experiment are then processed using digital image correlation which yields the displacement field of slip on the fault. Ideally, the experiments run for a long time, to supply a large number of seismic cycles under constant experimental conditions ($N > 100$), for a good statistical analysis. For the presented experiments, this means a very large number of images which have to be processed which takes a long time, even when using a longer time interval and fewer images, the slip events have to be selected and individually processed.

In this study we present a new technique which allows for continuous monitoring of seismic cycles in seismotectonic scale models and analog earthquake models. The setup provides *in-situ* of shear stress and dilation, under variable normal stresses and loading rates, combined with a dynamic imaging technique. The measurements coming from the setup are used to trigger a switch from low to high framerates, resulting in drastically reduced amounts of data generated by the monitoring system. Moreover, the trigger system is combined with a buffer of images, supplying a temporary storage, which is used to fetch a certain amount of older images previously taken. Internally in the camera system this is implemented similar to a first-in-first-out (FIFO) but with access to the contained elements. This allows to increase the total duration of an experiment, while maintaining the ability to monitor the onset of seismic slip and the coseismic deformation at high rates.

2. EXPERIMENTAL SETUP AND METHODS

To produce regular stick-slip oscillations we utilize a rotary shear apparatus (ring-shear-tester), normally used for testing granular material properties (details in Schulze, 1994; ASTM International, 2016). Two different sets of experiments are used to show the performance and suitability of the triggering mechanism. The first configuration uses the ring-shear-tester in standard configuration, filled with rice which produces strong stick-slip events that are very regular (Rosenau et al., 2009). The second configuration is a rotary version of typical block sliders, featuring an annular gelatine block that slides on glass beads. The individual experiments are monitored using a camera system that is connected with the triggering system. A complete overview of all components used and how they are connected is provided by **Figure 2** and **Table 1**.

2.1. Experimental Setup

A Schulze ring-shear-tester (Schulze, 1994) is used as a basis for the experimental setups (**Figure 2**). This machine measures shear forces during rotary shear of a granular material (e.g., sand, glass beads; see also Panien et al., 2006; Klinkmüller et al., 2016; Ritter et al., 2016). During the experiment, it is possible to vary normal load and shear velocity. The ring-shear-tester uses a cantilever in combination with a motorized weight to hold a constant normal stress. The cantilever pulls the lid downwards onto the sample inducing normal stresses of 0.5–20 kPa. A digitally controlled motor rotates the shear cell at velocities V_L in the order of 10^{-4} to 10^{-1} mm/s. For the experiments in this study, we use velocities from 8.3×10^{-4} to 1.6×10^{-2} mm/s and normal stresses between 5 and 20 kPa. A twin beam system coupled to inductive displacement transducers measures the shear forces during the experiment at a frequency of up to $F = 50kHz$. The stiffness of the complete experimental setup is $k = 1,354Nm$ (Schulze, 1994).

2.1.1. Standard Configuration

We use the ring-shear-tester RSTpc.01 in standard configuration with the annular shear cell that has an inner sample diameter of 10 cm, an outer diameter of 20 cm, and a thickness of 4 cm (**Figure 2A**, cell type (Schulze, 1994). The aluminum shear cell has a high friction bottom, defined by evenly spaced grooves. As granular material we use a typical “thai” rice (sample “RI-1,” **Table 2**), which has previously been found to show ideal stick-slip characteristics that are needed to test the triggering

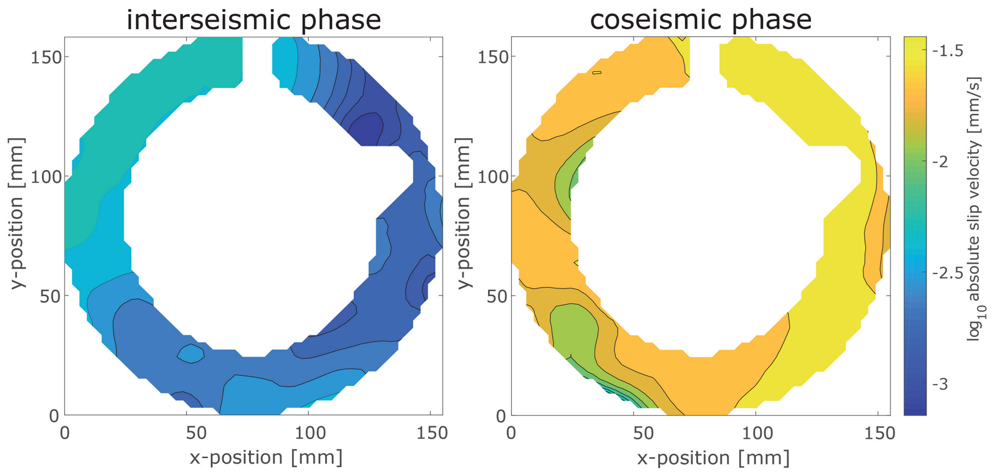

FIGURE 1 | Comparison of the slip velocity in the experimental setup during the interseismic **(Left)** and coseismic **(Right)** phase. The slip velocity during an event is almost 2 orders of magnitude higher than during the interseismic phase. The colorbar is valid for both plots.

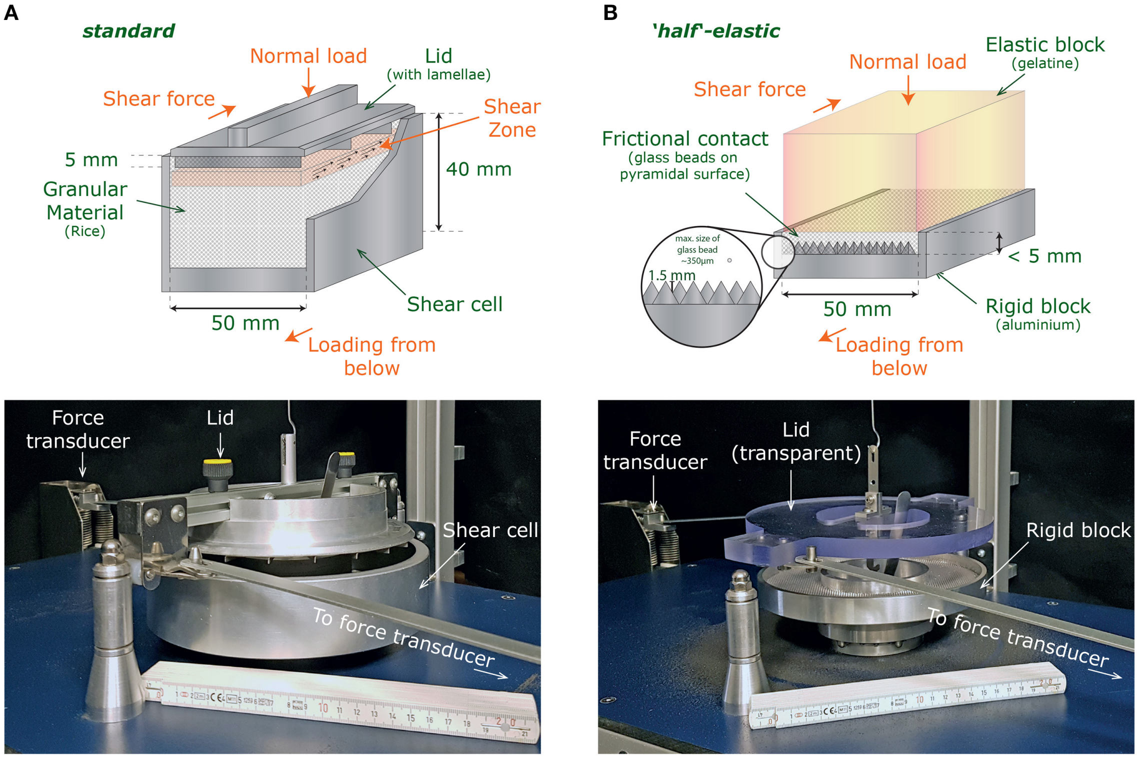

FIGURE 2 | Schematics and photographs of the setups on which the trigger algorithm is tested. **(A)** Standard configuration with cell and high stiffness. The basal cell is rotated while the lid is stationary and used to measure the shear force. According to Schulze (1994), a shear zone forms below the lamellae within the glass beads. **(B)** Half-elastic configuration with a rigid base block, an elastic gelatine ring with a layer of glass beads in between. Here the shear zone originates at the contact between gelatine and glass beads.

algorithm (Rosenau et al., 2009, 2017). A solid, aluminum lid, with lamellae providing a high friction interface, is placed on top of the rice. The upper surface of the lid is covered with a white-on-black random pattern of dots, which is ideal for the later digital image correlation (section 2.2). Because the lid is rigid, only the bulk deformation of the rice is recovered by monitoring the surface. We use this setup to illustrate the performance of the trigger system, because it produces almost perfect stick-slip cycles with a very long interevent phase in comparison to the slip events.

TABLE 1 | Components and input parameters needed for the triggering algorithm.

	Used	**Alternative**
Experimental setup	Ringsheartester - Schulze RST.pc01	Any other setup with sensors
Digitizer and triggering	National Instruments CompactRIO	Any programmable microcontroller with integrated FPGA, e.g., Arduino + MKR Vidor
	+4 channel analog card	
	+16 channel digital card	
Camera system	LaVision Strainmaster Controller	Digital camera that allows remote triggering with external signal
	+ Camera Imager MX4M (4MPx, 8–12 bit, 1–700Hz)	
Trigger software	“Ringshear-Control,” self developed LabView software	Software adapted for used microcontroller
Camera control software	LaVision StrainmasterDIC 1.1.0+ or DaVis 10+	Camera control software for used camera

TABLE 2 | Recording rates and data savings per experiment.

No.	V_L	**Framerate**		**Images**		**Data**		**Savings (%)**
	mm/s	**Low (Hz)**	**High (Hz)**	**Taken**	**Full**	**Used (GB)**	**Full (GB)**	
GB-1	8.2×10^{-4}	0.5	10	1,930	18,635	8.6	82.9 GB	89.6
GB-2	1.7×10^{-3}	1	25	4,335	47,767	19.1	210.6 GB	90.9
GB-3	1.7×10^{-2}	1	25	1,403	2,852	6.2	12.5	50.8
RI-1	8.2×10^{-4}	1	500	45,260	862,913	17.6	335.8	94.8

2.1.2. Block Slider Configuration

For the block slider model, we use a thinner shear cell (**Figure 2B**, gelatin not included in the image), which is completely filled with glass beads (samples “GB-1” to “GB-3,” **Table 2**). On top of the glass beads an annular ring of gelatin provides elastic boundary conditions and acts as a lid. The gelatine is 25w% pig skin gelatin (Italgelatin, see also Di Giuseppe et al., 2009) which has a Young’s Modulus $E \approx 150...200kPa$ and is transparent. On top of the gelatin a polycarbonate lid provides a stiff connection to the force transducers and provides the possibility to observe the glass bead layer from the top.

The shear cell has a bottom that is covered with a pattern of 2 × 2 × 2 mm pyramids which provides a very high basal friction along the bottom of the glass beads. The glass beads are filled into the shear cell according to the procedure given by Klinkmüller et al. (2016). The glass beads are spherical with an average diameter of 300–400 μm and a coefficient of friction μ of 0.3 to 0.5. For better detection with the image correlation algorithm 10% of glass beads are colored with diluted black acrylic paint. We use the same mixture of glass beads throughout all experiments.

2.2. Monitoring System

Over the whole experimental duration the top surface of the lid (standard configuration), or glass bead layer (block slider configuration), is monitored with a 4 MPx and 8–12 bit CMOS[1] camera (top left in **Figure 3**, Imager MX4M, by LaVision). Depending on the speed of the observed process the frame rate is adaptable to values between 0.5 and >500 Hz. The observed surface is illuminated by a continuous LED light (100 kHz, 100% duty cycle) to prevent changing brightness because of the 50 Hz power grid frequency. The images are calibrated with a rectangular pattern of dots. This calculates the spatial scale per pixel and adjusts for lens distortion.

In our study, each acquired image has a bit depth of 8 bit which gives 265 grayscale values. In combination with a spatial resolution of 2,048 × 2,048px this results in a file size of ≈ 8 MB per image. The images are processed using the built-in digital image processing algorithm by LaVision StrainMasterDIC (top right in **Figure 3**). It utilizes affine transformation to match patterns at equally spaced interrogation points (step width: 8 px) between two successive images (Bouguet, 2001; Fleet and Weiss, 2005). At each point, a subset of 31 pixels is matched using the least squares matching algorithm. The algorithm gives back the displacement in the form of a 2D vector at each interrogation point. This results in a high resolution displacement field over the whole analyzed domain.

To get an appropriate catalog size, the experiments run over at least 1 h. Usually, the camera takes a continuous time series of images at a fixed frequency, e.g., 10 Hz. Due to the nature of the modeled system, the deformation during the interseismic phase of a stick-slip cycle is very low. Previously, the acquisition rate was a tradeoff, between the amount of storage available, and the speed of the process. As an example, 1 h of continuous measurement at 10 Hz covers 60–70 seismic cycles and uses approximately 288 GB of storage. For this study, we developed a triggering system that uses the shear stress measurements from the ring-shear tester to trigger a change in camera frequency from 0.5 to 1 Hz during the interseismic phase, to 10–25 Hz in the coseismic phase.

---

[1] Complementary metal-oxide semiconductor.

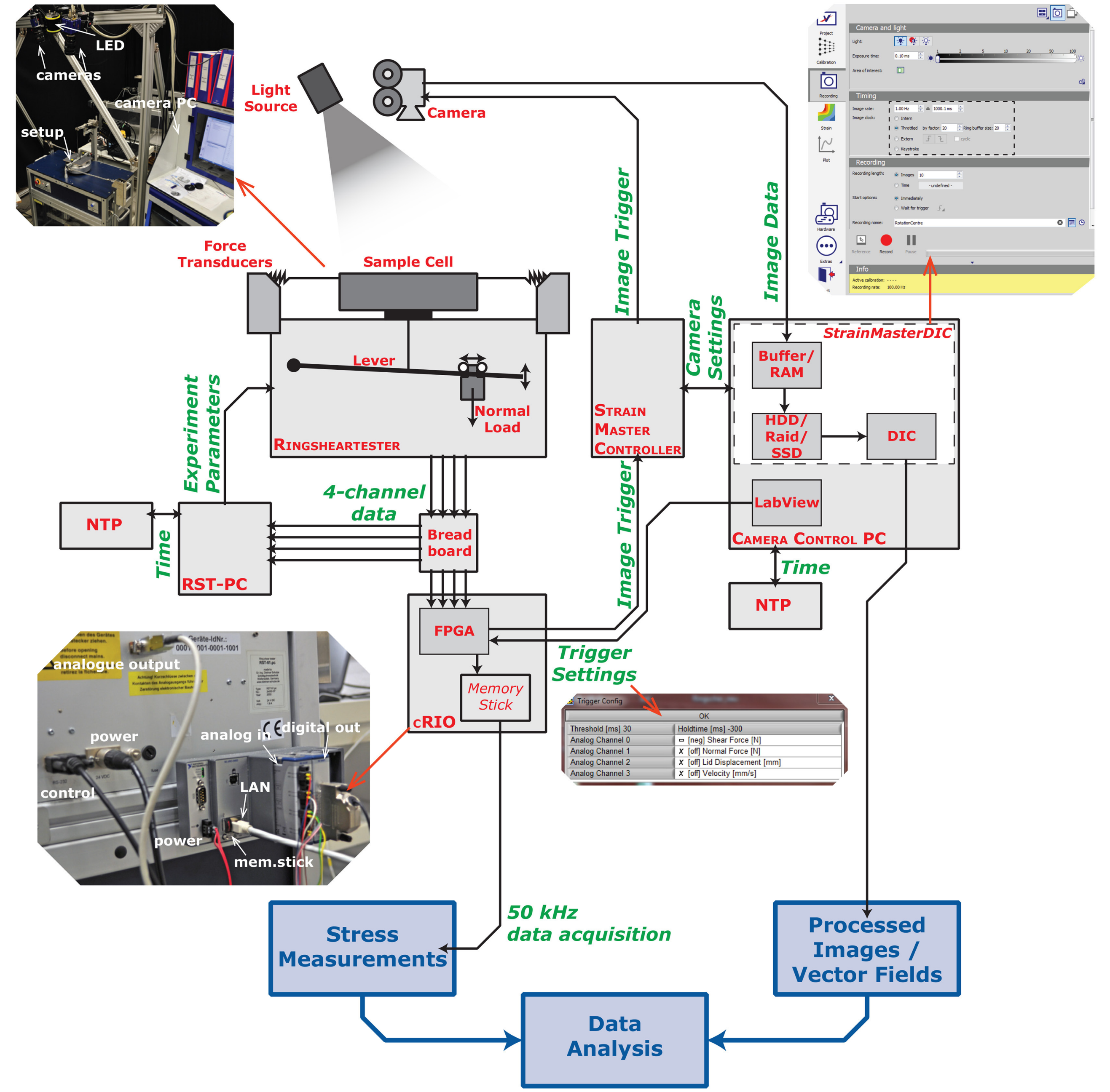

Threshold [ms] 30
Holdtime [ms] -300
Analog Channel 0: [neg] Shear Force [N]
Analog Channel 1: X [off] Normal Force [N]
Analog Channel 2: X [off] Lid Displacement [mm]
Analog Channel 3: X [off] Velocity [mm/s]

FIGURE 3 | Schematic diagram showing the setup and the connections to the monitoring system. The ring-shear-tester is controlled by a computer (RST-PC), which sets the parameters for the experiment (e.g., shear velocity, normal stress). The CompactRIO (cRIO) is connected to the output channels and provides the triggering and recording on all four channels ($F_{shear}, F_{normal}, \Delta H, V_L$). A second computer (Camera Control PC) is connected to the camera system which consists of a controller (StrainMaster Controller) and a software (StrainMasterDIC by LaVision). It supplies the settings for the camera (recording rate, exposure time,...) and stores the incoming image data for digital image correlation (DIC). All components are also listed in **Table 1**.

The trigger system consists of an embedded controller (center in **Figure 3**, National Instruments, CompactRIO) that is connected to the four channel analog output of the ring-shear tester and the trigger input of the camera system. The controller records the data with a frequency of 50 kHz which is downsampled to the requested recording frequency depending on what the user wants to record. The trigger algorithm independently utilizes the incoming 50 kHz stream and uses every 50th value to calculate the trigger level. Higher rates are theoretically possible with a more powerful logical processor (field-programmable gate array, FPGA) and digitizer (analog digital converter, ADC). Additionally, the algorithm is very simple and thus also able to run on less powerful, cheaper hardware, such as e.g., an Arduino MKR Vidor, although at a reduced rate.

2.3. Trigger Algorithm

The trigger algorithm consists of a set of conditions $T = \{T_1, T_2, T_3, T_4, T_5\}$ which are logically combined to determine the output of a trigger signal T_a (**Figure 4**). The algorithm uses any provided input signal x and detects changes in x by comparing two differences Δ_{short} and Δ_{long} over two time intervals. These two differences are the basis for the detection and are defined as follows:

$$t_{short} = [t_{-1}, t_0] \tag{1}$$

t_{short} is a small time interval between the current value at t_0 and the previous value at t_{-1} which leads to:

$$\Delta_{short} = x_{t_0} - x_{t_{-1}} \tag{2}$$

And the long time interval t_{long} is defined by:

$$t_{long} = [t_w \dots t_{-1}] \tag{3}$$

This is the time between the previous value t_{-1} and a value at a defined time the past t_w, leading to:

$$\Delta_{long} = x_{t_{-1}} - x_{t_w} \tag{4}$$

The moving window size t_w can be chosen by the user to adjust the sensitivity of the trigger algorithm. It mainly decides the time scale over which the change is going to occur. For example, if the targeted process happens over a time scale of 100 ms then the window size should be $t_w \leq 100ms$. The two differences show a different reaction to transients (**Figure 4A**). The long term difference is slower to react, but shows a larger amplitude, whereas the short term difference is quicker but with a much smaller amplitude.

To detect changes in the signal, we introduce the first condition T_1 which is true when the long term difference Δ_{long} is twice the amplitude of the short term difference Δ_{short} (**Figure 4B**):

$$T_1(\Delta_{long}, \Delta_{short}) := \begin{Bmatrix} 1 \ if \ |\Delta_{long}| > 2|\Delta_{short}| \\ 0 \ if \ |\Delta_{long}| \leq 2|\Delta_{short}| \end{Bmatrix} \tag{5}$$

The factor of two reduces the influence of noise on T_1. To keep the algorithm simple and easy to predict, the factor is predefined and not changeable by the user.

Because T_1 reacts on any change, negative and positive, a second condition T_2 is used to be able to switch the polarity of the trigger (**Figure 4C**). The user is able to select the polarity on which the trigger should detect. In our case the input signal for the trigger algorithm is the measured shear stress. During a slip event the shear stress decreases and therefore both differences show a negative polarity. As a result, in our case T_2 is true when Δ_{long} is negative:

$$T_2(\Delta_{long}) := \begin{Bmatrix} 1 \ if \ \Delta_{long} < 0 \\ 0 \ if \ \Delta_{long} \geq 0 \end{Bmatrix} \tag{6}$$

Equations (5) and (6) are used to determine a third condition T_3, which is true when both other conditions are true:

$$T_3 = T_1 \wedge T_2 \tag{7}$$

Although T_1 includes a noise reducing factor of two, T_3 is sometimes true for a few milliseconds and then deactivates again (**Figure 4D**). For a real slip event the conditions are met over a longer period of time, without switching off in between. As a consequence, the next trigger condition T_4 is set to true, when T_3 has been active for at least the long window size t_w (**Figure 4E**). This is facilitated with a simple counting variable k that is incremented when T_3 is true and set to zero when T_3 is false:

$$k := \begin{Bmatrix} k+1 \ if \ T_3 = 1 \\ 0 \quad if \ T_3 = 0 \end{Bmatrix} \tag{8}$$

As a result T_4 is defined by:

$$T_4 := \begin{Bmatrix} 1 \ if \ k \geq t_w \\ 0 \ if \ k < t_w \end{Bmatrix} \tag{9}$$

To capture processes happening after a slip event, e.g., afterslip, we implemented an optional hold time t_h which defines for how long the trigger should stay active after T_4 switches back to off. This is also facilitated with an internal clock type variable that defines the trigger condition T_5 (**Figure 4F**). As a result, the final trigger activity that is send to the camera system T_a is a logical OR connection of T_4 and T_5, where T_4 is a combination of all previously defined conditions and T_5 only depends on the hold time t_h (**Figure 4G**):

$$T_a = T_4 \vee T_5 \tag{10}$$

As **Figures 4B–G** shows, the combination of the individual trigger conditions leads to an increasingly precise detection of transients. It also detects transients which are not easily observed by the naked eye, such as the slow slip events marked in **Figure 4A**.

2.4. Implementation in LaVision StrainMasterDIC

Our trigger system has been integrated into the image analysis software suites StrainMasterDIC and DaVis 10 by LaVision, as an additional method of changing the framerate via an external trigger signal. The microcontroller that calculates the final trigger activity T_a gives out a 5V TTL (transistor-transistor logic) signal that is interpreted by the imaging software to trigger the cameras. The signal is in *low* state (0 V) when $T_a = 1$ and in *high* state (5 V) when $T_a = 0$. It is transferred over 50Ω coaxial cables to the programmable timing unit (LaVision Strainmaster Controller) of the camera system which then triggers the cameras.

Inherently, the trigger system is only activated when a slip event is already happening (**Figure 4**). Therefore, it is combined with a buffer of images (FIFO) on the memory of the computer (RAM) which is constantly filled with images from the camera at high-speed frequency F_{high}. The size of the buffer can be set

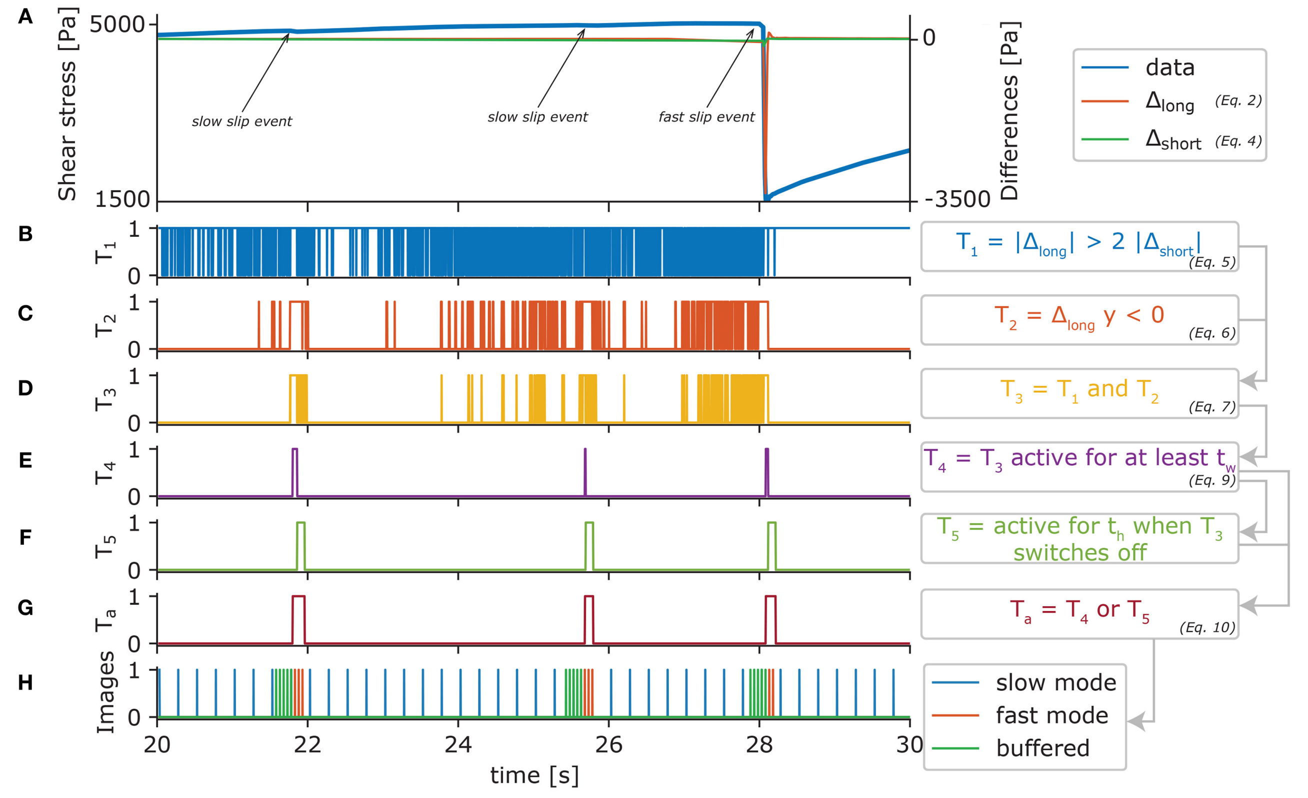

FIGURE 4 | Behavior of the trigger algorithm during an experiment. Input parameters are: $t_w = 30ms$, $t_h = 100ms$, polarity is negative, $F_{high} = 20Hz$, $n = 5$, $i = 5$. **(A)** Typical shear curve of an experiment. The data contains very fast slip events and slower slip events. The latter are very difficult to detect by eye. **(B–G)** Individual results of the trigger conditions, with successively increasing accuracy. **(H)** Images taken during the experiment, distinguished by low, fast, and buffer acquisition.

in the software. For this study it is set to be the number of high-speed images between two subsequent low-speed images, e.g., if $F_{low} = 1Hz$ and $F_{high} = 25Hz$, then the number of images in the buffer $i = 25$. The two different acquisition frequencies are realized by giving the high speed frequency F_{high} and a division factor n which slows down the acquisition when no slip event is happening. When the trigger is off ($T_a = 0$), the system only selects each nth image that comes out of the image buffer to be saved. As soon as the trigger is on ($T_a = 1$), all images in the buffer are fetched and marked for saving. Then it continues recording at high speed until the trigger switches back to off. **Figure 4H** shows the sequence of images recorded and whether they are taken in slow mode, fast mode, or loaded from the buffer.

3. RESULTS

3.1. Slip Events in the Different Configurations

Both configurations show quasiperiodic stick-slip oscillations of varying amplitude and recurrence (**Figure 5A**). The shear force in all experiments oscillates in a sawtooth shaped pattern analogs to the shear force along a seismogenic fault. This is characteristic for sheared granular shear materials (e.g., Losert et al., 2000). Here we only give a brief overview of some of their characteristics in our setup, to illustrate the application of the trigger system.

The experiment in standard configuration (RI-1, blue color) was carried out at a loading rate of $V_L = 8.2 \times 10^{-4}$ mm/s and a normal stress of 5 kPa. The strength of the rice grains is relatively high and reaches values above the normal stress several times. The recurrence time t_{rec} is very regular and is 18.3 ± 2.3s (**Figure 5B**). The stress drops $\Delta\tau = 3,650 \pm 150$ Pa, are two orders of magnitude higher that for the block slider configuration (**Figure 5C**).The duration of a slip event in rice is around 0.1 s (**Figure 5D**). The ratio between recurrence and duration is very high ($\frac{t_{rec}}{t_{dur}} \approx 360$), and as a result the potential for saving image data is very high.

In the block slider configuration three different shear rates are realized, which are in the range of the targeted values for the application of the trigger setup (GB-1, -2, and -3 in **Figure 5A**). Shear rates range from 8.2×10^{-4} to 1.7×10^{-2} at normal stresses of 5 kPa. The recurrence time nonlinearly decreases with increasing shear rate, which is an expected behavior for this rate-and-state-dependent material (**Figure 5B**). At the highest realized shear rate the recurrence time is reduced by one order of magnitude from around 60 s down to 4 s. This is due to the occurrence of some smaller precursory events, also reflected in the lower tail of the stress drop distribution. The slip events in

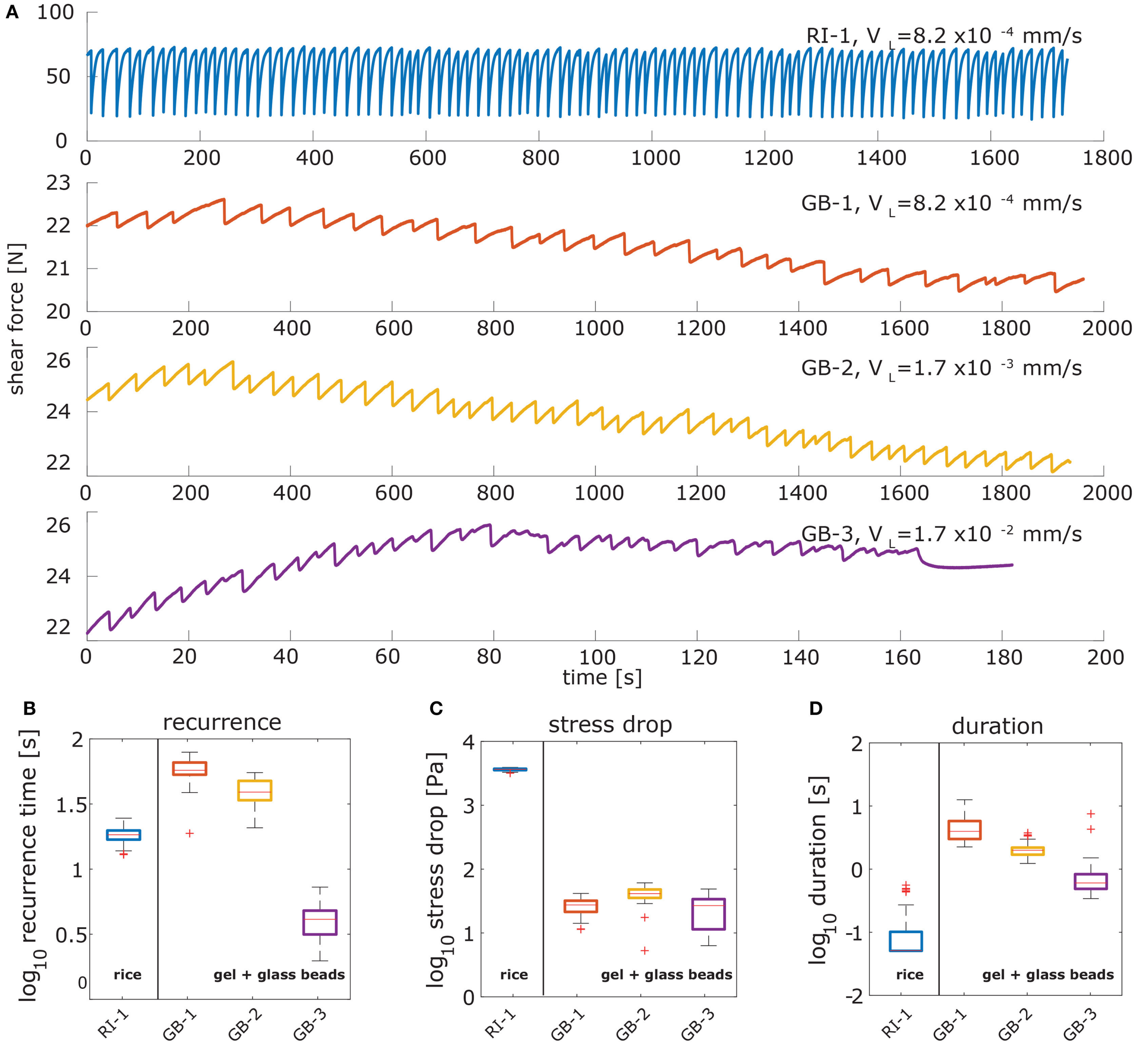

FIGURE 5 | Shear force curves and characteristic parameters derived from the stress measurements. **(A)** Shear force measurements during the experiments with a characteristic saw-tooth shape. The y-axis is shear force in Newton and the x-axis is time in seconds for all experiments. **(B)** The realized recurrence times cover two orders of magnitude and are similar for both setups. For higher shear rates the recurrence time is significantly reduced, which is in accordance with the rate-and-state-dependent friction. **(C)** Stress drops cover the same range for the block slider configuration and is much higher for the standard configuration. This results mostly from the stiffness of the setup, which is several orders of magnitude higher in the standard configuration. **(D)** The duration of the events decreases with increasing shear rate. The detected durations of the rice stick-slips are very low and truncated at 0.1 s.

the block slider configuration are of much lower magnitude than in standard configuration with median stress drop ranging from 27 ± 8 to 41 ± 14 Pa (**Figure 5C**). Furthermore, they are less regular and have a less homogenous magnitude-size distribution, log-normal instead of normal, especially at the highest shear rate the events cover a broad range of stress drops. The duration of slip in the block slider is also decreasing with increasing shear rate and ranges between 0.6 ± 0.6 and 4 ± 2 s. The resulting ratio between duration and recurrence is in the range of 14–20 for the two lower shear rates and 7 for the higher shear rate. This ratio is not as high as for rice but because the recurrence behavior is less regular a manual trigger switch is not feasible.

3.2. Trigger Algorithm

The amount of data saved during the image acquisition ranges between ≈50 and 95% (**Table 2**). Experiments which show a very regular and ideal stick-slip behavior show the highest amount of data saved (GB-1, GB-2, and RI-1). If the slip events are less regular, or are dissected by transient slip events that are much slower than the actual event, the algorithm triggers more often, and therefore more data is produced (GB-3). Nevertheless, the trigger system is able to save more than 50% of data. Slight refinements to the detection thresholds or frame rates can help to push this limitation a bit further. Correctly adjusting the window size to the faster events lowers the amount of false detections and a higher "slow" framerate helps to cover the slower events with more accuracy.

The trigger algorithm also decreases the average framerate over the duration of the whole experiment, e.g., ≈26Hz for RI-1. This limits the average amount of data per second from 200 to 10 MB/s which enables the use of inexpensive single hard-drive systems instead of a raid configuration. The software does not immediately save the images onto the harddrive, but transfers the selected images into another buffer (FIFO) in the RAM that saves the images as fast as the harddrive can save them. Therefore, the incoming images are distributed over a longer period of time which reduces the storage rate needed. The delay between trigger signal and reaction of the camera system is in the order of a few μs which provides a very quick reaction to the trigger signal. If the two window sizes are well adjusted, the complete onset of the slip event and the postseismic effects are recorded at high speed, whereas the interseismic phase is covered at reduced rate. In extreme cases (full resolution and framerate) the camera used in this study produces around 1 GB/s which can be lowered to around 100 MB/s, assuming a typical reduction by 90%. Usually this system requires a multi-disk raid that can store up to 1.8 GB/s in combination with a large RAM (>128 GB) to record images over the duration of 1 h. This is not needed anymore, when using the provided trigger system.

4. DISCUSSION AND CONCLUSION

4.1. Time Synchronization

Combining experimental results from different monitoring systems requires a reliable time stamp on the images and on the signal data. To synchronize the time between multiple computers in our setup we use the network time protocol (NTP). A specialized software continuously synchronizes each computer with the two network time servers of the local area network at the institute. The network time servers synchronize with GPS signals and the software automatically calculates the delay and offset within the network. This is a standard facility that is necessary for many LAN networks and should be generally available at most universities or research institutions. If only the time synchronization with internet servers provided by the operating system is used, e.g., Windows time service, we found that the time difference between two individual computers can be up to several seconds. For seismotectonic scale models with slip events that occur on the millisecond time scale, this is not feasible. Therefore, it is advised to either use a single computer for everything, or to synchronize the time between the individual devices by using an external clock generator using a specialized software.

4.2. Digital Image Correlation

The reduction of produced images yields much faster processing times for the digital image correlation. This speeds up the typical workflow of an analog experiment. Additionally, the signal to noise ratio is improved during the interseismic time. Because the framerate is adjusted to the coseismic velocities, the interseismic deformation often is below the detection threshold of the digital image correlation algorithm, which is usually in the subpixel range. Lower framerates during the interseismic time increase the total amount of deformation recorded per image providing a much more accurate estimation of interseismic deformation, that is needed for example to calculate the interseismic locking.

4.3. Alternative Triggering Systems

4.3.1. With a Priori Data Reduction

Our trigger system serves as an a priori reduction of data. It is therefore most efficient when the observations are preceded by some sort of precursor, or if additional observations, such as the force measurements, are available. Furthermore, it relies on the temporal storage of images with dynamic access to the buffer which is not available for most systems. Some camera systems allow for post-triggering, which means that they have a static buffer which is emptied after an event has been triggered. These only support one frame rate, and the triggering process has to be fast enough, that an overflow of the buffer is prevented. The triggering can be automated with the presented setup, or manual by visual inspection of the experiment. This technique can be feasible when a reliable signal is not available and should be accompanied by a continuous monitoring at lower frequency with a second camera.

In some cases a reliable secondary signal, such as the force measurements, is not available because the setup is technically not feasible. This is the case for many analog experiments, like wedges and sandboxes. For these experiments a reliable stress measurement is geometrically hindered or the stress transmission to a sensor is limited. Such experiments can be monitored using a simultaneous strain measurement by digital image correlation. Especially when the observed deformations are too small to be visible by the naked eye, which makes the manual post-triggering impossible. The real-time strain gage also requires a buffer and a performant computer system which is able to compute a quick strain estimation from the images. If these requirements are met, the system is similar to our trigger system and can either use a velocity or acceleration threshold to trigger the high-speed acquisition of images.

4.3.2. With a Posteriori Data Reduction

If a buffer on the computer ram or camera ram is not available, e.g., for consumer grade digital cameras, the above algorithm can be used to do quick a posteriori sorting of images. During the experimental run but with some time delay. Then the images have to be transmitted to a computer during the experimental run which is also possible for many standard digital cameras where the manufacturer supplies a specialized software to remote control the camera via USB. Using a script, or the PC component of the embedded microcontroller ("RealTime" for the CompactRIO), the trigger is used to delete the unnecessary images during the interseismic phase. Alternatively, the recorded signal can be used after the experiment, to select only the images where a slip event has happened which quickens the post-experiment analysis.

4.4. Conclusions

In this study we developed a smart speed imaging technique based on an external trigger algorithm that allows for a well defined, feedback controlled change of image rate during an experiment. Our experiments verify that it is able to greatly reduce the needed amount and speed of storage. The use of a double time-frame approach is easy to adjust, while maintaining a rapid and robust response to changes in the triggering signal. The fully modular specification of the algorithm and hardware system, allows to add further input signals (e.g., acoustic emissions) without major changes. Furthermore, the lower amount of images provides a faster processing speed because less images have to be processed during digital image correlation.

In comparison with traditional approaches, such as manual triggering, the presented algorithm provides a well defined and quantifiable constraint on the detection of slip events in real-time data. It only relies on the triggered event itself and does not require any knowledge about precursory phenomena. In addition, only a few observations are needed to adjust the parameters to the optimal value.

DATA AVAILABILITY STATEMENT

The datasets generated and analyzed for this study, including the scripts to generate the figures, have been published in Rudolf et al. (2019).

AUTHOR CONTRIBUTIONS

MiR planned and performed the experiments, analyzed the data, and wrote the research paper. MaR was involved in planning the research, analyzing the results and writing. TZ, VL, TS, and HN facilitated the technical realization of the study. OO was involved in supervising the research and writing.

FUNDING

This research has been funded by Deutsche Forschungsgemeinschaft (DFG) through grant CRC 1114 Scaling Cascades in Complex Systems, Project B01 Fault networks and scaling properties of deformation accumulation. Additional funding was provided by the European Union Initial Training grant 674899-SUBITOP.

ACKNOWLEDGMENTS

F. Neumann is acknowledged for his technical assistance in the laboratory. This study has benefitted from discussions with J. Bedford.

REFERENCES

ASTM International (2016). *Standard Test Method for Bulk Solids Using Schulze Ring Shear Tester.* West Conshohocken, PA: ASTM International. doi: 10.1520/d6773-16

Avouac, J.-P. (2015). From geodetic imaging of seismic and aseismic fault slip to dynamic modeling of the seismic cycle. *Annu. Rev. Earth Planet. Sci.* 43, 233–271. doi: 10.1146/annurev-earth-060614-105302

Ben-Zion, Y., Eneva, M., and Liu, Y. (2003). Large earthquake cycles and intermittent criticality on heterogeneous faults due to evolving stress and seismicity. *J. Geophys. Res.* 108:B6. doi: 10.1029/2002JB002121

Bouguet, J.-Y. (2001). *Pyramidal Implementation of the Affine Lucas Kanade Feature Tracker Description of the Algorithm.* Intel Corporation.

Bürgmann, R. (2018). The geophysics, geology and mechanics of slow fault slip. *Earth Planet. Sci. Lett.* 495, 112–134. doi: 10.1016/j.epsl.2018.04.062

Caruso, F., Pluchino, A., Latora, V., Vinciguerra, S., and Rapisarda, A. (2007). Analysis of self-organized criticality in the olami-feder-christensen model and in real earthquakes. *Phys. Rev. E* 75:055101. doi: 10.1103/PhysRevE.75.055101

Di Giuseppe, E., Funiciello, F., Corbi, F., Ranalli, G., and Mojoli, G. (2009). Gelatins as rock analogs: a systematic study of their rheological and physical properties. *Tectonophysics* 473, 391–403. doi: 10.1016/j.tecto.2009.03.012

Dinther, Y., Gerya, T. V., Dalguer, L. A., Mai, P. M., Morra, G., and Giardini, D. (2013). The seismic cycle at subduction thrusts: insights from seismo-thermo-mechanical models. *J. Geophys. Res.* 118, 6183–6202. doi: 10.1002/2013JB010380

Fleet, D., and Weiss, Y. (2005). "Optical flow estimation," in *Handbook of Mathematical Models in Computer Vision,* eds N. Paragios, Y. Chen, and O. Faugeras, O (Springer), 239–258. Available online at: http://www.cs.toronto.edu/~fleet/research/Papers/flowChapter05.pdf

Heinecke, A., Breuer, A., Rettenberger, S., Bader, M., Gabriel, A. A., Pelties, C., et al. (2014). "Petascale high order dynamic rupture earthquake simulations on heterogeneous supercomputers," in *SC14: International Conference for High Performance Computing, Networking, Storage and Analysis* (New Orleans, LA), 3–14. doi: 10.1109/SC.2014.6

Hyndman, D., and Hyndman, D. (2016). *Natural Hazards and Disasters.* Cengage Learning. Verlag: Boston, MA.

Ide, S., Beroza, G. C., Shelly, D. R., and Uchide, T. (2007). A scaling law for slow earthquakes. *Nature* 447, 76–79. doi: 10.1038/nature05780

Klinkmüller, M., Schreurs, G., Rosenau, M., and Kemnitz, H. (2016). Properties of granular analogue model materials: a community wide survey. *Tectonophysics* 684, 23–38. doi: 10.1016/j.tecto.2016.01.017

Losert, W., Bocquet, L., Lubensky, T. C., and Gollub, J. P. (2000). Particle dynamics in sheared granular matter. *Phys. Rev. Lett.* 85, 1428–1431. doi: 10.1103/PhysRevLett.85.1428

Marković, D., and Gros, C. (2014). Power laws and self-organized criticality in theory and nature. *Phys. Rep.* 536, 41–74. doi: 10.1016/j.physrep.2013.11.002

Panien, M., Schreurs, G., and Pfiffner, A. (2006). Mechanical behaviour of granular materials used in analogue modelling: insights from grain characterisation, ring-shear tests and analogue experiments. *J. Struct. Geol.* 28, 1710–1724. doi: 10.1016/j.jsg.2006.05.004

Reid, H. (1910). *The Mechanism of the Earthquake*. The California earthquake of april 18, 1906: Report of the State Investigation Commission, Vol. 2. Washington, DC: Carnegie Institution of Washington.

Ritter, M. C., Leever, K., Rosenau, M., and Oncken, O. (2016). Scaling the sand box - mechanical (dis-) similarities of granular materials and brittle rock. *J. Geophys. Res. Solid Earth* 121, 6863–6879. doi: 10.1002/2016JB012915

Rosenau, M., Corbi, F., and Dominguez, S. (2017). Analogue earthquakes and seismic cycles: experimental modelling across timescales. *Solid Earth* 8, 597–635. doi: 10.5194/se-8-597-2017

Rosenau, M., Lohrmann, J., and Oncken, O. (2009). Shocks in a box: an analogue model of subduction earthquake cycles with application to seismotectonic forearc evolution. *J. Geophys. Res.* 114:B1. doi: 10.1029/2008JB005665

Rudolf, M., Rosenau, M., Ziegenhagen, T., Ludwikowski, V., Schucht, T., Nagel, H., et al. (2019). Supplement to: smart speed imaging in digital image correlation: application to seismotectonic scale modelling. *GFZ Data Serv*. 1–2. doi: 10.5880/GFZ.4.1.2018.002

Scholz, C. H. (2010). Large earthquake triggering, clustering, and the synchronization of faults. *Bull. Seismol. Soc. Am.* 100, 901–909. doi: 10.1785/0120090309

Schulze, D. (1994). Development and application of a novel ring shear tester. *Aufbereit. Tech.* 35, 524–535.

Schurr, B., Asch, G., Hainzl, S., Bedford, J., Hoechner, A., Palo, M., et al. (2014). Gradual unlocking of plate boundary controlled initiation of the 2014 iquique earthquake. *Nature* 512, 299–302. doi: 10.1038/nature13681

Tse, S. T., Dmowska, R., and Rice, J. R. (1985). Stressing of locked patches along a creeping fault. *Bull. Seismol. Soc. Am.* 75:709.

Conflict of Interest Statement: The outcomes of this research are partially used by LaVision Germany GmbH, who also provided access to development versions of the camera systems that they resell.

The authors declare that the research was conducted in the absence of any commercial or financial relationships that could be construed as a potential conflict of interest.

frontiers
in Earth Science

ORIGINAL RESEARCH
published: 25 February 2019
doi: 10.3389/feart.2019.00018

The Effect of Obliquity of Slip in Normal Faults on Distribution of Open Fractures

Christoph von Hagke[1*†], *Michael Kettermann*[1], *Nicolai Bitsch*[1], *Daniel Bücken*[1], *Christopher Weismüller*[2] *and Janos L. Urai*[1]

[1] *Institute of Structural Geology, Tectonics and Geomechanics, RWTH Aachen University, Aachen, Germany,* [2] *Institute of Neotectonics and Natural Hazards, RWTH Aachen University, Aachen, Germany*

Edited by:
Valerio Acocella,
Università degli Studi Roma Tre, Italy

Reviewed by:
Daniele Trippanera,
King Abdullah University of Science and Technology, Saudi Arabia
Lorenzo Bonini,
University of Trieste, Italy

***Correspondence:**
Christoph von Hagke
christoph.vonhagke@emr.rwth-aachen.de

†Present Address:
Christoph von Hagke,
Institute of Geology & Palaeontology, RWTH Aachen University, Aachen, Germany

Specialty section:
This article was submitted to Structural Geology and Tectonics, a section of the journal Frontiers in Earth Science

Received: *23 July 2018*
Accepted: *30 January 2019*
Published: *25 February 2019*

Citation:
von Hagke C, Kettermann M, Bitsch N, Bücken D, Weismüller C and Urai JL (2019) The Effect of Obliquity of Slip in Normal Faults on Distribution of Open Fractures. Front. Earth Sci. 7:18. doi: 10.3389/feart.2019.00018

Close to surface, cohesive rocks fail in extension, which results in open fractures that can be several tens of meters wide, so-called massively dilatant faults. These open fractures make fault slip analysis in rifts challenging, as kinematic markers are absent. Faults in rifts often have oblique slip kinematics; however, how the amount of obliquity is expressed in the surface structure of massively dilatant faults remains enigmatic. Furthermore, the structures of oblique dilatant faults at depth is largely unconstrained. To understand the subsurface structures we need to understand how different obliquities of slip influence the surface structures and the corresponding structures at depth. We present analog models of oblique massively dilatant faults using different cohesive materials in a sandbox with adjustable basement fault slip obliquity from 0° to 90°. Experiments with different mean stress and material cohesion were run. Using photogrammetric 3D models, we document the final stage of the experiments and investigate selected faults by excavation. We show that fault geometry and dilatancy changes systematically with angle of obliquity. Connected open fractures occur along the entire fault to a depth of 6–8 cm, and as isolated patches down to the base of the experiments. Using the scaling relationship of our models implies that transition from mode-1 to shear fracturing occurs at depths of 250–450 m in nature. Our experiments show the failure mode transition is a complex zone and open voids may still exist at depths of at least 1 km. We apply our results to the dilatant faults in Iceland. We show that the relationship between angle of obliquity and average graben width determined on faults on Iceland matches experimental results. Similarly, fracture orientation with respect to fault obliquity as observed on Iceland and in our experiments is quantitatively comparable. Our results allow evaluation of the structure of massively dilatant faults at depth, where these are not accessible for direct study. Our finding of a complex failure mode transition zone has consequences for our understanding of fracture formation, but also influences our interpretation of fluid flow in rift systems such as magma ascent or flux of hydrothermal waters.

Keywords: fault, mechanics, geometry, dilatant, analog modeling, Iceland, rift

INTRODUCTION

Oblique rifts form when the relative movement of two plate boundaries is not perpendicular to the rift trend. More than 70% of Earth's divergent plate boundaries exhibit an oblique character (Woodcock, 1986; Philippon and Corti, 2016; Brune et al., 2018; Jeanniot and Buiter, 2018). Prominent examples include the Ethiopian rift, the Reykjanes Peninsula on Iceland, or the Mohns Ridge in the Arctic Ocean (e.g., Dauteuil and Brun, 1993; Grant and Kattenhorn, 2004; Corti, 2008). The influence of oblique spreading directions on fault geometries and orientations, as well as linkage processes and fault evolution, have been studied on crustal and lithospheric scale (Withjack and Jamison, 1986; Dauteuil and Brun, 1993; Clifton and Schlische, 2001, 2003; Clifton and Kattenhorn, 2006; Agostini et al., 2009; Brune, 2014; Zwaan et al., 2016; Zwaan and Schreurs, 2017). These studies show that obliquity of rifting influences geometry of structures at the surface, even though local stress reorientations may result in dip-slip motion along faults trending obliquely to extension direction (Morley, 2010; Corti et al., 2013; Philippon et al., 2015). Despite these efforts, we still know little about the detailed structures of these faults at depth, as they are commonly not accessible in the field. Furthermore, it remains poorly understood which structural features observed at the surface are characteristic for the amount of obliquity of slip. In this study, we investigate the influence of fault obliquity on fault evolution and geometries, focusing on the uppermost few 100 m of the rift system, where cohesive rocks fail in extension. This is vital, as understanding the geometry of open fracture distribution is essential for predicting fluid flux through the crust.

Analog modeling of oblique rifts has shown that many aspects of the geometric complexity of these systems can be reproduced, including releasing and restraining bends, fault step-overs, antithetic faults, bookshelf structures, or fault lenses. Early analog experiments of oblique rifting with soft clay (a mixture of mostly kaolinite and quartz) showed that steeply dipping rift parallel strike-slip faults form at obliquities $> 60^\circ$ (Withjack and Jamison, 1986). Lithosphere-scale models of oblique rifts with a layer cake of sand and silicone putty were used to establish first order geometries characterizing oblique rifts, such as mean fault trend differing from extension direction, common en-échelon pattern, or curved faults (Tron and Brun, 1991). Models including the asthenosphere represented by a honey syrup layer show that pull apart basins formed separately during early stages of rifting can still be recognized in the evolved unified rift (Mart and Dauteuil, 2000). These experiments were performed at obliquity angles of 15° and 30°. For highly oblique settings (60°), Clifton et al. (2000) and Clifton and Schlische (2001) used scaled clay models to show that fault nucleation, growth and interaction influences the time evolution and geometry of faults in oblique rifts. Experimental results are comparable to structures observed on an obliquely rifting section of the Mid Atlantic Ridge outcropping on the Reykjanes Peninsula, SW-Iceland, including three sets of faults: rift-perpendicular right-lateral oblique-slip faults, rift-subparallel left-lateral oblique-slip faults and normal faults striking 20° counter clockwise to the rift trend (Clifton and Schlische, 2001; Clifton and Kattenhorn, 2006). Lithosphere-scale centrifuge models with K-feldspar powder representing the brittle upper crust, plasticine the lower crust, and a plasticine-silicone mixture the upper mantle show that the angle of obliquity changes fault geometries observed at the surface, and that dominant strike-slip forms at obliquities $>45^\circ$ (Agostini et al., 2009). These studies show how obliquity of slip influences rift geometry. However, we have little knowledge on fault geometries in the upper few 100 m of the crust, where rocks fail in extension. Particularly it remains enigmatic how obliquity of slip influences the distribution of open fractures at surface and depth.

Massively dilatant faults form in cohesive rocks under low differential stresses, mostly close to the surface but also at depth under high pore fluid pressure (e.g., van Gent et al., 2010; Holland et al., 2011). They are ubiquitous features occurring at a range of scales, with opening widths from mm-size to several tens of meters as found along rift zones. Dilatant faults and associated fractures form high-permeability corridors and thus are major pathways for fluids such as water, hydrocarbons, or magma (Ingram and Urai, 1999; Ferrill and Morris, 2003; Crider and Peacock, 2004; Faulkner et al., 2010; Trippanera et al., 2015; Kettermann et al., 2016). Consequently, dilatant faults are of great economic interest for water and geothermal energy supply (Jafari and Babadagli, 2011), geohazard assessment and geodynamics (Crone and Haller, 1991; Caine et al., 1996; Gudmundsson et al., 2001; Ehrenberg and Nadeau, 2005; Belayneh et al., 2006; Lonergan et al., 2007), or mineral deposits (Zhang et al., 2008). Dilatant fault systems occur at mid ocean ridges (Gudmundsson, 1987; Angelier et al., 1997; Wright, 1998; Friese, 2008; Sonnette et al., 2010; Trippanera et al., 2014), intra-plate volcanoes (Holland et al., 2006), continental rifts (Acocella et al., 2003; Acocella, 2014; Trippanera et al., 2015), but also in cemented carbonates and clastic sediments (McGill and Stromquist, 1979; Moore and Schultz, 1999; Ferrill and Morris, 2003; Lonergan et al., 2007; Wennberg et al., 2008; van Gent et al., 2010; Kettermann et al., 2015). Their internal structure has been studied using analog and numerical models (Abe et al., 2011; Holland et al., 2011; Hardy, 2013; Kettermann et al., 2016). These studies, in combination with field observations, show that distinctive features of dilatant faults include sub-vertical fault scarps, rotating hangingwall blocks, and tens of meters wide open fractures (e.g., Acocella et al., 2003; Grant and Kattenhorn, 2004). Conceptual models for 3D geometries of dilatant faults are based on outcrops and scaled models (e.g., McGill and Stromquist, 1979; Schultz-Ela and Walsh, 2002; Holland et al., 2006; Sonnette et al., 2010; Vitale and Isaia, 2014). Analog and numerical models have been used to understand joint development, evolution of dilatant faults, and the influence of mechanical stratigraphy or pre-existing structures on surface geometries and fault processes (Clifton and Schlische, 2001; Seyferth and Henk, 2006; Schöpfer et al., 2007a,b; van Gent et al., 2010; Abe et al., 2011; Holland et al., 2011; Holohan et al., 2011; Hardy, 2013; Kettermann and Urai, 2015; Kettermann et al., 2015, 2016; Bonini et al., 2016). Most of these studies focus on dip-slip normal faults.

Here, we report results from analog models using cohesive powder as modeling material, representing the uppermost few km of basaltic crust. We build on results of Galland et al. (2006);

Holland et al. (2006); Kettermann et al. (2016), and van Gent et al. (2010) and extend these to oblique slip kinematics. We show that there is a first order similarity between surface expression of models and features observed in nature such as wide open fractures, tilted blocks, or fissures (**Figure 1**). This supports the inference that experiments will also be representative for the deeper structure and provide insights into fault structures that are commonly not accessible in the field, and into the time-evolution of dilatant faults. However, whether the surface structures are not only qualitatively but quantitatively comparable remains to be tested. To this end we quantitatively analyze the surface structure of fault zones developed in the sandbox and formed at different obliquity angles. We then compare our observations with field data from southwest and northern Iceland and finally we provide a conceptual model of evolution of massively dilatant faults in cohesive rocks.

EXPERIMENTS

Experimental Setup

To test the effect of obliquity on normal fault evolution we designed a new apparatus that allows for adjusting obliquity on a rigid basement fault in 15° steps. We use a single basement fault dipping at 60°, modeling structures at a single rift shoulder. The box has no lateral walls and the sample is set up with natural slopes in strike direction. Because of the slopes, the 70 cm wide sandbox provides fault length of about 40 cm (**Figure 2**). An advantage of this setup is the experiment is not affected by friction of sidewalls influencing the evolving geometries.

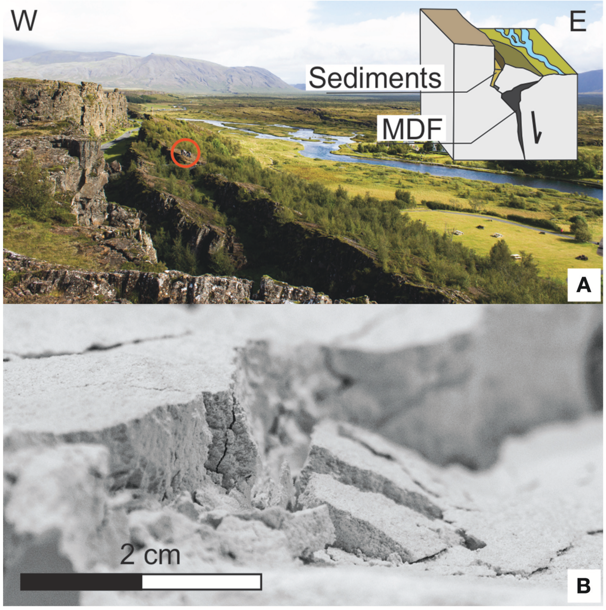

FIGURE 1 | Examples of massively dilatant faults in nature and experiment. **(A)** Thingvellir Fault in Iceland. For exact location see **Figure 10**. Red circle shows four geologists for scale. Top right shows sketch of fault geometry. The river flows on the hangingwall. Between hangingwall and footwall Massively Dilatant Faults (MDF) develop, which may be several tens of meters wide. These open fractures may be partly filled with sediments, water, ice or lava flows. Close the surface tilted blocks can form. **(B)** Experiment in hemihydrate powder shows open fractures and tilted blocks similar to the geometries observed in the field. Quantitative mapping of the geometry of analog examples may provide insights on the kinematics and deep structure of the system.

The box is driven by a geared motor to displacements of up to 70 mm. Our experiments are rate independent; we chose a speed of 3 mm/min so that fault evolution is captured in pictures taken in 10 s intervals. We use high-resolution digital single-lens reflex cameras to monitor the experiment. We use top- side- and front-view time lapse photography to create digital elevation models using "structure from motion" technique (Westoby et al., 2012), which allows for analyzing the structure of the fault zone in 3D. We use a vacuum cleaner to excavate parts of the fault zone from the top in order to look at the fault surface at resolutions much higher than by CT-scanning (Holland et al., 2006). This method has limitations: loose fragments of fault rock, bifurcations of the fault surface and parallel fault planes can produce structures which are difficult to interpret. Alternatively, we fill the open fractures with fine grained (<0.2 mm) sand to stabilize the structures. The experiments can then be sliced horizontally; however small open fractures and fractures which were not filled with sand may become damaged during excavation. Combining both excavation routines provides insights on the width of the fault zone and the distribution of open fractures down-dip.

We performed a first set of seven experiments with hemihydrate powder thickness of 20 cm and obliquity angles of 0°, 15°, 30°, 45°, 60°, 75°, and 90°. 0° obliquity corresponds to a dip-slip experiment; 90° corresponds to strike-slip faulting without a normal fault component. In a second set with a total of 20 experiments we used the same angles of obliquity but reduced powder thickness to 10 cm. We repeated the 10 cm hemihydrate experiments to test their reproducibility and to apply the different excavation methods. A third series was performed with a 10 cm thick layer of a 1:10 wt% hemihydrate-sand mix, also testing the seven different obliquities from 0 to 90°.

To analyze the results quantitatively, we use top view images of the time when the first visible fractures form, and images captured at 24 mm displacement. The latter is a stage where the fault has reached a mature phase, i.e., further extension is almost exclusively accommodated by widening of pre-existing fractures.

Material Properties and Scaling

Fine powders provide the cohesion and spatial resolution required to investigate dilatant fault processes (Walter and Troll, 2001). Holland et al. (2006) and Galland et al. (2006) REF presented the first experiments with full analog material characterization and thus a more complete understanding of the scaling relationships. Since then, different fine powders have been extensively used to model fractures in cohesive materials (Walter and Troll, 2001; Galland et al., 2006, 2015; Rodrigues et al., 2009; Gressier et al., 2010; van Gent et al., 2010; Holland et al., 2011; Trippanera et al., 2014). We use pure hemihydrate ($CaSO_4{*}^1/_2\ H_2O$) powder for our experiments, which is commercially available "Probau Baugips."

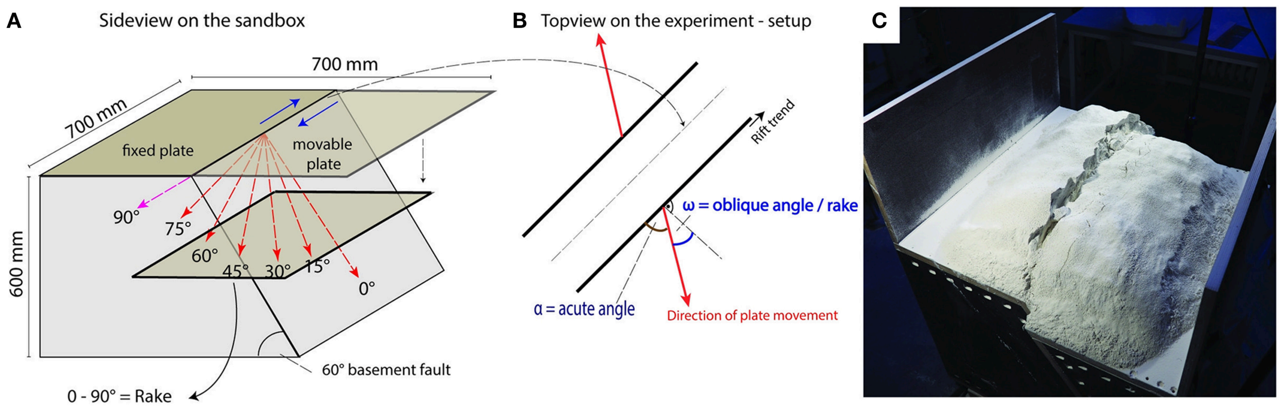

FIGURE 2 | Experimental setup. **(A)** The box consists of a stable block and a hangingwall block that can move at different obliquities ranging from dip-slip to strike-slip. Angle of the of basement fault has been set to 60°. **(B)** In top view, the rift trend is parallel to the basement fault, obliquity ω is defined as the angle between dip direction of the basement fault and direction of plate movement (i.e., ω = 0° for dip-slip, and ω = 90° for strike-slip; a dip-slip fault has no or 0° of obliquity). **(C)** Example picture of an experiment with 45° obliquity. Note the box does not have sidewalls, and thus the fault is unencumbered by sidewall friction.

TABLE 1 | Mechanical properties of analog materials.

Material	Density [kg/m^3]	True cohesion	Tensile strength
Hemihydrate	898	31.35	15.68
1:10 mixture	1,404	4.78	2.39

In a second experimental series, we use a 1:10 wt-% sand-powder mixture (1:10 mixture hereafter). This material has a 6.6 times lower cohesion than pure hemihydrate powder, representing weaker materials such as hyaloclastites, ashes, or scoria.

To characterize the materials, we measured densities and performed shear tests for normally consolidated and over-consolidated material, following the procedures of Holland et al. (2006) and van Gent et al. (2010). To characterize the tensile strength of cohesive powders at varying normal stresses, we constructed a tensile strength measuring setup similar to the Tensile Strength Tester (TST) of Schweiger and Zimmermann (1999). **Table 1** shows the results of material characterization. Shear tests and tensile strength measurements can be combined in a Cam-Clay type model (Roscoe et al., 1963; van Gent et al., 2010). This plot (**Figure 3**) summarizes material properties, showing friction angle, tensile strength and cohesion as a function of over-consolidation.

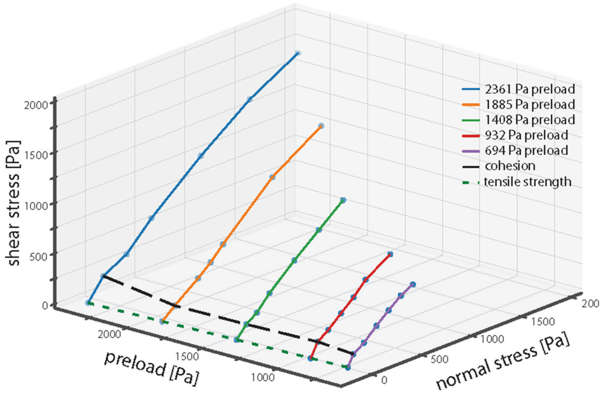

FIGURE 3 | Combination of material characteristics in a cam-clay type plot. Normal stress is plotted on the x-axis, shear stress along the y-axis. Along the z-axis, pre-loading is plotted. Stippled green line represents tensile strength, stippled black line is cohesion.

To determine the scaling factor, the density and strength of Icelandic basaltic rocks were used, as these rocks represent the natural prototypes of the experiments. Using the scaling relationships of Hubbert (1937) and the cohesion and density of pure hemihydrate powder, 1 cm in the model would represent ∼500–2,800 m of intact basalt, depending on chemistry or degree of weathering (see **Table 1** for material properties and **Supplementary Data Sheet 1** for detailed discussion and scaling calculations). However, for modeling large-scale systems, bulk rock strength must be considered. Cohesion of basaltic rock mass is one to two orders of magnitude lower than the value for intact rock (Schultz, 1996). This is because consists not of a homogenous rock package but an intercalation of effusive and eruptive lavas of different origins, variable thicknesses, and different degrees of fracturing. Consequently, 1 cm of the hemihydrate represents ∼50 m of basalt (**Table S1**). This value matches observations in the field, where scarps of that height are common (**Figure 1**).

Strength of the 1:10 mixture is 6.6 times weaker than the hemihydrate strength. This is similar to the strength contrast between intact basalt and weathered basalt or hyaloclastite or scoria. Thus, the 1:10 mixture is suitable to model weak rock as commonly outcropping in Iceland (**Figure 1**). 1:10 mixture is an alternative to crashed quartz sand, which is another material commonly used to model cohesive rocks (Galland et al., 2015). Details on material characterization and scaling are provided in the **Supplementary Data Sheet 1**.

RESULTS

For all experiments, we provide time-lapse videos in the digital appendix. All experiments have the same boundary conditions, that is a 60° dipping basement fault and no sidewalls along strike the fault. They differ in the amount of obliquity. Here, we first report results of hemihydrate powder experiments, Structures for the two sets of 10 and 20 cm powder thickness are very similar, why it makes sense to discuss them jointly. We then compare these with results from 1:10 mixture experiments, before reporting (semi-) quantitative results of all experiments.

Hemihydrate Powder Experiments

Surface Structures

En-échelon fractures are the earliest structures that develop in all but pure dip slip experiments after ∼2 mm of displacement (**Figure 4**). They develop above the basement fault, as well as above future antithetic faults. At low obliquities (0° and 15°), orientation of the earliest fractures is largely parallel to the basement fault. At obliquities of 30° and larger, en-échelon fractures form. Their orientation is variable, depending on the angle of obliquity (**Figure 5**). In experiments with obliquities between 15 and 45°, en-échelon structures are soon linked to form a through-going main fault. Both, underlapping and overlapping of fractures occur, leading to different linkage mechanisms. In most cases, fracture segments coalesce via hard linking of single underlapping fractures. Overlapping fractures develop into relay ramps that often breach during progressive deformation. Underlapping fault-parallel fractures often continue to grow parallel to the basement fault until they link with another fault segment along strike (see **Supplementary Videos**). En-èchelon fractures in the experiments with high obliquity (>60°) eventually also link to form a through-going fault, but linkage occurs after 5–10 mm of displacement (**Figure 5**; **Supplementary Videos**). En-échelon fractures form not only during early stages of deformation, but also develop later in the graben center (**Figure 5**). If orientated approximately perpendicular to the direction of relative movement of the hanging wall, dilatancy of these fractures increases gradually during the experiment. Generally, orientation, curvature, location as well as amount of en-échelon fractures control main fault evolution as individual segments link during progressive deformation.

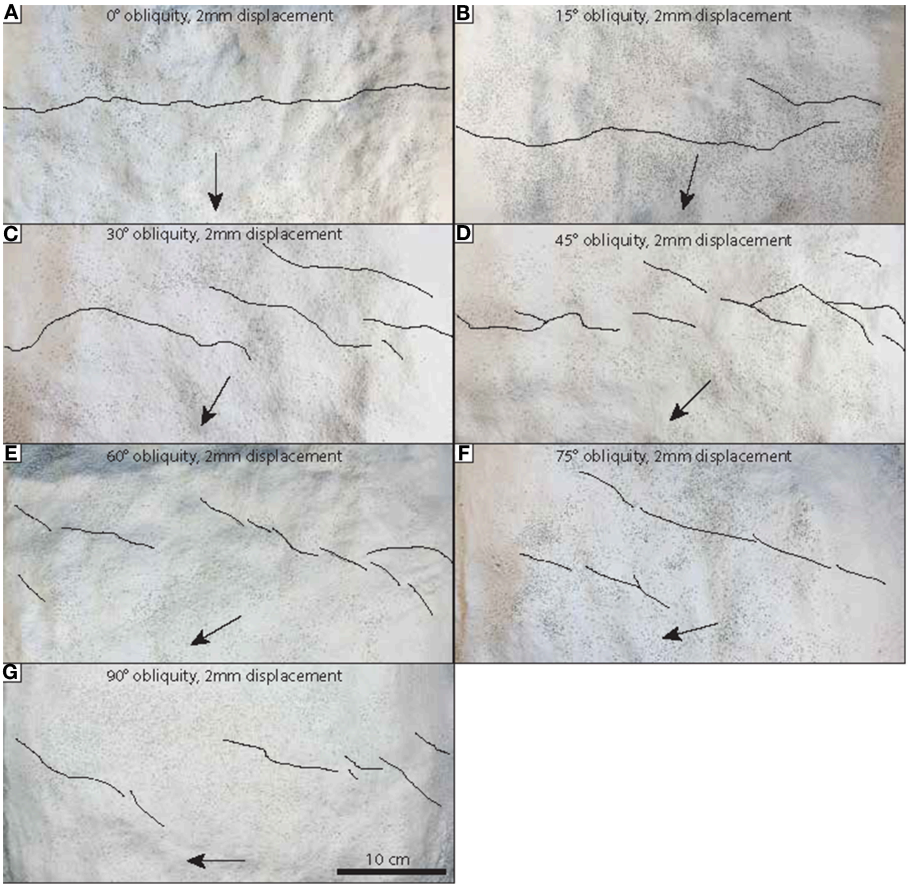

FIGURE 4 | Compilation of mapped initial fractures. With increasing obliquity, fracture orientation changes progressively. **(A–G)** Obliquity increases from 0 to 90°; fractures mapped after 2 mm displacement. These early fractures control geometries of mature faults. Experiments with 20 cm hemihydrate thickness. Black arrows denote movement direction of the lower plate.

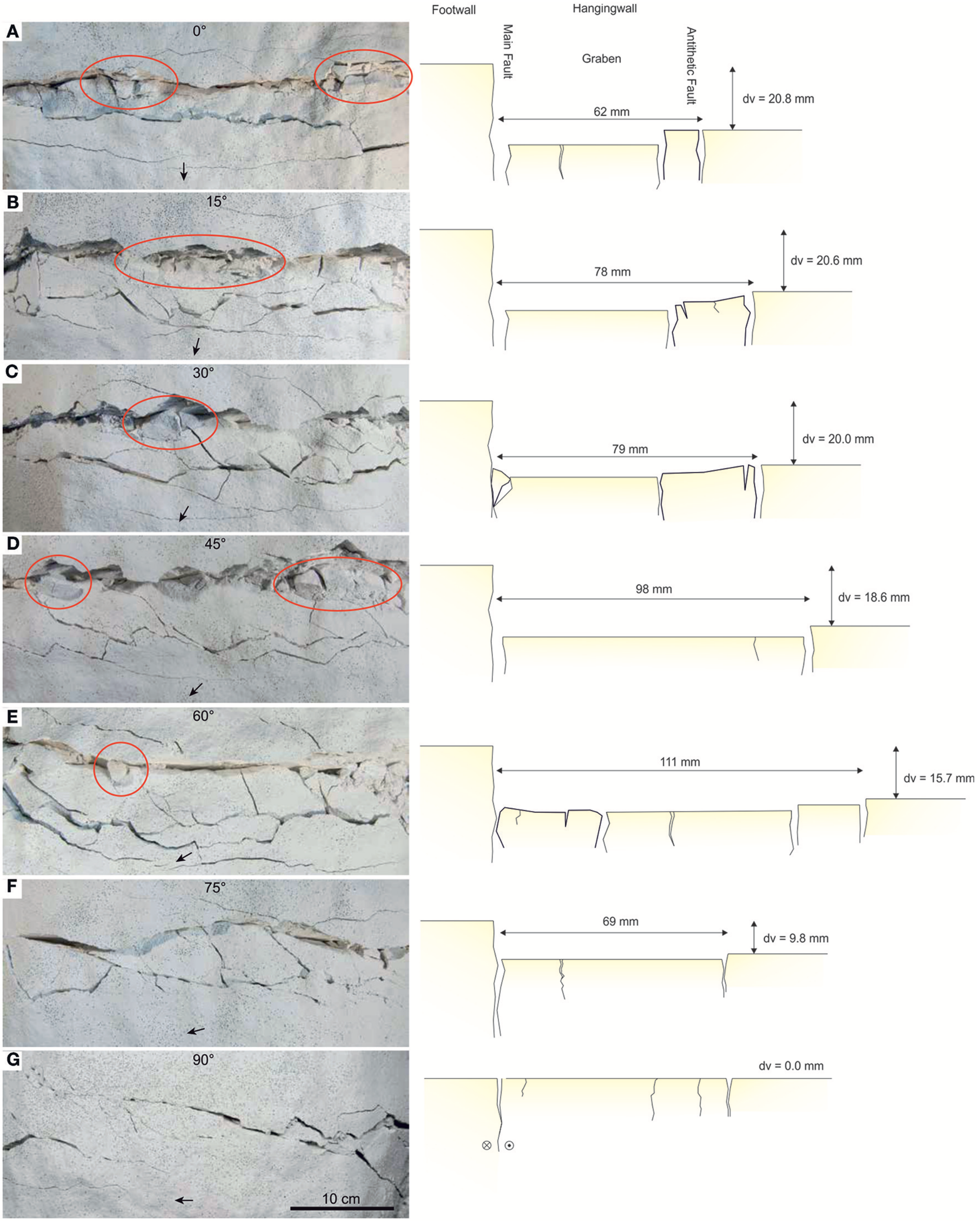

FIGURE 5 | Top view of final stages of 20 cm powder experiments and schematic cross section perpendicular to basement fault strike. **(A–G)** Obliquity increases from 0 to 90°. Same experiments as shown in **Figure 4**. Pictures were taken after 24 mm of deformation. This is a stage where the fault has reached a mature phase, i.e., further extension is almost exclusively accommodated by widening of pre-existing fractures. At obliquities between 0 and 60° a graben forms between the main fault and the antithetic fault on the hangingwall. At low obliquities, the entire fault shows dilatancy, whereas at higher obliquities dilatancy is restricted to releasing bends. Note how final fault geometries are influenced by orientation of early fractures (**Figure 4**). Red circles denote tilted blocks. Cross sections show vertical throw associated with fault movement (dv), and average widths of grabens.

Influence of strike-slip motion is most pronounced in all 75° and 90° obliquity experiments, where a set of R-shears forms at an angle between 15° and 30° to the underlying basement-fault. Because of linkage of en-échelon fractures during progressive deformation, fault geometries resemble a zig-zag pattern (**Figure 5**). Long R-Shears in experiments with obliquity of 75° and 90°, result in large wavelength of the structure (**Figures 5F,G**; **Figure S3**).

During progressive deformation, fractures step into the footwall, incorporating individual blocks of the main fault into the graben structure. This results in formation of tilted blocks and breached relay structures and thus decreasing fault sinuosity (defined as the curvilinear length of the fault divided by the linear distance between two points). This is most pronounced in experiments of 30–60° obliquity. This is surprising, as intuitively this effect may be expected to be highest for experiments with highest obliquities. However, in experiments of 75–90° obliquity, R-shears instead of early en-échelon fractures dominate final geometry (**Figure 5**; **Supplementary Videos**). Generally, in pure powder experiments, the final geometry of the main fault is established after 24 mm displacement.

Because the fault dip in the model is steeper than basement fault dip, antithetic faults develop, resulting in graben structures. Antithetic faults are prominent features that are observed in all experiments except in 75°-90° powder. Antithetic faults form commonly after 4–10 mm displacement (see **Supplementary Videos**). Consequently, total displacements and apertures are smaller, ranging between 1 and 5 mm. At antithetic faults, tilted blocks are rare. Resulting graben geometries, sizes and formation mechanism differ between the individual experiments. Grabens do not form in strike-slip experiments and are rare in 75° experiments. At low obliquities, narrow and deep grabens form, as observed in the 0° 10 and 20 cm powder experiments (**Figure 5**).

Dilatancy along the main fault has been observed in all experiments with hemihydrate powder (**Figure 5**). The amount and localization of dilatancy depends on obliquity, sinuosity, cohesion of the material, and presence or absence of tilted blocks. Tilted blocks are typical features formed at the model surface. They are features developing at the hangingwall and tilting toward the graben center. In high obliquity experiments, tilted blocks are bound to transtensional areas (releasing bends) and are absent in strike-slip experiments. Tilted blocks form in different amounts and sizes, show different amount of tilting as well as variable degrees of fragmentation. There is no clear relationship between amount of tilt and amount of displacement. In many low-obliquity experiments, the blocks rotate back toward the hangingwall during late stages of deformation or collapse into dilatant faults. They always dip approximately at 90° to the basement fault; we observe no variation of block orientation with increasing obliquity. In powder experiments, dilatant faults particularly fill where tilted blocks collapse. Where no tilted blocks form, wide dilatant fractures are present, and may be stable during the entire experiment.

Increase of obliquity changes the amount and location of dilatant parts along the main fault. The higher the angle of obliquity, the more dilatant releasing bends develop. In restraining bends, dilatancy is negligible. This effect becomes most pronounced at obliquities of 75 and 90°. In these experiments, open fractures are isolated. These fractures remain open during the entire experiments, as no tilted blocks form. Where restraining and releasing bends are less well-developed, the fault is open along its entire length.

Fault Plane and 3D Structure

To determine dilatancy at depth and to inspect individual fault surfaces, we excavated two experiments with 15° and 60° fault obliquity (**Figure 6**). It was only possible to excavate powder experiments, as the 1:10 mixture immediately collapsed and filled all open fractures. Open fractures exist down to depths of 6–8 cm, and can be linked to the surface or are found below collapsed tilted blocks. Dilatant fractures are interconnected along the entire fault in experiments with low obliquities. In the graben center, open fractures are observed down to a depth of 10 cm. Generally, the amount and size of dilatant fractures decreases with depth. Smaller fractures are rapidly filled with debris, particularly in areas where tilted blocks collapse. The deepest cavities of up to 12 cm have been preserved at antithetic faults. Dilatancy close to the surface is much lower as compared to the main fault, and thus more easily filled at shallow depths. This prevents loose material from reaching the lower parts. Furthermore, because tilted blocks are rare, the amount of debris falling into the fault is relatively small. Consequently, permeability of the antithetic faults may be higher at depth as compared to the main fault, both in 15° and 60° obliquity powder experiments. While rubble fillings partly clog the entire main fault, antithetic faults show connected cavities along strike (**Figure 6**).

With increasing obliquity, dilatancy along the main fault is often restricted to releasing bends at the surface, separated by intensively sheared zones. Consequently, dilatancy close to the surface becomes smaller with increasing obliquity. Releasing bends can remain open at depth as due to absence of tilted blocks little debris is filling them. This results in the (somewhat counterintuitive) general trend that faults with intermediate to high obliquities show dilatancy at greater depths than less oblique faults and a high vertical permeability. In all experiments, the area fraction of dilatancy decreases with depth.

Excavated fault planes show slickensides on the surfaces of shear fractures, tracing the moving direction of the hangingwall block (**Figure 7**). Slickensides are observable in all experiments. In strike slip experiments, they are observed from close to the surface down to the bottom of the experiment. In dip-slip experiments, they only occur at depths >5 cm, as closer to the surface only dilatant fractures occur. Size of the slickenside planes is variable along strike individual slip planes, and may range between few millimeters to centimeters.

Sand-Powder Mixture Experiments

Results from 1:10 mixture experiments, scaled to weaker rocks such as hyaloclastites or scoria, can be compared to powder experiments (**Figure 8**). Generally, the 1:10 mixture experiments display similar surface structures as observed in experiments with hemihydrate powder only. These include the formation of

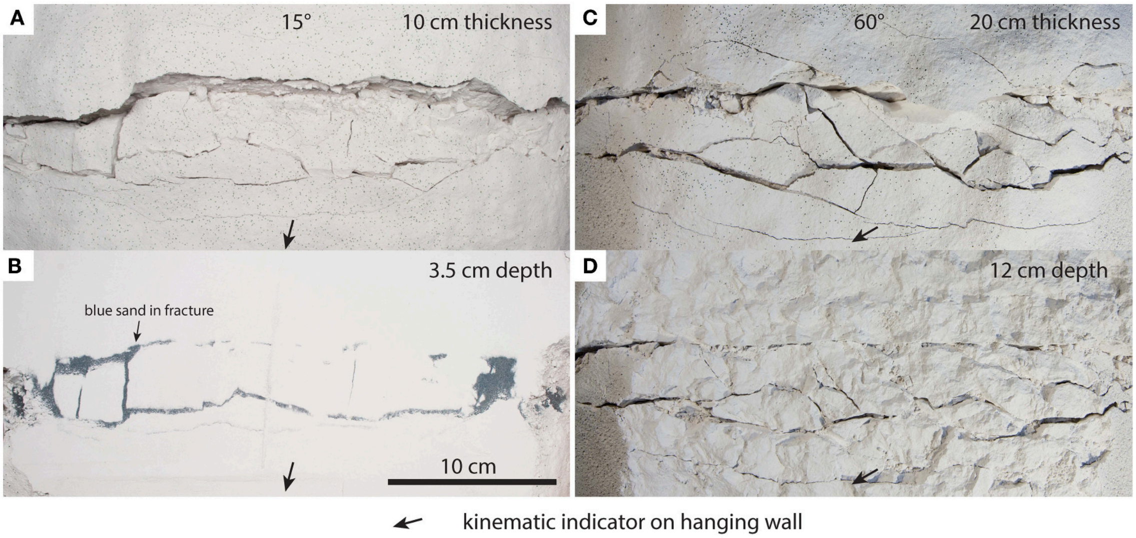

FIGURE 6 | Excavated experiments. Two excavation techniques have been applied to visualize open fractures at depth. First, open fractures were filled with dyed sand, and the experiment was sliced from top to bottom. **(A)** Top view on surface structures of experiment with 10 cm powder thickness and 15° obliquity. Down-thrown block at bottom, arrows indicate direction of movement. **(B)** Excavated experiment. Blue sand filled the open fractures at depth. At 3.5 cm wide open fractures exist at depth. Tilted blocks at the hangingwall collapsed and reduce area fraction of open gaps at the main fault. The antithetic fault remains open. **(C)** Top view of powder experiment with 20 cm powder thickness and 60° obliquity. **(D)** Surface excavated with vacuum cleaner. Vacuum cleaning results in more rugged surface as opposed to slicing, but small open fractures are unencumbered by the excavation process. Similar to **(B)**, the area fraction of open gaps is larger at the antithetic fault, as the main fault is filled with debris of collapsing tilted blocks.

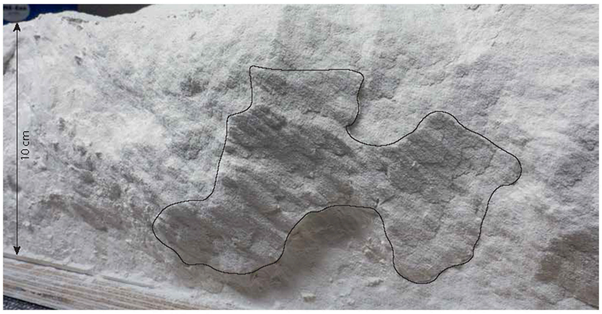

FIGURE 7 | Slickensides on an excavated fault surface of a hemihydrate experiment. Slickensides are best visible in the encircled area, and absent in dilatant parts of the fault.

cliffs, tilted blocks, (breached) relays, dilatant faults, antithetic faults, local areas of extension and compression as well as en-échelon faults and R-shears. We observe the strain is more localized in a narrow band around the basement fault trace. The influence of obliquity on the geometry and curvature of the antithetic fault is much smaller as compared to the hemihydrate powder. Generally, dilatant parts in the 1:10 mixture experiment are quickly filled as the sidewalls rapidly loose cohesion.

Like in the powder experiments, en-échelon fractures are the first observable structures at the surface. However, while in powder experiments fractures form over a large area they are mainly restricted to a narrow band in the 1:10 mixture experiments. In experiments with 30° obliquity and higher, underlapping fault segments do not link during early stages of the experiment. Instead, they continue to grow subparallel to each other, forming overlapping fault segments that are subsequently linked by the formation of a relay. During late stages of the experiments, these relays are breached and a through-going main fault forms (**Figure 8**, see also **Supplementary Videos**). Generally, in pure powder experiments, the final geometry of the main fault is established after 2 mm displacement. In 1:10 mixture experiments geometries change until 20 mm displacement.

Similar to powder experiments, in 1:10 mixture experiments grabens develop between main and antithetic fault except at high obliquities. Antithetic faults form generally after 4–10 mm displacement. The graben in 1:10 mixture experiments shows a decrease in graben width with increasing obliquity at lower obliquities as compared to powder experiments (**Figure 9**). At higher obliquities (>45°) 1:10 mixture experiments also show restraining and releasing bends, but apertures are much smaller than in the pure powder experiments and the open parts are less connected. The 75° 1:10 mixture experiment shows a distinct shear zone in its center without any opening (**Figure 8**). In summary, weaker material shows similar structural elements but observed geometries are often less pronounced than in powder experiments (e.g., smaller tilted blocks, narrow graben). Often features occur only transiently (**Supplementary Videos**), as sidewalls loose cohesion. Even small vibrations during the experiment can lead to a total disintegration of structures.

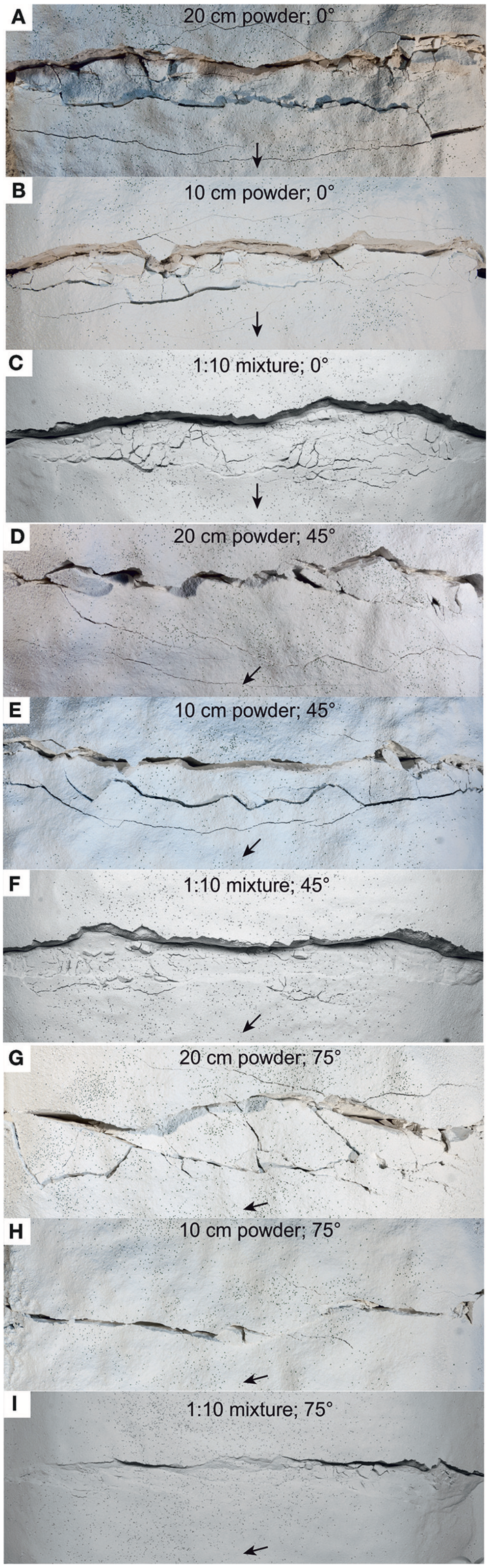

FIGURE 8 | Comparison between experiments with different powder thickness and material strength. **(A–C)** Experiments with 0° obliquity. In 20 and *(Continued)*

FIGURE 8 | 10 cm powder experiments, open fractures form on both sides of a central graben between main and antithetic fault. Tilted blocks from that may collapse and fill parts of the fault with rubble. In weaker material (1:10 mixture) open fractures are rapidly filled with material collapsing from the sidewalls **(C)**. Vertical cliffs form, but open fractures are only sustained close to the surface. **(D–F)** Experiments with 45° obliquity. A shallow and wide graben forms in the 20 cm powder experiment; the influence of early en-échelon fractures is visible in the hangingwall. Dilatant fractures at the surface are less continuous and narrower as compared to the experiments with 0° obliquity. In the 10 cm and 1:10 mixture experiments, a narrow graben forms **(F)**. Rotated and collapsed blocks oriented parallel to the basement fault are visible in all experiments. Dilatant fracturing in the 1:10 mixture experiments is much lower than in powder experiments. **(G–I)** Experiments with 75° obliquity. Typical strike-slip structures occur and fault geometry is dominated by orientation of R-shears. Dilatancy in powder experiments is most pronounced at releasing bends. Width of the fault zone decreases in the 1:10 mixture experiments **(I)**.

(Semi-) Quantitative Analysis

For quantitative analysis, we determine dilatancy, graben width, fracture distribution, sinuosity (defined as the ratio of the curvilinear length of the fault trace divided by fault length), and the shape and distribution of tilted blocks along strike the fault. Results of quantitative analysis are provided in **Figure 9**.

Graben width correlates with obliquity (**Figure 9A**). With increasing obliquity, grabens first tend to become slightly wider before decreasing at obliquities >45° for 10 cm powder experiments, and obliquities >60° for 20 cm powder experiments, respectively. Expectedly graben width is zero for 90° obliquity, i.e., strike slip faulting without normal fault component (**Figure 9**).

To characterize fracture orientation, we report mean azimuth with respect to the basement fault and length. Orientation of early fractures in dip slip experiments is dominantly parallel to the basement fault, as expected. With increasing obliquity en-échelon fractures form and the strike of the fractures changes progressively, until it stabilizes at an angle of 15 ± 5° with respect to the basement fault (**Figure 9B**). At final stage of deformation and zero obliquity (dip-slip deformation), fractures longer than 6 mm are oriented parallel to the basement fault. Smaller fractures occur in all directions. With increasing obliquity, fewer small fractures are observed, particularly in the graben, and their orientation is more similar to that of the main fault. Strike of fractures progressively changes with increasing obliquity, to a deviation of ∼20° from the basement fault in strike slip experiments (**Figure 9C**). This is consistent with expected orientations of R-Shears. In all experiments, the area between main and antithetic fault is progressively more fractured during the experiments. Therefore, mean fracture length does not change during the experiments.

A general decrease in fault dilatancy with increasing obliquity can be observed in all experiments (**Figures 9D,E**). The thickness of the powder layer does not change measured dilatancy, as it depends on slip of the basement fault (as opposed to graben width, which correlates with layer thickness). Similarly, dilatancy measured in pure powder experiments is comparable to values in 1:10 mixture experiments, and depends on the amount of horizontal displacement on the fault. However, dilatancy determined at the surface is always higher than the

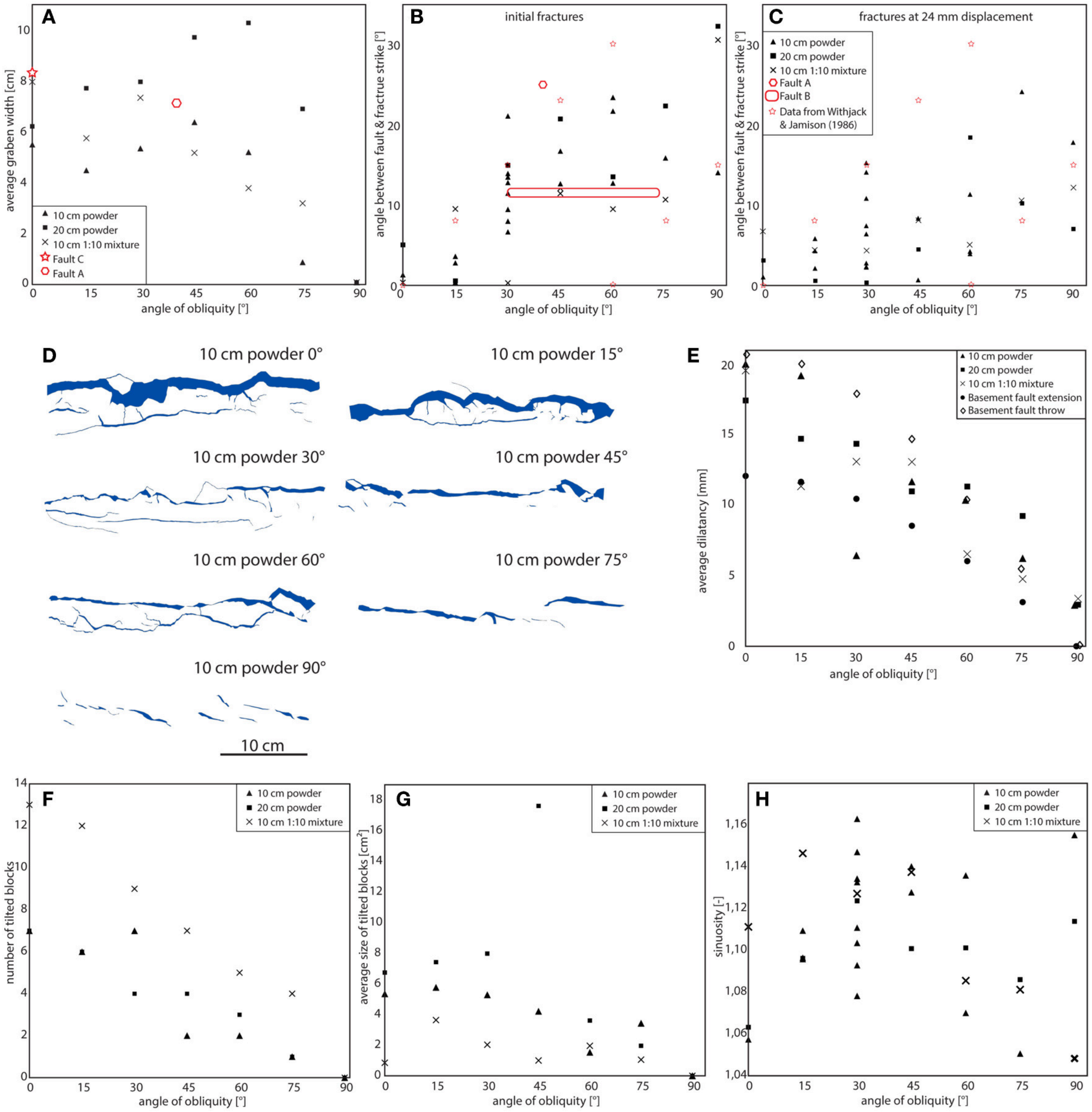

FIGURE 9 | Quantitative evaluation of all experiments. **(A)** Average graben width (i.e., the distance between the main fault and the antithetic fault) for experiments with 10 and 20 cm powder thickness and 1:10 mixture experiments as a function of obliquity. Graben width is constant or slightly increasing for low to medium obliquities and drops to zero at high obliquities. No graben forms in strike-slip experiments. Faults **(A,C)** are natural examples from Iceland (**Figure 13**). **(B)** Orientation of initial fractures for different obliquities as observed in experiments, as measured after 2 mm of displacement. Progressive change of strike direction can be seen until ∼45°, after which the orientation is roughly constant at an angle of 15 ± 5° with respect to the basement fault. Red markers represents fracture orientation observed at an evolving fault in Iceland. **(C)** Orientation of fractures as observed after 24 mm of displacement in experiments. Mean strike values are variable, but a general trend with increasing obliquity can be inferred. The values measured in our experiments are similar to values obtained from soft clay models (Withjack and Jamison, 1986) **(D)** examples of dilatancy as determined in 10 cm powder experiments. Top view of experiments, blue areas are dilatant parts. **(E)** Quantification of changes of dilatancy with increasing obliquity. The general decreasing trend can be seen in all experiments. Dilatancy scales with horizontal displacement on the basement fault (black dots). **(F)** Number of tilted blocks plotted vs. fault obliquity. A general decrease is observed. The size of tilted blocks remains constant for low obliquities, but decreases slightly when obliquity is larger than 45° **(G)**. This trend is less apparent for 1:10 mixture experiments. **(H)** Fault sinuosity as a function of obliquity.

horizontal displacement at the basement fault. This is an exciting observation, as it implies it is not straightforward to determine the amount of fault slip by measuring dilatancy. As observed in the sliced experiments, dilatancy deceases with increasing obliquity, as it is successively more concentrated in releasing bends in strike slip setting.

Closely linked to the amount of dilatancy is the number of tilted blocks along the main fault (**Figure 9F**). We counted the number and measured sizes of tilted blocks in 10 cm powder, 20 cm powder and 1:10 mixture experiments. The number of tilted blocks decreases with increasing obliquity. 1:10 mixture experiments show consistently more tilted blocks as compared to pure powder experiments. This is because the lower cohesion of the material results in fractionation of the blocks during the experiment. The size of tilted blocks is constant for low obliquities, but decreases at obliquities >45°. This trend is less apparent for 1:10 mixture experiments; size of tilted blocks in 1:10 mixture experiments is lower than in powder experiments. Blocks are largest at low obliquities and in 20 cm powder experiments (**Figure 9G**). During progressive deformation, tilted blocks are successively disintegrated. Consequently, the volume of open voids at the final stage of deformation is lower the more tilted blocks formed.

We determined sinuosity (defined as the ratio of the curvilinear length of the fault and its length) of the main fault in all experiments from mapping fault traces (**Figure 9H**). In powder experiments with 10 cm powder thickness, fault sinuosity increases for obliquities from 0 to 60°, followed by a decrease. This pattern evolves because early fractures and their linkage influence sinuosity (see also above). In low obliquity experiments, early fractures are oriented approximately parallel to the basement fault, resulting in a main fault with low sinuosity after early fracture linkage. With increasing obliquity, en-échelon fractures form, progressively deviating from basement fault strike (**Figure 9B**). Linkage leads to successively higher sinuosity of the mature fault. At obliquities of 60° and higher, initial fractures are crosscut by the later main fault, resulting in a sinuosity decrease. In experiments with 20 cm powder thickness, the decrease occurs already at 45°; for 1:10 mixture experiments, sinuosity of experiments with low obliquity is higher than observed in powder experiments. Despite these general trends, considerable variation of sinuosity can be observed in the repeated experiments (**Figure 9H**). This is because local material heterogeneities influence fault geometry. This implies that for individual faults, sinuosity is not always a good measure to determine fault obliquity. In summary, our analyses show the angle of obliquity influences fault geometry systematically. Parameters particularly indicative for obliquity are orientation of initial fractures, graben width, dilatancy at the surface and at depth, and number of tilted blocks. In this study, we focus mostly on dilatant structures, as other parameters have been studied earlier (see e.g., Acocella, 2014 for a recent review).

DISCUSSION

Analog Models

A general observation in our experiments is that the geometry of the fault is strongly affected by the orientation of the initial fractures. Location, orientation and densitiy of en-échelon fractures then affects the formation of tilted blocks, graben geometry, and fault sinuosity in the massively dilatant zone. The location of initial fractures is strongly dependent on local heterogeneities in the model material, and this has also been seen in DEM models (Abe et al., 2011). In the natural prototype, this corresponds to the state of jointing in the basalt (Holland et al., 2011). This implies that much of the variability of fractures is controlled by heterogeneities in the model material.

In our experiments, the deepest open fractures that can be followed along strike (i.e., the massively dilatant part of the fault) form to a depth of 5–9 cm in hemihydrate powder. Down to this depth no slickensides were observed. Below this, in the hybrid fracture zone, open fractures occur together with slickensided patches. Using our scaling relationship, the failure mode transition in the Iceland basalts occurs at depths of 250–450 m, possibly down to 1.5–2 km for stronger intact rock (see details on scaling in the **Supplementary Data Sheet 1**). Considering a tensile strength of 6 MPa and a mean density of 2,400 kg/m^3, Acocella et al. (2003) calculate the depth of failure mode transition to occur between 260 and 780 m, which is similar to our results. Depth of open fractures are comparable to estimates of Gudmundsson (1992), Acocella et al. (2003), Grant and Kattenhorn (2004), or Hardy (2013), who predict open fractures in basalts to occur down to depths of up to 800 m, c. 500 m, and several hundred meters, respectively, depending on tensile strength and rock density.

In our hemihydrate powder models, dilatant jogs still exist at the base of the box, i.e., at a depth of 20 centimeters, independent of fault kinematics. For intact basalt rock, this suggests that in dilatant jogs in normal faults may exist down to depths of ∼5 km and possibly deeper. Weak materials such as hyaloclastite or scoria are not able to sustain open fractures, at these depths. Consequently, depending on the material involved in the faulting process, as well as its degree of fragmentation and weathering, different depths of failure mode transition may occur in nature. Interlayering of weak and strong materials, as often observed in rift systems, will result in a complex failure mode transition zone that can be spread out over hundreds of meters (Smart and Ferrill, 2018).

The observation of dilatancy is consistent with findings of earlier studies, using hemihydrate powder and a dip-slip experimental setup (Holland et al., 2006; van Gent et al., 2010; Kettermann et al., 2016). This study shows additionally that obliquity influences the location of dilatant patches at depth and at the surface. While dip-slip experiments show a continuous connection of open fractures at the surface, strike-slip experiments show open fractures only in releasing bends. Average dilatancy at the surface reduces approximately linearly with increasing obliquity for the same slip vector (**Figure 9E**). In dip slip experiments, tilted blocks form, which are later disintegrated and fill the open fractures with rubble. With increasing obliquity, smaller tilted blocks form, and they have not been observed in our strike slip experiments. Hence, the open fractures are not filled with collapsing material.

Our models build on previous work that showed how obliquity influences rift geometries at crustal to outcrop scale. Discrete element models by Deng et al. (2018) show how fracture patterns at the surface are affected by a pre-existing weakness. Based on analog models, Withjack and Jamison (1986) predict maximum extension direction at oblique rifts (which is perpendicular to orientation of early en-échelon fractures) is a function of the angle between rift trend and displacement of the rift walls. This relationship has been corroborated in clay models and field data in Iceland (Clifton and Schlische, 2003), and is also observed in our experiments (**Figures 9B,C**). Furthermore, it has been suggested that fault sinuosity depends on obliquity, and reaches a maximum at 60° obliquity (Clifton et al., 2000).

This agrees with findings of our study (**Figure 9H**). However, our experiments show that fault sinuosity is variable, and depends on location of early fractures, their position with respect to the basement fault, and fault linkage processes. Particularly early fracture localization depends on small scale heterogeneities, and fault linkage processes do not depend on obliquity but on the local stress field and its variation (e.g., Mansfield and Cartwright, 2001; Clifton and Kattenhorn, 2006), as well as on the amount of stretching (Acocella et al., 2005); see Fossen and Rotevatn (2016) for a review. Sinuosity values obtained in our experiments vary between 1.05 and 1.16. For clay experiments; Clifton et al. (2000) obtained values between 1.4 and 2.26. The higher values are a result of two linking fault populations, whereas in our experiments sinuosity mostly depends on linkage of en-échelon fractures. As observed in our experiments and reported from field data (e.g., MacDonald et al., 1979; Kureth and Rea, 1981), sinuosity of the fracture zone in transform settings controls formation of releasing and restraining bends along the fault, which in turn influence dilatancy at depth.

Oblique Faults on Iceland

The results of our study may be applied to faults on Iceland located on the Mid Atlantic Ridge. Iceland is the only place on Earth where a mid ocean ridge is exposed above sea level, atop the extensional plate boundary separating the North American plate and the Eurasian plate. The reason for the aerial exposure of the Mid Atlantic Ridge in Iceland is the presence of a mantle plume, the Icelandic hotspot (Kaban et al., 2002). This mantle plume is the cause for increased volcanic activity and a wider, more complex deformation zone compared to oceanic plate boundaries where no plume activity occurs, as the relative movement of the plate boundary with respect to the Icelandic hotspot leads to rift jumps and unstable boundaries (Einarsson, 2008).

The mid-Atlantic ridge breaks up into a series of more of less oblique segments on the Icelandic main land (**Figure 10**). Zones of active rifting in Iceland are indicated by increased volcanic activity. Some of the rifting segments are purely divergent and characterized by normal faulting and fissuring. This type of fracturing and volcanism is observed in the Northern Volcanic Zone, and in two sub-parallel rift zones in South Iceland, the Western and Eastern Volcanic Zones, respectively. Other segments of the rift are transform zones characterized by strike-slip movement, such as the South Iceland Seismic Zone connecting the Western and Eastern Volcanic Zones, and the Tjörnes Fracture Zone in the North of Iceland. Additionally, oblique segments such as the Reykjanes Volcanic Belt are characterized by interlinked volcanism and strike-slip faulting (e.g., Einarsson, 2008; Savry and Cañón-Tapia, 2014). On Iceland dilatant faults similar to those observed along all mid ocean ridges are spectacularly exposed (e.g., Bubeck et al., 2017), **Figure 11**. It has been shown that these dilatant faults control fluid pathways and geothermal anomalies (Walter et al., 2018).

The Reykjanes Peninsula is situated in the south-western most part of Iceland (**Figure 10**). It is the direct prolongation of the Reykjanes ridge, i.e., the region where the mid-Atlantic ridge hits land. It is the only onshore oblique rift segment of the mid-Atlantic ridge, with the plate boundary oriented at ∼30% obliquity to spreading direction of the mid ocean ridge (Gudmundsson, 1987; Grant and Kattenhorn, 2004; Clifton and Kattenhorn, 2006; Villemin and Bergerat, 2013). The northern and western rift zones are dominated by axial spreading (Angelier et al., 1997; Friese, 2008; Sonnette et al., 2010; Hjartardóttir et al., 2012). In Thingvellir, located in the western rift zone, the rift axis trends approximately normal to the plate spreading direction at 30°. Similarly, the Krafla fissure swarm and the Theistareykir fissure swarm of the northern volcanic zone are also dominated by axial rift. Faults observed in Iceland show different amounts of dilatancy, ranging from several tens of meters to cm scale. Vertical depths of dilatant fractures measurable in the field can be >40 m, before the open fractures are filled with water, aeolian sand, or rubble (**Figure 11**). Vertical walls show lava flows with columnar joints and different degrees of fracturing, and weathering intensity varies. Particularly for large openings it is challenging to correlate geometries at the surface. Climbing into the open fractures allows correlations in deeper sections. Along all faults, tilted blocks occur, with lengths ranging from few to several hundreds of meters. As in our analog models, collapsing of the blocks into the open fractures can be observed. Relays and breached relays are common. Similar to our analog models, antithetic faults can be observed, with less vertical throw and dilatancy as compared to the main fault. In the Western Rift Zone, newly developing faults exist, showing en-échelon fractures as observed in our models. 1:10 mixture experiments may be compared to mechanically weaker rock, such as hyaloclastite, ignimbrites or tuff layers exposed in Iceland. These rocks are capable of supporting vertical cliffs but are much more prone to weathering. In weathered parts, no tilted blocks are preserved, and dilatant sections are often filled with rubble.

To quantitatively compare our analog models with nature, we focused on the Northern and Western Rift Zones, which offer exquisite outcrop conditions and good accessibility to faults (**Figure 11**). We used unmanned aerial vehicles to photograph the faults and successively create a digital elevation model at 5–15 cm resolution (**Figure 12**). In total, we cover an area of roughly 12 km². Details on data gathering and DEM building are provided in the **Supplementary Data Sheet 1**. These high-resolution data sets enable us to characterize fault geometries in the models at the decimeter scale. The average graben width represents the mean distance between the bounding faults, measured along scanlines between the manually mapped graben boundaries in intervals of 1 m orthogonally to the average fault strike. Angles of obliquity are calculated from the opening width and horizontal displacement of associated features along the fault. The strike values for the faults and en-échelon fractures were calculated as linear directional mean from the vectors of the fault traces.

We chose three faults, where geometries of dilatant fractures on both sides can be correlated to determine obliquity. Fault A is located in the Krafla Fissure Swarm (Kelduhverfi are) of the Northern Rift Zone, near the Asbyrgi canyon. Faults B and C are on the Reykjanes Peninsula in the Western Rift Zone. Fault B belongs to the Reykjanes and Fault C to the Vogar fissure swarms, respectively. Five en-échelon fractures were identified along fault A (in Asbyrgi), intersecting the main fault at an angle of 25°. Two antithetic faults are present, and the respective graben widths are

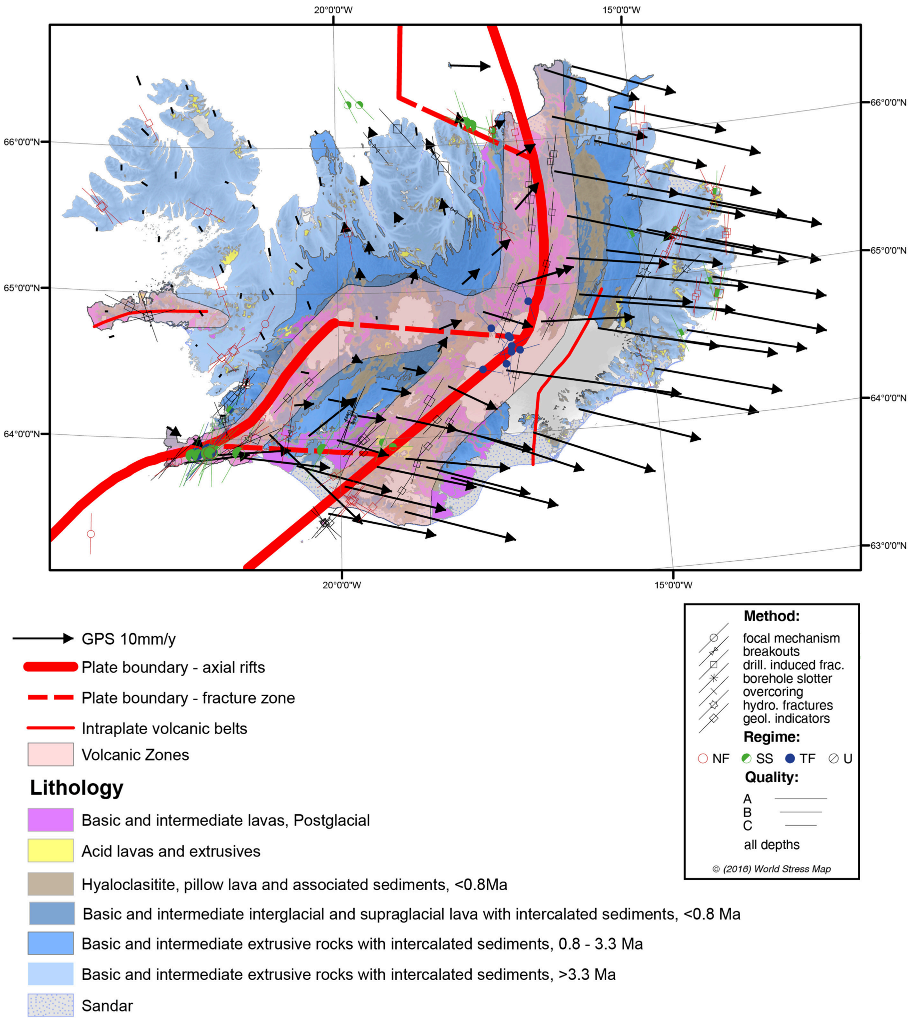

FIGURE 10 | Geological map of Iceland including main fault strucutres and volcanic belts. RR, Reykjanes Ridge; RP, Reykjanes Peninsula; RVB, Reykjanes Volcanic Belt; WVZ, EVZ, and NVZ, Western, Eastern and Northern Volcanic Zone; TFZ, Tjörnes Fracture Zone; Thv, Thingvellir. Geological map modified after Jóhannesson (2014). Rift zones from Thordarson and Larsen (2007), GPS data from Árnadóttir et al. (2008), stress data from Heidbach et al. (2016).

285 m for the proximal and 363 m for the distal fault. To quantify obliquity, we inspected geometries of the adjacent fault-plane traces and connected matching features. Fault A has an angle of obliquity of 41° (**Figure 12**). (The general extension direction in the area is orthogonal.) The 33° average strike direction of Fault B has been calculated from a vector from fault tip to fault tip of the analyzed segment. The initial en-échelon fractures were mapped as straight lines from fault tip to fault tip, from which the mean strike direction of all en-échelon fractures was calculated. Average en-échelon direction is 47°. Thus, the en-échelon fractures are oriented in an acute angle of 13.5° to the main fault. For fault C (Vogar) the mean graben width of 422 m has been measured from the main fault in the SE toward the next antithetic fault (**Figure 12**). The fault traces have been mapped and projected toward the adjacent fault trace to illustrate this fault has no oblique slip component. Measurements of graben width and orientation of early fractures are in good agreement with results from analog models (**Figure 9**). This suggests that structures are not only qualitatively but also quantitatively comparable, and thus the structures we observe at depth in our analog models are also present in the faults on Iceland. That surface structures in the field and the models are quantitatively comparable suggests structures at depth observed in the models are also present in nature. **Figure 13** shows a conceptual model of geometries at faults with different obliquities, summarizing robust features of the models. In dip slip deformation, tilted blocks form and dilatancy occurs at the main and the antithetic fault. Early fractures are oriented parallel to the main fault. Tilted blocks may collapse, filling open fractures. Because at antithetic faults tilted blocks are rare, open fractures remain open. Below a depth of ~6–8 cm, the volume of open fractures decreases and they are often not connected. This depth of open fractures is consistent with predictions from the Mohr-Coulomb diagram and natural data from fractured rocks (Gudmundsson, 1992;

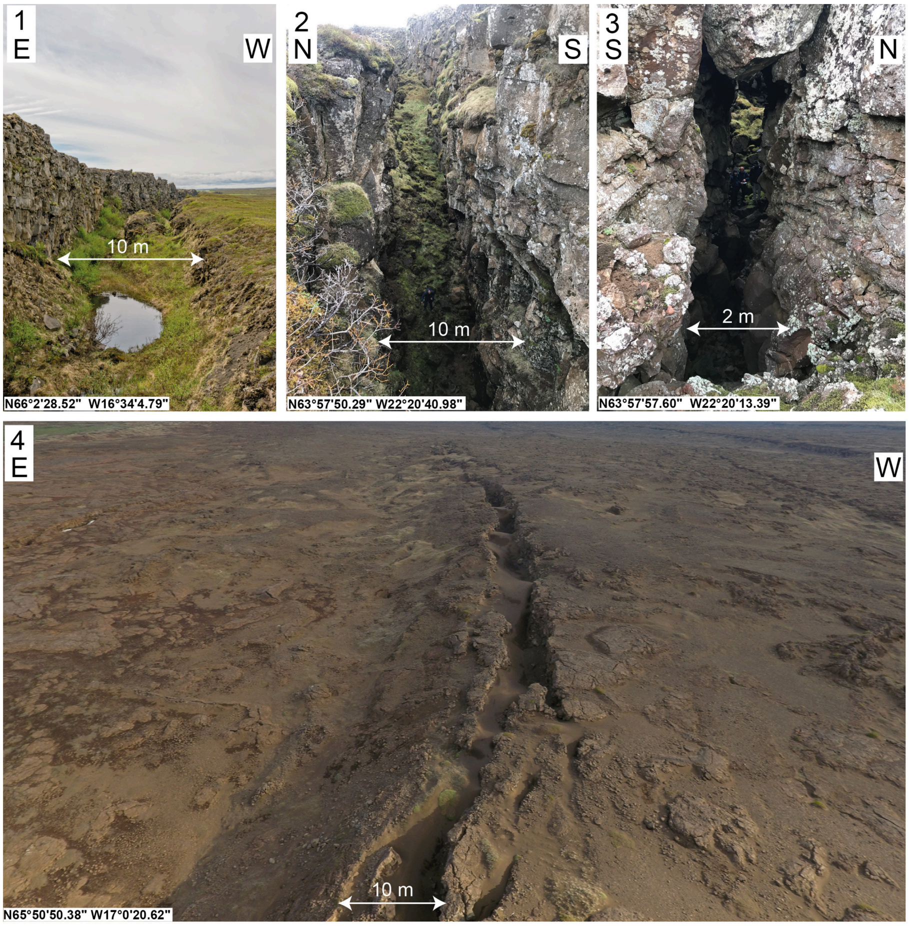

FIGURE 11 | Field sites on Iceland that may be compared to our analog models. Field impressions show exceptional outcrop conditions of the rift system, allowing for high-resolution mapping of structures close to the surface. Apertures of open fractures at the surface range from few cm to several tens of meters, as for instance observed at the famous world heritage site of Thingvellir. Correlating both sides of the open fracture is commonly possible at fractures of widths of 10 meters or less. Fractures are partly filled with rubble. Image 4 was taken with an unmanned aerial vehicle. Note the tilted block in foreground of image 4.

Acocella et al., 2003; Trippanera et al., 2015). The open fractures are partly filled with debris from collapsing tilted blocks. In strike-slip kinematics, dilatancy is constrained to releasing bends. This results in lower connectivity of open fractures at the surface.

Open fractures are present also at depths greater than predicted by standard mechanical models, reaching the base of our experiments. This implies the failure mode transition from dilatant to shear fracturing is a complex zone that may extend to depths of at least 1 km. Open fractures at depth are not connected along strike, but are separated by shear fractures. In our analog models this is witnessed by slickensides on the fault surfaces. During oblique slip early fractures are oriented at an angle to the main fault, which is increasing with increasing obliquity. This results in increasing sinuosity and possibly a decrease of connectivity of open fractures. Tilted blocks are smaller with increasing obliquity and are absent in strike-slip experiments. This influences the distribution of open fractures because collapsing tilted blocks fill open voids at depth. Releasing bends close to the surface and at depth can remain open where less tilted blocks are present. Dip-slip faults feature a pronounced decrease of dilatancy with depth, partly because of collapsing tilted blocks. Strike-slip faults do show a much weaker trend, and dilatant patches occur close to the surface and at depth.

This model may be applied to Iceland. We show that faults are dilatant to depths of several hundred meters. At depths below 450 m transition to shear fracturing occurs, and more intermittent dilatant fractures may exist at depths of at least one kilometer. Fractures may be well-connected at depth, and large caves may exist. At faults with an oblique component such as observed in the Northern Rift Zone and the Reykjanes Peninsula open fractures also exist at deep levels. However, their fracture network is less well-connected. Partly the faults may be more permeable at depth, as rubble fillings are less common. These findings extend our previous knowledge on the fault systems in Iceland and other rift zones (**Figure 14**). Close to the surface and down to depths of at least 450 m but as deep as the critical depth of ~800 m (Gudmundsson, 1992; Acocella et al., 2003), exclusively mode one fractures form. Below this, the failure mode transition to shear fracturing occurs. Our experiments show this is a complex zone in which locally open fractures

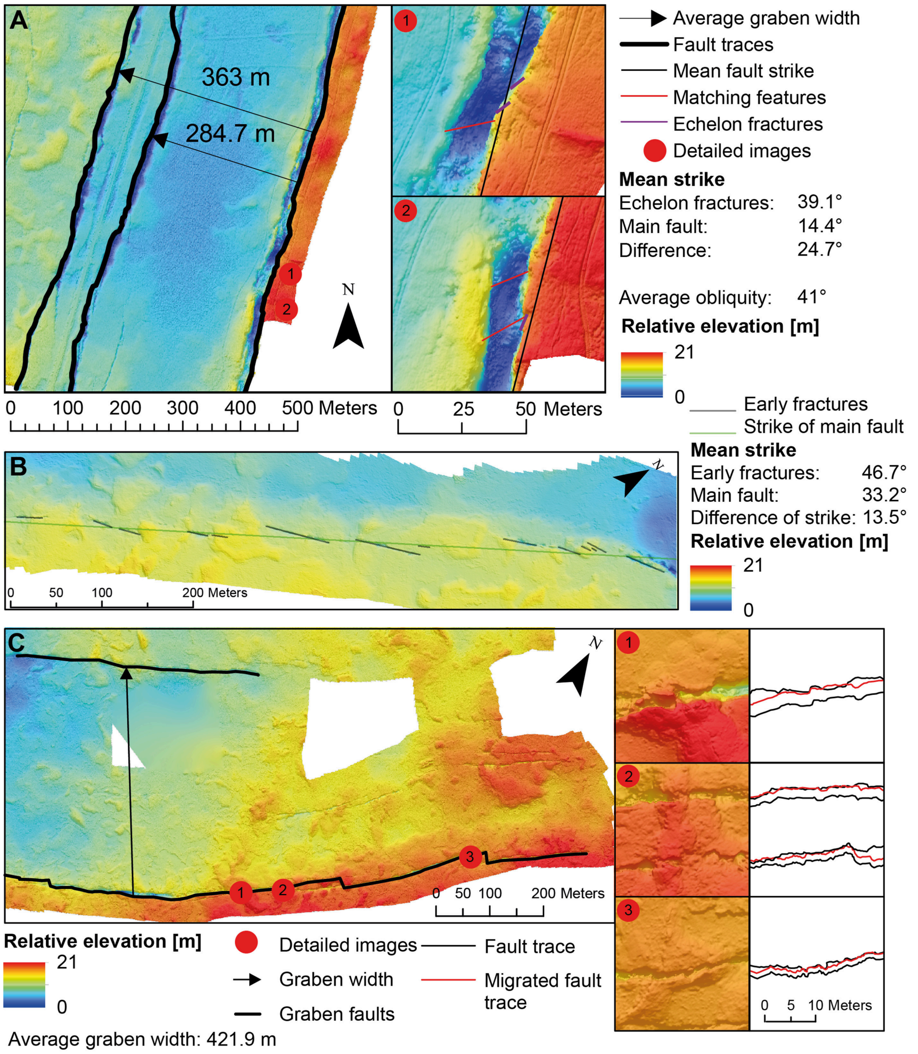

FIGURE 12 | High resolution digital elevation models of the selected field sites where obliquity can be determined. Fault **(A)** shows two antithetic faulty that can be used for determining graben width. Insets 1 and 2 show how both fracture surfaces can be linked. Fault **(B)** shows a series of early fractures and their angle to the main fault. Early fractures are indicative for fault obliquity. Fault **(C)** shows no obliquity, as determined by matching the respective fracture surfaces on both sides.

may be maintained to depths of at least 1 km, however in dilatant jogs. The deepest possible occurrence of open fractures has yet to be determined. This depth is not only controlled by mechanical stratigraphy resulting from interlayering of lava flows and ash and scoria layers; lava flows themselves have different strengths depending on their degree of fracturing and jointing. Furthermore, the occurrence of open fractures at depth depends on fluid pressure (Townend and Zoback, 2000); in cohesive carbonates dilatant open fractures have been observed at depths of several kilometers, associated with high fluid pressures (Hilgers et al., 2006; Grobe et al., 2018). We are not aware of fluid pressure data from Iceland measured at depths >1 km and consequently as of now the depth below which open fractures can be maintained remains speculative.

Below the complex zone of failure mode transition only shear fracturing can occur. Ultimately, the faults are connected to the dike system that accommodates rift extension, as has been suggested by field studies in different rift systems (Nobile et al., 2012; Phillips et al., 2017), as well as and analog models (Trippanera et al., 2014; Galland et al., 2015). Modeling of dike intrusion into cohesive powders shows that surface fractures propagate from top to bottom, growing toward the upward-propagating dike (Abdelmalak et al., 2012). Strain analysis of the experiments show that at the tip of the dike shear bands form which connect to the surface fault during later stages of the experiments (Abdelmalak et al., 2012). Field evidence for these processes is rare, as outcrops are very limited. In Iceland, few outcrops of the deeper section of the rift system exists on the east coast of the Trollaskagi Peninsula in North Iceland (Gudmundsson, 2000). Here, primarily dikes and normal faults have been observed. In some areas the faults are only observed in the shallow part of the lithological column

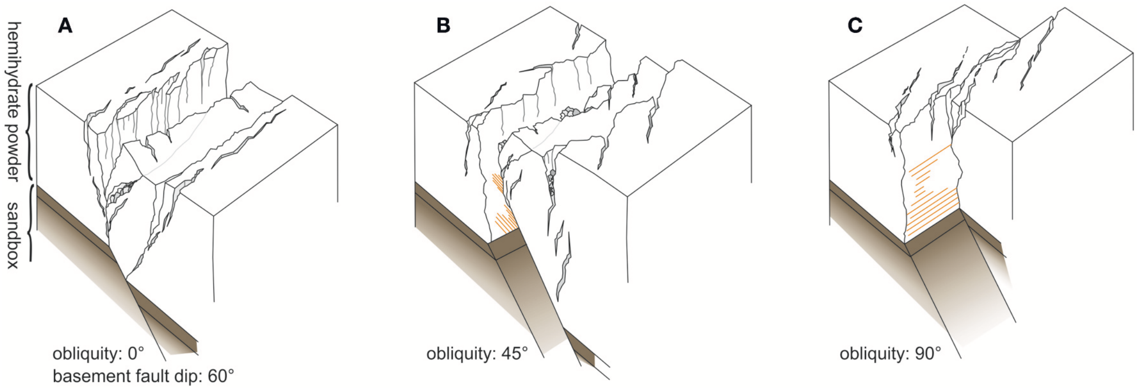

FIGURE 13 | Generic model of the observed structures depending on obliquity. **(A)** Dip slip deformation. A graben develops and tilted blocks form. Dilatancy is large close to the surface and decreases with depth. Fractures strike roughly parallel to the basement fault. In the graben, fractures perpendicular to the fault form occasionally. Sinuosity of the main fault is low. Open fractures are connected along the entire fault. **(B)** Oblique slip deformation. Graben is less wide, and tilted blocks are smaller. Sinuosity is high and influenced by early en-échelon fractures. Dilatancy occurs close to the surface and at depth. Red lines show slickensides on the fault surface. **(C)** Strike-slip faulting. No graben is present, and dilatancy is bound to Riedl Shears and releasing bends. This leads to potentially higher dilatancy at depth as compared to dip-slip faulting.

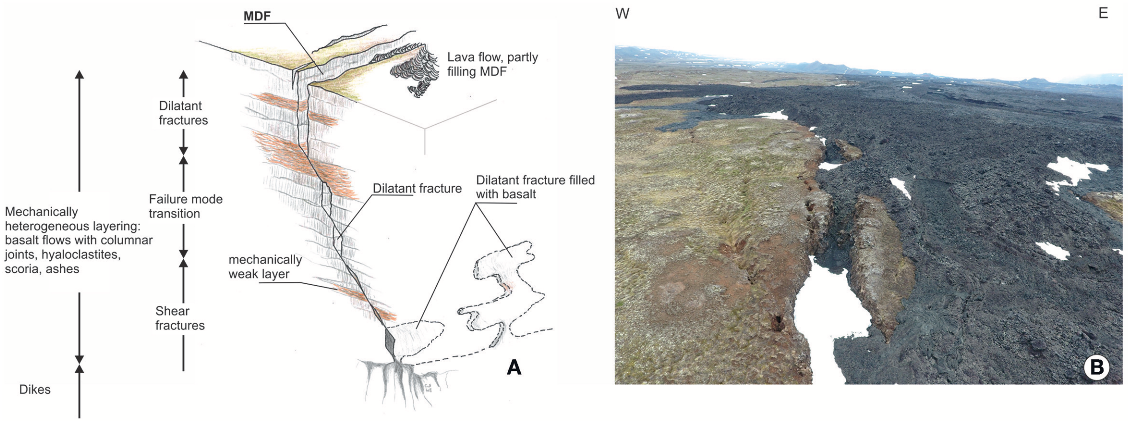

FIGURE 14 | (A) Conceptual model of the results applied to a rift (not to scale). In the uppermost section down to a depth of up to 800 m only dilatant fractures occur in cohesive rocks. Below this critical depth, transition to shear fracturing can be observed. Dilatant parts of the fault are isolated patches. Location of these patches depends on the heterogeneity and mechanical stratigraphy of the rock column. At greater depths elevated pore pressures may result in Mode 1 fracturing. The depth below which only shear fracturing can occur is unknown. If extension is large enough the surface fracture connects with the dike system at depth and may guide magma ascent. This can result in fissure eruptions and lava flows filling the MDF **(B)**.

(Acocella and Trippanera, 2016). These may represent areas where the connection between the feeder dike and fracture has not yet been established, or where rifting was fast enough that a new dike formed before fracture and dike connected. However, as soon as the dike and fracture connect, dike propagation will be guided by the fracture (Magee et al., 2016). Our models suggest that dike propagation a within the failure mode transition zone may be guided by occurrence of open fractures in the subsurface (**Figure 14**). This may help understanding how dikes propagate through the fractured crust. Additionally these findings may help guiding geothermal exploration in the area, as the fracture pattern influences fluid flux.

CONCLUSIONS

In this study, we studied the influence of fault obliquity on fault evolution and geometry in extensional settings, using cohesive powders. Our analog models offer a quantitative evaluation of how changes in the kinematic boundary conditions influences fault zone evolution in 3D. We conclude from our analog models that evolution of fault geometry, formation of tilted blocks, graben geometry and fault sinuosity are prescribed already during the earliest stages of deformation and a result of progressive linkage of early fractures. The most important aspect of this study is the variability of dilatant fractures developed during different slip obliquity. In particular our models show that

- Dilatancy changes progressively with increasing obliquity. Low fault obliquities are characterized by long open fractures with large apertures close to the surface and smaller dilatant fractures at depth, often filled with rubble.
- High fault obliquity results in dilatancy localized close to the surface, but more, deeper reaching vertical open conduits in releasing bends as compared to lower obliquities.
- Deepest open fractures occur at antithetic faults, as absence of tilted blocks and smaller opening width and displacement reduces the amount of available debris.
- Dilatancy determined at the surface is higher than horizontal displacement of the basement fault.

These findings have implications for our understanding of the connectivity of massively dilatant faults at depth. Main fault lateral connectivity at depth is decreasing with increasing obliquity as dilatancy is increasingly bound to small transtensional areas formed along the main fault.

These observations can be applied to faults in active rift systems such as Iceland. In addition to being qualitatively comparable, detailed mapping of outcrops in Iceland shows that quantitatively, structures are comparable, too. Consequently, our results allow prediction of the geometry of the structure of massively dilatant faults at depth, where these are not accessible for direct study. The finding that open fractures may possibly occur at depths of at least 1 km for strong rocks (even if only as isolated patches) has consequences for our understanding of geothermal systems. Open fractures form major fluid pathways, and knowing their distribution at depth is vital for fluid flux modeling studies.

AUTHOR CONTRIBUTIONS

CvH, MK, and JU conceived of the study, DB performed material tests with input from MK, JU, and CvH. NB performed experiments including fault analysis with input from other authors. CW produced and interpreted DEMs with input from MK and CvH. CvH and MK wrote the manuscript with input from other authors. All authors contributed to interpretation and discussion of the results. This is publication #1 of the MDF project.

FUNDING

This study is part of the project MDF: The structure and evolution of near-surface massively dilatant faults funded by the German Science Foundation (DFG). Grant number: 316167043.

ACKNOWLEDGMENTS

Daniele Trippanera, Lorenzo Bonini and a third reviewer are thanked for constructive comments that helped improve the manuscript. We thank Valerio Acocella for fruitful discussions and editorial handling.

SUPPLEMENTARY MATERIAL

The Supplementary Material for this article can be found online at: https://www.frontiersin.org/articles/10.3389/feart.2019.00018/full#supplementary-material

Supplementary Videos 1–15 | Videos show top view of the experiments with hemihydrate powder (10 and 20 cm thickness), and experiments with 1:10 mixture for comparison. Slip of basement fault is dextral.

REFERENCES

Abdelmalak, M. M., Mourgues, R., Galland, O., and Bureau, D. (2012). Fracture mode analysis and related surface deformation during dyke intrusion: results from 2D experimental modelling. *Earth Planet. Sci. Lett.* 359–360, 93–105. doi: 10.1016/j.epsl.2012.10.008

Abe, S., Van Gent, H. W., and Urai, J. L. (2011). DEM simulation of normal faults in cohesive materials. *Tectonophysics* 512, 12–21. doi: 10.1016/j.tecto.2011.09.008

Acocella, V. (2014). Structural control on magmatism along divergent and convergent plate boundaries: overview, model, problems. *Earth Sci. Rev.* 136, 226–288. doi: 10.1016/j.earscirev.2014.05.006

Acocella, V., Korme, T., and Salvini, F. (2003). Formation of normal faults along the axial zone of the Ethiopian Rift. *J. Struct. Geol.* 25, 503–513. doi: 10.1016/S0191-8141(02)00047-0

Acocella, V., Morvillo, P., and Funiciello, R. (2005). What controls relay ramps and transfer faults within rift zones? Insights from analogue models. *J. Struct. Geol.* 27, 397–408. doi: 10.1016/j.jsg.2004.11.006

Acocella, V., and Trippanera, D. (2016). How diking affects the tectonomagmatic evolution of slow spreading plate boundaries: overview and model. *Geosphere* 12, 867–883. doi: 10.1130/GES01271.1

Agostini, A., Corti, G., Zeoli, A., and Mulugeta, G. (2009). Evolution, pattern, and partitioning of deformation during oblique continental rifting: Inferences from lithospheric-scale centrifuge models. *Geochem. Geophys. Geosyst.* 10:Q11015. doi: 10.1029/2009GC002676

Angelier, J., Bergerat, F., Dauteuil, O., and Villemin, T. (1997). Effective tension-shear relationships in extensional fissure swarms, axial rift zone of northeastern Iceland. *J. Struct. Geol.* 19, 673–685. doi: 10.1016/S0191-8141(96)00106-X

Árnadóttir, T., Geirsson, H., and Jiang, W. (2008). Crustal deformation in Iceland: plate spreading and earthquake deformation. *Jökull* 58, 59–74.

Belayneh, M., Geiger, S., and Matthai, S. K. (2006). Numerical simulation of water injection into layered fractured carbonate reservoir analogs. *AAPG Bull.* 90, 1473–1493. doi: 10.1306/05090605153

Bonini, L., Basili, R., Toscani, G., Burrato, P., Seno, S., and Valensise, G. (2016). The effects of pre-existing discontinuities on the surface expression of normal faults: insights from wet-clay analog modeling. *Tectonophysics* 684, 157–175. doi: 10.1016/j.tecto.2015.12.015

Brune, S. (2014). Evolution of stress and fault patterns in oblique rift systems: 3-D numerical lithospheric-scale experiments from rift to breakup. *Geochem. Geophys. Geosyst.* 15, 3392–3415. doi: 10.1002/2014GC005446

Brune, S., Williams, S., and Müller, D. (2018). Oblique rifting: the rule, not the exception. *Solid Earth.* 9, 1187–1206.

Bubeck, A., Walker, R. J., Imber, J., Holdsworth, R. E., MacLeod, C. J., and Holwell, D. A. (2017). Extension parallel to the rift zone during segmented fault growth: application to the evolution of the NE Atlantic. *Solid Earth* 8, 1161–1180. doi: 10.5194/se-8-1161-2017

Caine, J. S., Evans, J. P., and Forster, C. B. (1996). Fault zone architecture and permeability structure. *Geology* 24, 1025–1028.

Clifton, A., and Schlische, R. W. (2003). Fracture populations on the Reykjanes Peninsula, Iceland: comparison with experimental clay models of oblique rifting. *J. Geophys. Res. Solid Earth* 108. doi: 10.1029/2001JB000635

Clifton, A. E., and Kattenhorn, S. A. (2006). Structural architecture of a highly oblique divergent plate boundary segment. *Tectonophysics* 419, 27–40. doi: 10.1016/j.tecto.2006.03.016

Clifton, A. E., and Schlische, R. W. (2001). Nucleation, growth, and linkage of faults in oblique rift zones: results from experimental clay models and implications for maximum fault size. *Geology* 29, 455–458. doi: 10.1130/0091-7613(2001)029<0455:NGALOF>2.0.CO;2

Clifton, A. E., Schlische, R. W., Withjack, M. O., and Ackermann, R. V. (2000). Influence of rift obliquity on fault-population systematics: results of experimental clay models. *J. Struct. Geol.* 22, 1491–1509. doi: 10.1016/S0191-8141(00)00043-2

Corti, G. (2008). Control of rift obliquity on the evolution and segmentation of the main Ethiopian rift. *Nat. Geosci.* 1:258. doi: 10.1038/ngeo160

Corti, G., Philippon, M., Sani, F., Keir, D., and Kidane, T. (2013). Re-orientation of the extension direction and pure extensional faulting at oblique rift margins: comparison between the Main Ethiopian Rift and laboratory experiments. *Terra Nova* 25, 396–404. doi: 10.1111/ter.12049

Crider, J. G., and Peacock, D. C. (2004). Initiation of brittle faults in the upper crust: a review of field observations. *J. Struct. Geol.* 26, 691–707. doi: 10.1016/j.jsg.2003.07.007

Crone, A. J., and Haller, K. M. (1991). Segmentation and the coseismic behavior of Basin and Range normal faults: examples from east-central Idaho and southwestern Montana, U.S.A. *J. Struct. Geol.* 13, 151–164. doi: 10.1016/0191-8141(91)90063-O

Dauteuil, O., and Brun, J.-P. (1993). Oblique rifting in a slow-spreading ridge. *Nature* 361, 145. doi: 10.1038/361145a0

Deng, C., Gawthorpe, R. L., Fossen, H., and Finch, E. (2018). How does the orientation of a preexisting basement weakness influence fault development during renewed rifting? Insights from three-dimensional discrete element modeling. *Tectonics* 37, 2221–2242. doi: 10.1029/2017TC004776

Ehrenberg, S., and Nadeau, P. (2005). Sandstone vs. carbonate petroleum reservoirs: a global perspective on porosity-depth and porosity-permeability relationships. *AAPG Bull.* 89, 435–445. doi: 10.1306/112304 04071

Einarsson, P. (2008). Plate boundaries, rifts and transforms in Iceland. *Jökull* 58, 35–58.

Faulkner, D., Jackson, C., Lunn, R., Schlische, R., Shipton, Z., Wibberley, C., et al. (2010). A review of recent developments concerning the structure, mechanics and fluid flow properties of fault zones. *J. Struct. Geol.* 32, 1557–1575. doi: 10.1016/j.jsg.2010.06.009

Ferrill, D. A., and Morris, A. P. (2003). Dilational normal faults. *J. Struct. Geol.* 25, 183–196. doi: 10.1016/S0191-8141(02)00029-9

Fossen, H., and Rotevatn, A. (2016). Fault linkage and relay structures in extensional settings—A review. *Earth Sci. Rev.* 154, 14–28. doi: 10.1016/j.earscirev.2015.11.014

Friese, N. (2008). Brittle tectonics of the Thingvellir and Hengill volcanic systems, Southwest Iceland: field studies and numerical modelling. *Geodinamica Acta* 21, 169–185. doi: 10.3166/ga.21.169-185

Galland, O., Cobbold, P. R., Hallot, E., De Bremond D'ars, J., and Delavaud, G. (2006). Use of vegetable oil and silica powder for scale modelling of magmatic intrusion in a deforming brittle crust. *Earth Planet. Sci. Lett.* 243, 786–804. doi: 10.1016/j.epsl.2006.01.014

Galland, O., Holohan, E., De Vries, B. V. W., and Burchardt, S. (2015). "Laboratory modelling of volcano plumbing systems: a review," in *Physical Geology of Shallow Magmatic Systems-Dykes, Sills and Laccoliths,* eds C. Breitkreuz and S. Rocchi (Berlin; Heidelberg: Springer), 1–68. doi: 10.1007/11157_2015_9

Grant, J. V., and Kattenhorn, S. A. (2004). Evolution of vertical faults at an extensional plate boundary, southwest Iceland. *J. Struct. Geol.* 26, 537–557. doi: 10.1016/j.jsg.2003.07.003

Gressier, J.-B., Mourgues, R., Bodet, L., Matthieu, J.-Y., Galland, O., and Cobbold, P. (2010). Control of pore fluid pressure on depth of emplacement of magmatic sills: an experimental approach. *Tectonophysics* 489, 1–13. doi: 10.1016/j.tecto.2010.03.004

Grobe, A., Virgo, S., Von Hagke, C., Urai, J. L., and Littke, R. (2018). Multiphase Structural evolution of a continental margin during obduction orogeny: insights from the Jebel Akhdar Dome, Oman Mountains. *Tectonics* 37, 888–913. doi: 10.1002/2016TC004442

Gudmundsson, A. (1987). Tectonics of the thingvellir fissure swarm, sw Iceland. *J. Struct. Geol.* 9, 61–69. doi: 10.1016/0191-8141(87)90044-7

Gudmundsson, A. (1992). Formation and growth of normal faults at the divergent plate boundary in Iceland. *Terra Nova* 4, 464–471. doi: 10.1111/j.1365-3121.1992.tb00582.x

Gudmundsson, A. (2000). Dynamics of volcanic systems in Iceland: example of tectonism and volcanism at juxtaposed hot spot and mid-ocean ridge systems. *Annu. Rev. Earth Planet. Sci.* 28, 107–140. doi: 10.1146/annurev.earth.28.1.107

Gudmundsson, A., Berg, S. S., Lyslo, K. B., and Skurtveit, E. (2001). Fracture networks and fluid transport in active fault zones. *J. Struct. Geol.* 23, 343–353. doi: 10.1016/S0191-8141(00)00100-0

Hardy, S. (2013). Propagation of blind normal faults to the surface in basaltic sequences: insights from 2D discrete element modelling. *Mar. Petrol. Geol.* 48, 149–159. doi: 10.1016/j.marpetgeo.2013.08.012

Heidbach, O., Rajabi, M., Reiter, K., and Ziegler, M. (2016). World stress map 2016. *Science* 277, 1956–1962. doi: 10.5880/WSM.2016.002

Hilgers, C., Kirschner, D. L., Breton, J. P., and Urai, J. L. (2006). Fracture sealing and fluid overpressures in limestones of the Jabal Akhdar dome, Oman mountains. *Geofluids* 6, 168–184. doi: 10.1111/j.1468-8123.2006.00141.x

Hjartardóttir, Á. R., Einarsson, P., Bramham, E., and Wright, T. J. (2012). The Krafla fissure swarm, Iceland, and its formation by rifting events. *Bull. Volcanol.* 74, 2139–2153. doi: 10.1007/s00445-012-0659-0

Holland, M., Urai, J. L., and Martel, S. (2006). The internal structure of fault zones in basaltic sequences. *Earth Planet. Sci. Lett.* 248, 286–300. doi: 10.1016/j.epsl.2006.05.035

Holland, M., Van Gent, H. W., Bazalgette, L., Yassir, N., Hoogerduijn-Strating, E. H., and Urai, J. L. (2011). Evolution of dilatant fracture networks in normal faults – evidence from 4D model experiments. *Earth Planet. Sci. Lett.* 304, 399–406. doi: 10.1016/j.epsl.2011.02.017

Holohan, E. P., Schöpfer, M. P. J., and Walsh, J. J. (2011). Mechanical and geometric controls on the structural evolution of pit crater and caldera subsidence. *J. Geophys. Res.* 116:B07202. doi: 10.1029/2010JB008032

Hubbert, M. K. (1937). Theory of scale models as applied to the study of geological structures. *Bull. Geol. Soc. Am.* 48, 1459–1520. doi: 10.1130/GSAB-48-1459

Ingram, G. M., and Urai, J. L. (1999). Top-seal leakage through faults and fractures: the role of mudrock properties. *Geol. Soc.* 158, 125–135. doi: 10.1144/GSL.SP.1999.158.01.10

Jafari, A., and Babadagli, T. (2011). Effective fracture network permeability of geothermal reservoirs. *Geothermics* 40, 25–38. doi: 10.1016/j.geothermics.2010.10.003

Jeanniot, L., and Buiter, S. J. (2018). A quantitative analysis of transtensional margin width. *Earth Planet. Sci. Lett.* 491, 95–108. doi: 10.1016/j.epsl.2018.03.003

Jóhannesson, H. (2014). *Geological Map of Iceland 1:600 000. Bedrock Geology, 2nd Edn.* Reykjavik: Icelandic Institute of Natural History.

Kaban, M. K., Flóvenz, Ó. G., and Pálmason, G. (2002). Nature of the crust-mantle transition zone and the thermal state of the upper mantle beneath Iceland from gravity modelling. *Geophys. J. Int.* 149, 281–299. doi: 10.1046/j.1365-246X.2002.01622.x

Kettermann, M., Grützner, C., Van Gent, H. W., Urai, J. L., Reicherter, K., and Mertens, J. (2015). Evolution of a highly dilatant fault zone in the grabens of Canyonlands National Park, Utah, USA – integrating fieldwork, ground-penetrating radar and airborne imagery analysis. *Solid Earth* 6, 839–855. doi: 10.5194/se-6-839-2015

Kettermann, M., and Urai, J. L. (2015). Changes in structural style of normal faults due to failure mode transition: First results from excavated scale models. *J. Struct. Geol.* 74, 105–116. doi: 10.1016/j.jsg.2015.02.013

Kettermann, M., Von Hagke, C., Van Gent, H. W., Grützner, C., and Urai, J. L. (2016). Dilatant normal faulting in jointed cohesive rocks: a physical model study. *Solid Earth* 7, 843–856. doi: 10.5194/se-7-843-2016

Kureth, C. L., and Rea, D. K. (1981). Large-scale oblique features in an active transform fault, the Wilkes fracture zone near 9° S on the East Pacific Rise. *Mar. Geophys. Res.* 5, 119–137.

Lonergan, L., Jolly, R. H. J., Rawnsley, K., and Sanderson, D. J. (2007). *Fractured Reservoirs.* London: Geological Society of London.

MacDonald, K. C., Kastens, K., Spiess, F., and Miller, S. (1979). Deep tow studies of the Tamayo transform fault. *Mar. Geophys. Res.* 4, 37–70. doi: 10.1007/BF00286145

Magee, C., Muirhead, J. D., Karvelas, A., Holford, S. P., Jackson, C. A., Bastow, I. D., et al. (2016). Lateral magma flow in mafic sill complexes. *Geosphere* 12, 809–841. doi: 10.1130/GES01256.1

Mansfield, C., and Cartwright, J. (2001). Fault growth by linkage: observations and implications from analogue models. *J. Struct. Geol.* 23, 745–763. doi: 10.1016/S0191-8141(00)00134-6

Mart, Y., and Dauteuil, O. (2000). Analogue experiments of propagation of oblique rifts. *Tectonophysics* 316, 121–132. doi: 10.1016/S0040-1951(99)00231-0

McGill, G. E., and Stromquist, A. W. (1979). The Grabens of Canyonlands National Park, Utah: geometry, mechanics, and kinematics. *J. Geophys. Res.* 84, 4547–4563. doi: 10.1029/JB084iB09p04547

Moore, J. M., and Schultz, R. A. (1999). Processes of faulting in jointed rocks of Canyonlands National Park, Utah. *Geol. Soc. Am. Bull.* 111, 808–822.

Morley, C. (2010). Stress re-orientation along zones of weak fabrics in rifts: An explanation for pure extension in 'oblique'rift segments? *Earth Planet. Sci. Lett.* 297, 667–673. doi: 10.1016/j.epsl.2010.07.022

Nobile, A., Pagli, C., Keir, D., Wright, T. J., Ayele, A., Ruch, J., et al. (2012). Dike-fault interaction during the 2004 Dallol intrusion at the northern edge of the Erta Ale Ridge (Afar, Ethiopia). *Geophys. Res. Lett.* 39:L19305. doi: 10.1029/2012GL053152

Philippon, M., and Corti, G. (2016). Obliquity along plate boundaries. *Tectonophysics* 693, 171–182. doi: 10.1016/j.tecto.2016.05.033

Philippon, M., Willingshofer, E., Sokoutis, D., Corti, G., Sani, F., Bonini, M., et al. (2015). Slip re-orientation in oblique rifts. *Geology* 43, 147–150. doi: 10.1130/G36208.1

Phillips, T. B., Magee, C., Jackson, C. A.-L., and Bell, R.E. (2017). Determining the three-dimensional geometry of a dike swarm and its impact on later rift geometry using seismic reflection data. *Geology* 46, 119–122. doi: 10.1130/G39672.1

Rodrigues, N., Cobbold, P. R., and Løseth, H. (2009). Physical modelling of sand injectites. *Tectonophysics* 474, 610–632. doi: 10.1016/j.tecto.2009.04.032

Roscoe, K., Schofield, A., and Thurairajah, A. (1963). Yielding of clays in states wetter than critical. *Geotechnique* 13, 211–240. doi: 10.1680/geot.1963.13.3.211

Savry, C., and Cañón-Tapia, E. (2014). Iceland structure and volcanism: an alternative vision based on the model of volcanic systems. *Tectonophysics* 636, 201–215. doi: 10.1016/j.tecto.2014.08.016

Schöpfer, M. P. J., Childs, C., and Walsh, J. J. (2007a). Two-dimensional distinct element modeling of the structure and growth of normal faults in multilayer sequences: 1. Model calibration, boundary conditions, and selected results. *J. Geophys. Res.* 112:B10401. doi: 10.1029/2006JB004902

Schöpfer, M. P. J., Childs, C., and Walsh, J. J. (2007b). Two-dimensional distinct element modeling of the structure and growth of normal faults in multilayer sequences: 2. Impact of confining pressure and strength contrast on fault zone geometry and growth. *J. Geophys. Res.* 112:B10404. doi: 10.1029/2006JB004903

Schultz, R. A. (1996). Relative scale and the strength and deformability of rock masses. *J. Struct. Geol.* 18, 1139–1149. doi: 10.1016/0191-8141(96)00045-4

Schultz-Ela, D. D., and Walsh, P. (2002). Modeling of grabens extending above evaporites in Canyonlands National Park, Utah. *J. Struct. Geol.* 24, 247–275. doi: 10.1016/S0191-8141(01)00066-9

Schweiger, A., and Zimmermann, I. (1999). A new approach for the measurement of the tensile strength of powders. *Powder Technol.* 101, 7–15. doi: 10.1016/S0032-5910(98)00117-X

Seyferth, M., and Henk, A. (2006). A numerical sandbox: high-resolution distinct element models of halfgraben formation. *Int. J. Earth Sci.* 95, 189–203. doi: 10.1007/s00531-005-0034-x

Smart, K. J., and Ferrill, D. A. (2018). Discrete element modeling of extensional fault-related monocline formation. *J. Struct. Geol.* 115, 82–90. doi: 10.1016/j.jsg.2018.07.009

Sonnette, L., Angelier, J., Villemin, T., and Bergerat, F. (2010). Faulting and fissuring in active oceanic rift: surface expression, distribution and tectonic-volcanic interaction in the Thingvellir Fissure Swarm, Iceland. *J. Struct. Geol.* 32, 407–422. doi: 10.1016/j.jsg.2010.01.003

Thordarson, T., and Larsen, G. (2007). Volcanism in Iceland in historical time: volcano types, eruption styles and eruptive history. *J. Geodyn.* 43, 118–152. doi: 10.1016/j.jog.2006.09.005

Townend, J., and Zoback, M. D. (2000). How faulting keeps the crust strong. *Geology* 28, 399–402. doi: 10.1130/0091-7613(2000)28<399:HFKTCS>2.0.CO;2

Trippanera, D., Acocella, V., and Ruch, J. (2014). Dike-induced contraction along oceanic and continental divergent plate boundaries. *Geophys. Res. Lett.* 41, 7098–7104. doi: 10.1002/2014GL061570

Trippanera, D., Acocella, V., Ruch, J., and Abebe, B. (2015). Fault and graben growth along active magmatic divergent plate boundaries in Iceland and Ethiopia. *Tectonics* 34, 2318–2348. doi: 10.1002/2015TC003991

Tron, V., and Brun, J.-P. (1991). Experiments on oblique rifting in brittle-ductile systems. *Tectonophysics* 188, 71–84. doi: 10.1016/0040-1951(91)90315-J

van Gent, H. W., Holland, M., Urai, J. L., and Loosveld, R. (2010). Evolution of fault zones in carbonates with mechanical stratigraphy–Insights from scale models using layered cohesive powder. *J. Struct. Geol.* 32, 1375–1391. doi: 10.1016/j.jsg.2009.05.006

Villemin, T., and Bergerat, F. (2013). From surface fault traces to a fault growth model: the Vogar fissure swarm of the Reykjanes Peninsula, Southwest Iceland. *J. Struct. Geol.* 51, 38–51. doi: 10.1016/j.jsg.2013.03.010

Vitale, S., and Isaia, R. (2014). Fractures and faults in volcanic rocks (Campi Flegrei, southern Italy): insight into volcano-tectonic processes. *Int. J. Earth Sci.* 103, 801–819. doi: 10.1007/s00531-013-0979-0

Walter, T., and Troll, V. (2001). Formation of caldera periphery faults: an experimental study. *Bull. Volcanol.* 63, 191–203. doi: 10.1007/s004450100135

Walter, T. R., Jousset, P., Allahbakhshi, M., Witt, T., Gudmundsson, M. T., and Hersir, G. P. (2018). Underwater and drone based photogrammetry reveals structural control at Geysir geothermal field in Iceland. *J. Volcanol. Geotherm. Res*. doi: 10.1016/j.jvolgeores.2018.01.010

Wennberg, O. P., Malm, O., Needham, T., Edwards, E., Ottesen, S., Karlsen, F., et al. (2008). On the occurrence and formation of open fractures in the Jurassic reservoir sandstones of the Snøhvit Field, SW Barents Sea. *Petrol. Geosci.* 14, 139–150. doi: 10.1144/1354-079308-739

Westoby, M., Brasington, J., Glasser, N., Hambrey, M., and Reynolds, J. (2012). 'Structure-from-Motion'photogrammetry: a low-cost, effective tool for geoscience applications. *Geomorphology* 179, 300–314. doi: 10.1016/j.geomorph.2012.08.021

Withjack, M. O., and Jamison, W. R. (1986). Deformation produced by oblique rifting. *Tectonophysics* 126, 99–124. doi: 10.1016/0040-1951(86)90222-2

Woodcock, N. H. (1986). The role of strike-slip fault systems at plate boundaries. *Philos. Trans. R. Soc. Lond. Ser. A Math. Phys. Sci.* 317, 13–29. doi: 10.1098/rsta.1986.0021

Wright, D. J. (1998). Formation and development of fissures at the East Pacific Rise: implications for faulting and magmatism at Mid-Ocean Ridges. *Fault. Magmat. Mid Ocean Ridges* 106, 137–151. doi: 10.1029/GM106p0137

Zhang, Y., Schaubs, P., Zhao, C., Ord, A., Hobbs, B., and Barnicoat, A. (2008). Fault-related dilation, permeability enhancement, fluid flow and mineral precipitation patterns: numerical models. *Geol. Soc. Lond.* 299, 239–255. doi: 10.1144/SP299.15

Zwaan, F., and Schreurs, G. (2017). How oblique extension and structural inheritance influence rift segment interaction: Insights from 4D analog models. *Interpretation* 5, SD119–SD138. doi: 10.1190/INT-2016-0063.1

Zwaan, F., Schreurs, G., Naliboff, J., and Buiter, S. J. H. (2016). Insights into the effects of oblique extension on continental rift interaction from 3D analogue and numerical models. *Tectonophysics* 693, 239–260. doi: 10.1016/j.tecto.2016.02.036

Conflict of Interest Statement: The authors declare that the research was conducted in the absence of any commercial or financial relationships that could be construed as a potential conflict of interest.

frontiers in Earth Science

ORIGINAL RESEARCH
published: 04 April 2019
doi: 10.3389/feart.2019.00062

An Inside Perspective on Magma Intrusion: Quantifying 3D Displacement and Strain in Laboratory Experiments by Dynamic X-Ray Computed Tomography

Sam Poppe[1]*, *Eoghan P. Holohan*[2], *Olivier Galland*[3], *Nico Buls*[4], *Gert Van Gompel*[4], *Benyameen Keelson*[4], *Pierre-Yves Tournigand*[1], *Joost Brancart*[5], *Dave Hollis*[6], *Alex Nila*[6] *and Matthieu Kervyn*[1]

[1] *Department of Geography, Vrije Universiteit Brussel, Brussels, Belgium,* [2] *UCD School of Earth Sciences, University College Dublin, Dublin, Ireland,* [3] *Physics of Geological Processes, The Njord Center, University of Oslo, Oslo, Norway,* [4] *Department of Radiology, Universitair Ziekenhuis Brussel (UZ Brussel), Vrije Universiteit Brussel, Brussels, Belgium,* [5] *Physical Chemistry and Polymer Science (FYSC), Vrije Universiteit Brussel, Brussels, Belgium,* [6] *LaVision UK Ltd., Oxford, United Kingdom*

Edited by:
Mélody Philippon,
UMR5243 Géosciences Montpellier,
France

Reviewed by:
Alessandro Tibaldi,
University of Milano-Bicocca, Italy
Eric B. Grosfils,
Pomona College, United States

***Correspondence:**
Sam Poppe
sam.poppe@vub.be;
sam35poppe@gmail.com

Specialty section:
This article was submitted to
Volcanology,
a section of the journal
Frontiers in Earth Science

Received: *12 October 2018*
Accepted: *13 March 2019*
Published: *04 April 2019*

Citation:
Poppe S, Holohan EP, Galland O, Buls N, Van Gompel G, Keelson B, Tournigand P-Y, Brancart J, Hollis D, Nila A and Kervyn M (2019) An Inside Perspective on Magma Intrusion: Quantifying 3D Displacement and Strain in Laboratory Experiments by Dynamic X-Ray Computed Tomography. Front. Earth Sci. 7:62.
doi: 10.3389/feart.2019.00062

Magma intrusions grow to their final geometries by deforming the Earth's crust internally and by displacing the Earth's surface. Interpreting the related displacements in terms of intrusion geometry is key to forecasting a volcanic eruption. While scaled laboratory models enable us to study the relationships between surface displacement and intrusion geometry, past approaches entailed limitations regarding imaging of the laboratory model interior or simplicity of the simulated crustal rheology. Here we apply cutting-edge medical wide beam X-ray Computed Tomography (CT) to quantify in 4D the deformation induced in laboratory models by an intrusion of a magma analog (golden syrup) into a rheologically-complex granular host rock analog (sand and plaster). We extract the surface deformation and we quantify the strain field of the entire experimental volume in 3D over time by using Digital Volume Correlation (DVC). By varying the strength and height of the host material, and intrusion velocity, we observe how intrusions of contrasting geometries grow, and induce contrasting strain field characteristics and surface deformation in 4D. The novel application of CT and DVC reveals that distributed strain accommodation and mixed-mode (opening and shear) fracturing dominates in low-cohesion material overburden, and leads to the growth of thick cryptodomes or cup-shaped intrusions. More localized strain accommodation and opening-mode fracturing dominates in high-cohesion material overburden, and leads to the growth of cone sheets or thin dikes. The results demonstrate how the combination of CT and DVC can greatly enhance the utility of optically non-transparent crustal rock analogs in obtaining insights into shallow crustal deformation processes. This unprecedented perspective on the spatio-temporal interaction of intrusion growth coupled with host material deformation provides a conceptual framework that can be tested by field observations at eroded volcanic systems and by the ever increasing spatial and temporal resolution of geodetic data at active volcanoes.

Keywords: magma intrusion, surface deformation, analog, laboratory modeling, X-ray computed tomography, digital volume correlation

KEYPOINTS

- Cutting-edge dynamic wide beam X-ray Computed Tomography and Digital Volume Correlation allows an inside view on the temporal behavior of analog magma intrusion in granular host material in laboratory experiments.
- Intrusion-induced 3D displacement and strain can be quantified over time.
- Thick cryptodomes form with distributed strain and mixed-mode fracturing in weak host materials.
- Thin dikes form with localized strain and opening-mode fracturing in strong host materials.
- A continuum of cone sheet geometries occurs in between these end-members.

INTRODUCTION

Magma intrusion induces crustal deformation, which in turn results in surface displacements, in changes in the local gravimetric field and in earthquake swarms, all of which can be monitored with geodetic and geophysical techniques (Brenguier et al., 2016; Fernández et al., 2017 and references therein; **Figure 1A**). Because direct observations of the intrusion emplacement are impractical, analytical, and numerical models are used to invert surface geodetic and/or geophysical monitoring data in order to constrain intrusion geometry and volume (Calais et al., 2008; Wauthier et al., 2012; Pinel et al., 2014; Sigmundsson et al., 2014; Fernández et al., 2017; Poland et al., 2017; Ebmeier et al., 2018). The most widely-used inverse geodetic models are limited by the simplifications and boundary conditions that are implemented to make mathematical solutions possible. For instance, they assume simple elastic or visco-elastic crustal deformation, and they represent intrusions as infinitesimal point pressure sources, finite pressurized spheroids or rectangular dislocation planes (Mogi, 1958; Okada, 1985; Yang et al., 1988; **Figure 1C**). In principle, model complexity can be increased by allowing for multiple sources (or segments) and by combining different source geometries (e.g., Battaglia et al., 2013; Sigmundsson et al., 2018).

Observations of natural outcrops of frozen and exhumed magmatic intrusions, however, have revealed a great variability and complexity of intrusion geometry. In terms of their shape, intrusions vary from thick stocks, cryptodomes, laccoliths, fingers, and cup shapes to thinner cone sheets, inclined sheets, layer-parallel sills and layer-perpendicular dikes (e.g., Gudmundsson, 2011; Bistacchi et al., 2012; Burchardt et al., 2013; Tibaldi, 2015; Galland et al., 2018; Magee et al., 2018; **Figure 1B**). Natural magma intrusion may also comprise complex combinations of the above-mentioned forms. Limitations of such field observations are that they represent a final static and commonly incomplete account of the intrusion processes, and they usually lack any link with the surface. Nonetheless, some aspects of these intrusion geometries, such as sharp tips on sheet intrusions, are consistent with Linear Elastic Fracturing Mechanics (LEFM) theory of their formation as planar, opening-mode hydraulic fractures containing low- to medium-viscosity magma propagating within an elastically deforming host rock (e.g., Pollard et al., 1983; Dahm, 2000b; Muirhead et al., 2012; Rivalta et al., 2015). Other aspects of some sheet intrusion geometries and their field relationships, such as folds and reverse faults around blunt, irregularly-shaped intrusion tips, are alternatively interpreted as formed by “viscous indentation” of magma within plastically deforming host-rock (e.g., Mathieu et al., 2008; Abdelmalak et al., 2012; Delcamp et al., 2014; Spacapan et al., 2017; Bertelsen et al., 2018; Haug et al., 2018).

Given the natural variability of intrusion geometry, the physical meaning of simple but widely-used numerical pressure source geometries and linear elastic host-rock rheologies remains subject to vivid scientific debate (Grosfils et al., 2013; Rivalta et al., 2015; Townsend et al., 2017; Haug et al., 2018). For instance, such simple elastic analytical and numerical models commonly associate sill-like intrusions with dome-shaped ground deformation, while they link vertical dikes with ground deformation patterns that comprise two bulges either side of a central trough —i.e., “bulges-and-trough”—and that are correspondingly M-shaped in cross-section, with the M centered above the dike’s upper tip (e.g., Mastin and Pollard, 1988; Lundgren et al., 2013; Sigmundsson et al., 2014, 2018). On the other hand, some non-elastic experimental models have linked both sill-like intrusions and vertical dikes with dome-shaped ground deformation patterns (Abdelmalak et al., 2012; Guldstrand et al., 2017).

Scaled laboratory experiments are complementary to field observations and numerical models, in that they can simulate under controlled conditions the geometric development of magma intrusions within materials of complex rheology (Hubbert, 1937; Barenblatt, 2003; Merle, 2015; Galland et al., 2018). To investigate the range of geometries observed in nature, past studies have involved various magma analogs (silicon PDMS, golden syrup, water, vegetaline oil) injected into either granular materials or transparent pig-skin gelatin (e.g., Donnadieu et al., 2001; Galland et al., 2014; Schmiedel et al., 2017; Kavanagh et al., 2018). These laboratory models have shown how intrusion geometry relates to a range of physical parameters, such as host rock strength and rheology, host rock anisotropy, overburden depth, magma injection velocity, and magma viscosity.

For experiments with opaque granular materials, magma is injected either against a transparent vertical sidewall in a “half-box” (e.g., Mathieu et al., 2008; Le Corvec and Walter, 2009; Abdelmalak et al., 2012) or “blindly” into the middle of the sand box (e.g., Mathieu et al., 2008; Delcamp et al., 2012; Galland et al., 2014). In the former case, the intrusion’s growth and host material displacement are quantified in 2D along the sidewall, but undesirable friction occurs between the granular material and the vertical sidewall exactly at the plane of observation, with an unknown effect on the quantified data (Le Corvec and Walter, 2009; Abdelmalak et al., 2012). In the latter case, the laboratory model surface displacement is quantified in 3D, but the host material’s internal structural evolution and the intrusion’s geometric development are not observed. In both cases, the final 3D geometries of the intrusion and host material structure are observed only by excavation at the end. This is why Rivalta et al. (2015) concluded that moving modeling into

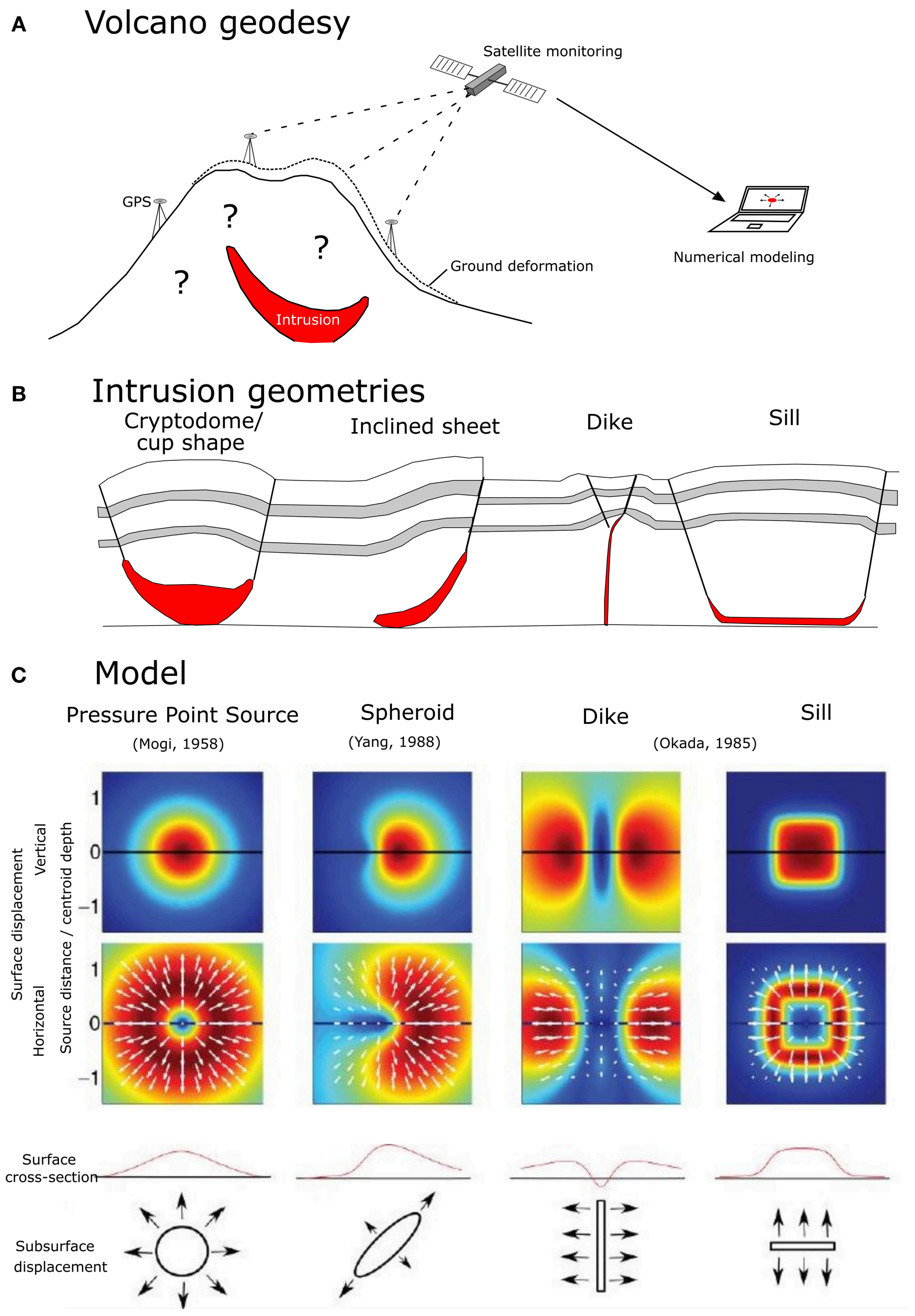

FIGURE 1 | (A) Subsurface geometrical growth of a magma intrusion can only be derived indirectly through numerical modeling of observations of seismicity or geodetic monitoring of the induced ground deformation using satellite monitoring (GPS, InSAR) or photogrammetry; **(B)** Geometries of now-chilled magma intrusions as observed at natural outcrops vary widely in geometry, ranging from thick cryptodomes and cup shapes over inclined sheets and cone sheets to thin vertical (i.e., dikes) and horizontal (i.e., sills) sheet intrusions (adapted from Schmiedel et al., 2017); **(C)** Geodetic models invert measured ground deformation to obtain best-fit magmatic deformation sources (i.e., intrusions) using a range of simplified geometries, ranging from Mogi point-sources to rectangular Okada sources (adapted from Sigmundsson et al., 2018).

3D plus time would be a most important step to improving our insight into magma propagation through the crust.

X-ray Computed Tomography (CT) provides a solution to observe the interior of laboratory models with granular host material (Mees et al., 2003; Kervyn et al., 2010; Cnudde and Boone, 2013). While high-resolution micro-CT scanners only allow imaging of the final model geometry (Kervyn et al., 2010; Poppe et al., 2015), medical scanners can acquire a time-series of 3D CT images at any desirable time interval, but at the cost of lower spatial resolutions (Schreurs et al., 2003). This technique has been used to image structural geometries in sandbox models simulating tectonic compression (Adam et al., 2013) or extension (Holland et al., 2011; Zwaan et al., 2018), or viscous magma intrusion in a sand-plaster cone (Rincón et al., 2018). Standard CT scanners have narrow X-ray detectors and only allow for "helical scanning" by moving the model box through the X-ray gantry while experimental deformation has to be arrested (Schreurs et al., 2003). The recent development of Digital Volume Correlation (DVC) techniques enables one to quantify displacement and strain in 4D throughout the entire laboratory model volume (Adam et al., 2013; Zwaan et al., 2018).

We here present a novel application of medical wide beam CT to dynamically image the propagation of analog magma intrusions of distinct geometries in laboratory models. For each intrusion geometry, the displacement and strain of the granular host material is quantified in 4D by using DVC on the CT time series, while the surface deformation is extracted as well. We demonstrate that cutting-edge medical wide beam CT makes *in-situ* dynamic scanning of fluid propagation possible through non-transparent material from a stationary position, and holds great potential to study the spatio-temporal behavior of deformation caused by igneous emplacement in the Earth's upper crust.

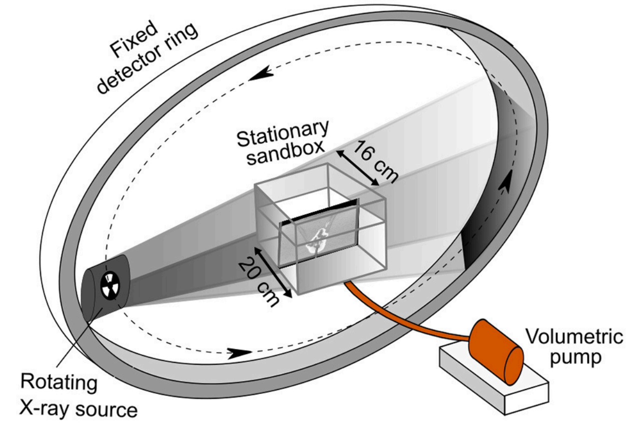

FIGURE 2 | Experimental set-up at the medical wide beam X-ray Computed Tomography scanner (GE Healthcare) of the UZ Brussel hospital, Belgium. The experimental box containing the compacted granular analog is in a fixed position—in the location of the "patient"—and is connected by a flexible tube to a computer-controlled constant-rate volumetric syringe pump containing the magma analog golden syrup. During syrup injection, a 3D CT image is obtained every 20 s over an acquisition time of 1 s by rotating an X-ray source within a fixed 16 cm wide X-ray detector ring.

METHODOLOGY

Model Materials and Protocol

The model materials are golden syrup and a mixture of silica sand and gypsum powder, analogs to magma and crustal host rock, respectively. Golden syrup (Tate and Lyle, UK) is a Newtonian fluid with a temperature-dependent density and viscosity (**Table 1**; **Appendix A**; Beckett et al., 2011). The ambient air temperature in the laboratory varied between 22 and 26°C, and was used to calculate syrup viscosities for each experiment (**Appendix A**). The silica sand was MAM1ST-300 of industrial purity from Sibelco (Mol, Belgium) and the gypsum powder was Goldband building plaster (Knauf). The mechanical behavior of silica sand as a Mohr-Coulomb material is well-constrained (Lohrmann et al., 2003; Panien et al., 2006). Mixing sand and plaster at different ratios creates a range of frictional-plastic granular materials with a more complex rheology that simulates a range of rock strengths; we used sand:plaster ratios of 90:10, 80:20, 65:35, and 50:50 wt%. Values of cohesion and angle of internal friction were obtained by using a combination of tensile tests and direct shear tests (cf. Abdelmalak et al., 2016) on samples that were poured and compacted manually to obtain the same bulk densities as those obtained in the model box. Direct shear test results were corrected for the silo effect (Mourgues and Cobbold, 2003). We ensured that humidity did not affect the strength of the granular materials by oven-drying overnight; ambient air humidity in the lab and CT room remained below 20% at all times.

For each experiment, a weighed mass of granular material was deposited in a plexiglas box (20 cm wide, 20 cm long, 16 cm high) by pouring to preserve homogeneous mixing of the sand with the fine-grained plaster. The material was then covered and shaken mechanically with a pneumatic vibrator (OT25, Olivibra, Italy) to compact down to 76–83% of its pre-compacted height to control density and hence mechanical strength. Shaking was limited to ∼10 s to avoid segregation of the coarse-size sand and fine-size plaster grains. Golden syrup was placed in a syringe and allowed to settle to remove air bubbles. The syringe was then placed on a syringe pump and connected through a flexible tube with the model box. The outlet of the tube with 4 mm internal diameter sat 2 cm above the base of the box within the granular material to avoid syrup percolating along the plexiglass-sand boundary. The experiment was started by injecting syrup into the sand at a constant pump discharge ranging between 20 and 100 ml hr^{-1} for different experiments. This is equivalent to flow velocities at the outlet of 0.4×10^{-3}-2.2×10^{-3} m s^{-1}. The pump—and the experiment—was stopped when syrup was seen to break through the model surface. The experiment box was then frozen overnight, after which the solidified intrusion was excavated to confirm its geometry. **Figure 2** illustrates the experimental set-up.

Model Scaling

Our laboratory models were scaled to obtain geometric, kinematic, and dynamic similarity with nature by using six dimensionless $\prod$-numbers (**Table 1**), similar to the dimensional analysis proposed by Galland et al. (2014). The length scaling of our experiments is 10^{-5} so 1 cm equals 1–2 km in nature. Our experiments thus simulate intrusion into the upper crust. Two dimensionless numbers are useful to explain the formation of contrasting intrusion geometries, and these are used to classify our experiments further on. The first is a geometric parameter scaling the intrusion depth to its source dimensions:

$$[1]\Pi_1 = \mathrm{H/d};$$

TABLE 1 | Scaling parameters and dimensionless equations used to compare the experiments to nature; natural values come from Schultz (1996), Galland et al. (2014), and Merle (2015).

Parameter	Symbol and Unit	Experiment	Nature
GENERAL			
Gravitational acceleration	g (m.s^{-2})	~9.81	~9.81
MAGMA			
Density	ρ_m (kg.m^{-3})	1,440	2,500–2,700
Viscosity	η (Pa.s)	20–70	10^1-10^7
Inlet diameter	d (m)	0.004	1×10^{-1}-5×10^4
Injection velocity	v (m.s^{-1})	0.4×10^{-3}-2.2×10^{-3}	1×10^{-4}-1×10^{-1}
HOST MATERIAL			
Overburden height	H (m)	0.06–0.10	1×10^1 -15×10^3
Density	ρ_r (kg.m^{-3})	1,268–1,700	2,500–2,700
Cohesion	C (Pa)	66–298	10^5-10^8
Internal friction angle	Φ (°) $= \Phi_3$	21–35	25–45
DIMENSIONLESS PARAMETERS			
Geometry	$\prod_1 = H/d$	15–25	2×10^{-4}-1.5×10^5
Viscous stress:rock strength	$\prod_2 = \eta v/Cd$	0.02–0.6	2×10^{-15}-1×10^2
Gravitional stress:cohesion	$\prod_4 = \rho_r gH/C$	2.5–25.3	$0.015\text{x}10^{-4}$-$4\text{x}10^3$
Reynolds number	$\prod_5 = Re = \rho_m dv/\eta$	0.3×10^{-3}-6.3×10^{-3}	2.5×10^{-9}-1.4×10^6
Magma buoyancy	$\prod_6 = 1 - \rho_m/\rho_r$	–0.14–0.15	-8×10^{-2}-7×10^2

where H is the overburden height above the analog magma inlet and d is the diameter of that inlet. The second parameter scales the viscosity of the magma to the strength of the analog host material:

$$[2]\Pi_2 = \eta v/Cd;$$

Where η is the analog magma viscosity, v is the analog magma intrusion velocity at the inlet and C is the host material's cohesion. The other four parameters scale host material strength, lithostatic stress, analog magma flow regime and buoyancy (**Table 1**).

In contrast to natural rocks, it is currently unclear how elastic properties could be quantified in granular analogs (Lohrmann et al., 2003; Panien et al., 2006; Ritter et al., 2016; Galland et al., 2018). In terms of cohesion and angle of internal friction, however, the low-strength granular mixtures (90:10 wt% sand-plaster) represent unconsolidated to weakly consolidated sediments, breccias or tuffs; medium-strength granular mixtures (80:20 and 65:35 wt% sand-plaster) represent weakly consolidated or heavily fractured sediments and rocks, such as shale; and high-strength granular mixtures (50:50 wt% sand-plaster) represent competent and consolidated rocks, such as limestone or crystalline rock (Mathieu et al., 2008; Abdelmalak et al., 2016; Schmiedel et al., 2017; Galland et al., 2018). Whereas regional stress fields, topographic loads, and pre-existing structures are known to affect magma intrusion emplacement (Acocella and Neri, 2009; Sigmundsson et al., 2014; Koehn et al., 2019), our laboratory models assume the simple boundary conditions of zero far-field stresses and a low relief topography, and they assume magma intrusion into pristine host rock unaffected by fracturing, faulting or magma intrusion. Note that the natural values of scaling parameters are largely uncertain, which leads to the broad ranges in the values of dimensionless parameters listed in **Table 1**, a recurrent issue when scaling laboratory models (e.g., Barenblatt, 2003; Merle, 2015; Galland et al., 2018).

Wide Beam X-Ray Computed Tomography

In 12 selected experiments (**Table 2**), syrup intrusion into the granular volume was recorded by a 3D X-ray CT image time-series. CT experiments were conducted at the UZ Brussel on a medical wide beam CT scanner (Revolution CT, GE Healthcare), centered in the CT gantry along the x-, y-, and z-axis, respectively (**Figure 2**). To obtain sufficient image contrast, we calibrated the average X-ray value of the sand-plaster mixtures and golden syrup prior to the intrusion experiments (**Appendix B**). In addition, three pre-experiment 3D CT images were acquired of each experiment with the aim of assessing image noise and DVC precision.

Dynamic CT acquisition and syrup injection were started simultaneously. Dynamic CT images were acquired in a single rotation with the following settings: X-ray tube voltage 120 kV, tube current 150 mA, rotation time 1 s, interval between two successive 3D images 19 s. Voxels are 3D pixels with horizontal (x, z) and vertical (y) dimensions and are anisotropic in clinical CT. Slice distance in z-direction is 0.625 mm and is a fixed attribute to the scanner, the voxel size in in-slice xy-directions is 0.391 mm (SPCTIN06) to 0.504 mm (SPCTIN02;−04) and depends on the selected scan field-of-view. The reconstructed 3D volume of X-ray values represents the X-ray attenuation in each voxel, expressed in Hounsfield units (HU), a measure relative to water, and defined such that the X-ray value of water is 0 HU. The intrusion bodies were rendered from the 3D CT images for each

TABLE 2 | Set-up parameters and outcome of analog models of golden syrup intrusion in granular materials run in the UZ Brussel hospital CT scanner and in the laboratory; see **Table 1** for abbreviations.

Experiment name	S-P (wt%)	ρ_r (kg m^{-3})	C (Pa)	$\Phi = \Pi_3$ (°)	H (m)	v_{pump} (ml hr^{-1})	v (m s^{-1})	V_{final} (ml)	μ (Pa s)	Duration (min)	Π_1	Π_2	Intrusion geometry
SPCTIN01	90:10	1700	66 ± 1	40 ± 4	0.08	50	0.00111	92	37	44	20	0.154	Cryptodome
SPCTIN02	90:10	1666	66 ± 1	40 ± 4	0.10	50	0.00111	48	37	60	25	0.154	Cryptodome
SPCTIN03	65:35	1465	195 ± 7	29 ± 3	0.10	50	0.00111	15	37	20	25	0.052	Inclined sheet
SPCTIN04	50:50	1268	298 ± 13	26 ± 2	0.10	50	0.00111	81	37	25	25	0.034	Dike
SPCTIN05	90:10	1666	66 ± 1	40 ± 4	0.06	50	0.00111	23	51	27	15	0.213	Cryptodome
SPCTIN06	80:20	1650	105 ± 3	40 ± 3	0.06	35	0.00077	23	51	42	15	0.094	Cone sheet
SPCTIN07	50:50	1268	298 ± 13	26 ± 2	0.06	30	0.00066	11	51	23	15	0.028	Cone sheet
SPCTIN08	50:50	1268	298 ± 13	26 ± 2	0.06	30	0.00066	6	51	15	15	0.028	Inclined sheet
SPCTIN09	80:20	1650	105 ± 3	40 ± 3	0.08	75	0.00166	36	51	30	20	0.201	Cone sheet
SPCTIN10	65:35	1465	195 ± 7	29 ± 3	0.08	50	0.00111	27	51	38	20	0.072	Cone sheet
SPCTIN11	80:20	1650	105 ± 3	40 ± 3	0.08	25	0.00055	40	51	98	20	0.067	Cone sheet
SPCTIN12	50:50	1268	298 ± 13	26 ± 2	0.08	50	0.00111	23	51	28	20	0.047	Inclined sheet
SP16-SPin01	90:10	1700	66 ± 1	40 ± 4	0.08	50	0.00111	18	43	32	20	0.181	Cryptodome
SP16-SPin02	90:10	1700	66 ± 1	40 ± 4	0.08	100	0.00221	46	51	60	20	0.426	Cryptodome
SP16-SPin03	90:10	1700	66 ± 1	40 ± 4	0.06	50	0.00111	39	51	45	15	0.213	Cryptodome
SP16-SPin04	90:10	1700	66 ± 1	40 ± 4	0.06	20	0.00044	30	51	90	15	0.085	Cryptodome
SP16-SPin05	90:10	1700	66 ± 1	40 ± 4	0.08	50	0.00111	24	51	30	20	0.213	Cryptodome
SP17-SPin06	90:10	1666	66 ± 1	40 ± 4	0.10	50	0.00111	42	28	41	25	0.117	Cryptodome
SP17-SPin07	65:35	1465	195 ± 7	29 ± 3	0.10	50	0.00111	21	29	26	25	0.041	Dike
SP17-SPin08	50:50	1268	298 ± 13	26 ± 2	0.10	50	0.00111	21	29	26	25	0.027	Dike
SP17-SPin09	90:10	1666	66 ± 1	40 ± 4	0.10	75	0.00166	58	32	46	24	0.198	Cryptodome
SP17-SPin10	80:20	1650	105 ± 3	40 ± 3	0.10	75	0.00166	25	32	28	25	0.124	Cone sheet
SP17-SPin11	65:35	1465	195 ± 7	29 ± 3	0.10	75	0.00166	19	32	16	25	0.067	Dike
SP17-SPin12	50:50	1268	298 ± 13	26 ± 2	0.10	75	0.00166	17	32	15	25	0.044	Dike
SP17-SPin13	50:50	1268	298 ± 13	26 ± 2	0.10	25	0.00055	16	34	47	25	0.016	Dike
SP17-SPin14	80:20	1650	105 ± 3	40 ± 3	0.06	50	0.00111	13	34	18	15	0.090	Cone sheet
SP17-SPin15	65:35	1465	195 ± 7	29 ± 3	0.06	50	0.00111	7	34	9	15	0.048	Cone sheet
SP17-SPin16	50:50	1268	298 ± 13	26 ± 2	0.06	50	0.00111	8	34	11	15	0.032	Cone sheet
SP17-SPin17	90:10	1666	66 ± 1	40 ± 4	0.04	90	0.00199	4	45	5	10	0.337	Cryptodome
SP17-SPin18	90:10	1666	66 ± 1	40 ± 4	0.06	50	0.00111	4	45	6	15	0.187	Cryptodome
SP18-SPin19	50:50	1268	298 ± 13	26 ± 2	0.06	25	0.00055	7	37	16	15	0.017	Cone sheet

Cohesion C and angle of internal friction Φ were quantified on samples of the same density as listed below, using the methodology of Abdelmalak et al. (2016).

time step using seed growth segmentation in the 3D Slicer image processing software (www.slicer.org; Fedorov et al., 2012).

Digital Volume Correlation

We used the Digital Volume Correlation (DVC) Strainmaster module of the commercial DaVis software (LaVision Ltd., UK) to calculate the displacement vector fields in the time series of each experiment. We first resampled the original anisotropic ($x = y \neq z$) CT volumes to produce isotropic voxel dimensions ($x = y = z$) as required by the DVC algorithm. This preprocessing was implemented in C++ and Python code based on the open-source Insight segmentation and registration toolkit (ITK; Yoo et al., 2002). The images were resampled to yield isotropic voxels by super-sampling along the inter-slices resolution (z). The in-plane resolution (x,y) was chosen as the desired value of isotropic resolution and passed on as an argument to the code for the resampling step. The resampling process required a transform to map point coordinates and an interpolator to compute intensity values for the new resampled image. We used an identity transform in order to maintain the physical extent of the sampled image and a nearest neighborhood interpolator. The resampled images were then converted to unsigned byte format, with values in the range [0, 255] to allow compatibility with the DVC software.

The Strainmaster DVC module characterizes image texture in a small sub-volume in the first CT volume, and it then searches the best-fit sub-volume in the subsequent CT volume by using a direct correlation algorithm. In contrast, Adam et al. (2013) previously used a Fast Fourier Transform algorithm. Strainmaster DVC then calculates the length and orientation of the 3D vector *V* that describes the differential displacement that occurs during the time increment [u(x),v(y),w(z)] (**Figure 3**). This process is repeated for each sub-volume to construct an incremental 3D displacement field. DaVis then calculates the differential strain tensor $E_{ij} = \delta V_i = \delta_j$ (with $i \in$ {x, y, z} and j {x, y, z}), as well as the incremental shear strain components (ε_{xy}, ε_{xz}, ε_{yz}), maximum 3D shear strain (ε_x-ε_z) and incremental rotational shear strain around the horizontal z-axis (rot-z = ε_{yx}-ε_{xy}). The differential spatio-temporal variation of material transport and volumetric deformation is thus described; Lagrangian summation of the incremental displacement fields then allows calculation of the cumulative—i.e., total—displacement and finite strain field throughout the experiment volume (**Figure 3**).

By repeating calculation runs four times at progressively decreasing sub-volume, binning and peak search sizes, the final correlation result can be optimized. The two last calculation runs were repeated twice each. A sub-volume size of 32 × 32 × 32 voxels and a sub-volume overlap of 75% in the last of four DVC runs resulted in a spatial resolution of the displacement vector field of 4.032 mm, where each vector represents the displacement of a 16.128 × 16.128 × 16.128 mm sub-volume. Displacements of equal vector length and orientation that occur over the entire imaged volume (i.e., "rigid body movements") were subtracted from the 3D displacement vectors for each sub-volume to remove artifacts due to potential small movements of the entire experimental box during CT imaging.

The DVC algorithm in theory achieves a sub-voxel precision of 0.05–0.1 pixel of displacement, which depends on the sub-volume size, image quality and image texture (Adam et al., 2013 and references therein). In the three pre-experiment CT images acquired before syrup injection, any displacement calculated by DaVis between the second and third CT images and the first one theoretically represent background noise (**Figure 4A**). For the three experiments discussed below, the median value and standard deviation of such background noise was on average 0.10 ± 0.05 mm for displacement vector length and on average 0.075 ± 0.060 for maximum shear strain. **Figures 4B–D** demonstrates that in experiment SPCTIN02 the median values of displacement vector length, 3D volumetric strain and maximum shear strain measured in the pre-experiment images are below one voxel size, or 20–30% of the values measured in the syn-experiment time-series.

Surface Data

We extracted the model surface from the resampled, isotropic CT volume at each time increment in an elevation map by using a dedicated MATLAB® script. Each slice image (in PNG format) was converted into a binary image by using a threshold gray value that separated image pixels representing the granular pile from pixels representing the box or the surrounding air. The elevation of the threshold gray value was then progressively recorded in a raster matrix for each slice. This process was repeated for each incremental CT volume to produce a time series of surface elevation.

RESULTS

Intrusion Growth

We performed 19 experiments at Vrije Universiteit Brussel to control experimental reproducibility. A further 12 experiments were monitored with dynamic wide beam X-ray Computed Tomography (CT). Between experiments, we varied the granular material strength (cohesion C, angle of internal friction Φ), material height (H), and the syrup injection discharge (v) (**Table 2**). $\prod_2$ thus exerted the greatest influence on the results. Intrusion geometries differed dominantly across the different strengths of the granular host material. The **Supplementary Material** contains videos documenting the development of the intrusions and overburden deformation in the three experiments discussed below.

In low-strength materials (90:10; high $\prod_2$), intrusions initially form a spherical, radially expanding intrusion (**Figure 5A**; **Movie 1**). Such a geometry is here called a cryptodome. A cm-thick dense percolation layer in which the syrup fills the sand pore space is observed on the CT imagery as a volume with high gray values (i.e., white) wrapped around the lighter syrup that is imaged with lower gray values (i.e., dark gray; **Figure 5A**). The percolation aureole is 1–5 mm thick in the low strength materials, but is negligible in the higher strength materials (see below). As the intrusion expands, the overburden is uplifted and an inverted-cone-shaped ring fracture forms. The intrusion becomes asymmetric in its top half, developing one or more cusps that expand into the overburden fracture (**Figure 5C**). One of the cusps then develops into a finger or a thick leaf-shaped curved sheet that propagates toward the surface along the overburden ring fracture (**Figure 5D**). Percolation of syrup into the granular material is much less developed around the rapidly propagating finger or thick sheet compared to the slowly inflating body of the intrusion. At the surface, the uplift of the overburden results in an initially symmetric bell-shaped uplift, bound by the intersection of the outer ring fracture with the surface (**Figure 5C**). The center of the doming surface develops shallow polygonal opening-mode fractures over time, and a steep edge forms at the dome boundary as material is thrusted upwards and slumps outwards (**Figures 5D,E**). The uplift becomes progressively asymmetric, and propagation of the finger eventually intersects the model surface in the area of maximum uplift leading to eruption (**Figure 5E**).

In medium-strength materials (65:35; intermediate $\prod_2$), intrusions initially form an oblate, ellipsoidal intrusion that expands laterally, associated with a mm-thick percolation aureole of syrup into the sand (**Figure 6A**; **Movie 2**). The overburden is bent upwards and fails along a steep through-going ring fracture that is shaped as an inverted cone, similar to low-strength materials (**Figure 6B**). A thin sheet intrusion then propagates upwards into that ring fracture (**Figure 6C**). Such conical intrusion shapes are here called cone sheets. The propagation velocity may be faster in one section of the cone-shaped part of the intrusion compared to other sections, in such case leading to asymmetrical geometries. The basal part of the intrusion around the inlet then continues to inflate as the cone-shaped part propagates (**Figures 6D–E**). At the surface, opening-mode fractures form directly above the inlet and propagate from the surface downward as the overburden above the intrusion is uplifted (**Figure 6A**). With continued uplift, extension of the dome surface creates additional opening-mode fractures arranged in a polygonal pattern defined by intersecting radial and

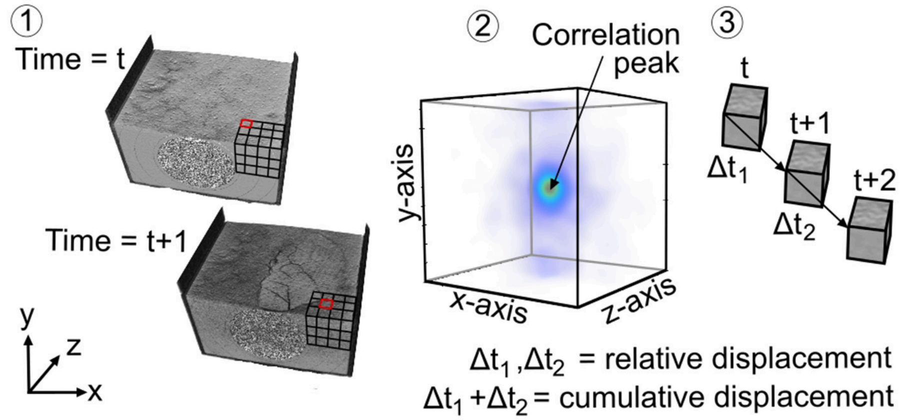

FIGURE 3 | The quantification of model deformation using Digital Volume Correlation (DVC) occurs in three steps. In step 1 voxel data of a time series of CT scans of a deforming experiment are subdivided in subvolumes consisting of a predefined number of voxels. In step 2 a pattern correlation peak is determined through a direct 3D correlation function that does not require tracking individual particles. In step 3 differential vector fields are calculated for each consecutive time step; the differential vector fields can be optionally summed up to obtain the cumulative displacement.

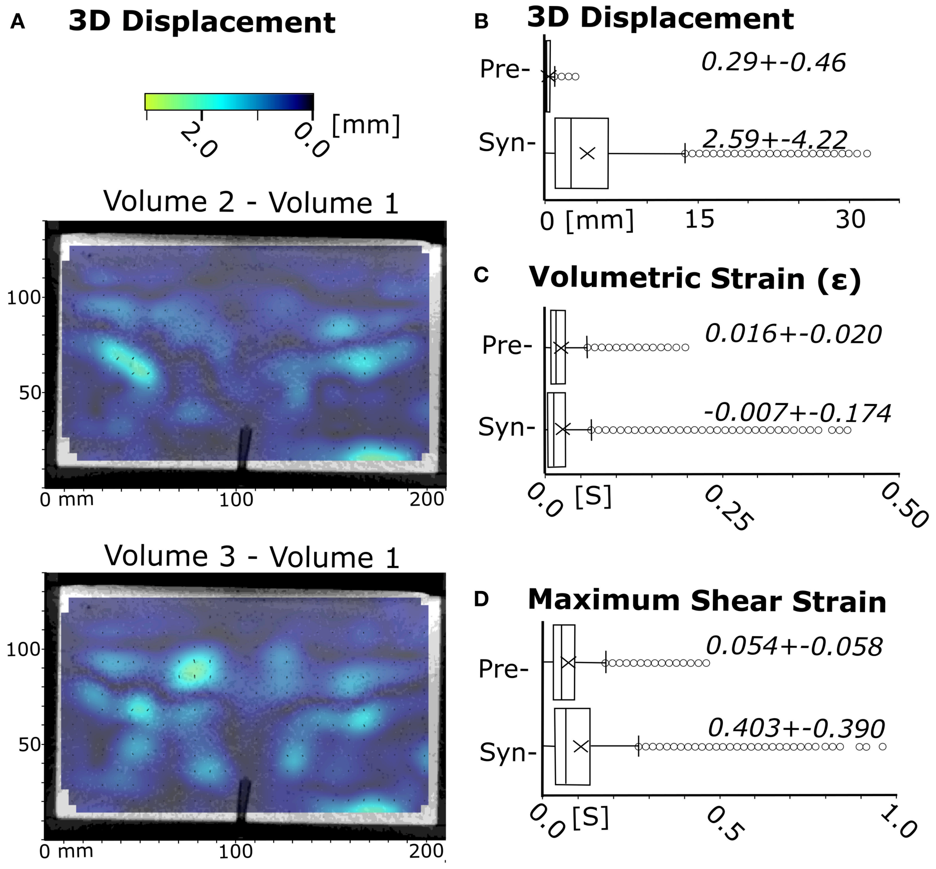

FIGURE 4 | Assessment of Digital Volume Correlation precision in experiment SPCTIN02. **(A)** x-z vertical cross-sections through 3D displacement fields calculated between, respectively the second and third CT image and the first one acquired prior to golden syrup injection, i.e., a pre-experimental state; **(B–D)** Median and standard deviations of 3D displacement vector lengths, volumetric strain and maximum shear strain in pre-experiment CT images and the last differential syn-experiment timestep, $n = 47{,}400$ voxels.

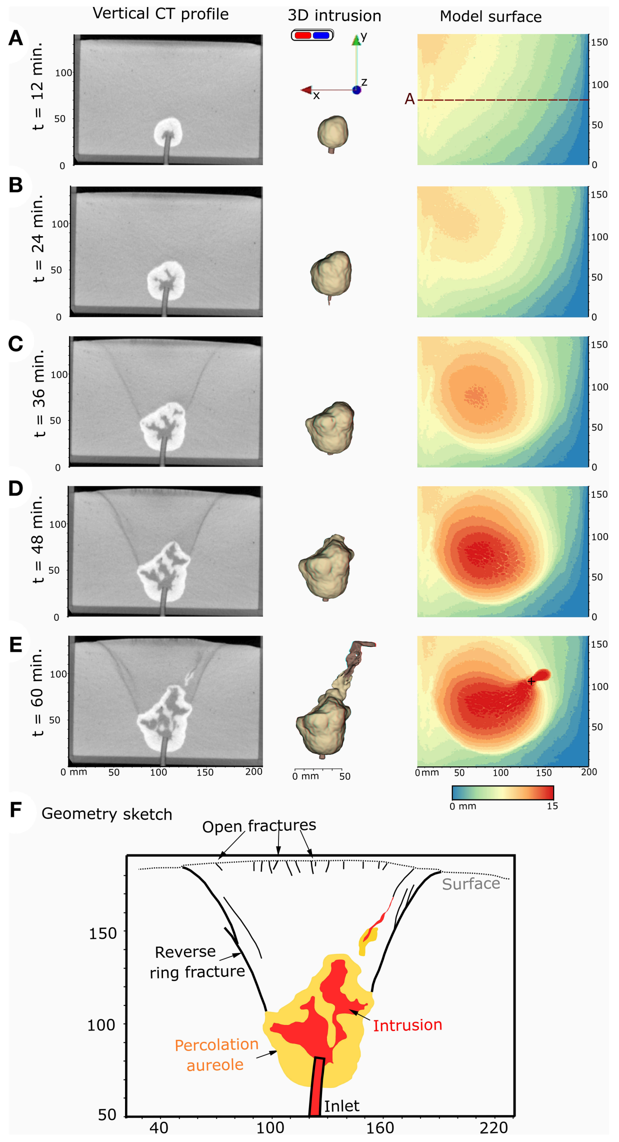

FIGURE 5 | (A–E) Temporal evolution of a cryptodome intrusion in a 90:10 wt% sand:plaster mixture (SPCTIN02 in **Table 2**); (Left column) vertical x-y slice of reconstructed CT volumes through the model center; Central column: 3D anaglyphs of the intrusion geometry, including both syrup (red), and the percolation aureole (yellow), rendered from CT images, to be viewed with blue-red 3D glasses; (Right column) Model surface elevation extracted from resampled CT images, the black cross marks where syrup broke through the surface (i.e., eruption); **(F)** Structural sketch of the final intrusion and induced deformation structures in the overburden through the central x-y slice in **(E)** (*t* = 60 min).

subconcentric fracture trends. The syrup finally breaks through the surface via one of the opening-mode surface fractures that lies on the flank of the surface dome (**Figure 6E**).

In high-strength materials (50:50; low $\prod_2$), intrusions initially open a triple-branched, star-shaped set of opening-mode fractures in plan-view, with the three branches oriented randomly relative to the box (**Figure 7A**; **Movie 3**). The angles between these branches range from a symmetric $\sim$120 to up to $\sim$180° for the widest angle. Syrup then propagates vertically through one or two dominant branches, and creates a thin, leaf-shaped vertical sheet intrusion, here called a dike (**Figure 7B**). The second and third branch—or only the third one if two branches are dominant—remain underdeveloped at the base of the dominant branch and have a penny shape with a vertical or inclined orientation. At 3–5 cm depth below the model surface, the intrusion deviates from its vertical path and forms an inclined tip, or splits into a V-shaped geometry that fills steeply inclined open fractures (**Figure 7C**). Some of the final intrusion geometries resemble an incomplete cone sheet but in fact are a combination of two en-echelon vertical dike segments under a minor ($<$10°) strike angle (**Figure 7D**). Surface deformation is much less developed compared to low- or medium-strength host materials because the intruded volume is lower (**Table 2**). Initially, a set of opening-mode fractures that are markedly deeper than in medium-strength materials forms at the surface above the dike tip (**Figure 7B**). The surface is then uplifted asymmetrically in a trapdoor-like fashion along some of the formed fractures (**Figure 7C**). Syrup eventually erupts from the open fracture bounding the area of trapdoor uplift and the final intrusion geometry is a complex of vertical or steeply inclined planar segments (**Figure 7D**).

At lower host material overburden heights (H), intrusions in all three material strengths initially expand laterally more than vertically compared to those in higher overburden heights. In low- and medium-strength materials, the intrusions then inflate vertically in a later stage. In low-strength overburden this results in a thick intrusion geometry with a concave upward roof, here called a cup shape. The basal diameter of cone sheet intrusions in medium-strength materials with lower overburden height and lower injection velocity (v) is smaller compared to the experiments with a higher overburden and a higher injection velocity (**Table 2**). In high-strength materials, the lowest segments of dike intrusions are vertical in high material heights and their upper segments are steeply inclined ($>$8 cm), but only inclined sheets or cone sheets form in low material heights ($<$6 cm). While two experiments presented here were run under a minor slope ($<$4%; **Figures 5**, **7**), experiments under a flat topography produced the same results as those described above.

The geometrical outcomes of the full range of experiments carried out at different $\prod_1$ and $\prod_2$ numbers are reproducible, and they confirm the finding of Galland et al. (2014) that a continuum of geometries forms with varying host material strength, fluid injection depth and injection velocity (**Table 2**, **Figure 8**). At low $\prod_1$ and high $\prod_2$ numbers (dominantly controlled by low host material strength), thick cryptodomes and cup shapes form. At high $\prod_1$ and low $\prod_2$ numbers (dominantly controlled by high host material strength), triple-branched star-shaped rifts form that develop into thin vertical dikes or steep inclined sheets. At intermediate dimensionless parameter values, a continuum of cone sheet geometries results with a range of basal diameters and inclined sheet angles.

3D Displacement and Strain

The evolution of the incremental 3D displacement vector field and the derived incremental strains in the experiments indicates

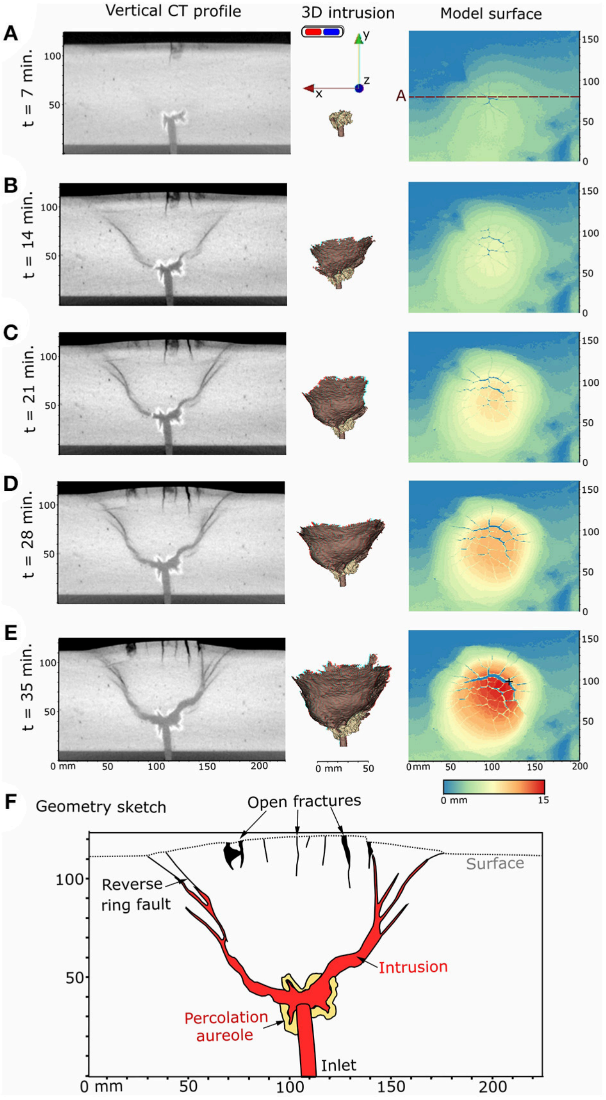

FIGURE 6 | (A–E) Temporal evolution of a cone sheet intrusion in a 80:20 wt% sand:plaster mixture (SPCTIN06 in **Table 2**); (Left column) vertical x-y slice of reconstructed CT volumes through the model center; (Central column) 3D anaglyphs of the intrusion rendered from CT images, to be viewed with blue-red 3D glasses; (Right column) Model surface elevation extracted from resampled CT images, the black cross marks where syrup broke through the surface (i.e., eruption); **(F)** Structural sketch of the final intrusion and induced deformation structures in the overburden through the central x-y slice in **(E)** (*t* = 35 min).

that each intrusion's development can be divided into three to four phases (**Figures 9–11**). For the parameters held constant in the experiments, the nature of these phases depends on the strength of the granular host material.

In low-strength materials (90:10; **Figure 9**), a radially outward displacement field develops around the syrup inlet at syrup injection onset (**Figure 9A**). The longitudinal strain data show that expansion of the intrusion is mostly accommodated by a concentric zone of contraction (compaction) within the surrounding granular host material (**Figures 9A,B**). The maximum shear strain within this zone concentrates close to the inlet and decreases radially outward. In a second phase, the overburden is displaced upward, and displacement vectors diverge away from the newly-developed ring fracture under opposite angles, indicating mixed-mode failure in which opening-mode is dominant and shear displacement is subordinate (**Figure 9C**). Incremental shear strain values are now highest within the narrow, axisymmetric, inverted cone shape of the ring fracture, which shows expansion along it and contraction in the host material. The contraction in the host material is concentrated in the footwall of the conical fracture; the central hanging-wall block delimited by the ring fracture displays relatively low strains. In a third stage, displacement along the ring fracture begins to die out, the intrusion inflates further, and the regions of maximum displacement and strain refocus around the

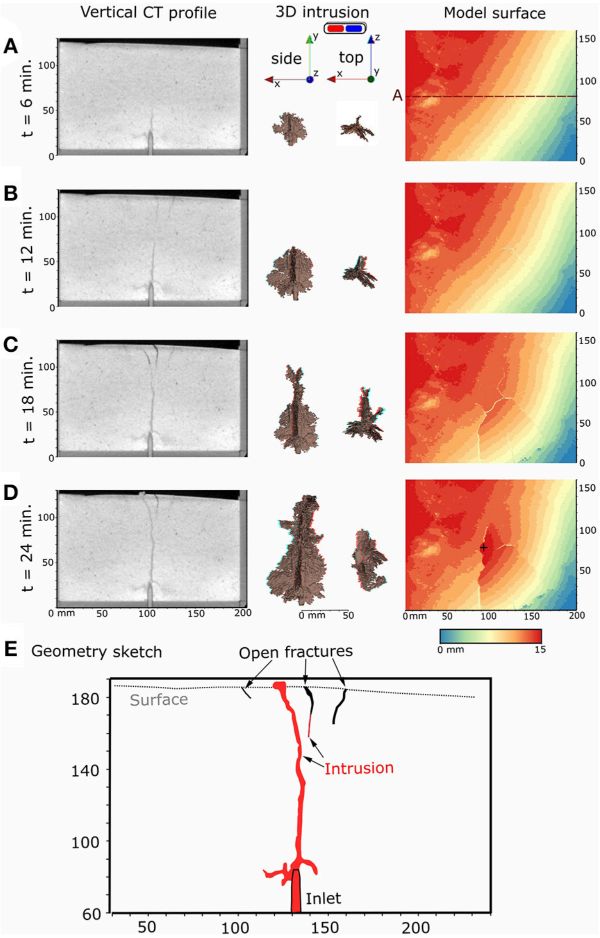

FIGURE 7 | (A–D) Temporal evolution of a dike intrusion in a 50:50 wt% sand:plaster mixture (SPCTIN04 in **Table 2**): (Left column) vertical x-y slice of reconstructed CT volumes through the model center; (Central column) 3D anaglyphs of the intrusion seen from its side (left) and its top (right) rendered from CT images, to be viewed with blue-red 3D glasses; (Right column) Model surface elevation extracted from resampled CT images, the black cross marks where syrup broke through the surface (i.e., eruption); **(E)** Structural sketch of the final intrusion and induced deformation structures in the overburden through the central x-y slice in **(D)** (*t* = 24 min).

intrusion top (**Figure 9D**). In a final stage, strain concentrates in a zone along the roof top of the cryptodome, from which an inclined secondary mixed-mode fracture propagates toward the surface and is intruded by a syrup finger or a thick, leaf-shaped sheet (**Figure 9E**). Overburden uplift becomes asymmetric with the highest displacements located within the hanging wall of the intruding finger and orientated at a high angle to it. Maximum shear strain occurs in the volume immediately around the ascending finger, from which golden syrup erupts (**Figure 9E**). Contractional strains are now greatest in the uplifting hanging-wall of the finger fracture, different from the development of the ring fracture.

In medium-strength materials (65:35; **Figure 10**), a radially outward displacement field develops around the inlet at intrusion onset as well (**Figure 10A**). Overburden contraction and uplift propagate rapidly toward the surface and cause the opening of a surface fracture above the inlet (**Figure 10A**). In a second phase the largest strains measured throughout the experiment concentrate along a through-going cone-shaped ring fracture (**Figure 10B**). The displacement vector field shows both opening and shear components along the ring fracture as the central overburden block is moved upwards and outward along it. This fracture then rapidly fills with syrup from the inlet toward the surface, accompanied by minor displacements (**Figure 10C**). Again the ring fracture shows mainly expansion along it as it develops (i.e., extensional strain in x and y directions—**Figures 10A,B**), while the host material surrounding the fracture shows mainly contraction focused in the fracture's foot-wall. Secondary fractures that open at the model surface arise from continued horizontal extension within the uplifted central block (**Figures 10B,C**); these are underlain by a subtle zone of vertical contraction arising as the upward and outward moving central block is stretched and thinned. In a third phase, the basal sill-like section of the intrusion then continues to inflate and vertical uplift of the central overburden block dominates (**Figure 10D**). Secondary conical fractures splay from the upper sections of the ring fracture. The splays again form through a mixed-mode combination of opening-mode and shear displacement, and result in the flower-shaped intrusion geometry consisting of concentric rings (**Figure 6E**). Strains within the central block and in the host material around the ring fracture are smaller than in earlier stages; they are distributed through the central block, and they mainly comprise a vertical shortening in response to the vertical opening of the underlying sill. In a last phase, shear and extensional strain localize along a vertical splay from the ring fracture that connects to one of the opening-mode surface fractures, which eventually becomes the eruptive fissure (**Figure 10E**).

In high-strength materials (50:50; **Figure 11**), intrusion onset is characterized also by radially outward displacement (**Figure 11A**), but unlike in low-strength materials (**Figure 9A**), no material is displaced vertically downward and compressed at the intrusion's base. In this first phase, the dike itself shows dominantly horizontal extension, which is accommodated by horizontal contraction in the host material at the dike walls and by vertical contraction above the dike tip. In a second phase (**Figure 11B**), upward propagation of the dike is characterized by an inverted cone shape volume that is linked to the dike base and in which displacements are upward and outward from the dike, indicating a dominantly opening-mode fracture. The patterns of host material contraction are similar to before (**Figure 11A**), but maximum shear strain values are highest in a bulb-shaped volume around the rising dike tip (**Figure 11B**). The largely horizontal displacement on the dike's side walls produces a downward-propagating, opening-mode fracture at the surface above the intrusion tip, which is seen as a zone of relatively low horizontal extension near the model surface. In a third phase (**Figure 11C**), the intrusion now interacts more with the surface as it links with the downward-propagating opening-mode fracture. The cone-shaped volume of host material uplift becomes strongly asymmetric: one of the two sides of the fluid-filled fracture is displaced upward and outward more than the other. The model surface is uplifted in an asymmetric or trapdoor-like fashion. The zones of highest displacement are now located in the host material around the upper half of the dike. The zones of maximum horizontal extension, vertical contraction and shear strain around the dike tip migrate upward accordingly. As they do so, areas that were under vertical contraction ahead of the dike tip now undergo vertical extension and horizontal contraction as they become the dike walls (**Figure 11C**). In a final phase (**Figure 11D**), the dike reaches the surface, and the patterns of displacement and strain migrate further upward to become focused in the shallowest part of the overburden.

The cumulative strain patterns for the three experiments further differ. In low-strength materials, most of the cumulative strain is distributed within and around the cryptodome intrusion close to the inlet (**Figure 9F**), while in medium- (**Figure 10F**) and high-strength (**Figure 11E**) materials most of the cumulative strain is localized along the entire length of the thin, fluid-filled sheet fracture and the immediately surrounding host material.

DISCUSSION

CT Image Quality and DVC Precision

Medical CT imaging allows us to visualize the interior of optically opaque granular material. Our results show that medical wide beam X-ray CT provides novel advantages over standard CT scanners for gaining unique insights into the mechanisms of subsurface magma propagation as modeled in laboratory experiments. The short detectors of standard CT scanners (4–8 cm) require minute-long helical scanning, during which the model deformation has to be paused. This can be done with tectonic laboratory models which involve externally forced deformation (Schreurs et al., 2003; Adam et al., 2013; Zwaan et al., 2018), but it is impracticable once analog magma intrusion has initiated. That is why Poppe et al. (2015) used radiographs, rather than 3D CT scans, to monitor their laboratory model development. Wide beam CT detectors (16 cm) allow syn-experiment dynamic scanning of the stationary model box and the acquisition of time-series of 3D CT images with a much higher signal:noise ratio compared to helical imaging at standard CT-scanners. The slow rotation speeds (26 s for one 3D image) and large voxel sizes (1 mm) used by Rincón et al. (2018) make imaging complex intrusion geometries and overburden

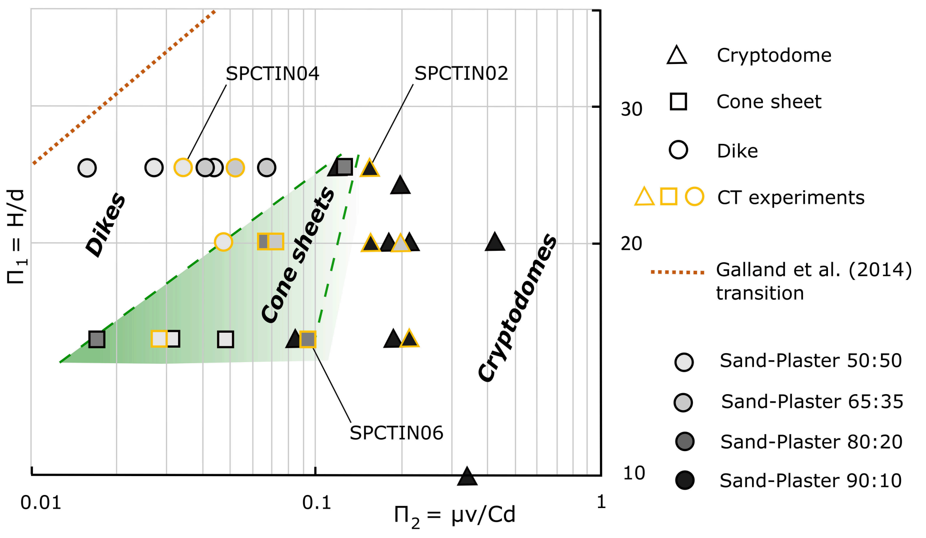

FIGURE 8 | Experimental outcome of intrusion geometries expressed relative to their dimensionless parameter values. Symbol shapes mark intrusion geometries; color-coding marks sand:plaster ratios as an indicator of granular host material strength; yellow symbol edges mark CT experiments. The cone sheet to dike transition is offset to lower ∏2 and higher ∏1 values compared to that experimentally determined by Galland et al. (2014) (red dashed line).

faulting patterns difficult and DVC application impossible. Image noise was sufficiently low in our case and, in contrast to the existing analog CT studies (Adam et al., 2013; Zwaan et al., 2018), imaging several times at each time step and stacking CT images to improve image texture proved unnecessary. Instead, the sufficiently small voxel sizes and the high frequency of image acquisition (1 s) at our wide beam CT set-up enabled a complete 4D (3D + time) view of the growth of analog intrusions and the development of deformation structures induced in the granular host material.

Panien et al. (2006) showed that sufficient grayscale contrast between different materials in CT images is obtained when their X-ray value differs by at least 100 HU. This criterion is obtained in our experiments, because golden syrup has a low X-ray attenuation of ~300 HU and the denser sand-plaster mixtures range between 500 and 800 HU (**Appendix B**). The overlap of X-ray attenuation for individual grains of different chemical composition, the air-filled intergranular pores and the syrup is large, however. Additionally, the coarse imaging resolution means that voxels commonly represent a mixed volume of grains, pore space and/or fluid. This results in difficulties for the seed growth segmentation algorithm to discriminate thin parts of the golden syrup intrusions from the surrounding sand-plaster material. Manual attribution of such voxels to one or the other reduces this problem, but is time-consuming. Segmentation is much more straightforward in low-strength material, where the dense percolation aureole of syrup into the granular material provides sharp X-ray value gradients that easily allow segmenting the intrusion volume. The ability to visualize the 3D geometry of syrup intrusions in high detail at any time step during the intrusion process is a unique feature of the presented laboratory method, and a clear advantage for comparison to geophysical monitoring data in nature.

A model box width of 20 cm was found to be the upper limit to acquire images of a satisfactorily high signal:noise ratio, because of the high density of sand and plaster (noise index = 14). Mourgues and Cobbold (2003) found that when the ratio of the overburden height to the container width is higher than ~0.53 in pure sand, a silo effect is detectable and vertical overburden load is counteracted at least partially by friction at the box side walls. At 8 cm material height, no detectable syn-experiment surface elevation change (SPCTIN06; **Figure 6**) and no interior 3D displacement or strain occurs near the box edges (**Figure 10**). At 12 cm material height, very minor cumulative 3D displacements and strains can be detected in the model interior at the box edges, but these are much smaller compared to the values that characterize the intrusion process (SPCTIN02, **Figure 9** & SPCTIN04, **Figure 11**). This effect is notable specifically for the cumulative rotational shear strain in the high-strength example (**Figure 11E**). These are absent however in the incremental time steps, suggesting that edge effects are negligible when looking at short time increments of deformation, but might play a minor role in the general emplacement behavior of an entire syrup intrusion event at roof aspect ratios above ~0.6.

The precision of displacement vectors calculated with modern DVC algorithms is typically claimed to be 0.05–0.1 voxel size (Li and Morgan, 2009; Pannier et al., 2010). Taking the upper bound to account for image quality, image texture and subvolume size, the vector length precision in our experiments should to be in the order of 0.050 mm. We found median pre-experiment displacements of ~0.10 ± 0.05 mm, even ~0.29 ± 0.46 in the example in **Figure 4B**, where in practice no displacement occurs. The precision of the displacement vector length results is thus probably rather in the order of half to one voxel sizes, but robustly represents realistic 3D displacement fields that occur in

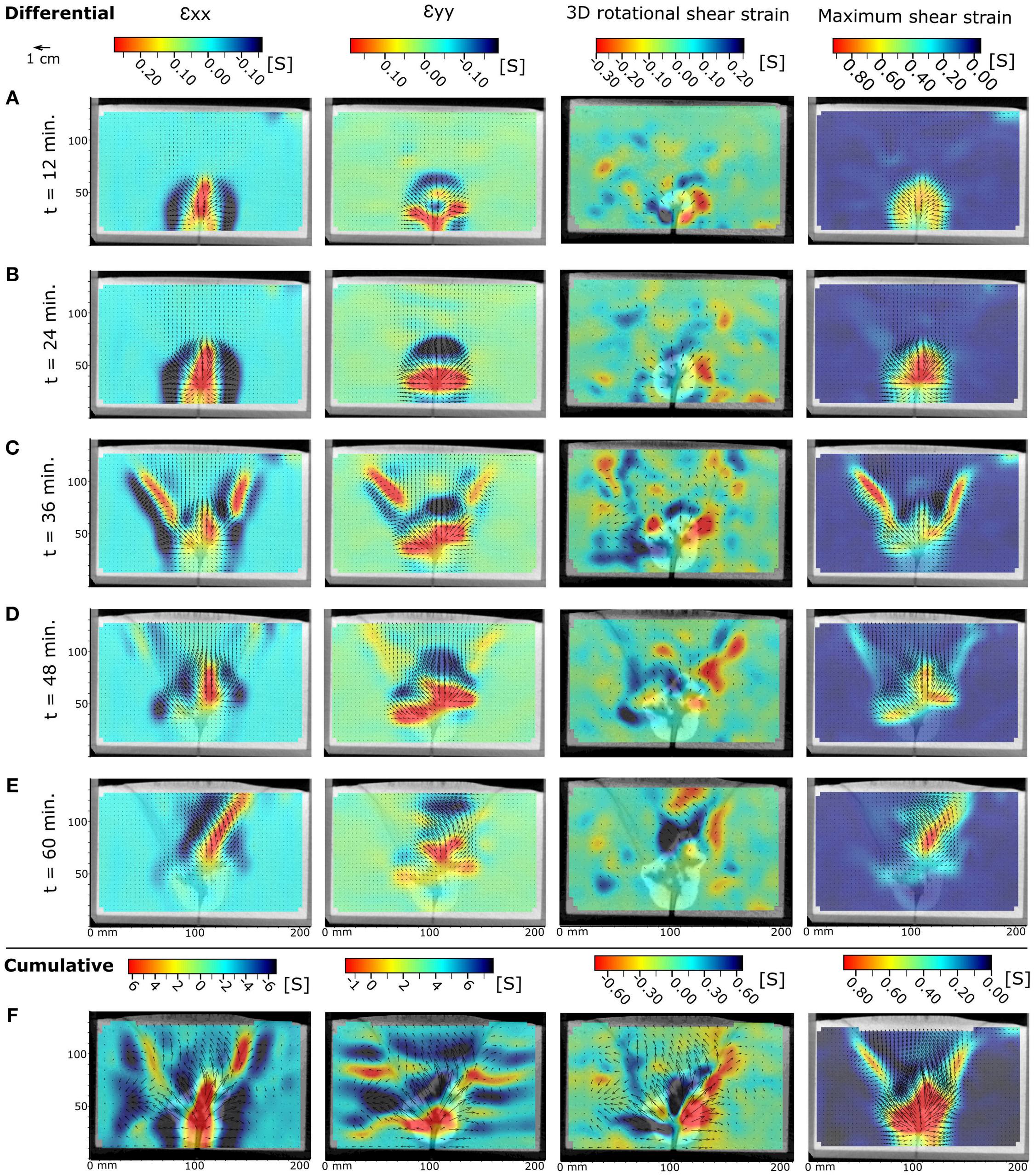

FIGURE 9 | DVC results for differential **(A–E)** and cumulative **(F)** host material deformation induced by a cryptodome intrusion in a 90:10 wt% sand:plaster mixture (SPCTIN02 in **Table 2**)—arrows indicate magnitude and orientation of calculated displacement vectors: (Left column) Horizontal (longitudinal) strain, shortening is negative/blue; (Central left column) Vertical (axial) strain, shortening is negative/blue; (Central right column) Horizontal rotational shear strain around the z-axis, anticlockwise rotation is positive/blue; (Right column) Maximum shear strain.

the laboratory models. By comparison, structure-from-motion photogrammetry reaches precisions of 0.05 mm on a 40 × 40 cm surface (Galland et al., 2016). The precision obtained with CT proves nevertheless high enough to study incremental deformation in 3D throughout the entire model volume, as opposed to what was possible before in typical laboratory model set-ups.

Contributions of CT: Intrusion Development and Magma Propagation

A variety of parameters has been proposed to control the wide range of magma intrusion geometries. Material properties include the density and viscosity of the magma, as well as the density, strength and mechanical heterogeneity and anisotropy of the host rock. Important geometric parameters include intrusion

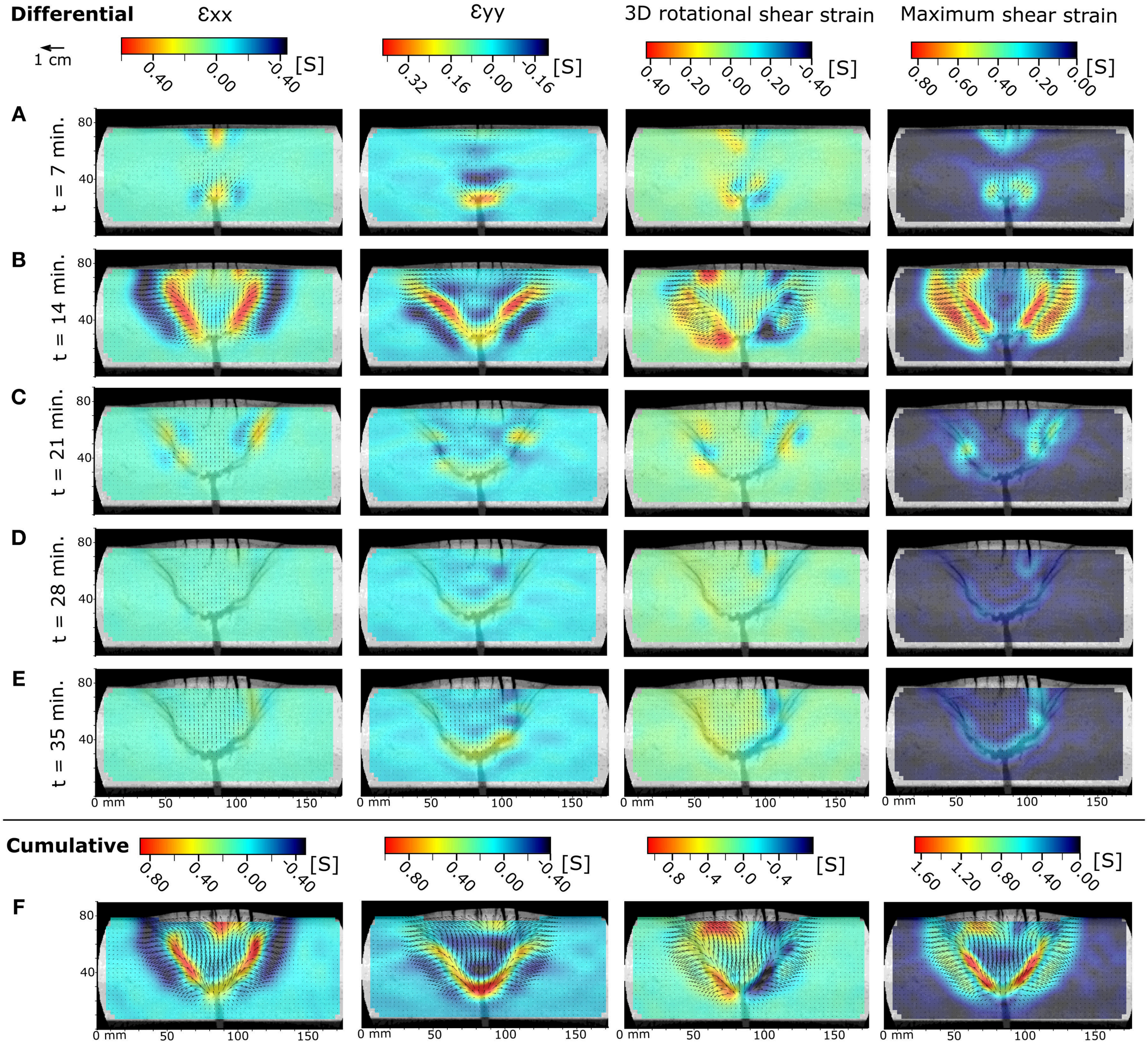

FIGURE 10 | DVC results for differential **(A–E)** and cumulative **(F)** host material deformation induced by a cone sheet intrusion in a 80:20 wt% sand:plaster mixture (SPCTIN06 in **Table 2**)—arrows indicate magnitude and orientation of calculated displacement vectors: (Left column) Horizontal (longitudinal) strain, shortening is negative/blue; (Central left column) Vertical (axial) strain, shortening is negative/blue; (Central right column) Horizontal rotational shear strain around the z-axis, anticlockwise rotation is positive/blue; (Right column) Maximum shear strain.

depth and surface topography, while dynamic parameters of the intrusion process include the magmatic pressure evolution and propagation velocity (cfr. Kavanagh et al., 2018). Host rock strength has been a particular point of interest for analog modeling studies (Mathieu et al., 2008; Abdelmalak et al., 2016; Guldstrand et al., 2017), but has also been shown to be a controlling factor in numerical models (e.g., Grosfils et al., 2013; Gerbault et al., 2018). With a varying ratio of sand to plaster and with other parameters held constant, our experiments confirm that thick cryptodome intrusions form in low-strength, loose or weakly consolidated sediments, while thin dikes form in high-strength materials such as limestones and other well-consolidated rocks (cfr. Mathieu et al., 2008) (**Figure 8**). In between these two end-members lies a range of hybrid cone sheets. A cone sheet to dike regime transition line in our experiments has a slope similar to that of Galland et al. (2014), although shifted laterally in $\prod_1$ vs. $\prod_2$ space. This discrepancy may arise from differences in experimental materials and from uncertainties regarding their properties, as well as the fact that the dimensionless parameter values explored in this study are slightly higher than those explored by Galland et al. (2014). Our values still lie well within natural ranges of occurrence of dikes and cone sheets (**Table 1**).

While standard laboratory monitoring techniques only enable access to the final 3D intrusion geometry, the dynamic CT imagery accesses the 3D geometrical development of the analog intrusions. Our experiments hence provide new insights into how the contrasting cryptodome, cone sheet and dike geometries develop in the subsurface. Regardless of the host rock strength, the initiation phase of all intrusions is associated with an axisymmetric displacement field, with displacements directed

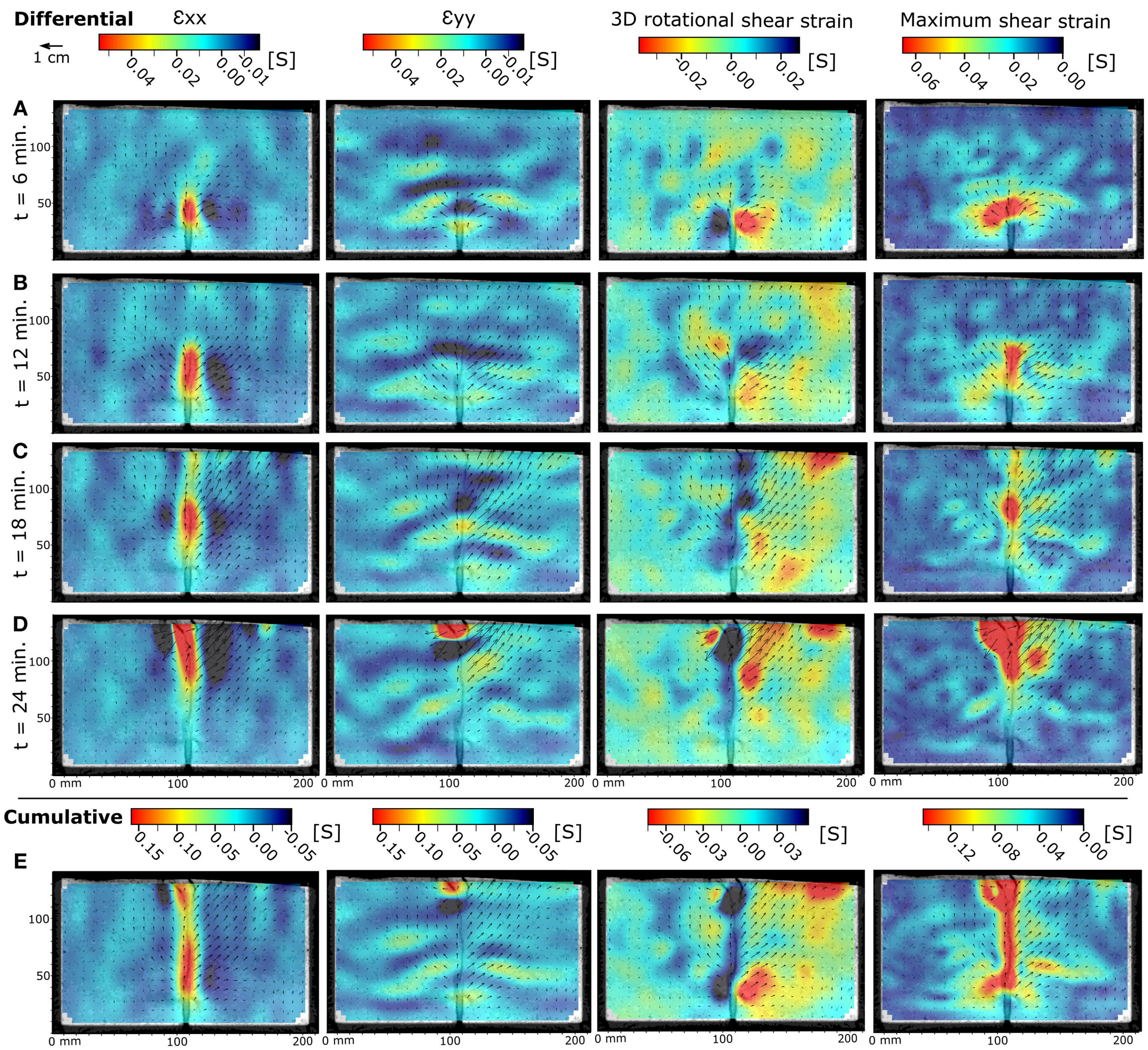

FIGURE 11 | DVC results for differential **(A–D)** and cumulative **(E)** host material deformation induced by a dike intrusion in a 50:50 wt% sand: plaster mixture (SPCTIN04 in **Table 2**)—arrows indicate magnitude and orientation of calculated displacement vectors: (Left column) Horizontal (longitudinal) strain, shortening is negative/blue; (Central left column) Vertical (axial) strain, shortening is negative/blue; (Central right column) Horizontal rotational shear strain around the z-axis, anticlockwise rotation is positive/blue; (Right column) Maximum shear strain.

radially outwards from the initiation point. Such an initial displacement field is similar to that derived from the point pressure source widely used in geodetic inversion models (Mogi, 1958). In low-strength material, a spherical intrusion develops from this displacement field due to distributed strain accommodation in the host material. In high-strength material, intrusion occurs into a set of opening-mode fractures reflecting highly localized strain accommodation.

A thick syrup percolation aureole forms around cryptodome intrusions in the low-strength material (**Figure 5**). Such percolation is much reduced or absent around fingers that propagate rapidly from the slowly inflating main intrusion body (**Figure 5E**). Limited percolation occurs around the syrup inlet in the medium- to high-strength material (**Figure 6**). This difference between low-strength and medium- and high-strength material may result from high permeability or a decreased threshold of capillary entry pressure in low-strength materials. While our sand-plaster mixtures overall simulate "dry-rock conditions"—i.e., no pore fluid pressure -, the percolation aureole itself is effectively a zone of elevated pore pressure with a probably unrealistically sharp boundary delimiting the presence/absence of pore fluids. Laboratory rock mechanics experiments show that lithostatic pore fluid pressures decrease a rock's effective strength (Jaeger et al., 2007). Consequently, reservoir rupture is favored at lower magma overpressure in elastic models that take into account lithostatic pore fluid pressure (Gudmundsson, 2012), while much higher magma overpressures are needed to fail a reservoir's wall in dry-rock elastic models (Grosfils et al., 2013). Exploration of such effects is not possible in our sand-box models however. Measurements of the strength of mixtures of sand and liquids has shown that the cohesion of such a mixture increases with respect to the dry material due to the liquid's surface tension (van Mechelen, 2004) up to a saturation point, after which the granular material is expected to lose its strength and becomes liquefied. We therefore expect that the percolating syrup increases the strength (i.e., cohesion) of the sand-plaster mixtures in our models initially, and may assist inflation of the intrusions before increased syrup overpressures can lead to cryptodome wall rupture and initiation of the finger and leaf-shaped intrusions. This assistance in the low-strength host material should be a small effect, however, because thick intrusion geometries similar to the ones in our experiments develop as well in laboratory models that used other analog materials in which percolation is very limited (Galland et al., 2006, 2014; Mathieu et al., 2008; Abdelmalak et al., 2012; Schmiedel et al., 2017; Guldstrand et al., 2018).

In a second phase, strain localization is seen to migrate into the overburden above the intrusion, but its nature varies with host material strength. In low-strength material, displacement of the overburden occurs mainly as uplift as strain localizes within a conical ring fault that propagates from the lateral edges of the cryptodome toward the surface (**Figures 5**, **9**; **Supplementary Material**). This process is well-known both in laboratory and numerical models (Marti et al., 1994; Gudmundsson, 2007; Gerbault et al., 2018). In medium-strength material, the intrusion propagates laterally in a horizontal disk shape, until it reaches a critical diameter (Haug et al., 2018) and a conical mixed-mode ring fracture with a dominant opening-mode component nucleates in the overburden (**Figures 6**, **10**). The observed opening-mode dominance is remarkable, because shear failure is predicted to dominate ring fault initiation in numerical models (Gerbault et al., 2018) and laboratory models using silica flour (Abdelmalak et al., 2012; Guldstrand et al., 2018). In high-strength material, displacement of the overburden is directed both upward and outward with strain localized around and ahead of the propagating dike tip and along the dike walls (**Figures 7**, **11**). Surface deformation in this second phase is dome-shaped in low- and medium-strength materials, making it hard to distinguish a cryptodome from a cone sheet intrusion based on surface deformation alone (**Figures 5C**, **6C**). In high-strength materials the surface deformation is a subdued broad arch (**Figure 7**). The first opening-mode fractures that open at the model surface in medium-strength overburden are positioned above the flat-lying center of cone sheets. The intrusions that propagate from cryptodomes in low-strength host material or the sill-like center of intrusions in medium-strength host material are always steeply inclined and oriented circumferentially with respect to the main intrusion body. Both observations are in agreement with predictions from "dry-rock" elastic models (Grosfils et al., 2013), but are in conflict with predictions of interpreted radial dike initiation at the lateral edges of a magma reservoir in elastic models that include lithostatic pore pressure (Gudmundsson, 2012). More detailed DVC analysis of shorter time increments in those critical locations in the overburden should be a focus of future work to explain these contradictions.

In a third phase, incremental displacement and strain fields in the host material tend to become markedly asymmetric, reflecting asymmetric, or tilted intrusion geometries at depth. In low-strength material, the strain localizes above the center of the intrusion, such that slip on the ring fault around the intrusion largely ceases. In medium-strength material, displacement concentrates along the ring fault. It accommodates the upward propagation of analog magma along its entire circumference to form a symmetric cone sheet, or only along a portion of the ring fault to form an inclined, leaf-shaped sheet, similar to findings of Schmiedel et al. (2017). In high-strength material, the strain and displacements are focused on the upper part of the ascending dike. Strain and displacements associated with the lower part of the dike become reduced, although the vertical longitudinal strains in the dike wall switch from dike-parallel contraction prior to the arrival of the dike tip at a particular level to dike-parallel extension after the tip has passed that level. Such a switch in strain regime may be evidenced by cross-cutting small-scale structures (fractures) in outcrop.

In a fourth and last phase, incremental strain and displacements are associated with the conduit bringing the analog magma to the surface. In low- or medium-strength material, this conduit is a thick finger, leaf or cone sheet that grows from the top of the intrusion, often asymmetrically into only a portion of the conical ring fault. Markedly, fingers or sheet tips often intrude into secondary faults or fractures (Haug et al., 2017, 2018); this highlights the preference of an intrusion to choose the path of least resistance (**Figures 5**, **6**). Examples of intrusions of magma fingers and dikes into faults and fractures are prevalent in nature, e.g., in the shallow plumbing system of the Lemptégy scoria cone in France, which corresponds to low-strength material (Mathieu et al., 2008; Delcamp et al., 2014). High-resolution seismicity recorded during the Bardarbunga 2014 dike intrusion on Iceland revealed a clear preference of the magma to propagate into pre-existing fractures created in the high-strength host rock by the extensional tectonic regime (Sigmundsson et al., 2014; Ágústsdóttir et al., 2016; Ruch et al., 2016).

In the cone sheet and dike examples (**Figures 6**, **7**, **10**, **11**), the presence of high material strength means that, as the tip of the fluid-filled fracture propagates upwards, there is a level within the overburden from where it becomes subject to the influence of the free surface, an effect well-document in elasticity-based numerical models (e.g., Dahm, 2000a; Sigmundsson et al., 2014; Maccaferri et al., 2015; Rivalta et al., 2015). This is evidenced by V- and cup-shaped upper intrusion parts, as well as inclined upper parts of dikes, developed in our analog magma intrusions and seen in previous experiments with granular materials (Mathieu et al., 2008; Abdelmalak et al., 2012). The depth of initiation of such dip angle transitions and splays most likely corresponds to the material-dependent transition of shallow opening-mode-dominated behavior to deeper mixed-mode or shear-dominated behavior (Jaeger et al., 2007; Mourgues et al., 2011; Abdelmalak et al., 2016). This effect is the most notable in the development of the eventual eruptive fissures in the cone sheet and dike examples, that propagate as an opening-mode fracture downwards from the surface, and connect to the syrup-filled fractures at depth that are either mixed-mode (opening and shear) as in the fingers and cone sheets or opening-mode as in the dikes (**Figures 10**, **11**).

In the cryptodome example, shear strain is focused around the finger or leaf and the surface uplift concentrates directly above it, toward the eventual break-out point at surface. The evolution from symmetric to asymmetric surface deformation (Guldstrand et al., 2017, 2018) is thus a consequence of the evolution of intrusion-induced displacements and strain from an initially symmetric and wide distribution around the injection point to a narrowly focused volume around an off-shoot finger or leaf-shaped sheet. The strong asymmetry of strain and displacement in the dike model reflects the inclination or V-shaped bifurcation of the upper-most section of the dike (**Figure 6D**). The asymmetry seen in displacement fields produced by model finger and dike intrusions is seen also at Fernandina, and is similarly inferred to be the result of a late-stage tilted geometry of the uppermost section of the dikes beneath the eruption sites (Bagnardi et al., 2013; Chestler and Grosfils, 2013).

The overall doming uplift pattern of surface displacement associated with dikes in our models is like that obtained in previous experiments of pressurized fluid injection into granular materials (e.g., Abdelmalak et al., 2012; Guldstrand et al., 2017). Such a simple doming pattern differs from the dike-related bulges-and-trough displacement pattern commonly observed in regional tectonic settings and on many volcanic edifices (e.g., Lundgren et al., 2013; Sigmundsson et al., 2014). The classic bulges-and-trough displacement profile is reproduced in experiments of pressurized fluid injection in gelatin (Kavanagh et al., 2018) and in experiments of a widening rigid body at fixed depth in granular materials (Mastin and Pollard, 1988; Trippanera et al., 2015). Our experimental results differ from those of the latter two works in particular in that the dike-perpendicular widening occurs within an overall upward-and-outward displacement field, and so a net central subsidence above the dike tip is not seen (**Figure 11**). Nonetheless, similar dome-like displacement patterns lacking a central subsidence area have been recorded geodetically above suspected dikes in some volcanic edifices (Peltier et al., 2017). Our experimental dikes may therefore be analogous to certain instances of shallow-level dike emplacement in volcanic edifices, although further investigation is needed to test this hypothesis.

Overall, the quantified displacement vectors and derived strains demonstrate how in low-strength materials the emplacement of thick cryptodome intrusions is accommodated largely by distributed, perhaps brittle-ductile or even ductile, strains in the host-material around the intrusion. Such mechanism is probably most similar to the local emplacement of magma at the basin scale in low-strength crustal rocks, such as shales (Pollard et al., 1975; Schofield et al., 2012; Spacapan et al., 2017). The $\prod_2$ scaling parameter suggests that the same mechanism might dominate when higher-viscosity magma intrudes, but we did not test that. In high-strength granular materials, opening-mode fractures develop as strain is more localized and possibly more brittle. Overall the experiments indicate that a transition exists in emplacement mechanism from mixed-mode viscous indentation at low strength to a deformation mode approaching classic hydraulic fracturing at high strength. The 4D imaging and displacement quantification of magma intrusion experiments by using CT and DVC thus confirms that numerical inverse modeling of surface deformation data ideally should take into account the strength and complex rheology of crustal rock as well as the associated mechanisms of magma intrusion and host rock deformation evidenced in our laboratory models and numerical models applied to e.g., Darwin Volcano, Galapagos (Manconi et al., 2007), Long Valley, U.S.A. (Long and Grosfils, 2009) or Piton de La Fournaise, La Réunion Island (Holohan et al., 2017).

CONCLUSIONS

This study reports on the novel combination of state-of-the-art wide beam X-ray Computed Tomography (CT) and Digital Volume Correlation (DVC) to dynamically image in 4D (3D + time) the geometrical development of analog magma intrusions (golden syrup) and quantify the induced displacements and strain in its granular host material (sand and plaster).

The power of the method was evidenced through a systematic series of experiments that demonstrates how the strength of a granular host material affects the 3D geometrical development of analog magma intrusions. Thick cryptodome intrusions with finger- and leaf-shaped protrusions form in low-strength material. Transitional thinner cone sheets form in medium-strength materials. Thin vertical sheet intrusions—i.e., dikes—form from triple-branched star-shaped opening-mode fractures in high-strength materials of sufficient overburden height.

The CT imaging enabled documentation of how in low-strength material strain is initially distributed above growing cryptodomes, and of how it eventually localizes on mixed-mode fractures that bound an inverted cone-shaped region of overburden uplift. In medium-strength material, those overburden fractures form through more dominantly opening-mode mechanisms. In high-strength material, formation of opening-mode vertical fractures dominates, and is accompanied by the localization and progressive upward migration of strain and displacement around the propagating intrusion tip. While numerical and laboratory models of magma intrusion in a linearly elastic medium previously simulated only tensile opening of hydraulic fractures, our experiments demonstrate how magma intruding in a material with complex rheology can induce both opening-mode fluid-filled fractures and the development of mixed-mode (opening plus shear) fractures in complex 3D deformation patterns.

Overall, this study establishes the combination of dynamic wide beam CT and DVC as useful techniques to acquire new insights into a complexly-evolving process of coupled fluid-solid deformation from laboratory experiments. Remote sensing techniques and analytical and numerical geodetic inversion models used in volcano monitoring are now increasingly providing a dynamic view of surface deformation induced by magma intrusion over time. Comparing such data from nature to laboratory models of magma intrusion in granular materials as imaged with the state-of-the-art techniques used here has the potential to generate new insights into the time-dependent, 3D geometrical development of magmatic intrusions and the associated deformation in the upper part of the Earth's crust.

DATA AVAILABILITY

The datasets generated for this study are available on request to the corresponding author.

AUTHOR CONTRIBUTIONS

SP led this work as part of his Ph.D. project supervised by MK. OG, EH, and MK contributed to the experimental design, interpretation of the results and revision of the text. NB and GV contributed to the experimental design, X-ray value quantification and CT scanning. BK wrote the CT volume resampling code and accompanying methodology. P-YT and SP wrote the MATLAB® (The Mathworks, Inc.,) script for extracting surface deformation from CT scans. DH and AN provided the DaVis software license and support with DVC calculations, precision assessment and interpretation. JB measured viscosities of golden syrup and wrote the accompanying **Appendix** section.

FUNDING

SP is funded by an Aspirant Ph.D. fellowship from the FWO-Flanders, Belgium and the Belgian foundation VOCATIO. NB, GV, and BK are supported by an academic interdisciplinary Research Project grant from the Vrije Universiteit Brussel, Belgium (Grant IRP10 KARMA-4D). LaVision Ltd., provided a monthly academic discount license and technical support for using the Strainmaster DVC module of their DaVis software.

ACKNOWLEDGMENTS

The UZ Brussel Radiology Department and Prof. Dr. Johan de Mey are thanked for making their medical CT facilities available at no cost. The FYSC group and Prof. Dr. Guy Van Assche are thanked for making their rheometers available at no cost. Luc Deriemaeker (VUB) is thanked for building the model boxes and setting up the syringe pump. M. Philippon is thanked for editorial handling. Reviewer E. Grosfils and reviewer considerably helped in improving this manuscript. J. Adam, M. Boone, A. Delcamp, P. Grosse, F. Guldstrand, E. Mae-Paguican, S. Poppe, T. Schmiedel, G. Schreurs, J. van Stappen, and F. Zwaan are thanked for valuable discussions.

SUPPLEMENTARY MATERIAL

The Supplementary Material for this article can be found online at: https://www.frontiersin.org/articles/10.3389/feart.2019.00062/full#supplementary-material

Movie S1 | Time-lapse movie of X-ray CT images of golden syrup cryptodome intrusion experiment SPCTIN02 in a 90 wt% sand-10 wt% plaster mixture, acquired at UZ Brussels, Belgium; **Upper left**: 3D model surface rendering; **Upper right**: saggital (N-S) vertical cross-section; **Bottom left**: 3D syrup intrusion rendering; **Bottom right**: axial (E-W) vertical cross-section.

Movie S2 | Time-lapse movie of X-ray CT images of golden syrup cone sheet intrusion experiment SPCTIN06 in a 80 wt% sand-20 wt% plaster mixture, acquired at UZ Brussels, Belgium; **Upper left**: plan-view model surface rendering; **Upper right**: saggital (N-S) vertical cross-section; **Bottom left**: 3D model surface rendering; **Bottom right**: axial (E-W) vertical cross-section.

Movie S3 | Time-lapse movie of X-ray CT images of golden syrup dike intrusion experiment SPCTIN04 in a 50 wt% sand-50 wt% plaster mixture, acquired at UZ Brussels, Belgium; **Upper left**: plan-view model surface rendering; **Upper right**: saggital (N-S) vertical cross-section; **Bottom left**: 3D model surface rendering; **Bottom right**: axial (E-W) vertical cross-section.

Appendix A | Golden Syrup Viscosity.

Appendix B | Material X-ray Attenuation.

REFERENCES

Abdelmalak, M. M., Bulois, C., Mourgues, R., Galland, O., Legland, J. B., and Gruber, C. (2016). Description of new dry granular materials of variable cohesion and friction coefficient: implications for laboratory modeling of the brittle crust. *Tectonophysics* 684, 39–51. doi: 10.1016/j.tecto.2016.03.003

Abdelmalak, M. M., Mourgues, R., Galland, O., and Bureau, D., (2012). Fracture mode analysis and related surface deformation during dyke intrusion: results from 2D experimental modelling. *Earth Planetar. Sci. Lett.* 359–360, 93–105. doi: 10.1016/j.epsl.2012.10.008

Acocella, V., and Neri, M. (2009). Dike propagation in volcanic edifices: overview and possible developments. *Tectonophysics* 471, 67–77. doi: 10.1016/j.tecto.2008.10.002

Adam, J., Klinkmüller, M., Schreurs, G., and Wieneke, B. (2013). Quantitative 3D strain analysis in analogue experiments simulating tectonic deformation: integration of X-ray computed tomography and digital volume correlation techniques. *J. Struct. Geol.* 55, 127–149. doi: 10.1016/j.jsg.2013.07.011

Ágústsdóttir, T., Woods, J., Greenfield, T., Green, R. G., White, R. S., Winder, T., et al. (2016). Strike-Slip Faulting during the 2014 Bároarbunga-Holuhraun Dike Intrusion, Central Iceland. *Geophys. Res. Lett.* 43, 1495–1503. doi: 10.1002/2015GL067423

Bagnardi, M., Amelung, F., and Poland, M. P. (2013). A new model for the growth of basaltic shields based on deformation of Fernandina Volcano, Galápagos Islands. *Earth Planetary Sci. Lett.* 377–378, 358–366. doi: 10.1016/j.epsl.2013.07.016

Barenblatt, G. I. (2003). *Scaling*. Cambridge: Cambridge University Press. doi: 10.1017/CBO9780511814921

Battaglia, M., Cervelli, P. F., and Murray, J. R. (2013). Modeling crustal deformation near active faults and volcanic centers-a catalog of deformation models. *US Geolog. Survey Techniq. Methods Book* 13:96. doi: 10.3133/tm13B1

Beckett, F. M., Mader, H. M., Phillips, J. C., Rust, A. C., and Witham, F. (2011). An experimental study of low-reynolds-number exchange flow of two newtonian fluids in a vertical pipe. *J. Fluid Mech.* 682, 652–670. doi: 10.1017/jfm.2011.264

Bertelsen, H. S., Rogers, B. D., Galland, O., Dumazer, G., and Abbana Bennani, A. (2018). Laboratory modeling of coeval brittle and ductile deformation during magma emplacement into viscoelastic rocks. *Front. Earth Sci.* 6:199. doi: 10.3389/feart.2018.00199

Bistacchi, A., Tibaldi, A., Pasquarè, F. A., and Rust, D. (2012). The association of cone-sheets and radial dykes: data from the isle of skye (UK), numerical modelling, and implications for shallow magma chambers. *Earth Planetary Sci. Lett.* 339–340, 46–56. doi: 10.1016/j.epsl.2012.05.020

Brenguier, F. P., Kowalski, N., Ackerley, N., Nakata, P., Boué, M., Campillo, M., et al. (2016). Toward 4D noise-based seismic probing of volcanoes: perspectives from a large- *n* experiment on piton de la fournaise volcano. *Seismol. Res. Lett.* 87, 15–25. doi: 10.1785/0220150173

Burchardt, S., Troll, V. R., Mathieu, L., Emeleus, H. C., and Donaldson, C. H. (2013). Ardnamurchan 3D cone-sheet architecture explained by a single elongate magma chamber. *Scient. Rep.* 3, 1–7. doi: 10.1038/srep02891

Calais, E., d'Oreye, N., Albaric, J., Deschamps, A., Delvaux, D., Déverchère, J., et al. (2008). Strain accommodation by slow slip and dyking in a youthful continental rift, East Africa. *Nature* 456, 783–787. doi: 10.1038/nature07478

Chestler, S. R., and Grosfils, E. B. (2013). Using numerical modeling to explore the origin of intrusion patterns on fernandina volcano, Galapagos Islands, Ecuador. *Geophys. Res. Lett.* 40, 4565–4569. doi: 10.1002/grl.50833

Cnudde, V., and Boone, M. N. (2013). High-resolution X-ray computed tomography in geosciences: a review of the current technology and applications. *Earth-Sci. Rev.* 123, 1–17. doi: 10.1016/j.earscirev.2013.04.003

Dahm, T. (2000a). Numerical simulations of the propagation path and the arrest of sluid-filled fracture in the earth. *Geophys. J. Int.* 141, 623–638. doi: 10.1046/j.1365-246x.2000.00102.x

Dahm, T. (2000b). On the shape and velocity of fluid- filled fractures in the earth. *Geophys. J. Int.* 142, 181–192. doi: 10.1046/j.1365-246x.2000.00148.x

Delcamp, A., van Wyk de Vries, B., James, M. R., Gailler, L. S., and Lebas, E. (2012). Relationships between volcano gravitational spreading and magma intrusion. *Bull. Volcanol.* 74, 743–765. doi: 10.1007/s00445-011-0558-9

Delcamp, A., van Wyk de Vries, B., Petit, S., and Kervyn, M. (2014). Endogenous and exogenous growth of the monogenetic lemptégy volcano, Chaîne Des Puys, France. *Geosphere* 10, 998–1019. doi: 10.1130/GES01007.1

Donnadieu, F., Merle, O., and Besson, J. C. (2001). Volcanic edifice stability during cryptodome intrusion. *Bull. Volcanol.* 63, 61–72. doi: 10.1007/s004450000122

Ebmeier, S. K., Andrews, B. J., Araya, M. C., Arnold, D. W. D., Biggs, J., Cooper, C., et al. (2018). Synthesis of global satellite observations of magmatic and volcanic deformation: implications for volcano monitoring and the lateral extent of magmatic domains. *J. Appl. Volcanol.* 7, 1–26. doi: 10.1186/s13617-018-0071-3

Fedorov, A., Beichel, R., Kalpathy-Cramer, J., Finet, J., Fillion-Robin, J. C., Pujol, S., et al. (2012). 3D slicer as an image computing platform for the quantitative imaging network. *Magnet. Resonan. Imaging* 30, 1323–1341. doi: 10.1016/j.mri.2012.05.001

Fernández, J., Pepe, A., Poland, M. P., and Sigmundsson, F. (2017). Volcano geodesy: recent developments and future challenges. *J. Volcanol. Geother. Res.* 344, 1–12. doi: 10.1016/j.jvolgeores.2017.08.006

Galland, O., Bertelsen, H. S., Guldstrand, F., Girod, L., Johannessen, R. F., Bjugger, F., et al. (2016). Application of open-source photogrammetric software micmac for monitoring surface deformation in laboratory models. *J. Geophys. Research-Solid Earth* 2, 1–21. doi: 10.1002/2015JB012564

Galland, O., Burchardt, S., Hallot, E., Mourgues, R., and Bulois, C. (2014). Dynamics of dikes versus cone sheets in volcanic systems. *J. Geophys. Res.* 119, 6178–6192. doi: 10.1002/2014JB011059

Galland, O., Cobbold, P. R., Hallot, E., de Bremond d'Ars, J., and Delavaud, G. (2006). Use of vegetable oil and silica powder for scale modelling of magmatic intrusion in a deforming brittle crust. *Earth Planetary Sci. Lett.* 243, 786–804. doi: 10.1016/j.epsl.2006.01.014

Galland, O., Holohan, E. P., van Wyk de Vries, B., and Burchardt, S. (2018). "Laboratory modelling of volcano plumbing systems: a review," in *Physical Geology of Shallow Magmatic Systems - Dykes, Sills and Laccoliths*, eds C. Breitkreuz and S. Rocchi (Heidelberg: Springer), 147–214. doi: 10.1007/11157_2015_9

Gerbault, M., Hassani, R., Lizama, C. N., and Souche, A. (2018). Three-dimensional failure patterns around an inflating magmatic chamber. *Geochem. Geophys. Geosyst.* 19, 749–771. doi: 10.1002/2017GC007174

Grosfils, E. B., McGovern, P. J., Gregg, P. M., Galgana, G. A., Hurwitz, D. M., Long, S. M., et al. (2013). Elastic models of magma reservoir mechanics: a key tool for investigating planetary volcanism. *Geolog. Soc. London Special Publ.* 401, 239–267. doi: 10.1144/SP401.2

Gudmundsson, A. (2007). Conceptual and numerical models of ring-fault formation. *J. Volcanol. Geoth. Res.* 164, 142–160. doi: 10.1016/j.jvolgeores.2007.04.018

Gudmundsson, A. (2011). Deflection of dykes into sills at discontinuities and magma-chamber formation. *Tectonophysics* 500, 50–64. doi: 10.1016/j.tecto.2009.10.015

Gudmundsson, A. (2012). Magma chambers: formation, local stresses, excess pressures, and compartments. *J. Volcanol. Geother. Res.* 237–238, 19–41. doi: 10.1016/j.jvolgeores.2012.05.015

Guldstrand, F., Burchardt, S., Hallot, E., and Galland, O. (2017). Dynamics of surface deformation induced by dikes and cone sheets in a cohesive coulomb brittle crust. *J. Geophys. Res.* 122, 8511–8524. doi: 10.1002/2017JB014346

Guldstrand, F., Galland, O., Hallot, E., and Burchardt, S. (2018). Experimental constraints on forecasting the location of volcanic eruptions from pre-eruptive surface deformation. *Front. Earth Sci.* 6, 1–9. doi: 10.3389/feart.2018.00007

Haug, Ø. T., Galland, O., Souloumiac, P., Souche, A., Guldstrand, F., and Schmiedel, T. (2017). Inelastic damage as a mechanical precursor for the emplacement of saucer-shaped intrusions. *Geology* 45, 1099–1102. doi: 10.1130/G39361.1

Haug, Ø. T., Galland, O., Souloumiac, P., Souche, A., Guldstrand, F., Schmiedel, T., et al. (2018). Shear versus tensile failure mechanisms induced by sill intrusions - implications for emplacement of conical and saucer-shaped intrusions. *J. Geophys. Res.* 123, 1–20. doi: 10.1002/2017JB015196

Holland, M., van Gent, H., Bazalgette, L., Yassir, N., Hoogerduijn Strating, E. H., and Urai, J. L. (2011). Evolution of dilatant fracture networks in a normal fault - evidence from 4D model experiments. *Earth Planetary Sci. Lett.* 304, 399–406. doi: 10.1016/j.epsl.2011.02.017

Holohan, E. P., Sudhaus, H., Walter, T. R., Schöpfer, M. P. J., and Walsh, J. J. (2017). Effects of host-rock fracturing on elastic-deformation source models of volcano deflation. *Scient. Rep.* 7:10970. doi: 10.1038/s41598-017-10009-6

Hubbert, M. K. (1937). Theory of scale models as applied to the study of geologic structures. *GSA Bull.* 48, 1459–1520. doi: 10.1130/GSAB-48-1459

Jaeger, J. C., Cook, N. G. W., and Zimmerman, R. W. (2007). *Fundamentals of Rock Mechanics*. Oxford: Blackwell Publishing, 475.

Kavanagh, J. L., Engwell, S., and Martin, S. (2018). A review of analogue and numerical modelling in volcanology. *Solid Earth* 9, 531–571. doi: 10.5194/se-2017-40

Kervyn, M., Boone, M. N., van Wyk de Vries, B., Lebas, E., Cnudde, V., Fontijn, K., et al. (2010). 3D imaging of volcano gravitational deformation by computerized X-ray micro-tomography. *Geosphere* 6, 482–498. doi: 10.1130/GES00564.1

Koehn, D., Steiner, A., and Aanyu, K. (2019). Modelling of extension and dyking-induced collapse faults and fissures in rifts. *J. Struct. Geol.* 118, 21–31. doi: 10.1016/j.jsg.2018.09.017

Le Corvec, N., and Walter, T. R. (2009). Volcano spreading and fault interaction influenced by rift zone intrusions: insights from analogue experiments analyzed with digital image correlation technique. *J. Volcanol. Geother. Res.* 183, 170–182. doi: 10.1016/j.jvolgeores.2009.02.006

Li, L., and Morgan, E. F. (2009). Accuracy and precision of digital volume correlation in quantifying displacements and strains in trabecular bone. *J. Biomech.* 40, 3516–3520. doi: 10.1016/j.jbiomech.2007.04.019

Lohrmann, J., Kukowski, N., Adam, J., and Oncken, O. (2003). The impact of analogue material properties on the geometry, kinematics, and dynamics of convergent sand wedges. *J. Struct. Geol.* 25, 1691–1711. doi: 10.1016/S0191-8141(03)00005-1

Long, S. M., and Grosfils, E. B. (2009). Modeling the effect of layered volcanic material on magma reservoir failure and associated deformation, with application to Long Valley Caldera, California. *J. Volcanol. Geother. Res.* 186, 349–360. doi: 10.1016/j.jvolgeores.2009.05.021

Lundgren, P., Poland, M., Miklius, A., Orr, T., Yun, S. H., Fielding, E., et al. (2013). Evolution of dike opening during the march 2011 kamoamoa fissure eruption, Kilauea Volcano, Hawai'i. *J. Geophys. Res.* 118, 897–914. doi: 10.1002/jgrb.50108

Maccaferri, F., Rivalta, E., Passarelli, L., and Aoki, Y. (2015). On the mechanisms governing dike arrest: insight from the 2000 miyakejima dike injection. *Earth Planetary Sci. Lett.* 1, 1–11. doi: 10.1016/j.epsl.2015.11.024

Magee, C., Stevenson, C. T. E., Ebmeier, S. K., Keir, D., Hammond, J. O. S., Gottsmann, J. H., et al. (2018). Magma plumbing systems: a geophysical perspective. *J. Petrol.* 59, 1–35. doi: 10.1093/petrology/egy064

Manconi, A., Walter, T. R., and Amelung, F. (2007). Effects of mechanical layering on volcano deformation. *Geophys. J. Int.* 170, 952–958. doi: 10.1111/j.1365-246X.2007.03449.x

Marti, J., Ablay, G. J., Redshaw, L. T., and Sparks, R. S. J. (1994). Experimental study of collapse calderas. *J. Geol. Soc.* 151, 919–929. doi: 10.1144/gsjgs.151.6.0919

Mastin, L. G., and Pollard, D. D. (1988). Surface deformation and shallow dike intrusion processes at inyo craters, Long Valley, California. *J. Geophys. Res.* 93, 13221–13235. doi: 10.1029/JB093iB11p13221

Mathieu, L., van Wyk de Vries, B., Holohan, E. P., and Troll, V. R. (2008). Dykes, cups, saucers and sills: analogue experiments on magma intrusion into brittle rocks. *Earth Planetary Sci. Lett.* 271, 1–13. doi: 10.1016/j.epsl.2008.02.020

Mees, F., Swennen, R., Van Geet, M., and Jacobs, P. (2003). *Applications of X-Ray Computed Tomography in the Geosciences.* London: Geological Society of London Special Publications. 7.

Merle, O. (2015). The scaling of experiments on volcanic systems. *Front. Earth Sci.* 3, 1–15. doi: 10.3389/feart.2015.00026

Mogi, K. (1958). Relations between the eruptions of various volcanoes and the deformations of the ground surfaces around them*Earthq. Res. Inst*. 36, 99–134.

Mourgues, R., and Cobbold, P. R. (2003). Some tectonic consequences of fluid overpressures and seepage forces as demonstrated by sandbox modelling. *Tectonophysics* 376, 75–97. doi: 10.1016/S0040-1951(03)00348-2

Mourgues, R., Gressier, J. B., Bodet, L., Bureau, D., and Gay, A. (2011). 'Basin Scale' versus 'Localized' pore pressure/stress coupling - implications for trap integrity evaluation. *Marine Petrol. Geol.* 28, 1111–1121. doi: 10.1016/j.marpetgeo.2010.08.007

Muirhead, J. D., Airoldi, G., Rowland, J. V., and White, J. D. L. (2012). Interconnected sills and inclined sheet intrusions control shallow magma transport in the ferrar large igneous province, Antarctica. *Bull. Geol. Soc. Am.* 124, 162–180. doi: 10.1130/B30455.1

Okada, Y. (1985). Surface deformation due to shear and tensile faults in a half space. *Bull. Seismol. Soc. Am.* 75, 1135–1154.

Panien, M., Schreurs, G., and Pfiffner, A. (2006). Mechanical behaviour of granular materials used in analogue modelling: insights from grain characterisation, ring-shear tests and analogue experiments. *J. Struct. Geol.* 28, 1710–1724. doi: 10.1016/j.jsg.2006.05.004

Pannier, Y., Lenoir, N., and Bornert, M. (2010). Discrete volumetric digital image correlation for the investigation of granular type media at microscale: accuracy assessment. *EPJ Web Conferences* 6:35003. doi: 10.1051/epjconf/20100635003

Peltier, A., Froger, J. L., Villeneuve, N., and Catry, T. (2017). Assessing the reliability and consistency of InSAR and GNSS data for retrieving 3D-displacement rapid changes, the example of the 2015 piton de la fournaise eruptions. *J. Volcanol. Geother. Res.* 344: 106–120. doi: 10.1016/j.jvolgeores.2017.03.027

Pinel, V., Poland, M. P., and Hooper, A. (2014). Volcanology: lessons learned from synthetic aperture radar imagery. *J. Volcanol. Geother. Res.* 289, 81–113. doi: 10.1016/j.jvolgeores.2014.10.010

Poland, M. P., Peltier, A., Bonforte, A., and Puglisi, G. (2017). The spectrum of persistent volcanic flank instability: a review and proposed framework based on kilauea, Piton de La Fournaise, and Etna. *J. Volcanol. Geother. Res.* 339, 63–80. doi: 10.1016/j.jvolgeores.2017.05.004

Pollard, D. D., Delaney, P. T., Duffield, W. A., Endo, E. T., and Okamura, A. T. (1983). Surface deformation in volcanic rift zones. *Tectonophysics* 94, 541–584. doi: 10.1016/0040-1951(83)90034-3

Pollard, D. D., Otto, H. M., and Dockstader, D. R. (1975). The form and growth of fingered sheet intrusions. *GSA Bull.* 86, 351–363. doi: 10.1130/0016-7606(1975)86<351:TFAGOF>2.0.CO;2

Poppe, S., Holohan, E. P., Pauwels, E., Cnudde, V., and Kervyn, M. (2015). Sinkholes, pit craters, and small calderas: analog models of depletion-induced collapse analyzed by computed X-ray microtomography. *Bull. Geol. Soc. Am.* 127, 281–96. doi: 10.1130/B30989.1

Rincón, M., Márquez, A., Herrera, R., Alonso-Torres, A., Granja-Bruña, J. L., and van Wyk de Vries, B. (2018). Contrasting catastrophic eruptions predicted by different intrusion and collapse scenarios. *Scient. Rep.* 8:6178. doi: 10.1038/s41598-018-24623-5

Ritter, M. C., Leever, K., Rosenau, M., and Oncken, O. (2016). Scaling the sandbox—mechanical (dis) similarities of granular materials and brittle rock. *J. Geophys. Res.* 121, 6863–6879. doi: 10.1002/2016JB012915

Rivalta, E., Taisne, B., Bunger, A. P., and Katz, R. F. (2015). A review of mechanical models of dike propagation: schools of thought, results and future directions. *Tectonophysics* 638, 1–42. doi: 10.1016/j.tecto.2014.10.003

Ruch, J., Wang, T., Xu, W., Hensch, M., and Jónsson, S. (2016). Oblique rift opening revealed by reoccurring magma injection in central iceland. *Nat. Comm.* 7:12352. doi: 10.1038/ncomms12352

Schmiedel, T., Galland, O., and Breitkreuz, C. (2017). Dynamics of sill and laccolith emplacement in the brittle crust: role of host rock strength and deformation mode. *J. Geophys. Res.* 122, 8860–8871. doi: 10.1002/2017JB014468

Schofield, N. J., Brown, D. J., Magee, C., and Stevenson, C. T. (2012). Sill morphology and comparison of brittle and non-brittle emplacement mechanisms. *J. Geol. Soc.* 169, 127–141. doi: 10.1144/0016-76492011-078

Schreurs, G., Hanni, R., Panien, M., and Vock, P. (2003). Analysis of analogue models by helical X-ray computed tomography. *Geol. Soc.* 215, 213–223. doi: 10.1144/GSL.SP.2003.215.01.20

Schultz, R. A. (1996). Relative scale and the strength and deformability of rock masses. *J. Struct. Geol.* 18, 1139–1149. doi: 10.1016/0191-8141(96)00045-4

Sigmundsson, F., Hooper, A., Hreinsdóttir, S., Vogfjörd, K. S., Ófeigsson, B. G., Heimisson, E. R., et al. (2014). Segmented lateral dyke growth in a rifting event at Bárðarbunga volcanic system, iceland. *Nature* 517, 119–195. doi: 10.1038/nature14111

Sigmundsson, F., Parks, M., Pedersen, R., Jónsdóttir, K., Ófeigsson, B. G., Grapenthin, R., et al. (2018). Magma movements in volcanic plumbing systems and their associated ground deformation and seismic patterns. *Volcan. Igneous Plumbing Syst.* 285–322. doi: 10.1016/B978-0-12-809749-6.00011-X

Spacapan, J. B., Galland, O., Leanza, H. A., and Planke, S. (2017). Igneous sill and finger emplacement mechanism in shale-dominated formations: a field study at cuesta del chihuido, Neuquén Basin, Argentina. *J. Geol. Soc.* 174, 422–433. doi: 10.1144/jgs2016-056

Tibaldi, A. (2015). Structure of volcano plumbing systems: a review of multi-parametric effects. *J. Volcanol. Geother. Res.* 298, 85–135. doi: 10.1016/j.jvolgeores.2015.03.023

Townsend, M. R., Pollard, D. D., and Smith, R. P. (2017). Mechanical models for dikes: a third school of thought. *Tectonophysics*. 703, 98–118. doi: 10.1016/j.tecto.2017.03.008

Trippanera, D., Ruch, J., Acocella, V., and Rivalta, E. (2015). Experiments of dike-induced deformation: insights on the long-term evolution of divergent plate boundaries. *J. Geophys. Res. B* 120, 6913–6942. doi: 10.1002/2014JB011850

van Mechelen, J. L. M. (2004). Strength of moist sand controlled by surface tension for tectonic analogue modelling. *Tectonophysics* 384, 275–284. doi: 10.1016/j.tecto.2004.04.003

Wauthier, C., Cayol, V., Kervyn, F., and D'Oreye, N. (2012). Magma sources involved in the 2002 nyiragongo eruption, as inferred from an InSAR analysis. *J. Geophys. Res.* 117, 1–20. doi: 10.1029/2011JB008257

Yang, X. M., Davis, P. M., and Dieterich, J. H. (1988). Deformation from inflation of a dipping finite prolate spheroid in an elastic half- space as a model for volcanic stressing. *J. Geophys. Res. Solid Earth* 93, 4249–4257.

Yoo, T. S., Ackerman, M. J., Lorensen, W. E., Schroeder, W., Chalana, V., Aylward, S., et al. (2002). Engineering and algorithm design for an image processing api: a technical report on ITK–the insight toolkit. *Studies Health Technol. Informat.* 85, 586–592.

Zwaan, F., Schreurs, G., and Adam, J. (2018). Effects of sedimentation on rift segment evolution and rift interaction in orthogonal and oblique extensional settings: insights from analogue models analysed with 4D X-ray computed tomography and digital volume correlation techniques. *Global Planetary Change* 171, 110–133. doi: 10.1016/j.gloplacha.2017.11.002

Conflict of Interest Statement: DH and AN were both employed by company LaVision UK Ltd.

The remaining authors declare that the research was conducted in the absence of any commercial or financial relationships that could be construed as a potential conflict of interest.

Advantages of publishing in Frontiers

OPEN ACCESS
Articles are free to read
for greatest visibility
and readership

FAST PUBLICATION
Around 90 days
from submission
to decision

HIGH QUALITY PEER-REVIEW
Rigorous, collaborative,
and constructive
peer-review

TRANSPARENT PEER-REVIEW
Editors and reviewers
acknowledged by name
on published articles

Frontiers
Avenue du Tribunal-Fédéral 34
1005 Lausanne | Switzerland

Visit us: www.frontiersin.org
Contact us: info@frontiersin.org | +41 21 510 17 00

REPRODUCIBILITY OF RESEARCH
Support open data
and methods to enhance
research reproducibility

DIGITAL PUBLISHING
Articles designed
for optimal readership
across devices

FOLLOW US
@frontiersin

IMPACT METRICS
Advanced article metrics
track visibility across
digital media

EXTENSIVE PROMOTION
Marketing
and promotion
of impactful research

LOOP RESEARCH NETWORK
Our network
increases your
article's readership